

High Density Frequency Mapping of Human
Intracardiac Persistent Atrial Fibrillation
Electrograms

Thesis submitted for the degree of
Doctor of Philosophy
at the University of Leicester

By
João Loures Salinet Júnior

December 2013

High Density Frequency Mapping of Human Intracardiac Atrial Fibrillation Electrograms

João Loures Salinet Júnior

ABSTRACT

Atrial fibrillation (AF) is the most common heart rhythm disturbance. Once AF is initiated, dynamic alterations of atrial electrophysiological properties occur invoking, in turn, AF inducibility. In patients for whom AF persists for long-term periods (persAF), identification of critical areas for successful ablation remains a challenge. Improving our understanding of the underlying AF behaviour is a key factor to contribute towards improving patient outcome. In this research, spectral analysis of simultaneous high density non-contact unipolar intracardiac atrial electrograms (AEGs) recorded from the left atrium (LA) of persAF patients (AF duration 34 ± 25 months) was applied after a coherent strategy of cancellation of the ventricular influence on the AEGs. Three-dimensional dominant frequency (DF) maps with 2048 measurement points from AEGs were generated over consecutive frames of up to 1 minute (windows of 4s with 50% overlap). The results of this thesis showed a lack of DF spatiotemporal stability, demonstrating that AF mapping would be preferable performed using simultaneous multipolar recordings. Although DF is not stable, a certain degree of DF reappearance was observed, mostly within 10 s. The spatiotemporal analysis of areas thought to be playing a role in AF maintenance, highest DF areas (HDFAs), revealed presence of three distinct patterns with predominance of cyclic behaviour (61.2 ± 12.4 % of the time) followed by local (27.0 ± 8.6 %) and irregular behaviour (11.9 ± 9.1 %), mostly concentrated in the LA roof and the pulmonary veins. Independently of the trajectory of the HDFAs, the regions located next to the HDFAs' core presented higher DF organisation than areas by the HDFAs' periphery ($p=0.0061$) providing further insight into the potential mechanisms of persAF. The research has demonstrated the importance of DF mapping as an auxiliary tool contributing to the investigation of persAF patients and would help clinicians to better understand the AF mechanisms. Real-time implementation was shown to be feasible with the use of Graphic Processing Units, where the processing time was 15 times faster than real time, representing an innovation that could have considerable impact on clinical practice, as part of the decision making process for persAF treatment.

ACKNOWLEDGEMENTS

I would like to thank God for being a live presence in my life.

I want to express a special thanks to my supervisor Dr. Fernando S. Schindwein and co-supervisor Prof G. André Ng for their excellent support, supervision, partnership and character. I know that without their advice and experience, the work would be even harder.

I am truly grateful and in debt to the people who worked with me in the Bioengineering and Cardiology Groups throughout these years. They were definitely essential for the success of this work and sharing the merits of this research with them is the minimum that I could do.

Finally, but by no means least, I want to express a very special thanks to my always present lovely wife, Angela, for her commitment, partnership, patience and suggestions. Thank you for making me do better. To my parents, João and Maria Eliza and my sisters and brother, Janaina, Juliana and Jivago for teaching me all the tools needed to pursue my dreams making the difference and for Eduardo Costa, Sandra and Carlos César for being part of it.

Thanks to my sponsor The National Council for Scientific and Technological Development (CNPq) of Brazil, Ministry and Technology (MCT), process n°. 200598/2009-0 for not just supporting me in this research, but also allowing me to contribute with several other Brazilians.

Dedicated to my family,

Angela, João, Maria Eliza, Cibele, Janaina, Juliana, Jivago e Lara

In memoriam of Cinira Nallin Salinet and Carlos César Castro Costa

LIST OF PUBLICATIONS

Journals

Ahmad, A., Salinet Jr, J.L., Brown, P., Tuan, J.H., Stafford, P.J., Ng, G.A., Schlindwein, F.S. (2011). "QRS subtraction for atrial electrograms: flat, linear and spline interpolation" *Medical & Biological Engineering & Computing* 49:1321-1328

Salinet Jr, J.L., Oliveira, G., Vanheusden, F., Comba, J.L.D., Ng, G.A., Schlindwein, F.S. (2013). "Visualization of intracardiac atrial electrograms of patients with atrial fibrillation using spectral analysis" *Computing in Science & Engineering* 15(2): 79-87

Salinet Jr, J.L., Madeiro, J.P.V., Cortez, P.C., Stafford, P., Ng, G.A., Schlindwein, F.S. (2013). "Analysis of QRS-T Subtraction in atrial fibrillation electrograms" *Medical & Biological Engineering & Computing* 51:1381-1391

Salinet, J.L., Tuan, J.H., Sandilands, A.J., Stafford, P.J., Schlindwein, F.S., Ng, G.A., (2013). "Distinctive patterns of dominant frequency trajectory behaviour in drug-refractory persistent atrial fibrillation: Preliminary characterisation of spatio-temporal instability" *Journal of Cardiovascular Electrophysiology* (In Press) DOI 10.1111/jce.12331

Salinet Jr, J.L., Brown, P., Masca, N., Ng, G.A., Schlindwein, F.S. (2013). "Autoregressive Spectral Estimation and Model Order Selection for Atrial Fibrillation Signals" *Medical & Biological Engineering & Computing* (Submitted June-2013)

Academic and research prizes

Student Santander Travel Awards 2012/2013

Shortlisted to Young Investigators Competition (3 investigators) Heart Rhythm Congress 2012. "Distinctive Patterns of Dominant Frequency Trajectory Behaviour Exist in Persistent Atrial Fibrillation: Characterisation of Spatio-Temporal Instability"

David Holme Memorial Prize 2012. Engineering Department, University of Leicester. "Multiple Distinct Behaviours of Trajectory Propagation Paths in Patients with Atrial Fibrillation". BEng Student Joseph Ahuja (Co-supervisor: Salinet Jr, J.L.)

Project Presentation Prize 2011. Engineering Department, University of Leicester. "Signal Processing of Atrial Fibrillation". BEng Student Samuel Bidder (Co-supervisor: Salinet Jr, J.L.)

Mech. E Best Project Prize 2011. Engineering Department, University of Leicester. "Signal Processing of Atrial Fibrillation". BEng Student Samuel Bidder (Co-supervisor: Salinet Jr, J.L.)

Conferences

Salinet Jr, J.L., Ahmad, A., Brown, P., Stafford, P.J., Ng, G.A., Schlindwein, F.S. (2010). "Three-dimensional frequency mapping from the non-contact unipolar electrograms in atrial fibrillation" Computers in Cardiology (Computing in Cardiology) IEEE Xplore Digital Library 745-748

Salinet Jr, J.L., Tuan, J.H., Brown, P., Stafford, P.J., Ng, G.A., Schlindwein, F.S. (2010). "The spatial and temporal variability of 3D dominant frequency mapping from 2048 noncontact unipolar electrograms in human atrial fibrillation" Heart Rhythm Congress. Europace 12(suppl 2) ii22

Salinet Jr, J.L., Brown, P., Bidder, S., Stafford, P.J., Ng, G.A., Schlindwein, F.S. (2011). "Where Engineering meets Medicine: New treatment hope for the most common cardiac arrhythmia" House of Commons, Parliament, London

Salinet Jr, J.L., Brown, P., Ahmad, A., Tuan, J.H., Stafford, P.J., Schlindwein, F.S., Ng, G.A. (2011). "High density noncontact frequency mapping reveals distinct dominant frequency behaviour in persistent atrial fibrillation" Heart Rhythm 8(suppl 5) S146

Salinet Jr, J.L., Brown, P., Lohiya, G.R., Bidder, S., Stafford, P.J., Schlindwein, F.S., Ng, G.A. (2011). "Evidence for cyclic temporal variability from high frequency re-entrant circuits in persistent atrial fibrillation" Heart Rhythm Congress. Europace 13 iv20-iv24

Salinet Jr, J.L., Ahuja, J., Brown, P., Stafford, P.J., Schlindwein, F.S., Ng, G.A. (2012). "Trajectory propagation of dominant frequency areas using high density noncontact mapping reveals distinct behaviour in persistent atrial fibrillation" Heart Rhythm 9 (Suppl 5) S4-S5

Salinet Jr, J.L., Marques, J.A.L., Tuan, J.H., Stafford, P.J., Schlindwein, F.S., Ng, G.A. (2012). "A new approach to identify and measure fractionated atrial electrograms" Heart Rhythm 9 (Suppl 5) S365-S366

Salinet Jr, J.L., Tuan, J.H., Sandilands, A.J., Madeiro, J.P.V., Stafford, P.J., Schlindwein, F.S., Ng, G.A. (2012). "Distinctive patterns of dominant frequency trajectory behaviour exist in persistent atrial fibrillation: Characterisation of spatio-temporal instability" Heart Rhythm Congress. Young Investigator Competition. Europace 14(suppl 4) iv3

Salinet Jr, J.L., Stafford, P.J., Ng, G.A., Schlindwein, F.S. (2012). "*Distinct patterns in the most common clinical arrhythmia: What is the mechanism?*" XXIII Congresso Brasileiro de Engenharia Biomédica 1-6

Salinet Jr, J.L., Marques, J.A.L., Cortez, P.C., Marques, J.A.L., Stafford, P.J., Ng, G.A., Schlindwein, F.S. (2012). "*Removing ventricular influence from intracardiac atrial fibrillation electrograms*" XXIII Congresso Brasileiro de Engenharia Biomédica 1984-1988

Salinet Jr, J.L., Tuan, J.H., Stafford, P.J., Schlindwein, F.S., Ng, G.A. (2013). "*High Density Noncontact Mapping of Persistent Atrial Fibrillation: Spatiotemporal Characteristics of Dominant Frequency and Organization Index During Sequential Mapping*" Heart Rhythm 10 (Suppl 5) S1-S2

Almeida, T. P., Salinet Jr, J.L. Chu, G., Tuan, J.H., Schlindwein, F.S., Ng, G.A. (2013). "*Atrial electrogram complexity as an objective measurement of fractionation during atrial fibrillation*" Heart Rhythm 10 (Suppl 5) S2

Almeida, T. P., Salinet Jr, J.L. Chu, G., Ng, G.A., Schlindwein, F.S., (2013). "*Different definitions of complex fractionated atrial electrograms do not concur with clinical perspective*" Computers in Cardiology (Computing in Cardiology) September 2013

Almeida, T. P., Salinet Jr, J.L. Chu, G., Ng, G.A., Schlindwein, F.S., (2013). "*Atrial electrogram complexity as a clinical instrument for measuring temporal fractionation variability during atrial fibrillation*" Heart Rhythm Congress October 2013

Other Publications:

Vanheusden, F., Salinet Jr, J.L. et al. (2012). "*Patient-Specific Three-Dimensional Torso Models for Analysing Cardiac Activity*" Computers in Cardiology (Computing in Cardiology) IEEE Xplore Digital Library 973-976

Vanheusden, F., Salinet Jr, J.L. et al. (2012). "*Structured 3D Finite Element Torso Models for Cardiac Activity Analysis*" Bioengineering Society Conference

CONTENTS

ABSTRACT	II
ACKNOWLEDGEMENTS.....	III
LIST OF PUBLICATIONS.....	V
LIST OF TABLES	XIII
LIST OF FIGURES.....	XIV
LIST OF ABBREVIATIONS.....	XX
1. RESEARCH INTRODUCTION	1
1.1. NORMAL HEART (ATRIUM).....	2
1.1.1. <i>Anatomy of the Atrium</i>	2
1.1.2. <i>Physiology of the Atrium</i>	4
1.1.2.1. <i>Characteristics of the Cell Membrane and Channels</i>	4
1.1.3. <i>Factors which may affect the Natural Order of the Cell Membrane, Action Potential and Atrium Electrical Propagation</i>	13
1.2. ATRIAL FIBRILLATION	16
1.2.1. <i>Epidemiology</i>	16
1.2.2. <i>Economic Aspects</i>	17
1.2.3. <i>Definition of AF and Collateral effects</i>	17
1.2.4. <i>Classification of AF</i>	18
1.2.5. <i>Classical Mechanisms of AF: historical perspective</i>	20
1.2.6. <i>Current Clinical Treatments</i>	28
1.3. SPECTRAL ANALYSIS ON AF ELECTROGRAMS.....	33
1.4. ELECTROANATOMICAL MAPPING SYSTEMS.....	37
1.4.1. <i>Contact Mapping</i>	39
1.4.2. <i>Noncontact Mapping</i>	41
1.4.3. <i>Intracardiac Electrogram Recording and Morphology</i>	46
1.5. SPECTRAL ANALYSIS	50

1.5.1.	<i>Electrogram pre-processing prior to spectral Analysis</i>	50
1.5.2.	<i>AF frequency range</i>	51
1.5.3.	<i>Discrete Fourier Transform and Fast Fourier Transform Technique</i>	51
1.5.4.	<i>FFT window size</i>	52
1.5.5.	<i>Anti-leakage window</i>	53
1.5.6.	<i>Zero Padding</i>	53
1.5.7.	<i>Dominant Frequency 'Organisation' Indices</i>	54
1.5.8.	<i>DF estimation of noncontact electrograms vs. current contact mapping techniques</i> ...	55
1.5.9.	<i>Limitations</i>	56
1.6.	<i>Study Design</i>	57
1.6.1.	<i>Recruitment</i>	57
1.6.2.	<i>Ethical Approval</i>	59
1.6.3.	<i>Electrophysiological study</i>	59
1.6.4.	<i>Study Population's characteristics</i>	60
1.6.5.	<i>Filter settings</i>	61
1.6.6.	<i>Electrograms</i>	61
1.6.7.	<i>Ventricular Far-field influence subtraction</i>	61
1.6.8.	<i>FFT Specifications</i>	62
1.7.	<i>THESIS OUTLINE</i>	64
1.7.1.	<i>Aims</i>	64
1.7.2.	<i>Overview of the Coming chapters</i>	65
2.	THREE-DIMENSIONAL ATRIUM MAPPING REPRESENTATION	67
2.1.	<i>INTRODUCTION</i>	67
2.2.	<i>METHODS</i>	67
2.2.1.	<i>Three-dimensional representation of the patient's endocardium</i>	67
2.2.2.	<i>Colouring the Atrium: 3D colour coded representation</i>	70
2.3.	<i>DEVELOPMENT OF VIDEOS AS AN AUXILIARY TOOL FOR AF INVESTIGATIONS</i>	77
2.4.	<i>CONCLUSIONS</i>	79
3.	ANALYSIS OF QRS-T SUBTRACTION IN ATRIAL FIBRILLATION ELECTROGRAMS	80
3.1.	<i>INTRODUCTION</i>	80

3.2.	METHODS	82
3.2.1.	<i>Proposed QRS-T cancellation method</i>	82
3.2.2.	<i>Time and frequency analysis approaches used to compare the cancellation methods</i>	90
3.3.	RESULTS.....	97
3.3.1.	<i>Time domain analysis</i>	97
3.3.2.	<i>Frequency domain analysis</i>	98
3.4.	DISCUSSION.....	101
3.5.	CONCLUSIONS.....	104
4. DISTINCTIVE PATTERNS OF DOMINANT FREQUENCY TRAJECTORY BEHAVIOUR EXIST IN PERSISTENT ATRIAL FIBRILLATION: CHARACTERISATION OF SPATIO-TEMPORAL INSTABILITY		106
4.1.	INTRODUCTION	106
4.2.	METHODS	107
4.2.1.	<i>Signal Processing</i>	107
4.2.2.	<i>Temporal DF Analysis</i>	107
4.2.3.	<i>Spatiotemporal Analysis</i>	108
4.3.	STATISTICAL ANALYSIS.....	109
4.4.	RESULTS.....	109
4.4.1.	<i>Temporal Stability analysis</i>	109
4.4.2.	<i>Reappearance of the DF</i>	114
4.4.3.	<i>Highest DF area and its trajectory</i>	117
4.5.	DISCUSSION.....	123
4.5.1.	<i>Significance of DF mapping</i>	123
4.5.2.	<i>Spatiotemporal stability</i>	123
4.5.3.	<i>3D Trajectory mapping</i>	126
4.5.4.	<i>Significance of findings and clinical implications</i>	127
4.5.5.	<i>Limitations</i>	128
4.6.	CONCLUSIONS.....	130
5. AUTOREGRESSIVE SPECTRAL ESTIMATION AND MODEL ORDER SELECTION FOR FREQUENCY MAPPING OF UNIPOLAR ATRIAL FIBRILLATION SIGNALS		131
5.1.	INTRODUCTION.....	131

5.2.	METHODS	132
5.2.1.	<i>Data Collection</i>	132
5.2.2.	<i>Spectrum Analysis</i>	132
5.2.3.	<i>Autoregressive Model Analysis</i>	133
5.2.4.	<i>Order Selection Criteria</i>	139
5.2.5.	<i>Statistical Analysis</i>	140
5.3.	RESULTS.....	141
5.3.1.	<i>Selection of Model Order for AF Signals</i>	143
5.3.2.	<i>Spectral Analysis and 3D DF Mapping</i>	146
5.4.	DISCUSSION	153
6.	REAL-TIME FREQUENCY MAPPING VISUALISATION USING GPUS	157
6.1.	INTRODUCTION	157
6.2.	MATERIALS AND METHODS.....	158
6.2.1.	<i>Hardware</i>	158
6.2.2.	<i>Signal Processing</i>	159
6.2.3.	<i>Frequency Mapping & Parallel Processing</i>	159
6.2.4.	<i>3D Frequency Mapping Visualization</i>	160
6.2.5.	<i>Processing Time</i>	160
6.3.	RESULTS.....	160
6.3.1.	<i>Processing Time</i>	160
6.3.2.	<i>Frequency Mapping Visualization</i>	162
6.4.	DISCUSSION	167
6.5.	CONCLUSION.....	168
7.	MAIN FINDINGS, ORIGINAL CONTRIBUTIONS AND FUTURE RESEARCH ACTIVITIES	170
7.1.	INTRODUCTION	170
7.2.	MAIN FINDINGS OF THE THESIS	170
7.3.	FUTURE RESEARCH OPPORTUNITIES.....	173
7.3.1.	<i>Phase Analysis</i>	173
7.3.2.	<i>Real Time DF ablation in Persistent AF Patients</i>	175
7.3.3.	<i>Three-dimensional Complex Fractionated Atrial Electrograms (3D CFAE maps)</i>	177

7.3.4.	<i>Wavelet Transform: analysis of nonstationary signals</i>	178
7.3.5.	<i>Nonlinear Analysis in Atrial Fibrillation</i>	179
APPENDIX		180
REFERENCES		190

LIST OF TABLES

Table 1.1 Patients' characteristics.....	60
Table 3.1 Population averaged ratio between the frequency components in the range [5.5-12 Hz] and [3-5.5 Hz] for each QRS-T subtraction approach and each atrial region.	100
Table 3.2 Ratio between the frequency components in the range [5.5 – 12Hz] and [3-5.5Hz] for each QRS-T subtraction method for the average of the entire LA.	100
Table 4.1 Overall DF temporal stability (time constant) and DF reappearance analyses of the 2048 simultaneous AEGs calculated for both DF thresholds (0.25 Hz and 0.5Hz).....	116
Table 4.2 Percentage of the time spent on each trajectory pattern for both short term (20 s) and long term (1 min) analysis during HDFAs trajectory propagation.	122
Table 5.1 Summary of the results of the estimation of 'optimum' AR model order for the Fs values tested.	146
Appendix Table 1 Overall DF and OI temporal stability (time constant)	184
Appendix Table 2 Degree of DF organisation at their core (OI_{CG}) vs. at the periphery (OI_{per})	189

LIST OF FIGURES

Figure 1.1 AP phases. Modified and used with permission from (Ahmad, 2011)	8
Figure 1.2 Different AP morphologies from the heart. With permission (Nerbonne and Kass, 2005)	9
Figure 1.3 Temporal Classification of AF. Modified from (Waktare and Camm, 2000)	20
Figure 1.4 Schematic drawing for (a) the normal rhythm cycle excitation and (b) an arrhythmic cycle excitation: the excited state is represented in dark red and the refractory state as dotted areas. In (a), the recirculation can't occur, because when the stimulation completes a cycle, the cells at that point are still refractory and can't re-trigger. In (b), re-triggering can occur with either a shorter refractory period and/or slower conduction, allowing the development of a circulating wave. Modified from (Mines, 1913)	22
Figure 1.5 The anatomical and arrhythmic mechanisms of AF. Reprinted by permission from Macmillan Publishers Ltd: [Nature Reviews Cardiology] (State-of-the-art and emerging technologies for AF ablation), Copyright (2010).....	28
Figure 1.6 The ablation catheter and the Ensite 3000 balloon array are first used to map the inner surface of the heart's chamber using the ablation catheter as a probe and the two tips of the balloon as a reference. Then the array collects atrial electrograms (potentials) at 1200 Hz. The system can display the potentials as a colour map. (Ensite array and Ensite are trademarks of St. Jude Medical or its related companies. This image is reprinted with permission of St. Jude medical, © 2012. All rights reserved.)	44
Figure 1.7 The activation voltage images (in the time domain) produced using the Ensite 3000 array. Two different views are presented simultaneously and can be independently reoriented by the clinician performing the EP study (in theatre), in preparation for the ablation.	44
Figure 1.8 Illustrative example of how a single channel is activated by wavefront propagation to characterize unipolar morphology.	47
Figure 1.9 Prof. G. André Ng during catheter ablation of an AF patient. The various computer screens show the fluoroscopy image of the catheters located inside the heart, the 3D image of the LA generated by the EP system and the selected electrograms over time from the areas under investigation.....	58

Figure 2.1 Typical example of a file exported from Ensite System 3000 for off-line analysis. Only the first 23 of the 2048 columns are shown..... 68

Figure 2.2 Diagram to generate the 3D endocardium surface of the LA colour-coded automatically by Matlab. The respective surface generated through the EnSite 3000 system during the clinical procedure is also presented. The colours are the Matlab representation of position in this case, but will be used to display the behaviour of a selected parameter (say 'DF', for example)..... 69

Figure 2.3 Diagram showing the steps to colour-code the 3D atrium's endocardium representation. Each matrix R element (64x32) corresponds to a particular spot of the 3D atrium. The element values are ranked according to colours where in this case, the lowest value receives colour purple and the highest red. 70

Figure 2.4 Spectral analysis methodology of the electrogram. The data collected by the Ensite 3000 system allow manipulation of the atrium on the screen (e.g. Rotating the 3D surface). We obtain the DF of the atrial electrograms for each segment along time and then colour code the surface according to the frequency of the each point (surface element). 72

Figure 2.5 3D DF mapping of the LA with two different views of the 3D DF mapping. RLPV is 'right lower PV', RUPV is 'right upper PV' and MV 12 is 'MV' in the 12 o'clock position..... 73

Figure 2.6 Sequence of 16 consecutive 3D DF mapping frames that are 2 seconds apart for each representation. 74

Figure 2.7 A sequence of three consecutive DF maps with an overlap of 97.5% (62.5 ms step between consecutive frames) showing a relative stable frequency distribution over the period displayed. 75

Figure 2.8 3D DF mapping and highest DF identification. (left-hand side) 3D representation including the mapping of the DFs. The DF mapping which will allow doctors to visualize the behaviour of the atrium's electrical activation in the frequency domain. (right-hand side) the system can also automatically identify the region corresponding to the HDFA..... 76

Figure 2.9 DF organisation from the HDFAs in two different positions: at the core and periphery. 77

Figure 2.10 Snapshots of a video presented at the Heart Rhythm 2012 (Salinet Jr *et al.*, 2012c). 78

Figure 3.1 General block diagram for the proposed QRS-T subtraction method..... 82

Figure 3.2 Detection of the QRS onset: (a) sliding moving window (WL) used to calculate the maximum area of the surface indicator $A[n]$ on the QRS envelope $E[n]$, (b) time position of the maximum value of the $A[n]$, and (c) respective time position identification of the QRS onset based at the beginning of the QRS envelope..... 85

Figure 3.3 General schematic diagram to calculate the QRS-T pattern. 88

Figure 3.4 VA detection: (a) QRS segmentation, (b) QRS-T segmentation using ABS, (c) QRS-T segmentation using the proposed method and (d) AEG simultaneously recorded with the ECG showing both QRS-T segmentation intervals (from b and c)..... 91

Figure 3.5 Ventricular subtraction in AEG signals: (a) AEG raw signal, (b) after QRS cancellation, (c) after QRS-T subtraction using ABS, (d) After QRS-T subtraction using the proposed method, e) QRS-T patterns for the proposed approach considering the intervals between 0-7s and 3s-10s respectively and (f) computed patterns calculated by the abs approach for the same intervals..... 93

Figure 3.6 Average spectrum of the Raw AEG and for each of the three subtraction methods in the following areas: close to PVs, roof, septum, close to the MV, and for the whole LA. 96

Figure 3.7 Frequency spectrum of the AEG of figure 3.4a compared between the different subtraction techniques: (a) proposed QRS-T subtraction (black trace) compared to raw signal (grey trace), (b) proposed QRS-T subtraction (black trace) compared to QRS subtraction only (grey trace), and (c) proposed QRS-T subtraction (black trace) compared to QRS-T/ABS technique (grey trace)..... 99

Figure 4.1 Plots of DF over time from single site AEGs. Examples of apparently stable (A) and unstable (B) DF behaviour in a patient are exhibited. Two longer recording examples showing transient stability of DF with subsequent fluctuations over time (C) and (D)..... 111

Figure 4.2 Sequence of 3D DF maps during AF for one patient and accompanying plot of percentage of stable DF points over time. It can be observed that the number of stable DF points out of 2048 AEGs decreases with time in an exponential pattern with time constants of 4.24 s and 9.79 s respectively for 0.25 Hz and 0.5 Hz thresholds. The 3D DF maps highlight the sites that remained temporally stable for 2 s, 6 s and 32 s within a threshold 0.25 Hz, with the sites that lost stability greyed out. (tags for RSPV, right superior PV): green, RLPV: blue, LSPV (left superior PV): brown and LLPV (left lower PV): cyan, not visible from this angle). 113

Figure 4.3 Illustration of the method used for DF reappearance analysis; every DF map within the duration of the recording is compared with a reference DF map within

the thresholds of ± 0.25 and ± 0.5 Hz for each of the 2048 points. This is carried out for every single point and repeated across the LA (a). An example of a DF map showing DF reappearance projected onto its 3D LA geometry is presented in (b) and also displayed as a 2D map (c) for better overall visualisation (at 4 s, 10 s and 18 s). Sites containing the higher DF values (in yellow and orange) at 4 s, no longer do so at 10 s, but reappear partially at 18 s (orange areas, for instance). The respective main lobe degree of DF reappearance for both thresholds is presented in (d)..... 114

Figure 4.4 Identification and tracking of the CG of the HDFA for a specific time segment (a). 3 types of behaviour were seen: type 1 - Localised (b), type 2 - Cyclical (c) and type 3 - Irregular (d). 118

Figure 4.5 DF reappearance analysis using different FFT window sizes. This shows a reduction in variability of DF with increasing windows size, giving rise to an impression of increased temporal DF stability..... 125

Figure 5.1 Illustration of the AEGs downsampling (DS) in the time domain with 9 different F_s values (from 600 Hz down to 37.5 Hz prior to spectral analysis). 133

Figure 5.2 Autocorrelation function of the residuals, calculated by the difference between the predicted sequence values by the AR modelling and the true signal sequence, showing that the residuals are random (or uncorrelated in time) falling inside of the 95% confidence interval (red lines) and close to zero at all lags except for lag zero. 134

Figure 5.3 AEG (raw signal) sampled at 1200 Hz (upper trace) and corresponding signal after down sampling 32 times ($F_s = 37.5$ Hz). PSD estimation of the raw signal using FFT, followed by the PSD of the down-sampled signal using AR YW approach with model orders $p=50$ and $p=18$ 142

Figure 5.4 AR model order estimation. (a) Histogram of 'optimum' AR model orders estimated for patient 1 for $F_s=75$ Hz over 20.478 seconds. (b) cumulative histogram of the estimation order for patient 1 for $F_s=75$ Hz over 20.478 s. (c) 'optimal' model order calculated using the technique CAT for various F_s values and 95% of confidence level. (d) 'optimal' model order using the same technique as presented in (c) now with the different confidence levels (95%, 90%, 85% and 80%). See text for details..... 144

Figure 5.5 Percentage of agreement between the DF calculated using FFT and the DF calculated using the AR spectral analyses techniques with different re-sampling frequencies for the 2048 AEGs during 20.478 second-long segments (3 consecutive windows of 6.826 s). Error bars represent 95% confidence intervals. 148

Figure 5.6 Percentage of agreement between the DF calculated using FFT and the DF calculated using the overall AR spectral analyses techniques with different re-sampling frequencies for the 2048 AEGs during AF for 20.478 second-long segments (3 consecutive windows of 6.826 s). Error bars represent 95% confidence intervals.....	149
Figure 5.7 3D representation of the DF maps using different techniques for spectral estimation: (a) FFT technique with the original Fs (1200 Hz); (b) AR – YW; (c) AR – Burg; (d) AR – Covariance and (e) AR – Modified Covariance. All AR methods used a re-sampled frequency of 37.5 Hz.	151
Figure 5.8 AR YW processing time.	152
Figure 6.1 (a) Comparison of processing times between single and multiple CPU cores and the GPU cores for a factor-2 zero-padding (frequency step of 0.125 Hz). (b) estimated processing time for different factors of zero-padding.....	162
Figure 6.2 3D DF mapping of the LA with two different views of the 3D DF mapping.	163
Figure 6.3 (a) Sequence of four consecutive 3D DF mapping frames that are 2 seconds apart for each representation (50% windows overlap). (b) consecutive DF maps using 92 % of overlapping between windows. Using more overlapping creates more frames and a smoother animation that helps to understand how the different DF zones evolve over the surface along time.	165
Figure 6.4 3D DF mapping and highest DF identification. (a) the LA’s 3D representation, including the mapping of the DFs. The DFs (represented in a colour scale) help doctors visualize the behaviour of the atrium’s electrical activation in the frequency domain in real time. (b) the system can also automatically identify the region corresponding to the HDFA.	166
Figure 6.5 3D DF mapping of the LA of a patient with persAF. (a) the baseline DF map. (b) the DF immediately after the standard PVI procedure. This figure demonstrates a general reduction of the size of the DF areas, a reduction of the DF values, and a reduction in the complexity of the DF areas after the PVI procedure in this case.	167
Figure 7.1 Colour code representation of the LA according to the phase analysis on the AEGs calculated using Hilbert Transform.....	175
Appendix Figure 1 Spectrum of an AF electrogram showing the DF and its harmonics. The OI is calculated by dividing the area of the DF and its harmonics by	

the total area of the AF spectrum range (see section 1.5.7 Dominant Frequency 'Organisation' Indices for more details). 181

Appendix Figure 2 Example of a 3D DF map with its respective 3D OI map. The OI values were obtained according to Equation 1.5 and illustrated in Figure 1. Both maps were generated simultaneously using the same colours range. 182

Appendix Figure 3 3D DF and OI maps focusing on the HDFAs identification. (left-hand side) 3D representation including the mapping of the DFs. (middle) The region with the HDFA is identified. (right-hand side) DF organisation from the HDFA showing that the OI at the core has a higher organisation when compared with its periphery. To calculate the OI_{CG} 25 points were selected: CG point in black and its 24 neighbours in light green. For OI_{Per} all points at boundary of the highest DF area were selected. 183

Appendix Figure 4 "H-DF-As correspond to Highest Dominant Frequency Areas". H-DF-As did not bear consistent spatial relationship with highest OI. (left-hand side) Case 1: HDFA (dark orange) presents higher DF organisation when compared with the remaining DF areas of the 3D DF frame. Looking inside of the HDFA there is a small area presenting even higher DF organisation. (right-hand side) HDFA (orange) presents lower OI but next to this area there is slight lower DF-value cloud (green) presenting much higher DF organisation..... 185

Appendix Figure 5 Percentage of stable DF and OI points over time. It can be observed that the number of stable DF and OI points out of 2048 AEGs decreases with time in an exponential pattern with time constants of 3.04 s and 2.37 s respectively for 0.25 Hz and 0.1 thresholds. 186

Appendix Figure 6 DF and OI mapping focusing on the HDFA identification. (left-hand side) 3D representation including the mapping of the DFs. (middle) The region with the HDFA is identified. (right-hand side) DF organisation from the HDFA shows that the OI at the core has a higher organisation when compared with its periphery. The electrogram of a point at the core and its spectrum are also presented and compared with a point at the periphery. 187

Appendix Figure 7 Another typical example showing the HDFA with a greater degree of organisation at the core (CG) compared to its periphery. 188

LIST OF ABBREVIATIONS

3D	three-dimensional
AA	atrial activity
ABS	average beat subtraction
AEG	unipolar noncontact intracardiac atrium electrograms
AF	atrial fibrillation
AIC	Akaike information criterion
AP	Action Potential
APD	action potential duration
AR	autoregressive
ARP	absolute refractory period
AV	atrioventricular
AW	anterior wall
CAT	criterion AR transfer function
CG	centre of gravity
CM	contact mapping
CS	coronary sinus
CUFFT	Nvidia CUDA fast Fourier transform library
DF	dominant frequency
EAM	electroanatomical mapping
EP	electrophysiology procedure
FIC	finite information criterion
FFT	fast Fourier transform

Fs	sampling frequency
GPU	graphic processor unit
HDFA	highest DF area
IVC	inferior vena cava
LA	left atrium
LAA	left atrium appendage
LLPV	left lower pulmonary vein
LSPV	left superior pulmonary vein
LV	left ventricle
MEA	noncontact multi-electrode array catheter
MV	mitral valve
ms	millisecond
NCM	noncontact mapping
OI	organisation index
persAF	persistent AF
PM	pectinate muscles
PS	phase singularity
PSD	power spectral density
PV	pulmonary vein
PVI	pulmonary vein isolation
PW	posterior wall
RA	right atrium
RF	radiofrequency
RLPV	right lower pulmonary vein
RMS	root mean square

RRP	relative refractory period
RSPV	right superior pulmonary vein
RUPV	right upper pulmonary vein
RV	right ventricle
SA	sinoatrial
SVC	superior vena cava
VA	ventricular activity
YW	Yule-Walker

1. RESEARCH INTRODUCTION

In this chapter the reader will be able to understand the differences in terms of biophysics and pathophysiology of a healthy atrium and one with atrial fibrillation (AF). Epidemiology, economic impact on the Health System's Budget and the AF mechanisms will be covered, together with the importance of using spectral analysis as an auxiliary tool to understanding the underlying mechanisms behind AF.

The principle of an Electroanatomical mapping (EAM) system and the different available systems on the market highlighting their advantages and disadvantages are also presented. In addition, two different types of intracardiac signals are introduced together with their intrinsic clinical characteristics and morphology.

The description of the most common spectral analysis techniques used to calculate the spectrum of the AF electrograms is presented together with the relevant AF frequency range and the electrograms' pre-processing prior to calculation of the DF.

Finally, the study's design of this research is presented and involves patients' recruitment, electrophysiology procedure (EP) system used to treat persAF patients during catheter ablation procedure. The filters and pre-processing steps applied on the electrograms recorded for off-line analysis are also presented. The fast algorithm of the Discrete Fourier transform (FFT) characteristics assumed for calculation of the DFs and the ventricular far-field cancellation for the AEGs are briefly explained. This chapter finishes with the thesis outline where a brief description of coming chapters is presented together with the principal aims of this study.

1.1.NORMAL HEART (ATRIUM)

In 1570s, the word 'atrium' was commonly used with the mean of a room with a hearth located close to the main entrance of an ancient Roman house (Etymonline, 2013). Although it is believed to be a word with origin from the Etruscan civilization (Pre-roman civilization living in Italy between 8th-4th century BC) (Encyclopedia, 2012a), evidences showed its use considerably earlier in the Proto-Indo-European language¹. The expression 'ater' (= 'fire') meant a place where smoke from the hearth escapes through a hole in the roof (Etymonline, 2013). The first use of the expression 'atrium' as the upper cavities of the heart was registered around 1870's (Etymonline, 2013).

1.1.1. ANATOMY OF THE ATRIUM

The atria are the two superior chambers of the heart. The right atrium (RA) is separated from the left atrium (LA) by the septum with no fluid communication between them. The atrium walls, as the heart walls, consist of three layers: epicardium, myocardium and endocardium. The epicardium is the outmost membrane and inside of it are the principal coronary blood vessels responsible for the supply and drainage of blood to the heart (Wynsberghe *et al.*, 1995, Tortora and Derrickson, 2006). The myocardium is the "muscle of the heart" and this layer gives the atrium the ability to pump blood. This layer is thick and localised in the middle of the three layers. It is composed of specialised cardiac muscle fibres with a nucleus and one or more branches. The fibres are 'connected' with their adjacent fibres

¹There is not an exact certainty in which age this civilization has lived. It is believed somewhere between 4000-8000 BC or even earlier ENCYCLOPEDIA, T. C. (2012b) Indo-European Language. *The Columbia Encyclopedia* 6th ed ed.

exemplifying a layer of muscle with striations in the junction between the fibres' ends or their branches, called intercalated discs. In general, skeletal striated muscles have a voluntary contractibility and smooth muscle involuntary contractibility and the heart is the only exception (Wynsberghe *et al.*, 1995, Tortora and Derrickson, 2006).

The thickness of the myocardium differs across the four chambers. In the atria it is thin by the fact that there is a lower downstream flow resistance as the atria deliver blood to the adjacent ventricles. As the right ventricle (RV) encounters a higher resistance pumping blood to the lungs its muscle layer is thicker. In the left ventricle (LV) the myocardium is even thicker by the fact that this chamber pumps blood to the whole body (Wynsberghe *et al.*, 1995, Tortora and Derrickson, 2006).

The endocardium is the innermost layer and it lines the inner atrium (or heart) cavities, valves and the blood vessels that enter and leave the heart. It is characterised by an anatomical arrangement between two thin membranes: endothelium and connective tissue that prevents stretching. This allows a smooth flow of blood (Wynsberghe *et al.*, 1995, Tortora and Derrickson, 2006).

1.1.1.1. RIGHT ATRIUM

The anterior wall (AW) of the RA is rough presenting ridges denominated pectinate muscles (PM). These ridges start on the AW and extend till the RV. In contrast, the posterior wall (PW) of the RA does not present ridges and this area is denominated smooth. Another characteristic of the RA is an apparent oval depression localised in the interatrial septum originated by the closed intercommunication between the atria after birth. This area is called Fossa Ovalis (Tortora and Derrickson, 2006).

The most important role of the RA is to receive deoxygenated blood from the body through the superior vena cava (SVC) and inferior vena cava (IVC) and from the heart through the coronary sinus (CS). The blood is then ejected to the RV through the tricuspid valve and is pumped by the RV to the lungs by the pulmonary trunks and pulmonary arteries (Wynsberghe *et al.*, 1995, Tortora and Derrickson, 2006).

1.1.1.2. LEFT ATRIUM

There are no ridges in the LA and both AW and PW are smooth. In contrast, the LV follows the RV and ridges are present on both sides of the ventricles (Tortora and Derrickson, 2006).

The principal function of the LA is to receive oxygenated blood from the lungs via the four PVs and pump it to the LV through the mitral valve (MV) (Wynsberghe *et al.*, 1995, Tortora and Derrickson, 2006).

1.1.2. PHYSIOLOGY OF THE ATRIUM

1.1.2.1. CHARACTERISTICS OF THE CELL MEMBRANE AND CHANNELS

The membrane of a cardiac cell is hydrophobic as a consequence of its double lipid layers. Specialised proteins identified as ion channels are present in the cell membrane to allow extracellular ions with hydrophilic characteristics to cross the membrane and penetrate the cell. When a channel is open, two distinct forces, a chemical and an electrical gradient, determine the ion direction (if it is inward to the cell or outward) (Baro and Escande, 2008).

The chemical gradient (osmosis) requires that an ion moves from an area of higher concentration to another of lower concentration. Examples of this are the K^+ and Na^+

ions. K^+ ions move from inside to outside of the cell and Na^+ ions move in the opposite direction. The second force, electrical gradient, rules that an ion should move into the direction of its opposite sign. In this case, as the resting potential of a cardiac cell is negative there is a natural electrical attraction to cations (ions that are charged positively) (Baro and Escande, 2008).

A transmembrane potential of equilibrium of a certain ion is reached when both forces are equal but with opposite directions. The equation below, denominated Nernst equation, models transmembrane equilibrium potential for a specific ion.

$$E_i = \frac{RT}{zF} \ln\left(\frac{\text{Extra [i]}}{\text{Intra [i]}}\right) \quad (1.1)$$

E_i is the ion equilibrium potential (V), R is the thermodynamic gas constant ($R=1.987$ cal/deg mole), T is the absolute temperature ($T= T_c + 273$) where T_c is the temperature in the Celsius scale, z is the ion charge, F is the Faraday constant ($F=23,062$ cal/volt equiv). Extra [i] and Intra [i] are respectively the extracellular and intracellular concentrations of the respective ion (Baro and Escande, 2008). For illustration, the potential of equilibrium for the ion potassium, K^+ , was calculated and is presented below ($z=+1$, ion monovalent), $T_c= 37^\circ$ C (normal body temperature), Intra [K^+] = 150 mM and Extra [K^+] = 4 mM).

$$E_{K^+} = \frac{1.987(273+37)}{(+1)(23,062)} \ln\left(\frac{4 \text{ mM}}{150 \text{ mM}}\right) = -96.8 \text{ mV}$$

During the resting potential of a cardiac cell, the membrane is essentially permeable to K^+ ions and the membrane potential is said to be close to its membrane potential (around -90 mV). This equilibrium is affected during the occurrence of an action

potential (AP) where the membrane permeability changes according to the phases of an AP event (see Figure 1.1) and other ions will influence the cardiac cell potential.

With changes of permeability in the cell membrane, ion channels will open and change the inward and outward flux of ions of the cell. This, consequently, generates currents that affect the membrane potential, which in turn also affect the ion channels opening. With an influx of cations into the cell, inward currents will be generated and will contribute to membrane depolarisation by bringing the membrane potential to values close to the AP trigger threshold (around -20 mV). In contrast, if cations leave the cell, an outward current is generated hyperpolarising the cell (values more negative than the resting potential) or repolarising the cell if the membrane was previously depolarised (Baro and Escande, 2008).

During the resting membrane potential the Na^+ channels are closed (inactive), but if the transmembrane potential is brought to values close to -20 mV ($E_{\text{Na}^+} = +70$ mV), these channels will open and, as consequence, an Na^+ inward current will be generated depolarising the cardiac cell. That in turn activates other Na^+ channels of the membrane. This 'recruitment' in cascade is stopped and the Na^+ channels become spontaneously inactive (please see section below) (Baro and Escande, 2008).

1.1.2.2. ACTION POTENTIAL OF A CARDIAC CELL

AP can be defined as a short-term change in the membrane electrical potential which can be propagated to its adjacent cells. Currently, the AP can be divided in up to five different phases: depolarisation, early repolarisation, plateau, repolarisation and resting potential (see Figure 1.1) (Baro and Escande, 2008).

Phase 0 or depolarisation is characterised by a very fast and large influx of Na^+ ions through sodium channels. This inwards Na^+ flux brings the transmembrane potential towards the Na^+ equilibrium potential being inactivated in a fraction of millisecond (ms). Almost simultaneously to the influx of Na^+ , the membrane permeability to the slow K^+ channels is reduced.

That is followed by the early repolarisation and plateau phases where the depolarisation is maintained due to an increase of Ca^{2+} influx through the slow voltage-gated Ca^{2+} channels. This flow of Ca^{2+} inwards is fundamental to the myocardium contraction (Wynsberghe *et al.*, 1995, Baro and Escande, 2008). A peculiar characteristic of the plateau phase is that for a very short time a membrane current stability occurs where the inward currents mainly Ca^{2+} equalise the outward currents, mainly K^+ (Baro and Escande, 2008).

This phase is followed by the repolarisation of the AP membrane cell (Phase 3). At this stage, an increase of K^+ permeability occurs (channels re-open) bringing the membrane potential towards the normal resting membrane potential (around -90 mV). Simultaneously, the Ca^{2+} permeability decreases contributing to the repolarisation (Wynsberghe *et al.*, 1995, Tortora and Derrickson, 2006).

Although at this stage the membrane potential is in its basal value, the ion concentrations are still not in equilibrium (more K^+ ions outside and more Na^+ ions inside the cell). The active pump Na^+/K^+ has a fundamental role to bring the ion concentration to the basal (equilibrium) levels (Wynsberghe *et al.*, 1995).

The action potential duration (APD) intrinsically depends of the absolute refractory period (ARP) and the relative refractory period (RRP) of the cardiac cell.

$$\text{APD} = \text{ARP} + \text{RRP} \quad (1.2)$$

The ARP is characterised by the time interval between the beginning of the depolarisation (phase 0) to the first half of repolarisation (phase 3) (see Figure 1.1). In this stage, a second AP cannot be triggered by the cardiac fibre preventing the heart to going into a sustained tetanus contraction (Tortora and Derrickson, 2006). The ARP is followed by RRP where the membrane can be depolarised and a second AP can be triggered by a stimulus of a high intensity (Wynsberghe *et al.*, 1995, Tortora and Derrickson, 2006, Baro and Escande, 2008). The RRP starts at the second half of repolarisation phase (phase 3) and ends at the resting potential (phase 4). During high frequency atrial firing rate the cardiac cells' refractoriness was identified to be around 85 ms to 100 ms (Winfree, 1997).

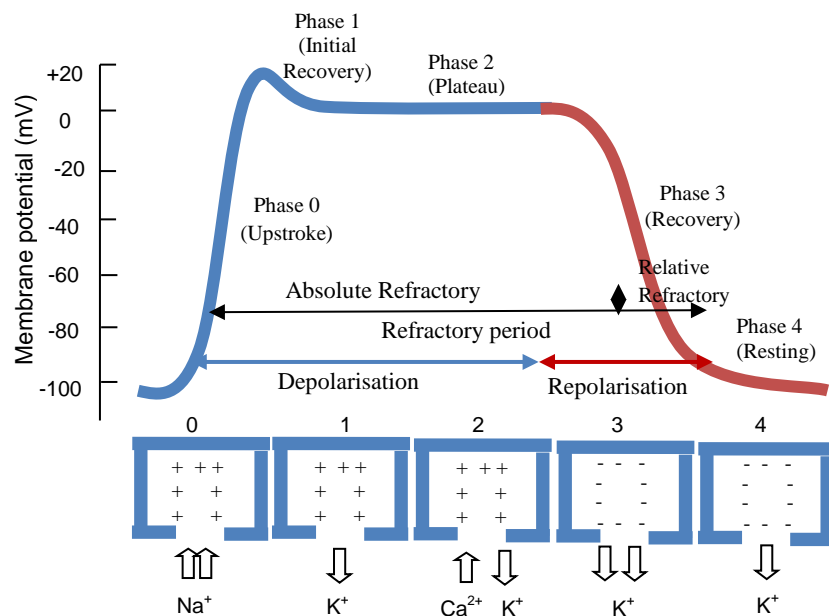


Figure 1.1 AP phases. Modified and used with permission from (Ahmad, 2011)

1.1.2.3. DIFFERENT ATRIAL ACTION POTENTIALS

Although every single AP in different parts of the atrium contains in general all phases previously described, the AP waveforms and durations differ from region to region (Figure 1.2). That can be consequence of the differences in size, shape and structure of the tissues (Saffitz *et al.*, 2004). The duration of the refractory period (RP) directly affects the excitation-contraction coupling of the atrium and also its electrical propagation path (Nerbonne, 2004).

Studies have shown that different sub-types of K^+ currents influence AP height and duration, refractoriness and repolarisation. In addition, cells from certain areas in the atrium have absence of Na^+ channels and the upstroke phase of their APs (phase 0) is compromised and dominated by inwards flow of increased Ca^{2+} (Nerbonne, 2004). Other factors have been shown also to be an important modulator, such as the specialised organelles on the intercalated discs responsible to gap junctions (Nerbonne, 2004).

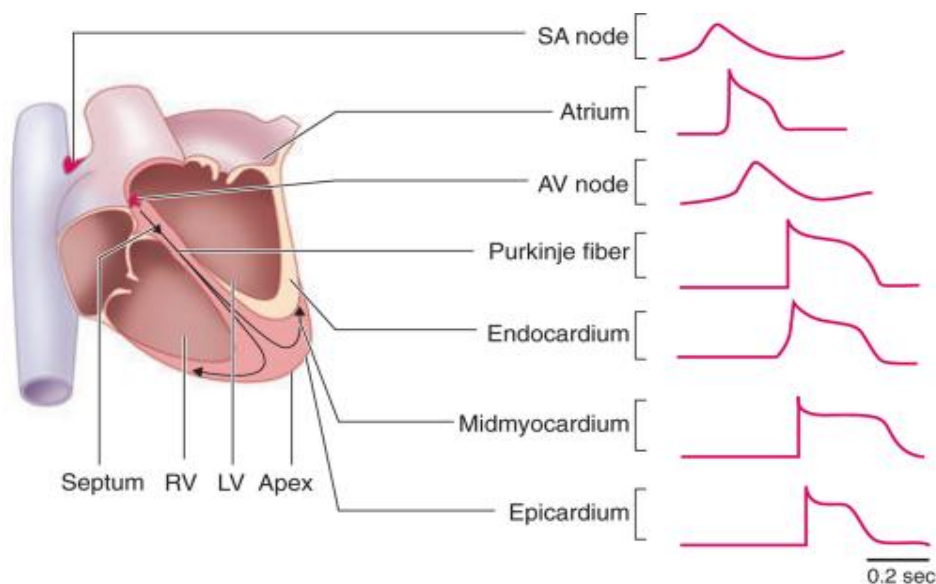


Figure 1.2 Different AP morphologies from the heart. With permission (Nerbonne and Kass, 2005)

1.1.2.4. ELECTRICAL CONDUCTING SYSTEM COMMUNICATION

The coordinated propagation of electrical impulses in the heart is a result of several complex intercellular mechanisms involving exchange of ions and molecules (Nerbonne, 2004). The intercalated discs are actively responsible for the communications and signal propagations between cells and they are composed of desmosomes and gap junctions. The specialised function of the desmosomes is to make sure that the cardiac fibres are held together and the gap junctions directly contribute with the AP propagation between cells to a 'quasi' instantaneous transmission (Tortora and Derrickson, 2006).

The gap junctions' regulation depends of several detailed and complex signalling pathways and it has been shown to be directly related with functional changes in the membrane channels (Nerbonne, 2004). In normal conditions, the cardiac fibres of the heart are well coupled through the gap junctions ensuring an accurate spatio-temporal propagation transfer (Nerbonne, 2004). If changes due any physiologic and pathophysiologic event occur, the heart adapts rapidly to that, with possible alterations in cardiac fibres' communication (Nerbonne, 2004).

1.1.2.5. ATRIUM ELECTRICAL PROPAGATION

1.1.2.5.1. SINOATRIAL NODE

The sinoatrial (SA) node is responsible for coordinating the beat rhythm of the heart through its specialised pacemaker cells localised in an area near the RA superior wall and the SVC (Wynsberghe *et al.*, 1995, Waugh and Grant, 2011). The cells rhythmicity ranges between 70 and 100 activations per minute, and, as expected, these cells have the fastest cell rate activations in the heart (Kodama *et al.*, 2004).

The SA node is formed by different types of cardiac cells resulting in differences between its AP waveforms. The APs are generated in the cells located in the centre of the SA node and these cells have intrinsic characteristics such as a slow upstroke velocity (permanent inactivation from the Na^+ current and the depolarisation occurs by slow Ca^{2+} currents), small amplitude, relatively long APD and the resting membrane potential is less negative (less background K^+ channels). As while moves to the periphery, the AP amplitude and maximal diastolic potential increase, the APD and resting membrane potential decrease (Kodama *et al.*, 2004).

The cells located in the centre of the SA node have poor electrical coupling characteristics resulting in a low conduction velocity. In addition, that also contributes to insulating these cells from surrounding or external influences avoiding any external signal influence in the pacemaker activity. With the electrical propagation to the cells located to the SA node periphery a significant increment of conduction velocity is observed 'boosting' the propagation of the APs to the adjacent atrial cells in the RA (Wynsberghe *et al.*, 1995, Kodama *et al.*, 2004).

The cells from the SA node are not the only ones with pacemaker activity inside the heart. Cells present in the plateau fibres, along the crista terminalis, intra-atrial septum, AV junction and His-Purkinje system also present 'pacemaker activity'. But the pacemaker hierarchy is such that the SA node has the fastest impulses activations and the distal Purkinje system the slowest, and normally the fastest inhibit the slower, so the SA node dominates (Macfarlane, 2011).

1.1.2.5.2. CRISTA TERMINALIS

The Crista terminalis cells conduct electrical impulses from the SA node periphery to the atrium till they reach the atrioventricular (AV) node. These cells are composed by a special bundle of atrium tissue organised vertically in the posterior RA (Waktare and Camm, 2000). The conduction velocity is considerably high (± 1 m/s), but there is considerable disparity in terms of propagation velocity in these cells due to a restriction on the number of connections and the pronounced differences of spatial orientations of the connections (Saffitz *et al.*, 2004).

1.1.2.5.3. INTERNODAL TRACTS

After passing through the Crista Terminalis, internodal tracts have been widely accepted as the preferable pathways to electrical pulses that spread throughout the RA and LA till the AV node. These cable-like structures are commonly cited and they go through the anterior, medial and posterior RA (Basso *et al.*, 2008). In addition, other 'specialised' group of fibres denominated Bachmann's bundle showed to be a preferential conduction pathway between the atria by presenting better alignment of fibres (Waktare and Camm, 2000, Basso *et al.*, 2008). In contrast, recent studies using light and electron microscopy showed that, apart the specialised pathway with high conduction velocity between the SA node and crista terminalis, no consistent histology evidence in the atrium was observed suggesting to a possible absence of the specialised tracts pathways (Saffitz *et al.*, 2004).

1.1.2.5.4. ATRIOVENTRICULAR NODE

The APs are conducted through both atria and reach a neuromuscular tissue, AV node, situated at the base of the RA septum wall and near the AV valves (Tortora

and Derrickson, 2006, Waugh and Grant, 2011). This region is responsible for the electrical communication between atria and ventricles and a 0.1 s delay is introduced to the signal propagation allowing the atria to contract while the ventricles are still relaxed and consequently being filled (Wynsberghe *et al.*, 1995, Waugh and Grant, 2011).

Apart of being an impulse conductor, a second function of the AV node is to behave as an oscillator with pacemaker rhythmicity between 40 and 60 activations per minute. This is crucial as it permits the ventricles to beat if either the SA node or a total conduction block in the atria walls is encountered (Waugh and Grant, 2011).

Once the AV node is activated, the APs travel a short pathway to cross the fibrous connective tissue that divides both atria and ventricles. Then the electrical pulses are propagated to the right and left bundles (bundle of His) towards the heart apex. After the apex is activated, the electrical impulses propagate through the Purkinje Fibres to activate the remainder of the ventricular walls (Wynsberghe *et al.*, 1995, Tortora and Derrickson, 2006, Waugh and Grant, 2011). The Purkinje Fibres arrangement propagates the activation to all areas of the ventricular muscle. These fibres have a large diameter and allow the electrical impulses to travel in higher velocity, producing a fast contraction (Wynsberghe *et al.*, 1995).

1.1.3. FACTORS WHICH MAY AFFECT THE NATURAL ORDER OF THE CELL MEMBRANE, ACTION POTENTIAL AND ATRIUM ELECTRICAL PROPAGATION

Changes in densities, distributions and properties of membrane channels can modify the electrical conduction and evoke abnormal impulse generation with consequent changes in rhythmicity (Nerbonne, 2004). For example, a decrease of outward current in the cells during an AP and an increase of inward current may result in

prolongation of repolarisation and an arrhythmia. In addition, alterations on both relative and ARP also may contribute to the occurrence of arrhythmias (Macfarlane, 2011).

Membrane potential oscillations can also depolarise the cell and trigger repetitive impulse initiation. For example, during diastolic relaxation, the atrium cell transmembrane reduces the intracellular Ca^{2+} ions concentration through a $3\text{Na}^+/\text{Ca}^{2+}$ pump active exchange (NCX). It produces an inward current triggered by a large inward Na^+ current which in fact brings the cell potential to values close to the Na^+ equilibrium potential (+40 mV). It can depolarize the cell, generating an afterdepolarisation (Nattel, 2002, Macfarlane, 2011). If afterdepolarisations reach the cell threshold potential, spontaneous AP will be generated (Nattel, 2002).

Alterations in the transmembrane properties such as the passive electrical components will also alter the speed of the electrical propagation of the AP. With increase of age the atrial histology changes. Elastic tissue and collagen replaces atrial cells changing the capability of the cells for transmitting electrical pulses throughout the atria. This phenomenon occurs also in areas inside of the SA node altering the pacemaker property (Waktare and Camm, 2000). In addition, with age the heart pumping efficiency is reduced and blood pressure increases. The atrial walls become less elastic and the myocardium must work harder to pump the same volume of blood, consequently enlarging the heart (Wynsberghe *et al.*, 1995).

Molecular and genetic disturbances, degenerative heart disorders, hemodynamic abnormalities, coronary artery diseases, inflammation of any of the three layers of the heart wall, heart dilatation (pressure or volume overload), scarring, ischemia, fibrosis and any cardiac complications will affect both the anatomy and the

physiology of the heart with serious consequences for the quality of life and life expectancy (Wynsberghe *et al.*, 1995, Waktare and Camm, 2000, Tortora and Derrickson, 2006, Antzelevitch *et al.*, 2008).

1.2. ATRIAL FIBRILLATION

1.2.1. EPIDEMIOLOGY

Atrial fibrillation (AF) is the most common heart rhythm disturbance of all sustained cardiac arrhythmias in the clinical practice (Haissaguerre *et al.*, 1998). Its prevalence is around 1% of the worldwide population (Go *et al.*, 2001, Bollmann and Lombardi, 2006, Heeringa *et al.*, 2006, Mommersteeg *et al.*, 2009) and AF has been predicted to increase 2.5-fold in the next 50 years, mainly due to the ageing of the population (Go *et al.*, 2001, Andrikopoulos *et al.*, 2009). The incidence of AF is approximately twofold higher among men compared to women (Go *et al.*, 2001, Houben *et al.*, 2010) and family history of AF has been found in one-third of all AF patients (Crandall *et al.*, 2009).

Its rate increases from 0.5% of adults younger than 55-60 years to 5% for the above 65 years and to over 9% for those with 80 years or older (Wolf *et al.*, 1996, Haissaguerre *et al.*, 1998, Crandall *et al.*, 2009, Kuijpers *et al.*, 2011). The median age of AF patients is 75 years and up to 84% of the AF worldwide population is above 65 years (70% of these are in between 65 and 85 years) (Chugh *et al.*, 2001).

AF affects approximately 7 million of people in Europe (Kirchhof and Eckardt, 2010) and it is estimated that around 1 million of those are in the UK (AFA, 2010). In the United States it affects about 2 million people and that is expected to increase to 6 million by 2050 (Jalife *et al.*, 2002, Andrikopoulos *et al.*, 2009). In Brazil it is estimated that 0.5% of the population has AF (Olmos, 2008).

Patients with obesity (Abed *et al.*, 2013) or previous history of heart disease such as coronary artery disease, pericarditis, MV disease, congenital heart disease,

congestive heart failure (CHF), thyrotoxic heart disease and hypertension are more likely to develop AF. But AF also has been seen in patients without previous heart disease, known as 'lone AF' patients (Nattel, 2002, Holmqvist *et al.*, 2011).

1.2.2. ECONOMIC ASPECTS

AF imposes great strain on healthcare resources. The set of symptoms and the morbidity associated with AF are responsible for frequent medical appointments and admissions and it is estimated that AF is responsible for one-third of all hospital admissions of cardiac rhythm disturbances (Fuster *et al.*, 2006) contributing to elevated costs of Health Care and becoming an expensive public health problem with the total cost of € 13.5 billion (around € 3,700/year per patient) in the European Union (Bollmann and Lombardi, 2006). The estimated annual cost in the United States was US\$ 6.65 billion in 2005 and the UK spends the equivalent of 1% of its total NHS budget in managing AF (Andrikopoulos *et al.*, 2009).

The patients' hospitalisations are the biggest contributor with a share of approximately 52% of the total cost spent and the remaining 48% are assumed to be directly related with the in-patient care (Andrikopoulos *et al.*, 2009). Therefore, any advances in the understanding of this condition, especially advances that might lead to more effective treatment are of great importance, both from the healthcare delivery and from the economical aspects.

1.2.3. DEFINITION OF AF AND COLLATERAL EFFECTS

Within the several definitions of AF, the American Heart Association/ American College of Cardiology/ European Society of Cardiology (AHA/ACC/ESC) guidelines (Fuster *et al.*, 2006) define AF as an uncoordinated electrical atrial activation with

consequent mechanical deterioration, associated fibrosis and loss of atrial muscle mass affecting the ability of the atria to pump blood effectively (Conditions, 2006, Fuster et al., 2006).

As the mechanical pumping ability of the atria is compromised in AF, the atria do not empty well between contractions and this might lead to the formation of blood clots and thromboembolic events (frequently on the left atrium appendage, LAA), increasing the risk of stroke fivefold and doubling mortality (Wolf *et al.*, 1996, Connolly, 2011). This arrhythmia is also associated with sufferers experiencing fast, irregular heartbeats or palpitation, tiredness, chest discomfort, breathlessness, light-headedness, dizziness or even blackouts (Fuster et al., 2006).

Its presence, especially in long-term (sustained), promotes pronounced electrical and structural atrial substrate remodelling (including successive shortening of RP and APs) and atrium enlargement with fibrosis (Crandall *et al.*, 2009), which contributes to its recurrence (Kirchhof and Eckardt, 2010). The most common clinical complications for patients whose AF persists are hypertension, heart failure, coronary artery and valvular heart diseases (Crawford, 2011).

1.2.4. CLASSIFICATION OF AF

Several classification approaches have been proposed to AF based on external and intracardiac recording patterns or clinical features. Alternatively, AHA/ACC/ESC guidelines (Fuster et al., 2006) suggest the temporal duration of the AF episodes as a classification factor for AF with clinical relevance (see Figure 1.3). According with (Fuster et al., 2006, Calkins et al., 2007), AF is considered recurrent when two or more AF episodes are identified. If the arrhythmia stops spontaneously within

seconds, hours or even days (till 7 days) it is said to be Paroxysmal AF (PAF). If the episodes are sustained beyond 7 days or less than 7 days but with medical procedure termination, the patients are identified as having persistent AF (persAF). The persAF division also includes cases where AF lasts for longer than one year, where in this case it is called long-standing AF. The last category is the permanent AF and is characterised when AF termination was not possible with medical procedure or when medical procedure is not applicable. AF can start from PAF or PersAF leading to permanent AF (AF begets AF) (Fuster et al., 2006).

Allessie and collaborators studied the concept that AF begets AF through an elegant study highlighted by (Prystowsky, 2008). In this experiment electrodes were sutured in the epicardium of both atria of goats (Wijffels *et al.*, 1995). The authors induced AF by pacing and observed that sinus rhythm would be restored and straight after the authors would pace again to re-induce AF. With this interactive process progressing along time, it was observed that the AF episodes were found to become longer until persisting for many hours (> 24 hours). Thus, in this experiment the atria went from paroxysmal to persistent state in a short time. Other researchers showed that in human progression of PAF to a more sustained form is sometimes slow and/or unusual. According to the authors, it is estimated to be around 10% at the first year and up to 30% at 5 years. In addition, 50% of patients with lone AF progress to sustained AF after a 25-year follow up (Shen *et al.*, 2011).

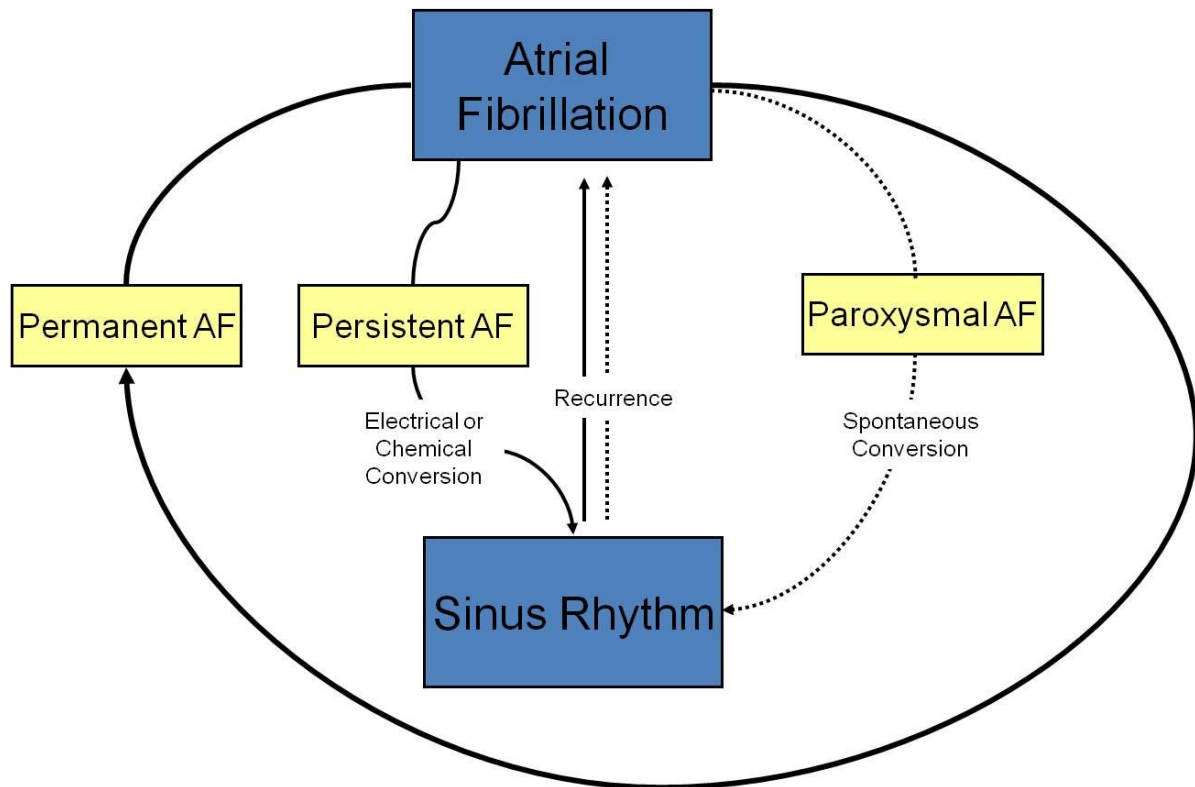


Figure 1.3 Temporal Classification of AF. Modified from (Waktare and Camm, 2000)

1.2.5. CLASSICAL MECHANISMS OF AF: HISTORICAL PERSPECTIVE

Although research groups are dedicating extensive investigations to understanding the physiopathology of AF, some of the mechanisms of triggering and maintenance of this arrhythmia are still unrevealed and there are controversies regarding the most acceptable theories (Nattel and Ehrlich, 2004, Prystowsky, 2008). Three different theories were postulated since the beginning of last century in an attempt to explain the mechanism of AF: (1) Ectopic foci, (2) Multiple, random propagating wavelets, and (3) Localised re-entrant activity with fibrillatory conduction.

1.2.5.1. EARLIER STUDIES: FROM THE BEGINNING OF THE 20TH CENTURY TO 1950S

- *Ectopic foci vs. circular movement* -

The hypothesis that AF is initiated by multiple rapid firing ectopic foci spread across the atria was first introduced on the beginning of the 20th century, highlighted in (Winterberg, 1907), and later evidenced in an AF modelling experiment (Scherf, 1947).

As opposite to the Ectopic activity theory, Mines (Mines, 1913) introduced the circus movement theory suggesting that AF is promoted by circus movement of re-entry circuits. Mines (Mines, 1913) described the excitation of the cardiac cells as being dependent of the rate of propagation (conduction velocity, CV) and the time required for this propagation (through the wavelength). According to the author, the wave of excitation in cardiac cells is rapid enough to propagate to the ventricles before starting a new depolarization of the atrium (rapid in terms of propagation but has long period of duration), then if the rate of propagation is faster than the duration of the wavelength all the circuit will be excited 'at the same time' and, as a result, the excitation will die out (Figure 1.4a), corresponding to sinus rhythm. In contrast, if we increase the activity of the cells, the wave of propagation becomes slower and shorter contributing for a second excitation after the first one is completed (fibrillation behaviour). This phenomenon happens by the fact that the excited state from the beginning of the wave will pass off and when the excitation wave reaches the end of the wavelength these cells will be ready for the next excitation, triggering a new activation (figure 1.4b).

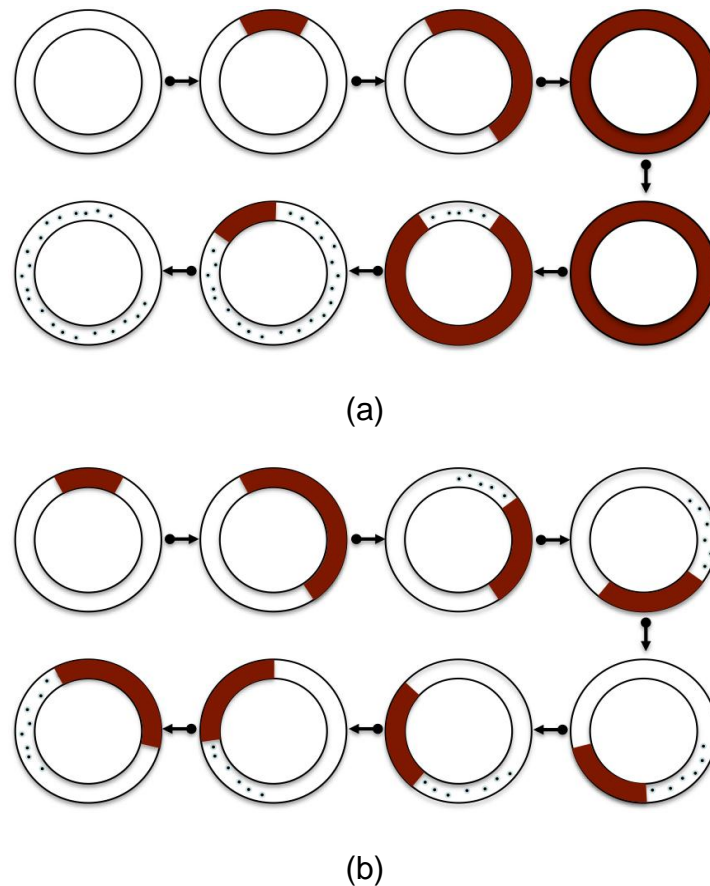


Figure 1.4 Schematic drawing for (a) the normal rhythm cycle excitation and (b) an arrhythmic cycle excitation: the excited state is represented in dark red and the refractory state as dotted areas. In (a), the recirculation can't occur, because when the stimulation completes a cycle, the cells at that point are still refractory and can't re-trigger. In (b), re-triggering can occur with either a shorter refractory period and/or slower conduction, allowing the development of a circulating wave. Modified from (Mines, 1913)

Garrey in his work (Garrey, 1914) confirmed this hypothesis by observing that induced fibrillatory contractions were not cessed in the atria after the investigator had separated the atria from the appendix (the fibrillatory contractions on the appendix stopped). He concluded that AF needs a minimum tissue mass to perpetuate AF. Within his important contribution on AF studies, Professor Thomas Lewis improved the concepts of the excitable circus movement theory stating the basic differences

on the tissue mass during refractoriness between an AF and Flutter circle circuit. Part of Thomas Lewis's work can be seen in (Lewis, 1909, Lewis, 1910, Lewis, 1921, Lewis *et al.*, 1921, Lewis, 1925). These two theories (ectopic foci and circular movement) together were predominantly the centre of all hypotheses proposed to explain the basic mechanism of AF till 1950s.

1.2.5.2. SUBSEQUENT STUDIES: FROM 1950S ON

1.2.5.2.1. MULTIPLE WAVELETS AND CIRCULAR MOVEMENT

Moe and Abildskov argued against both theories suggesting that they were inadequate by the fact that it was difficult to assume that either mechanism could be graced with natural stability to persist in long term, as usually AF does. They proposed that AF was a result of random multiple wavelets across the atria (Moe and Abildskov, 1959, Jalife *et al.*, 2002). Later, Moe and colleagues (Moe *et al.*, 1964) showed through a computer model of AF that a stable state could exist being self-sustained and independent of its trigger, but the perpetuation occurred only in cases where non-homogeneous atrial repolarisation was evidenced. In summary, the authors considered AF as a turbulent and self-sustained phenomenon taking place in a non-homogeneous excitable tissue mass.

The authors assumed that the wavelength of the propagation wave length can be found through the multiplication of the refractory period (RP) by the conduction velocity (CV). For example, once the fibrillatory activity is initiated, it is propagated to the tissue at a time when some of its components have recovered while others are still in their partial/fully refractoriness as a result of the preceding activation (circus movement) (Moe, 1962, Moe *et al.*, 1964, Jalife *et al.*, 2002). The increase in atrial

size and the heterogeneity of the refractory period should also promote the probability of re-triggering and maintenance of multiple-circuit re-entry (Zipes and Jalife, 2004, Aliot et al., 2008). In contrast, if the wavelength of the circuit is not small enough, the atrium could contain only a small number of multiple-circuit re-entry paths and the AF may not persist for long time.

Although Moe and colleagues supported that AF mechanism persists by multiple wavelets, they assumed that irregular activation from the atria could result from several factors which include single discharging of ectopic focus, multiple rapidly discharging foci, or rapidly circulating circus movement (Prystowsky, 2008). Later, with the advent of high-resolution optical mapping, Allesie and colleagues (Allesie et al., 1977, Rensma et al., 1988) observed for the first time, in studies on dog heart, the presence of multiple propagating wavelets (between 4 to 6 simultaneous wavelets) supporting the numerical study of Moe's theory. This experiment became a landmark demonstrating that multiple wavelets can exist during AF, but the question was that number of wavelets identified by Allesie and colleagues was significantly less than proposed by Moe (between 20 to 30 wavelets).

The observations by Allesie and colleagues described above were also endorsed by other investigators and subsequent analysis showed a concordance in terms of the number of simultaneous wavelets and their characteristics of propagation (Jalife et al., 2002). This was reported to be then strongly accepted from the clinical observation when Cox and colleagues could cure chronic AF by multiple surgical lesions (MAZE) (Cox et al., 1991, Cox et al., 2000, Jalife et al., 2002). This surgical procedure aimed in sub-dividing the atria into small regions in a way that the multiple AF wavelets were unable to be sustained (Cox et al., 1991, Cox et al., 2000).

The multiple-circuit re-entry together with the refinement of Moe's theory (Moe *et al.*, 1964) and the observation of the maximum number of simultaneous re-entry circuits have been the dominant conceptual AF model till recently and the Ectopic Foci and Localised re-entrant activity with fibrillatory conduction were less favoured by the scientists.

1.2.5.2.2. RAPID FOCI ELECTRICAL DISCHARGES

The multiple-circuit re-entry was strongly challenged by a series of three studies presented by Haissaguerre and colleagues (Haissaguerre *et al.*, 1994, Jais *et al.*, 1997, Haissaguerre *et al.*, 1998). The authors successfully demonstrated that in a subset of AF patients, AF was primarily triggered by rapidly firing foci originated on the PVs (majority on the upper PVs followed by the lower PVs and rarely observed near the SA node). Ablating (or 'burning') these discrete sites through catheter ablation therapy the PAF patients were free of AF in long term. This landmark achievement made the community to refocus the attention on areas such as PVs, PW of the LA and autonomic innervations in those regions.

As consequence of the rapid firing ectopic in the atrium a regular tachycardia would be expected due to the rapid firing ectopic activity. However, if the firing ectopic has fibrillatory rate faster than the normal areas of the atrium can support (pattern 1:1), the fibrillatory mechanism could be triggered (Zipes and Jalife, 2004).

1.2.5.2.3. LOCALISED RE-ENTRANT ACTIVITY WITH FIBRILLATORY CONDUCTION

In a study with dog atria preparation, AF was induced and multiple re-entrant circuits were observed. With the increase of concentration levels of acetylcholine the

investigators observed that the re-entry circuits were reduced by a single and stable re-entrant circuit of high frequency and generating fibrillatory conduction at the surrounding areas (Schuessler *et al.*, 1992). It was later explained by (Zipes and Jalife, 2004) where the authors observed that when a single rapid firing circuit collides into conduction block areas located across the atria, the conduction pattern will might not respond in the rate of 1:1 resulting in fibrillatory conduction maintaining the AF. Fibrillatory conduction may be due to different refractory periods spatially distributed or by structural properties of the atrial tissue.

According to Jalife and collaborators (Jalife *et al.*, 2002), advances on the understanding of re-entrant rhythms have contributed to introduce the concept of 'rotors' defined by them as excitable spiral waves propagating around an unexcited core. These rotors are self-sustained with possible stationary characteristics or if not they may drift but subsequently anchor to anatomical heterogeneities in the cardiac tissue (Jalife *et al.*, 1998).

Jalife and colleagues also showed that AF seems to be spatially and temporally organised in normal structured hearts (Skanes *et al.*, 1998, Mandapati *et al.*, 2000, Mansour *et al.*, 2001, Jalife *et al.*, 2002), but also complex excitation patterns (Gray *et al.*, 1995).

Using optical and bipolar mappings AF shows to be an uninterrupted periodic activity of stationary rotors activated by the highest dominant frequencies (DF) (Mandapati *et al.*, 2000). A vortex rotating clockwise localised on the LAA lasted for several minutes and the frequency of activation matched with the DF from both optical and bipolar contact recordings. In addition, studies were also performed to identify preferable inter-atrial pathways with evidence of fibrillatory conduction and presence

of frequency gradients between LA and RA (Skanes *et al.*, 1998, Mandapati *et al.*, 2000, Mansour *et al.*, 2001, Jalife *et al.*, 2002). Through these studies evidence was observed identifying that sites harbouring highest frequency activity were responsible for sustaining the arrhythmia and the fibrillatory activity was conducted to the remaining atrial areas.

Jalife and colleagues (Jalife *et al.*, 2002) believed that not all forms of AF are sustained by a single rotor in the LA with fibrillatory conduction to the RA and that the underlying mechanism may vary including several simultaneous mechanisms occurring in a certain patient (as also previously suggested by Moe and colleagues) .

1.2.5.3. THEORY'S LIMITATIONS AND CONTROVERSIES

Observations over the recent years have challenged the idea that all AF is caused by multiple-circuit re-entry as accepted since the 1950s.

Multiple wavelets were challenged during drugs treatment. The idea behind the use of drugs to treat patients with AF is that this therapy would suppress this arrhythmia by increasing the refractory period of cells (wavelength circuit), as a consequence the drugs delay the repolarisation of potassium channels and would limit the number of functional circuits. The main problem with the Multiple wavelets theory is that it does not explain how certain anti-arrhythmic drugs work according to what is already known, for example, antiarrhythmic drugs that block Na⁺ channels are effective in terminating AF, but should promote AF because they decrease conduction velocity and consequently decrease the AF path wavelength.

Other explanations are that in fact AF is not a circuit re-entrant arrhythmia, or that the ectopic activity is the principal factor in AF maintenance or that multiple-circuit re-entry theory can be imperfect (Aliot *et al.*, 2008). Recent studies showed that AF

persists by the presence of a single small re-entry circuit or an ectopic focus (Mandapati *et al.*, 2000, Mansour *et al.*, 2001). Also, LA sources of activity seem to be particularly important when compared with RA areas (Mandapati *et al.*, 2000, Mansour *et al.*, 2001). Ectopic triggers localised in the PVs seem to have a highly significant role (Haissaguerre *et al.*, 1998).

The recent evidences have brought the scientists back to the beginning of the twentieth century debates suggesting that ectopic activity, localised re-entrant circuit with fibrillatory propagation and multiple circuit re-entries may all be involved in human AF (see figure 1.5 for illustration of the simultaneous AF mechanisms).

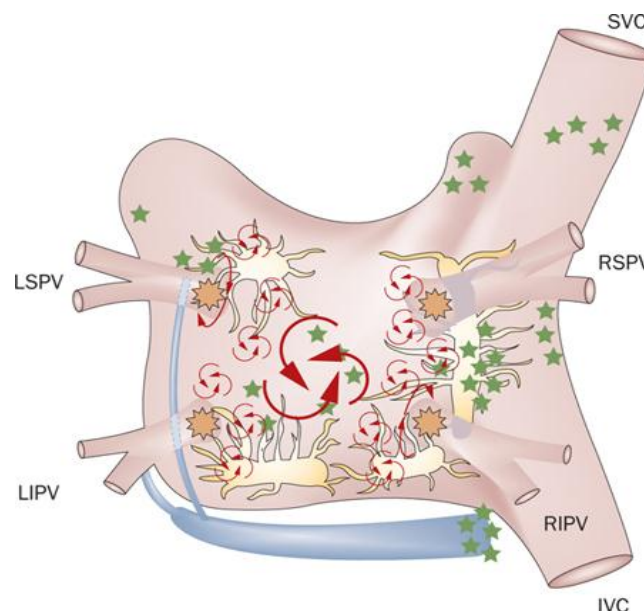


Figure 1.5 The anatomical and arrhythmic mechanisms of AF. Reprinted by permission from Macmillan Publishers Ltd: [Nature Reviews Cardiology] (State-of-the-art and emerging technologies for AF ablation), Copyright (2010).

1.2.6. CURRENT CLINICAL TREATMENTS

Two distinct interventions can be used in AF patients to prevent recurrent AF and its related complications (maintaining the sinus rhythm or controlling the ventricular rate (Crandall *et al.*, 2009). Ventricular Rate control during AF is usually achieved by

using drugs, such as flecainide and amiodarone, and beta blockers or channel blockers. Sometimes, ablation of the AV node is required to slow the ventricle rate down (Kirchhof and Eckardt, 2010). In addition, certain medications can be used in parallel to avoid occurrences of thrombotic events. The classical rhythm control therapy is done by the use of antiarrhythmic drug aiming at symptom reduction.

With recent advances on the understanding of the AF mechanism and the fact that unfortunately an effective drug treatment for the prevention of this rhythm disturbance is not available, catheter ablation has been widely accepted as a strategy to prevent AF (Kirchhof and Eckardt, 2010). In addition, recent studies showed that the use of catheter ablation to maintain the sinus rhythm was more efficient than the use of antiarrhythmic drugs (Calkins *et al.*, 2009, Arora *et al.*, 2010, Kirchhof and Eckardt, 2010).

The principal aim of AF ablation is the creation of myocardial lesions to block the AF electrical wavefront propagation and 1) eliminate arrhythmogenic tissue from an ectopic foci trigger (normally PV) or 2) modification of the atria substrate responsible for the re-entry (Crandall *et al.*, 2009, Kirchhof and Eckardt, 2010). Two different types of catheter ablation in AF patients can be highlighted. First, ablation of the AV node after implantation of pacemaker is done to achieve rate control in patients with accepted, symptomatic permanent AF. The second strategy is the ablation of the LA aiming to restore and maintain sinus rhythm (Kirchhof and Eckardt, 2010).

In terms of LA ablation, the most common ablation procedure involves electrical isolation of the PVs (Fuster *et al.*, 2006, Takahashi *et al.*, 2006, Miranda *et al.*, 2010). The PVs have electrically active tissues with a sleeve myocardium that extends from the atrium into the veins (Crandall *et al.*, 2009). Electrical isolation

involves circumferential ablation in the LA around the ostia of the PVs. Such technique electrically disconnects the PVs from the rest of the atria, so PV triggers will be unable to 'invade' the LA and initiate AF (Crandall *et al.*, 2009).

Another ablation strategy technique is called wide area circumferential ablation (WACA). In this procedure a circular lesion is performed beyond the PV ostium and continuing into the atrial antrum of the PV. Both PVs in each side are encircled by the circumferential wide ablation and with or without a linear ablation line connecting both circular PV sets lesions. The linear ablation also can be extended to the MV. This procedure evolves more extensive ablation and it increases the probability of AF re-entry circuits to propagate and also the elimination of possible foci triggers (Arora *et al.*, 2010).

Unfortunately, not all initiators of AF arise from the PVs. According to Crandall and colleagues (Crandall *et al.*, 2009), any intrathoracic vein can potentially trigger an ectopic activity, such as the vein of Marshall and SVC. Additionally, ablating PV trigger sites in PAF and normal atria substrate is effective, but its role showed to be less important in AF patients with triggers of cardiac diseases (including enlarged and fibrotic atria). For these patients, several approaches are provided aiming ablation from the substrate (Aliot and Ruskin, 2008, Brooks *et al.*, 2010, Elayi *et al.*, 2010). Exemplifying, ablation of the: roof, atrial lines, ganglionated plexi, macro- and micro re-entrant wavefronts and focal sources.

Another ablation approach is the target of high-frequency LA activity that manifests itself in the recording electrograms characterised by multiple rapid fractionated electrograms identified as Complex Fractionated Atrial Electrograms (CFAE) (Nademanee *et al.*, 2004). This strategy was effective in both acute termination of AF

and maintaining sinus rhythm (Nademanee, 2011), but the main problem is that still not a clear whether this ultra-rapid activity results from areas of abnormal conduction, rotors, neural activity or micro rotors (Crandall *et al.*, 2009). In addition, several 'subjective' definitions of CFAE exist and assumptions have been made by clinical groups regarding its detection in AF (Nademanee *et al.*, 2004, Monir and Pollak, 2008, Nademanee *et al.*, 2008, Porter *et al.*, 2008, Roux *et al.*, 2008, Verma *et al.*, 2008, Solheim *et al.*, 2010). CFAE identification is referred only to signals recorded using bipolar contact electrodes which makes studies performed by unipolar virtual electrode recordings difficult.

Recently, a stepwise approach aiming ablation of targets confined to the ganglionated plexi located along the posterior and superior portions of the LA has been shown to be a new exciting catheter strategy (Crandall *et al.*, 2009), but this strategy has not been yet applied worldwide by the clinical groups.

1.2.6.1. SUCCESS RATE USING CATHETER ABLATION

The success of using radiofrequency (RF) catheter ablation in paroxysmal AF patients has illustrated the usefulness of the technique (Terasawa *et al.*, 2009). Catheter ablation strategy targeting the PVs produces reasonable results in returning up to 80% of patients to a normal sinus rhythm (where between 30% and 40% of patients require a second procedure) (Wright *et al.*, 2008, Terasawa *et al.*, 2009, Arora *et al.*, 2010, Miranda *et al.*, 2010, Stevenson and Albert, 2012). In Glenfield Hospital the success rates are up to 80% with a redo procedure rate of 5%.

In contrast, success with rhythm control in persAF has been hampered by a lack of detailed understanding of atrial electrical behaviour during AF and how AF is

sustained. For these patients' group, the arrhythmia is in a more advanced stage where the atria substrate is remodelled opposing to a trigger mechanism commonly observed in PAF patients where aggressive interventions are needed (Fuster *et al.*, 2006, Takahashi *et al.*, 2006, Miranda *et al.*, 2010). Reports on termination of AF on persAF patients showed that 11% to 74% of the patients had successfully returned to sinus rhythm using different approaches (PV isolation; PV antrum isolation; PV isolation and linear ablation; PV antrum isolation and linear ablation; PW box isolation; CFAE ablation; or PV antrum isolation and CFAE ablation) (Brooks *et al.*, 2010, Elayi *et al.*, 2010, Rostock *et al.*, 2011). In Glenfield Hospital the success for returning persAF patients to sinus rhythm reach rates of up to 80%, where 20% of them require a second procedure.

In persAF, extensive ablation and repeated procedures are often required increasing the risks for collateral injury and complications. In addition, the decision of where to ablate to maximise efficacy and safety is still a challenge. Improving our understanding of the precise electrical mechanisms underlying AF is key to minimising the amount of 'burning' with ablation and maximising the patient outcome.

1.3. SPECTRAL ANALYSIS ON AF ELECTROGRAMS

Spectral analysis has been used as an investigative tool for the analysis of atrial electrograms to identify areas within the atria that contain high dominant frequency (DF) signals which may be 'driving' the rhythm (Skanes *et al.*, 1998, Langley *et al.*, 2000, Mandapati *et al.*, 2000, Everett *et al.*, 2001, Mansour *et al.*, 2001, Jalife *et al.*, 2002, Sarmast *et al.*, 2003, Sanders *et al.*, 2005, Bollmann and Lombardi, 2006, Jarman *et al.*, 2006, Fischer *et al.*, 2007, Lin *et al.*, 2007, Ng *et al.*, 2007, Pachón *et al.*, 2007, Stiles *et al.*, 2008b, Atienza *et al.*, 2009, Brooks *et al.*, 2009, Gojraty *et al.*, 2009, Raúl and José Joaquín, 2009, Ryu *et al.*, 2009, Singh *et al.*, 2009, Salinet Jr *et al.*, 2011a, Jarman *et al.*, 2012, Guillem *et al.*, 2013, Salinet Jr *et al.*, 2013a, Salinet Jr *et al.*, 2013b, Salinet Jr *et al.*, 2013d).

Investigators observed that representative signals during AF have important periodic components with different degrees of regularity and the time duration of an AF wavefront cycle in the LA correlated well with the DF peak of the spectral analysis, defined as the highest frequency peak of the whole AF frequency spectrum (Skanes *et al.*, 1998). Gray and colleagues (Gray *et al.*, 1998) showed that this wavefront with high frequency activity was stable in space and time and (Mandapati *et al.*, 2000) found that micro-source rotors with high-frequency periodic activity was responsible to maintaining AF, mostly located on the PVs.

Investigators using spectral analysis identified evidence that signals originating from certain regions of the atrium have higher DF components suggesting that AF could be originated by sites with high frequency activity in the LA that propagate to other locations of the atria (Mansour *et al.*, 2001). Therefore, DF mapping strategy would

facilitate the location of the possible AF triggers and hence targets for catheter ablation (Skanes *et al.*, 1998, Jason and Goldberger, 2007, Pachón *et al.*, 2007) .

Sanders and colleagues (Sanders *et al.*, 2005) used for this first time a commercial DF mapping system to track AF targets for ablation in AF patients (PAF and persAF). The authors reported that through the DF mapping strategy the cycle length at critical sites increased and the arrhythmia was terminated. In addition, they also observed that the spectral behaviour from distinct areas of the atrium were stable in space and time.

In the same year, a group from London (Jarman *et al.*, 2006) performed the first 3D DF mapping with 256 unipolar noncontact intracardiac atrium electrograms (AEGs) during AF off-line analysis. They observed that after pulmonary vein isolation (PVI) the arrhythmia persisted and some sites with high frequency just had slight changes in DF value before and after ablation, but in other sites DF decreased in value and in the number of DF. The noncontact mapping (NCM) used by this group (Jarman *et al.*, 2006) showed to be a remarkable technology that, contrary to the contact mapping (CM), allows simultaneous recording electrical activity of the inner surface of the atrium (>3000 different points) without the contact between the electrodes from the balloon and endocardium wall of the atrium (see next chapter for more details) (Schilling *et al.*, 1998, Gornick *et al.*, 1999, Kadish *et al.*, 1999, Schilling *et al.*, 1999).

The validation of spectral analysis between contact unipolar and noncontact unipolar electrograms was investigated by Lin and colleagues (Lin *et al.*, 2007) across 160 distinct points. They concluded that both electrograms were morphologically similar

but they are shifted in time and the DF between them correlated well in approximately 95% of cases. Later, Atienza and collaborators (Atienza et al., 2009) performed ablation on DF sites followed by PVI and observed that the DF values decreased and as consequence the left-to-right (LA-to-RA) DF gradient was eliminated. AF terminated in about 90% of the PAF patients and 55% of the persAF patients. In the same year, (Pachón et al., 2007) performed catheter ablation in CFAEs guided by a endocardial spectral mapping and after ablation AF could not be induced in 71% of the patients. Lin and collaborators (Lin et al., 2010) compared sites identified as CFAE with areas harbouring high DFs and observed that the locations of CFAE sites were correlated spatially with DF sites.

In clinical practice, ablation of the sites guided by frequency mapping has been mainly performed through advanced mapping systems that are based on point-by-point sequential acquisition (Lin et al., 2007) and thus the resolution of these maps is limited and its temporal variation is difficult to assess (Zipes and Jalife, 2004, Lin et al., 2007). Using this technology a single DF map takes up to 30 minutes to be generated (Lin et al., 2007, Gojraty et al., 2009). This approach intrinsically assumes temporal stability over long periods of time (Gojraty et al., 2009) and extends the overall time for an ablation procedure.

The validity of sequential mapping is open to question as to whether the same arrhythmia is being mapped at different time points and locations. In addition, the spatiotemporal DF stability has been studied by several research groups with conflicting results regarding its behaviour (stable or unstable) (Langley et al., 2000, Sanders et al., 2005, Krummen et al., 2009, Habel et al., 2010, Salinet Jr et al.,

2011a, Jarman *et al.*, 2012, Narayan *et al.*, 2012a, Salinet Jr *et al.*, 2012d, Salinet Jr *et al.*, 2013d).

A system with high-resolution simultaneous endocardial recordings of the entire chamber enables accurate mapping and facilitates targeting of potential arrhythmic sites and circuits without assumptions of stability between the recordings (Berenfeld *et al.*, 2008, Everett and Olgin, 2008, Lin *et al.*, 2010). Spectral analysis of these electrograms may serve as a powerful clinical tool for identifying potential candidates for ablation.

1.4. ELECTROANATOMICAL MAPPING SYSTEMS

'Mapping' in an EP study is characterised as a process of identifying and locating an arrhythmia (e.g. AF) using a computer based system. Understanding the arrhythmia behaviour is important for guiding interventions and treatments, such as catheter ablation (Jeff Hing, 2008).

During an EAM, catheters are placed within the cavity of interest and the endocardial surface electrical activity is recorded (Sra and Akhtar, 2007, Jeff Hing, 2008, LaPage and Saul, 2011). The 3D space locations of the tip of a roving catheter are identified by the EAM system (Tsuchiya, 2012) during the manipulation of the catheter within the cavity and electrograms are recorded and combined with their location to create activation or voltage maps in a 3D anatomical colour-coded representation (Sra and Akhtar, 2007, Jeff Hing, 2008, LaPage and Saul, 2011, Tsuchiya, 2012).

Unfortunately, these 3D geometries are less detailed than the cardiac anatomy obtained from a computed tomography (CT) or magnetic resonance image (MRI). In addition, geometry distortion tends to occur due to catheter distension of the cardiac tissue and non-uniform contact. The geometry creation depends considerably of the operator experience and requires acquisition of several points with a special attention to angles and structures (Burkhardt and Natale, 2009).

Due to the introduction of new technologies in the last decade, the principles and techniques for mapping have changed dramatically allowing the treatment of more complex arrhythmias (Sy *et al.*, 2012, Tsuchiya, 2012). Integration of pre-acquired CT, MRI, intracardiac echocardiography (ICE), ultrasound, and fluoroscopy images into the 3D mapping system allows clinicians to treat the arrhythmias using actual

patient geometry. In addition, it enables a higher degree of procedural accuracy due to the exact identification of the anatomical marks positions combined with the electrical information (Ahmed and Reddy, 2009, Christopher Piorkowski and Hindricks, 2009, Sy *et al.*, 2012, Tsuchiya, 2012). This integration also has improved success in the treatment of arrhythmias and has enhanced our understanding of cardiac electroanatomy and electrophysiology (LaPage and Saul, 2011).

A major limitation is that pre-acquired CT or MRI images do not consider potential variations of the chamber geometry as a result of dynamic physiological factors. As a result, near real-time acquisition of 3D cardiac images is now being explored with (1) rotational angiography, (2) “localized” ICE, and (3) 3D transesophageal echocardiography (TEE). (Ahmed and Reddy, 2009)

EAM systems can use either CM or NCM technologies and the most common applications are: (1) activation map of the arrhythmia, where the map shows the local activation timing difference of the recorded electrograms and the timing of a reference signal in order to either identify the earliest possible signal or a progression of activation; (2) propagation map, where the activation data is able to be reviewed, whereby the electrical wavefront is shown to propagate through the chamber and the conduction velocity can be estimated; and (3) voltage map, where the EAM systems catalogue the peak-to-peak amplitude (or first derivative) of each recording site (Lars Eckardt and Breithardt, 2009, Yitzhack Schwartz and Ben-Haim, 2009, Sy *et al.*, 2012).

1.4.1. CONTACT MAPPING

CM is the most frequent approach used to record endocardial electrical activity of AF patients during EP procedures allowing precise collection and accurate interpretation of data. In this method, electrodes attached to an intracardiac catheter make contact with the endocardial surface and sequentially acquire data, a technique known as a point-by-point mapping, over many cardiac cycles to create an activation/voltage map (i.e. CARTO™, NavX™, Localisa™ and Realtime Position Management, RPM™). Once all desired points inside the cavity of interest were recorded a 3D map colour-coded is generated. Another example of CM is the contact basket (Cardiac Pathways, EP Technologies, Sunnyvale, CA) where up to 64 electrodes are in contact with the endocardial surface allowing the system to record up to 32 simultaneous bipolar electrograms.

The systems also differ in the method of catheter localisation, the CARTO uses magnetic field, RPM uses ultrasonic transducers and NavX is based on impedance changes (Jeff Hing, 2008, Lars Eckardt and Breithardt, 2009, Sy *et al.*, 2012, Tsuchiya, 2012). Nowadays, sequential activation mapping is the preferred approach to study inducible, sustained, and hemodynamically tolerable arrhythmias (Christopher Piorkowski and Hindricks, 2009) and the two most common systems are NavX and CARTO.

1.4.1.1. NAVX™ SYSTEM

NavX allows acquisition of anatomical points recording local activation time during sequential mapping (proximal CS is usually chosen as the location of the reference catheter for atrial arrhythmias). The methodology of NavX is based on the voltage

gradient principle due to an electrical current applied between two electrodes. With a pair of electrodes placed on the thorax, NavX generates a low-power 5.7 kHz electrical potential across the body, to create a voltage gradient along the axis. Using any intracardiac electrode, NavX measures the local voltage on the electrode and calculates the electrode position along the axis. When three pairs of electrodes are placed on the body in orthogonal directions (neck-leg, front-back, left-right), NavX measures a voltage gradient on each axis, to create a 3D navigation field. Up to 64 electrodes can be located simultaneously (Christopher Piorkowski and Hindricks, 2009, Tsuchiya, 2012)

1.4.1.2. CARTO™

CARTO uses an ultralow magnetic field (0.05–0.5 G) created from three emitter coils placed underneath the patient (location pad). The emitted magnetic field has well defined spatial and temporal characteristics and it is identified by miniature passive magnetic field sensors (location sensors) integrated into the (proprietary) catheter. The identification of the magnetic field by the location sensor enables determination of the location and orientation of the sensor with 6 degrees of freedom (X, Y, Z, and roll, yaw, and pitch) (LaPage and Saul, 2011).

1.4.1.3. LIMITATIONS

CM requires a relatively stable and sustained arrhythmia because it collects sequential data from various points in order to create an activation map on the assumption that the same arrhythmia mechanism continues until the end of the mapping. Thus, CM is not suitable for non-sustained, polymorphic or hemodynamically unstable arrhythmias (Tsuchiya, 2012).

CM is time-consuming, especially when a single catheter is used. In addition, electrogram amplitude depends of electrode contact force. It will be under 'sensed' with poor contact and excessive pressure can promote catheter-induced ectopics (Sy *et al.*, 2012).

There is not an agreed standard for the minimum number of points that should be collected for these maps, but it is important to have in mind that the procedure ensures enough coverage of the anatomical and electrical fidelity. Inadequate sampling leads to activation being interpolated between widely separated points and areas with “slow conduction” or conduction block may be missed, leading to incorrect interpretation. Dismissing double potentials or low-amplitude fractionated signals may result in loss of crucial information such that macro-reentrant arrhythmias may mimic focal arrhythmias (Sy *et al.*, 2012).

In terms of the timing reference, it is important to choose an electrogram with a single sharp deflection such that the automatic sensing of the reference is reproducible. Reference electrograms with multiple components should be avoided, especially those contaminated with large far-field signals. In addition, dislocation of the positional reference causes a mis-alignment of the geometry map.

1.4.2. NONCONTACT MAPPING

1.4.2.1. ENSITE SYSTEM

NCM relies on the idea of recording simultaneous endocardial activity of the entire cavity without contact between the electrodes from the catheter and the heart walls

creating a detailed activation map even from a single beat (Figures 1.6 and 1.7) (Jeff Hing, 2008, Lars Eckardt and Breithardt, 2009, Sy *et al.*, 2012, Tsuchiya, 2012).

NCM is formed by a catheter-mounted with a multielectrode array (MEA), a custom-built amplifier system, and by a workstation to run specially designed software. This system has been used for complex arrhythmia cases, such as non-sustained arrhythmias as well as focal and re-entrant arrhythmias highlighting break-out points, earlier activation sites and identification of preferential pathways of conduction and propagation of the depolarisation wavefront (Sy *et al.*, 2012).

Each wire of the MEA has a 0.025 inch break in insulation arranged in an array of 64 noncontact unipolar electrodes. The raw far-field activity is acquired by a multichannel recorder and amplified. The electrograms are sampled at 1.2 kHz by the EnSite 3000 system (2034.5 Hz for the recently launched EnSite Velocity system). The signals can be filtered in a bandwidth frequency from 0.1 Hz or above by a high pass filter and up to 300 Hz by a low pass filter. The amplifier system also has 16 additional channels reserved by signals recorded using contact catheters and 12 channels for the surface ECG. Noncontact, contact and surface ECG signals are acquired simultaneously (Kim Rajappan and Schilling, 2009).

The reference electrode is located on the most proximal part of the shaft of the MEA catheter with a distance of 25 cm from the top of the catheter (The Pigtail Tip). This electrode is in contact with the blood pool outside of the cavity under investigation to provide a 'zero potential reference' for both noncontact and contact unipolar electrograms (Schilling *et al.*, 1998, Medical, 2011, Medical, 2012). At the beginning of the EP study, the 3D cavity geometry is created and validated and will later be

colour-coded according to the activation or voltage values at the respective measured points.

The system locates any catheter through a 5.68 kHz low-current “locator” signal between the catheter to be located and the ring electrodes proximal (E2) and distal (E1) of the MEA. The MEA detects and determines the locator signal angles and the positions of the source. As a first step, a roving EP catheter is moved along the inner wall of the cavity and as the catheter moves the Ensite System estimates its position by triangulation using the 2 tips of the balloon catheter. In addition, the system also records the roving electrode’s positions displayed on a computer screen in the theatre (see Figure 1.6). The system automatically displays the connections of these points (spline interpolation) as a geometric figure of the endocardium chamber and once the geometry is created the MEA should not move (Yitzhack Schwartz and Ben-Haim, 2009, Medical, 2011).

With the first geometry surface created, the EnSite system identifies 64 evenly distributed locations on the 3D geometry. Then, the software uses the measured electrograms in the 64 electrodes of the EnSite Array to find the inverse solution for Laplace’s equation at each position of the endocardial surface. It is known as the boundary element method (Yitzhack Schwartz and Ben-Haim, 2009). Values between the 64 elements are interpolated (via a bi-cubic spline algorithm) by the system to create up to 3360 isopotential points across the cavity. The thousands of reconstructed signals generated by the EnSite are then colour-coded onto the atrium’s 3D surface in real-time (see Figure 1.7) (Taccardi *et al.*, 1987, Schilling *et al.*, 1998, Gornick *et al.*, 1999, Kadish *et al.*, 1999, Schilling *et al.*, 1999, Tai *et al.*,

2002, Chinitz and Sethi, 2006, Earley *et al.*, 2006, Tai and Chen, 2009b, Yitzhack Schwartz and Ben-Haim, 2009, Medical, 2011).

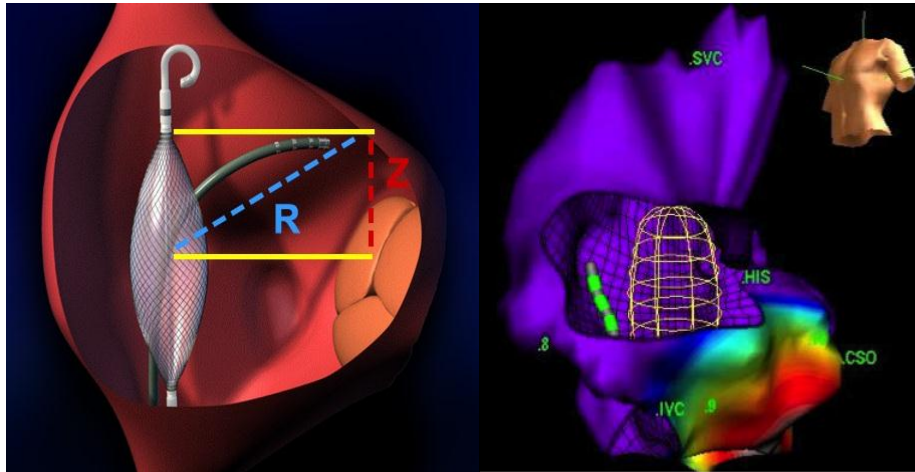


Figure 1.6 The ablation catheter and the Ensite 3000 balloon array are first used to map the inner surface of the heart's chamber using the ablation catheter as a probe and the two tips of the balloon as a reference. Then the array collects atrial electrograms (potentials) at 1200 Hz. The system can display the potentials as a colour map. (Ensite array and Ensite are trademarks of St. Jude Medical or its related companies. This image is reprinted with permission of St. Jude medical, © 2012. All rights reserved.)

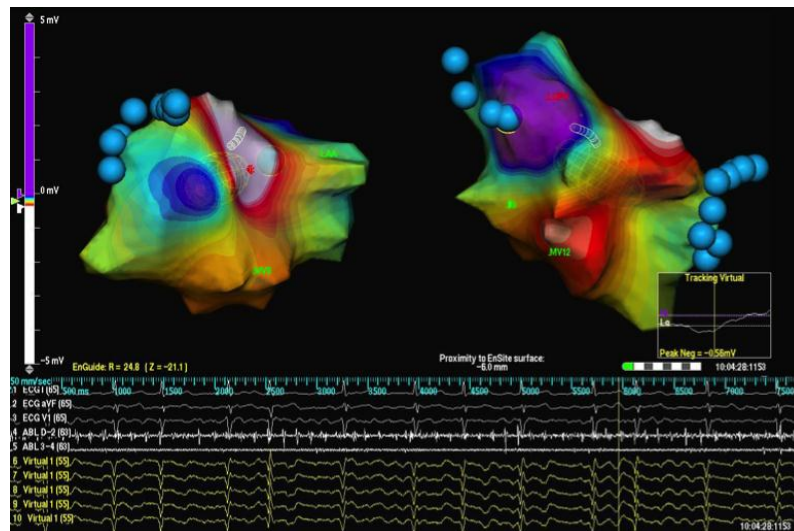


Figure 1.7 The activation voltage images (in the time domain) produced using the Ensite 3000 array. Two different views are presented simultaneously and can be independently reoriented by the clinician performing the EP study (in theatre), in preparation for the ablation.

The distance between centre of the MEA and the endocardium inner wall from the chamber affects the reconstruction quality of the signal estimation (inverse solution for Laplace's equation). The accuracy decreases significantly with the distance superior to 3.4-4.0 cm (Kadish *et al.*, 1999, Kim Rajappan and Schilling, 2009, Medical, 2012).

1.4.2.2. LIMITATIONS

Remote areas (>4.0 cm) from the centre of the MEA have their virtual unipolar electrogram attenuated making the technology not suitable for large cardiac chambers. In addition, if any movement of the MEA catheter happens the 3D geometry needs to be re-done.

The consequences of applying inappropriate filters cut-off frequencies on the electrograms altogether with 'equivocated' voltage thresholds selection may distort the arrhythmia interpretation (Sy *et al.*, 2012). The high pass cut-off is selected according to the type of the arrhythmia and it contributes to 'reject' far-filed during the identification of the earliest activation point. In addition, lowering the high-pass filter cut-off may permit visualising the slow conduction or exploring the region with CM.

The use of NCM to determine electrical activation in tubular structures accurately (i.e PV, SVC, IVC) is a challenge due a phenomenon called "line-of-sight issue". So, virtual electrograms around these areas are less reliable (Kim Rajappan and Schilling, 2009).

1.4.3. INTRACARDIAC ELECTROGRAM RECORDING AND MORPHOLOGY

Intracardiac electrical activity can be recorded during cardiac mapping by electrodes using two different configurations: unipolar or bipolar (Segal *et al.*, 2011). The respective electrograms differ in terms of morphology giving 'distinct' clinical information.

1.4.3.1. UNIPOLAR

A unipolar intracardiac electrode records electrical activity from the whole population of active cells surrounding the electrode and the unipolar electrogram is obtained by the potential difference between this single electrode and the reference electrode usually located at a relatively distant position (intravascular but outside the heart). It helps to minimize surface electrical noise generated by skeletal muscle or alternating current power supply (Segal *et al.*, 2011). In other words, unipolar electrogram is a summation-effect from all of the membrane currents along the wavefront 'line'.

The morphology of the unipolar electrogram allows identifying the direction of the wavefront activation. If the wavefront comes toward the electrode, a positive deflection will occur. Otherwise, negative deflection is produced (Figure 1.8). In addition to the wavefront direction, speed and width can also be assessed in unipolar electrograms (Sy *et al.*, 2012).

The negative down stroke deflection of the unipolar electrogram has been shown to coincide with the AP upstroke beneath to the local electrode. In addition, sites at which the wavefront activation wave arises reveal themselves by this initially

negative down stroke deflection in the unipolar recording (Lars Eckardt and Breithardt, 2009).

Although the intrinsic negative deflection is a reliable marker of local activation, its detection may be obscured by large, remote components mainly due to ventricular activity (VA) influence which, if not effectively eliminated, will hamper the AF analysis possibly distorting results (see Chapter 3) (Lars Eckardt and Breithardt, 2009, Ahmad *et al.*, 2011, Salinet Jr *et al.*, 2013a). In addition, adequate tissue contact and high-pass filtering are other two important requirements to be considered when the identification of focal arrhythmia activity area is desired (Segal *et al.*, 2011).

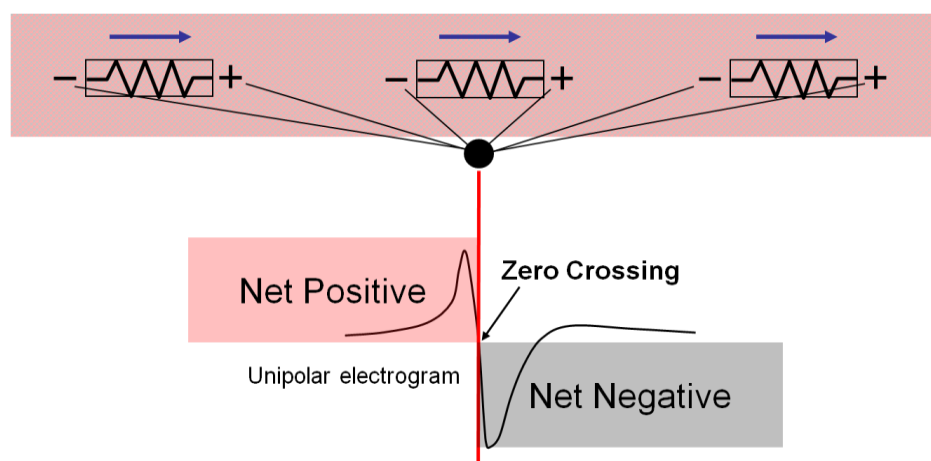


Figure 1.8 Illustrative example of how a single channel is activated by wavefront propagation to characterize unipolar morphology.

Studies were conducted to investigate the morphological characteristics of the AEGs with the conventional unipolar intracardiac contact catheters during sinus rhythm and heart rhythms disorders. The authors observed that both electrograms are reliably matched (Taccardi *et al.*, 1987, Schilling *et al.*, 1998, Gornick *et al.*, 1999, Kadish *et al.*, 1999, Schilling *et al.*, 1999, Schilling *et al.*, 2000, Schilling *et al.*,

2001, Tai *et al.*, 2002, Earley *et al.*, 2006, Lin *et al.*, 2007, Tai and Chen, 2009b, Sy *et al.*, 2012, Tsuchiya, 2012). In addition, no significant difference in timing of maximum $-dV/dt$ between contact catheter and reconstructed electrograms for areas below distances up to 4.0 cm was found (Kim Rajappan and Schilling, 2009).

Once the unipolar electrograms are acquired, a pre-processing filtering embedded into the EP systems is applied. It consists of a high-pass filter in the range of 0.1 Hz to 4 Hz (2 Hz or 4 Hz when the atrial activity (AA) overlaps with the ventricular repolarisation), and a low pass filter with cut-off frequency of 300 Hz (Schilling *et al.*, 2000, Hindricks and Kottkamp, 2001, Lin *et al.*, 2007).

1.4.3.2. BIPOLAR

It is known that unipolar signals provide the exact localization of target sites for ablation and a characteristic morphology at specific sites. However, low-amplitude local signals maybe buried in remote components in the unipolar mode so that bipolar recording may be favourable in such situations (Lars Eckardt and Breithardt, 2009).

Bipolar electrograms are originated by the potential difference between two closely spaced electrodes which are in contact with the endocardium. Electrical far-field endocardial effects will induce approximately the same potential at both electrodes so the remote effects will be reduced in the bipolar electrograms when compared with unipolar electrograms (Lars Eckardt and Breithardt, 2009).

Bipolar recording is the most common technique used in clinical practice during AF treatment as it allows a clear identification of local endocardial activity separated by

a flat baseline (Stevenson and Soejima, 2005, Lars Eckardt and Breithardt, 2009). Therefore, the time of local endocardial activation is better recognised in these recordings when compared with unipolar electrograms.

Bipolar electrograms also permit identifying information on wavefront propagation, but the relative orientation of the electrodes in relation to the wavefront propagation is a major determinant of the signal shape (Segal *et al.*, 2011). Once the electrograms are acquired, a pre-processing filtering embedded into the EP system is applied. It is well defined in the literature and consists of a high-pass filter with a cut-off frequency around 30 Hz (Jais *et al.*, 1997, Stevenson and Soejima, 2005, Fischer *et al.*, 2007) or 40 Hz (Botteron and Smith, 1996, Stevenson and Soejima, 2005) aiming to remove components generated by the repolarisation of the cells, followed by a low-pass filter centred in the range of 250 Hz (Botteron and Smith, 1996, Stevenson and Soejima, 2005) to 500 Hz (Jais *et al.*, 1997, Stevenson and Soejima, 2005) to remove possible high noise frequency influence. The output signals from the resulting band-pass filter contain mainly components of local depolarisation (Botteron and Smith, 1996, Stevenson and Soejima, 2005).

1.5. SPECTRAL ANALYSIS

Spectral analysis has been successfully applied for several decades to surface and intracardiac signals contributing to improve the knowledge of the physiological cardiovascular system behaviour for healthy volunteers and arrhythmia patients. In AF, since the experiments performed by Skanes and collaborators (Skanes *et al.*, 1998) where the authors showed that DF of a AF intracardiac electrogram correlated with the time duration of an AF wavefront cycle re-entry, DF analysis has been widely applied to identifying sites with high frequency and areas with high DF are suggested to being important sources of AF and hence targets for ablation (see Chapter 1 for more details).

1.5.1. ELECTROGRAM PRE-PROCESSING PRIOR TO SPECTRAL ANALYSIS

As described in the previous section (see 1.4.3.2 Bipolar) pre-processing using a band-pass filter in bipolar contact electrograms is needed prior to spectral analysis (Ng *et al.*, 2007). Each surrogate bipolar electrogram is then rectified and a low-pass filter with cut-off frequency of 20 Hz is applied (Botteron and Smith, 1996, Sanders *et al.*, 2005, Fischer *et al.*, 2007, Ng and Goldberger, 2007, Ng *et al.*, 2007). As described by (Botteron and Smith, 1996) the output of this procedure gives a smoothed envelope signal with equivalent components to the original raw electrograms.

For the unipolar intracardiac electrograms the process is more straightforward and no further filtering is needed prior to spectral analysis and computation of DF during intracardiac mapping (Ng and Goldberger, 2007, Ng *et al.*, 2007, Gojraty *et al.*, 2009).

1.5.2. AF FREQUENCY RANGE

The frequency range associated with atrium rate during AF is related to the capability of a cell during AF to contract (Biktashev, 1997). A general frequency range for AF in humans is accepted to be between 3 Hz to 15 Hz, but studies have shown that DFs usually fall within a range of 4–9 Hz (240–540 cycles/minute) (Ropella *et al.*, 1988, Sanders *et al.*, 2005, Ng and Goldberger, 2007). In addition, considering this narrow range, investigators are also studying the behaviour of the harmonic peaks correspondent to the DF, then a wider range (up to 20 Hz) would be necessary if we considered both the 1st and 2nd harmonics of a DF (Everett *et al.*, 2001).

1.5.3. DISCRETE FOURIER TRANSFORM AND FAST FOURIER TRANSFORM TECHNIQUE

The majority of the studies that applied spectral analysis to identify the DF and its harmonics within a relevant physiological AF range of intracardiac electrograms used the Discrete Fourier transform (DFT) (equation 1.3), or its fast algorithm version (FFT) as the approach for spectral estimation.

$$X\left(\frac{k}{NT}\right) = \sum_{n=0}^{N-1} x(nT)e^{-\frac{j2\pi nk}{N}} \quad (1.3)$$

In this technique, the sampled Fourier transform of a finite-duration, discrete time signal electrogram, $x(n)$ is known as DFT and it contains a finite number of samples (N), that is $k = 0, 1, 2, \dots, N-1$.

The main reason for the FFT algorithm's preference is its speed. The total number of operations (the processing time) required for obtaining an N-point DFT directly from its definition is proportional to N^2 . For a segment where N is an integer power of 2,

using the FFT algorithm, the number of operations is proportional to $N \log_2 N$ highlighting its clear speed advantage (Cooley *et al.*, 1969).

In Fourier-based spectral analysis, when N points of a signal $x(t)$ are sampled at frequency (F_s) and their FFT is obtained, the time linearly-spaced samples are at $T = 1/F_s$ apart in the time domain, and the resulting frequency samples are at $\Delta f = 1/NT$ apart in the frequency domain. The distance between two consecutive FFT estimates is known as frequency step (f_{step}).

Therefore, for longer FFT electrogram windows the frequency step became smaller, in contrast, if smaller electrogram segments are considered the capability of separating two or more close spectral peaks is considerably affected (poor spectral resolution).

1.5.4. FFT WINDOW SIZE

A decision of what is the best minimum size window which could accurately represent DF sites behaviour of the AF arrhythmia during catheter ablation was also investigated by several researchers (Sanders *et al.*, 2005, Ng *et al.*, 2006, Takahashi *et al.*, 2006, Lin *et al.*, 2007, Stiles *et al.*, 2008a) . Stiles and colleagues (Stiles *et al.*, 2008a) compared the DF of AF electrogram windows from 1 to 7 second-length with the DF obtained in its respective reference window of 8 second-length. The authors concluded that electrograms with duration of 5 seconds window (or more) accurately characterized DF sites for ablation. Ng and colleagues (Ng *et al.*, 2006) showed a good correlation on DF calculated in sub-widows of 2 s when compared with atrial activation rates obtained on windows of 4 s (Ng *et al.*, 2007). In addition, for both simulated and clinical AF electrograms, the authors observed that the mean DF

obtained through four consecutive windows of 4 s each improved the correlation of the DF reflects the atrial activation rate rather than using just a single window. That has also had been previously highlighted by (Everett *et al.*, 2001). Sanders *et al.* (2005) successfully terminated AF in patient undergoing catheter ablation guided by contact DF mapping using windows of 5 second-long segments. But during the spectral analysis calculation, the authors effectively used just 4,096 samples to compute the DF (sampling frequency, F_s of 1 kHz) which in turn shows that the authors effectively used windows of about 4 s.

1.5.5. ANTI-LEAKAGE WINDOW

Anti-leakage window is a weighting function which is applied to data to reduce undesirable effects related to spectral leakage due to abrupt discontinuities in the beginning or in the end of the segment (Harris, 1978). Several anti-leakage windows have been proposed through the years with different settings of the parameters (most common are: Peak Amplitude of Side Lobe and Approximate Width of Main Lobe). The selection of an anti-leakage window is done according to the objectives of the study and for the analysis performed in this thesis the Hanning or Hamming anti-leakage windows are the two best candidates when compared with the remaining anti-leakage windows by presenting smaller weighting peak amplitude values of side lobes with narrower width of the main lobe peak amplitude.

1.5.6. ZERO PADDING

The original sequence of samples from an electrogram $x(t)$ can be augmented with extra samples with zero amplitude to create longer sequences with, say $2N$ values (N original values of $x(t)$ augmented with N zeroes) or $5N$ values (N original values

and $4N$ zeroes) before the FFT. This process is referred to as zero-padding. Although the spectral resolution doesn't improve with zero-padding, the resulting spectral estimations will have a finer representation in the frequency domain at $k/2NT$ or $k/5NT$, where the extra values are interpolations of the original $X(k/NT)$ and the interpolator is a $\text{sinc}(f)$ kernel, reducing f_{step} and producing the smoothest series that contains the original samples (Marple, 1987).

1.5.7. DOMINANT FREQUENCY 'ORGANISATION' INDICES

Once the AF frequency spectrum is estimated, the DF can be identified. The DF value itself has been compared across different sites of the atria during AF to help the understanding of the AF pathophysiological behaviour and its propagation aiming at the identification of possible targets for ablation.

Several indices have been created to help investigators to identify the DF 'organisation' within the relevant frequency spectrum. These indices attempt to measure how 'dominant' the DF is within the AF physiological relevant range (Rosenbaum and Cohen, 1990, Everett *et al.*, 2001, Sanders *et al.*, 2005, Krummen *et al.*, 2009). The two indices most commonly used are the regularity index (RI) and Organisation Index (OI).

The RI was first introduced by (Rosenbaum and Cohen, 1990) and later used as a criterion of exclusion ($RI < 0.2$) of DF site selection as potential candidates for ablation (Sanders *et al.*, 2005) during 3D DF CM of high-frequency activity in patients undergoing PAF and persAF.

The index is calculated by identifying the area underneath the highest peak in the power spectrum (DF) and then dividing it by the total area within the frequency

spectrum (equation 1.4). Observe that for higher values of RI, the DF shows to be more 'influential' or 'dominant' if compared with other possible peaks in the AF frequency spectrum. In contrast, for lower values of RI, the DF seems to be less influential and other frequency peaks are 'competing' with the DF diminishing its importance (Sanders *et al.*, 2005, Ng *et al.*, 2006, Stiles *et al.*, 2008b, Brooks *et al.*, 2009).

$$RI = \frac{\text{Area (DF)}}{\text{Total AF Spectrum Area}} \quad (1.4)$$

The second index commonly used to 'quantify' DF organisation is the OI and has been first applied by (Everett *et al.*, 2001) who proposed that the spectral behaviour of AF electrograms had 'organisation' and that higher values of OI were associated with successful atrial defibrillation. The principal difference of OI and RI is that in this index the peaks corresponding to the harmonics of the DF are also considered together with the area underneath the DF. This area (DF+harmonics) is divided by the total area of the whole AF spectrum area (equation 1.5) (see Figure 1 in the Appendix for illustration).

$$OI = \frac{\text{Area (DF+harmonics)}}{\text{Whole AF Spectrum Area}} \quad (1.5)$$

1.5.8. DF ESTIMATION OF NONCONTACT ELECTROGRAMS VS. CURRENT CONTACT MAPPING TECHNIQUES

The technique of using NCM with the MEA has previously been described and validated in published literature, in the context of sinus rhythm as well as arrhythmia in humans (Schilling *et al.*, 1998, Schilling *et al.*, 1999, Hindricks and Kottkamp, 2001, Schilling *et al.*, 2001). Estimation of DF via spectral analysis from NCM has

been shown to be very well correlated (agreement in approximately 95% of cases) with DF estimation via spectral analysis from CM for both PAF and persAF (Lin *et al.*, 2007, Gojraty *et al.*, 2009).

1.5.9. LIMITATIONS

Spectral analysis of electrograms undergoing AF has been mainly performed mainly using FFT. Although this technique is well disseminated in clinical research groups it may not be the most adequate. Fourier based spectral analysis assumes that the signal is periodic during the sampling window and if that is not true the spectrum may be obscured by leakage (Lovett and Ropella, 1992). Another feature of spectral analysis based on the Fourier model is its inherent frequency resolution: when small segments are analysed the spectral resolution is poor, therefore its use can result in 'false' interpretations (Ng *et al.*, 2006, Ng and Goldberger, 2007, Ng *et al.*, 2007). Therefore, the use of other spectral analysis techniques such as Wavelet and Autoregressive (AR) might improve spectral analysis estimation of intracardiac AF electrograms contributing to the understanding of the dynamic physiological phenomena that underlie this arrhythmia (Lovett and Ropella, 1992, Houben *et al.*, 2010).

It also has been shown, in previous studies in time-frequency domain from contact mapping and frequency domain from contact and non-contact mapping (chapter 4), that the AF process in the atrium may change in time and space, which can obscure results when performing these Fourier-based approaches. AR-based spectrum seemed to be an alternative powerful tool to observe the dynamic behaviour of the AF electrograms (Lovett and Ropella, 1992).

During a sustained fibrillatory process over time, simultaneous dynamic phenomena (focal activity, rotor activity and multiple wavelets) may be involved in AF perpetuation at different stages of the arrhythmia history in any given individual. That highlights a lack of spatiotemporal stability hampering possible outcomes when performing these Fourier-based approaches. Other, more advanced signal processing techniques might also be considered for spectral analysis of atrial electrograms in persAF or long-standing persAF.

Linear and nonlinear analysis techniques have been successfully applied in AF epicardium and endocardium recordings (Lovett and Ropella, 1992, Hoekstra *et al.*, 1995, Mainardi LT *et al.*, 2001, Brooks *et al.*, 2009, Houben *et al.*, 2010, Kirchhof and Eckardt, 2010, Berenfeld *et al.*, 2011, Crawford, 2011, Ng and Goldberger, 2011). Analysis into this direction can also help scientists in the identification of sites responsible for maintaining the arrhythmia and their correlated paths of propagation of remodelled substrate for persAF patients.

1.6. STUDY DESIGN

1.6.1. RECRUITMENT

Eight patients undergoing catheter ablation of persAF for the first time and with no previous history of heart diseases were recruited. In keeping with the definition of persAF (Fuster *et al.*, 2006), all patients were in AF at the start of the procedure. Patients were treated in the Glenfield Hospital by doctors from the Cardiovascular Department led by Prof. G. André Ng.

Figure 1.9 presents a typical example of a theatre where the catheter ablation procedure of a patient with AF is being performed. In this figure, Prof. André Ng is leading the procedure. Four computer screens are used to show different and parallel information to help the clinician during the procedure.

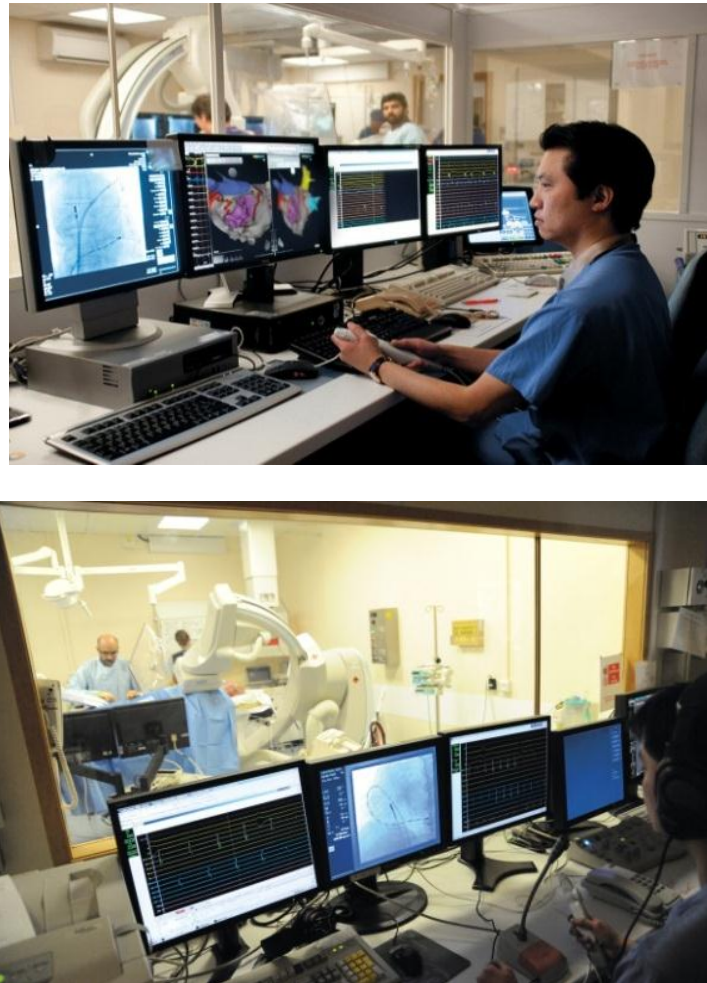


Figure 1.9 Prof. G. André Ng during catheter ablation of an AF patient. The various computer screens show the fluoroscopy image of the catheters located inside the heart, the 3D image of the LA generated by the EP system and the selected electrograms over time from the areas under investigation.

1.6.2. ETHICAL APPROVAL

Approval was obtained from the Local Ethics Committee for patients undergoing AF ablation including blood sampling and collection of electrical data and all procedures were carried out after informed consent and in accordance with institutional ethics guidance.

1.6.3. ELECTROPHYSIOLOGICAL STUDY

All antiarrhythmic drugs, apart from amiodarone, were stopped for at least five half-lives before the procedure. Once bilateral femoral venous access had been achieved, a deflectable decapolar catheter and a quadripolar catheter were positioned in the CS and His position, respectively, under fluoroscopic guidance. A single transseptal puncture technique was utilised in all cases to gain access to the LA with the use of a steerable transseptal sheath (Channel, Bard Electrophysiology, USA). A MEA catheter (EnSite 3000, St Jude Medical, USA) and a conventional deflectable mapping catheter were deployed via transseptal access, into the LA. Patients were anticoagulated with heparin and activated clotting time was maintained at >300 s. Detailed LA geometry was acquired with the mapping catheter and anatomical landmarks including PV ostia, LAA, roof, septum, anterior, PWs and MV annulus were identified and annotated. The array was not moved after geometry creation to avoid distortion of the isopotential maps (Schilling *et al.*, 1998, Gornick *et al.*, 1999, Kadish *et al.*, 1999, Chinitz and Sethi, 2006, Earley *et al.*, 2006, Tai and Chen, 2009a) and the distance between the centre of the MEA balloon and the LA endocardial wall did not exceed 4 cm (checked with fluoroscopy). AEGs projected to the LA surface were collected during steady state in AF over a 5 minute interval.

Following this, the MEA was removed and AF ablation proceeded as per standard practice. Standard practice ablation consists of ablation of the PVs ostia, aimed at the electrical isolation between the potential firing triggers localized in the PVs (Jais *et al.*, 1997) and the LA. Ablation was performed either using point-by-point ablation or with multi-electrode PV ablation catheter.

1.6.4. STUDY POPULATION'S CHARACTERISTICS

A total of 8 patients with persAF were included in the study. Patients' characteristics from both groups are summarised in Table 1.1 and are largely what may be expected in a persAF population.

Table 1.1 Patients' characteristics.

	n=8
Male, n	8
Age, y	47 ± 10
AF duration, mo	34± 25
Hypertension, n	2
LV function, n	
EF ≥55%	5
EF 45-54%	2
EF 36-44%	-
EF≤35%	1
LA Size, mm	48 ± 6
On amiodarone, n	3

EF, ejection fraction.

1.6.5. FILTER SETTINGS

AEGs were sampled at 1200 Hz and band-pass filtered between 1 Hz and 150 Hz. No further filtering was applied to the signals to preserve signal integrity and low frequency components (around 1 Hz) (Gojraty *et al.*, 2009).

For each patient, the surface ECG was also recorded and band-pass filtered between 0.5 Hz and 50 Hz. The filters previously described were embedded in the EP mapping system during catheter ablation of persAF included in this study.

When mains hum noise influence was observed in any signal recorded a digital 50 Hz notch filter was applied.

1.6.6. ELECTROGRAMS

AEGs during longer AF episodes (> 1 minute) were exported and analysed off-line using Matlab (MathWorks Inc., USA). For the offline analysis, the EnSite 3000 system (NCM) can export up to 7-second long segments of data for up to 2048 points (a matrix of 32 × 64 spatial points) along the geometric coordinates (x, y, z) of the inner wall of the atrium and also the anatomical landmarks which were annotated during the clinical EP procedure. I have exported several such segments and using an automatic code where carefully merged them to compose longer data segments of 1 minute in duration for each patient. A total of 16384 noncontact points and 232 sequential DF maps were analysed.

1.6.7. VENTRICULAR FAR-FIELD INFLUENCE SUBTRACTION

AEGs firstly underwent ventricular influence removal (only QRS segments) by a method previously validated by our research group (Ahmad *et al.*, 2011). In this

method, the ECG from the surface is used as a guide to identify the timing of the VA of the signals. After the identification of the QRS fiducial point, the QRS onset was defined to lay at 50 samples (41.67 ms) prior the QRS fiducial point and the QRS offset at 60 samples (50 ms) after the QRS fiducial point. The QRS segments (between QRS onset and QRS offset) were replaced with interpolated data, with the authors favouring a flat line interpolator instead linear and spline by preserving better the electrograms' DF and its respective power (Ahmad *et al.*, 2011) .

This method allows the researchers to investigate AEGs with reduced presence of VA and consequently avoiding that these signals hamper the analysis and possibly distorting results (Gojraty *et al.*, 2009, Ahmad *et al.*, 2011, Salinet Jr *et al.*, 2013a). Due to the limitations of this method a new recently validated approach was developed improving the removal of ventricular influence on AEGs while preserving the atrial activity (see Chapter 3 for more details) (Salinet Jr *et al.*, 2013a).

1.6.8. FFT SPECIFICATIONS

After carrying out ventricular cancellation of the AEGs, spectral analysis was performed for each of the 2048 points, using FFT with a Hamming window to produce high density 3D DF maps (Salinet Jr *et al.*, 2013b). A window size of 4 s was chosen and sequential windows were obtained with 50% overlap (shifting forward by 2 s) over a period of 1 minute to produce a total of 29 sequential frequency maps for each patient.

The spectral resolution was 0.25 Hz and fivefold zero padding was applied to improve the capability of identifying spectral peaks with a frequency step of 0.05 Hz. Although zero-padding does not increase the spectral resolution (the ability to

'resolve' close spectral peaks) it does interpolate the spectral estimates allowing a better ability to pinpoint the peak power of the DF (see section 1.5.6 for details)

DF was defined as the frequency with highest power within the physiological relevant range from 4 Hz to 10 Hz (Everett *et al.*, 2001). In addition, regularity index (RI) (Rosenbaum and Cohen, 1990, Sanders *et al.*, 2005) and OI (Everett *et al.*, 2001) were calculated during the analysis to help identify the 'organisation' of the DFs within the frequency spectrum.

1.7. THESIS OUTLINE

1.7.1. AIMS

The general objective of this research was to characterise the dynamic spatio-temporal behaviour of relevant DF areas identified by simultaneous AEGs recorded from patients with persAF aiming for a real-time application.

The secondary objectives were:

- (1) To implement an effective method to allow subtraction of ventricular far-field influences from unipolar electrograms to allow realistic DF mapping analysis in patients with persAF.
- (2) To develop real-time auxiliary tools on the frequency domain which might be integrated to the current commercial electroanatomical systems available on the market to help cardiologists to target potentially AF areas responsible to trigger and maintenance of AF.
- (3) To assess the spatiotemporal behaviour of DF and its organisation using 3D DF mapping of patients with persAF including characteristics of the highest DF area (H DFA).
- (4) To Implement non-traditional spectral analysis techniques, such as Autoregressive (AR) spectral estimation methods with emphasis on selection of appropriate sampling rate and AR model order to estimate the DF for each AEGs recorded in the LA from persAF patients.

1.7.2. OVERVIEW OF THE COMING CHAPTERS

Chapter 2 will describe a 3D high density DF mapping developed to help investigations on sites with high frequency activity of persAF patients who had NCM performed. This chapter also describes the alternative derivations of this mapping to be applied in specific studies such as trajectory propagation of possible AF triggers.

Chapter 3 will introduce the reader to the current method developed and used by our research group to remove ventricular far field influence (Salinet Jr *et al.*, 2013a). The results were compared with two other validated ventricular cancellation approaches.

Chapter 4 presents a study on analysis of spatiotemporal behaviour of DF and its organisation (see also Appendix for details) including characteristics of the HDFA (Salinet Jr *et al.*, 2013d).

Chapter 5 presents an investigation on the feasibility of using AR spectral estimation methods to estimate the DF for each of those 2048 AEGs. Three dimensional (3D) DF maps were generated and compared with the 3D DF maps recently validated using FFT-based approach (Salinet Jr *et al.*, 2010a, Salinet Jr *et al.*, 2011a, Salinet Jr *et al.*, 2013b).

Chapter 6 presents the use of 3D visualization techniques to highlight the visual aspects of the 3D frequency maps together with the calculation of the 2048 simultaneous DFs with 480 Graphic Processor Units (GPUs) for real time application of the 3D DF mapping.

Chapter 7 gives an overview of the most relevant achievements highlighted during the chapters, their clinical impact and their novelty. Finally, this chapter ends by suggesting new avenues of research and expected achievements.

Appendix details a specific study presented in Chapter 4 where the DF organisation at the core of the Highest DF areas showed to be more organised when compared with the areas at the Highest DF areas periphery.

2. THREE-DIMENSIONAL ATRIUM MAPPING REPRESENTATION

2.1. INTRODUCTION

Clinical studies in humans showed that ablation of DF regions in the atrium can contribute to terminate AF (Wright *et al.*, 2008, Brooks *et al.*, 2009, Gojraty *et al.*, 2009). In clinical practice, ablation of the sites guided by frequency mapping has been mainly performed through advanced mapping systems that are based on point-by-point sequential acquisition of contact endocardial activity (Lin *et al.*, 2007) and thus the spatial resolution of these maps can be limited and it is also difficult to assess temporal variation (Zipes and Jalife, 2004, Lin *et al.*, 2007).

This chapter introduces the methodology used to generate 3D representation of the inner surface of the atrium with simultaneous high resolution to allow the development of 3D colour-coded mapping from analyses performed on the AEGs, in special DF (Salinet Jr *et al.*, 2010a).

2.2. METHODS

2.2.1. THREE-DIMENSIONAL REPRESENTATION OF THE PATIENT'S ENDOCARDIUM

The AEGs recorded by the balloon catheter are stored digitally by the Ensite system during the procedure in the theatre; however, as highlighted in the previous chapter, the system export AEG segments with up to 2048 simultaneous points (a matrix of 32 × 64 spatial points) around the entire inner wall of the atrium together with their

geometric coordinates (x, y, z). Anatomical landmarks have been annotated during the clinical EP procedure and exported for off-line analysis. Several such segments were exported and using an automatic code they were merged to compose longer data segments of 1 minute in duration for each patient.

Figure 2.1 shows a typical example of a file exported by the EnSite 3000 system for off-line analysis. The heading shows the number of samples, 8407 samples (Fs 1200 Hz), and the number of simultaneous measured points on the atrium's endocardium, 2048. The coordinates (x, y, z) of the atrium landmarks annotated during the procedure are also presented. That is followed by the coordinates (x, y, z) of each point identified in the endocardium and the respective electrical activity (mV) measured over time.

St. Jude Medical Virtual data export; file format revision 3
 Exported from study_study_esi3050_2008:04:15:09:42:06
 Beginning sample number (time): 10:05:01:0932
 Ending sample number (time): 10:05:08:0938
 Number of signals (columns): 2048
 Number of samples (rows): 8407

* Map Labels and (x y z) coordinates and geometry name *

3DP LLPV (x y z) = (-2.03, 1.05, -38.65) LA
 3DP MV3 (x y z) = (-23.25, 26.04, -24.17) LA
 3D MV6 (x y z) = (-28.4, 26.15, -4.83)
 3DP MV9 (x y z) = (-30.98, 16.19, 9.82) LA
 3DP MV12 (x y z) = (11, 31.28, -3.95) LA
 3DP RUPV (x y z) = (13, -20.41, 26.49) LA
 3DP RLPV (x y z) = (25, -7.6, 36.2) LA
 3DP LAA (x y z) = (-23, -22.19, -18.05) LA
 LUPV (x y z) = (2.9, -14.19, -35.22) LA

* Map Lesion and (x y z) coordinates and geometry name *

3D 1 (x y z) = (14.35, -32.02, 41.27)
 3D 2 (x y z) = (16.58, -30.01, 36.27)
 3D 3 (x y z) = (14.86, -26.99, 35.21)
 3D 4 (x y z) = (17.89, -25.8, 32.95)
 3D 5 (x y z) = (21.38, -22.68, 28.19)
 3D 5 (x y z) = (28.61, -5.22, 31.75)
 3D 6 (x y z) = (22.74, 2.16, 41.51)
 3D 7 (x y z) = (27.84, -5.66, 39.38)

Begin data

	1.81	1.8	1.73	1.66	1.58	1.48	1.37	1.24	1.1	0.95	0.79	0.62	0.45	0.27	0.09	-0.09	-0.27	-0.44	-0.61	-0.77	-0.92	-1.06
0.09	0.27	0.4	0.62	0.79	0.95	1.1	1.24	1.37	1.48	1.58	1.67	1.73	1.79	1.82	1.83	1.83	1.8	1.76	1.7	1.63	1.53	1.42
37	37.12	37	37.4	37.49	37.57	37.62	37.62	37.62	37.6	37.57	37.53	37.48	37.47	37.4	37.34	37.27	37.14	37.02	36.84	36.6	36.37	36.1

Coordinates (X, Y, Z) for each point position

	0.12	0.119	0.1	0.119	0.119	0.119	0.119	0.119	0.119	0.12	0.121	0.122	0.123	0.124	0.126	0.127	0.129	0.131	0.133	0.134	0.136	0.137	0.139
0.14	0.135	0.1	0.135	0.135	0.135	0.135	0.136	0.136	0.137	0.138	0.139	0.14	0.141	0.143	0.144	0.146	0.148	0.149	0.151	0.153	0.154	0.155	0.155
0.15	0.151	0.2	0.152	0.152	0.152	0.152	0.153	0.154	0.155	0.156	0.157	0.157	0.158	0.159	0.161	0.163	0.164	0.166	0.168	0.169	0.17	0.171	0.171
0.16	0.161	0.2	0.161	0.162	0.162	0.162	0.163	0.163	0.164	0.165	0.166	0.167	0.167	0.168	0.17	0.171	0.173	0.175	0.176	0.178	0.179	0.18	0.181
0.16	0.161	0.2	0.162	0.162	0.162	0.163	0.163	0.164	0.165	0.166	0.167	0.168	0.168	0.169	0.171	0.173	0.175	0.176	0.178	0.179	0.18	0.181	0.182
0.15	0.152	0.2	0.153	0.153	0.154	0.154	0.155	0.155	0.156	0.157	0.158	0.159	0.161	0.163	0.165	0.166	0.168	0.169	0.171	0.172	0.173	0.173	0.173
0.14	0.143	0.1	0.144	0.144	0.144	0.145	0.145	0.146	0.147	0.148	0.149	0.15	0.151	0.151	0.153	0.155	0.156	0.158	0.159	0.16	0.162	0.163	0.164
0.14	0.138	0.1	0.139	0.139	0.14	0.14	0.141	0.141	0.142	0.143	0.144	0.145	0.147	0.148	0.15	0.151	0.153	0.155	0.156	0.157	0.159	0.159	0.159
0.14	0.141	0.1	0.142	0.142	0.143	0.143	0.144	0.144	0.145	0.146	0.147	0.148	0.148	0.15	0.151	0.153	0.154	0.156	0.158	0.159	0.16	0.162	0.162
0.15	0.146	0.1	0.147	0.148	0.148	0.149	0.149	0.15	0.15	0.151	0.153	0.154	0.155	0.157	0.158	0.16	0.162	0.163	0.165	0.166	0.167	0.168	0.168
0.15	0.148	0.1	0.149	0.15	0.15	0.151	0.151	0.152	0.153	0.154	0.155	0.156	0.157	0.159	0.161	0.162	0.164	0.166	0.167	0.168	0.17	0.17	0.17
0.14	0.142	0.1	0.143	0.143	0.144	0.144	0.145	0.145	0.146	0.147	0.148	0.148	0.15	0.151	0.153	0.154	0.156	0.158	0.16	0.161	0.163	0.164	0.164

Electrical Activity (mV) at the same instant of time for all 2048 points

Electrical Activity along time (mV)
 12 lines = 0.01 seconds

Figure 2.1 Typical example of a file exported from Ensite System 3000 for off-line analysis. Only the first 23 of the 2048 columns are shown.

With the coordinates identified and stored in vectors, the data were reshaped into matrices of (64x32) to allow a smooth 3D representation. The 3D was created with the function 'surface' from Matlab. Figure 2.2 shows a diagram with the steps used to generate the 3D endocardium surface colour-coded automatically by Matlab. The respective 3D representation generated by the Ensite 3000 System with 2048 noncontact points is also shown.

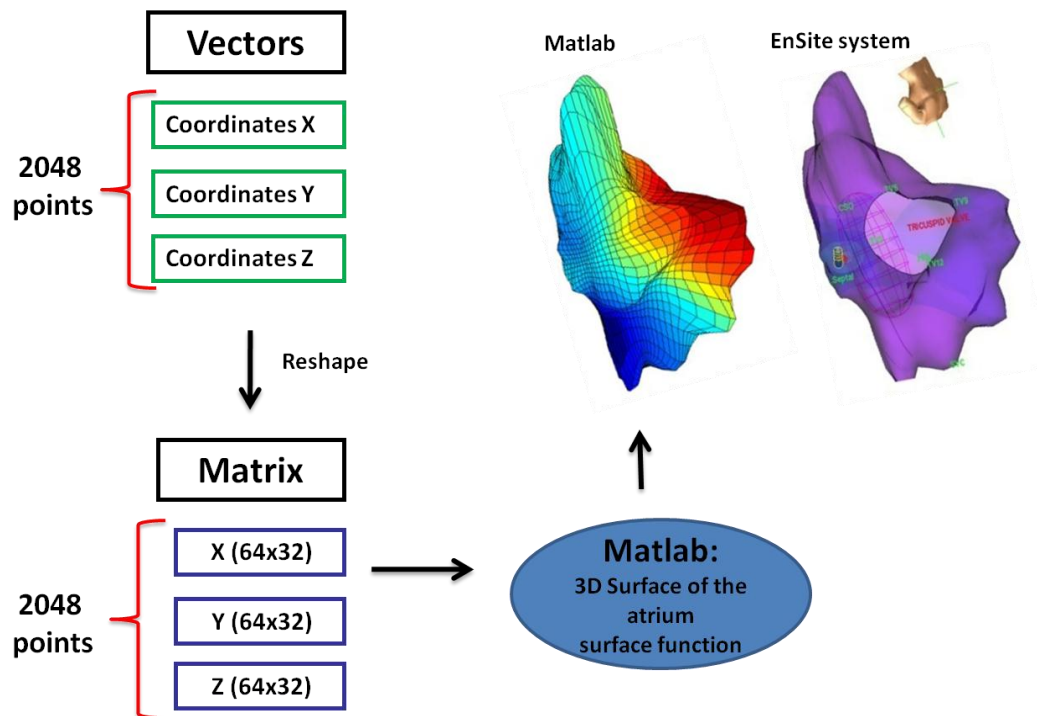


Figure 2.2 Diagram to generate the 3D endocardium surface of the LA colour-coded automatically by Matlab. The respective surface generated through the EnSite 3000 system during the clinical procedure is also presented. The colours are the Matlab representation of position in this case, but will be used to display the behaviour of a selected parameter (say 'DF', for example).

2.2.2. COLOURING THE ATRIUM: 3D COLOUR CODED REPRESENTATION

After validating the 3D surface geometry of the atrium using Matlab, we can colour-code the 3D maps with different colours according to the values obtained from analysis performed on the AEGs, such as DF, OI (see chapters 4-7 and Appendix).

Figure 2.3 illustrates the necessary steps to colour-code the 3D of the atrium endocardium representation using Matlab. The values contained in each matrix R element (64x32) correspond to a particular spot of the 3D atrium. The element values are ranked according to colours where in this case, the lowest value receives purple-blue and the highest is dark-red.

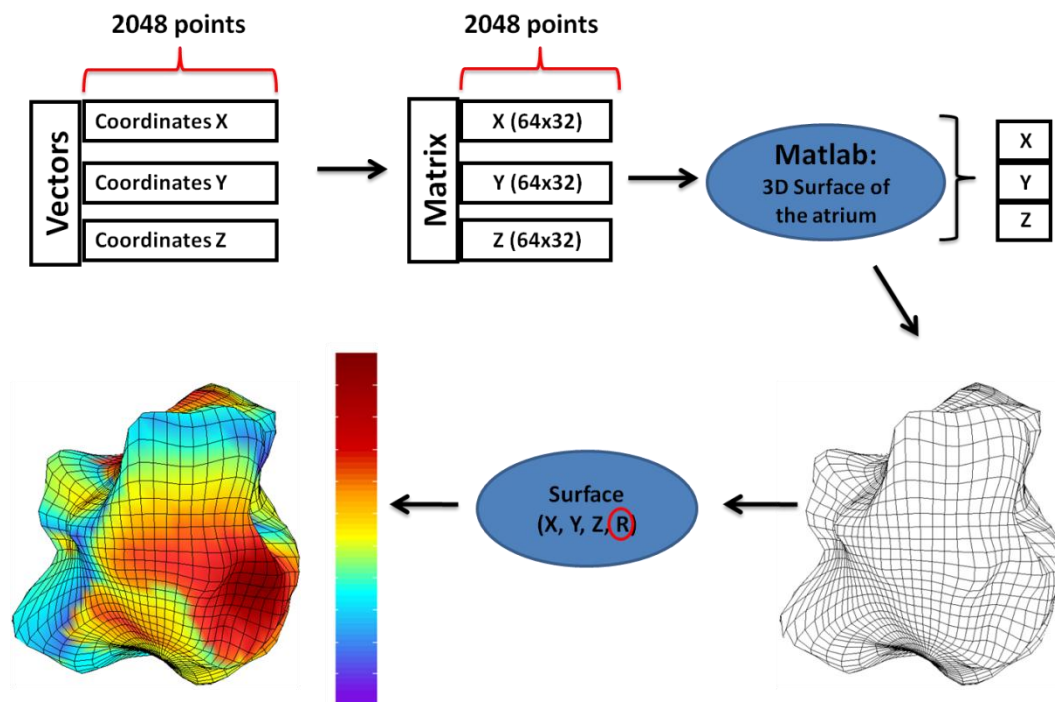


Figure 2.3 Diagram showing the steps to colour-code the 3D atrium's endocardium representation. Each matrix R element (64x32) corresponds to a particular spot of the 3D atrium. The element values are ranked according to colours where in this case, the lowest value receives colour purple and the highest red.

2.2.2.1. 3D HIGH DENSITY DF MAPPING

Figure 2.4 illustrates the whole spectral analysis procedure for each individual spatial point—the identification of the DF and colour coding according to the frequency of the DF for the 3D representation of DFs, with purple-blue representing the lower frequencies and red-dark red corresponding to higher frequencies. DF was defined at each of the 2048 points as the frequency with highest amplitude within the physiological relevant range (4 to 10 Hz). Frequencies outside this range were deemed to be of no physiological interest to AF. The DF of each of the 2048 AEGs was calculated using spectral analysis and colour-coded validating the first 3D DF map with high density of noncontact electrograms (Salinet Jr *et al.*, 2010a).

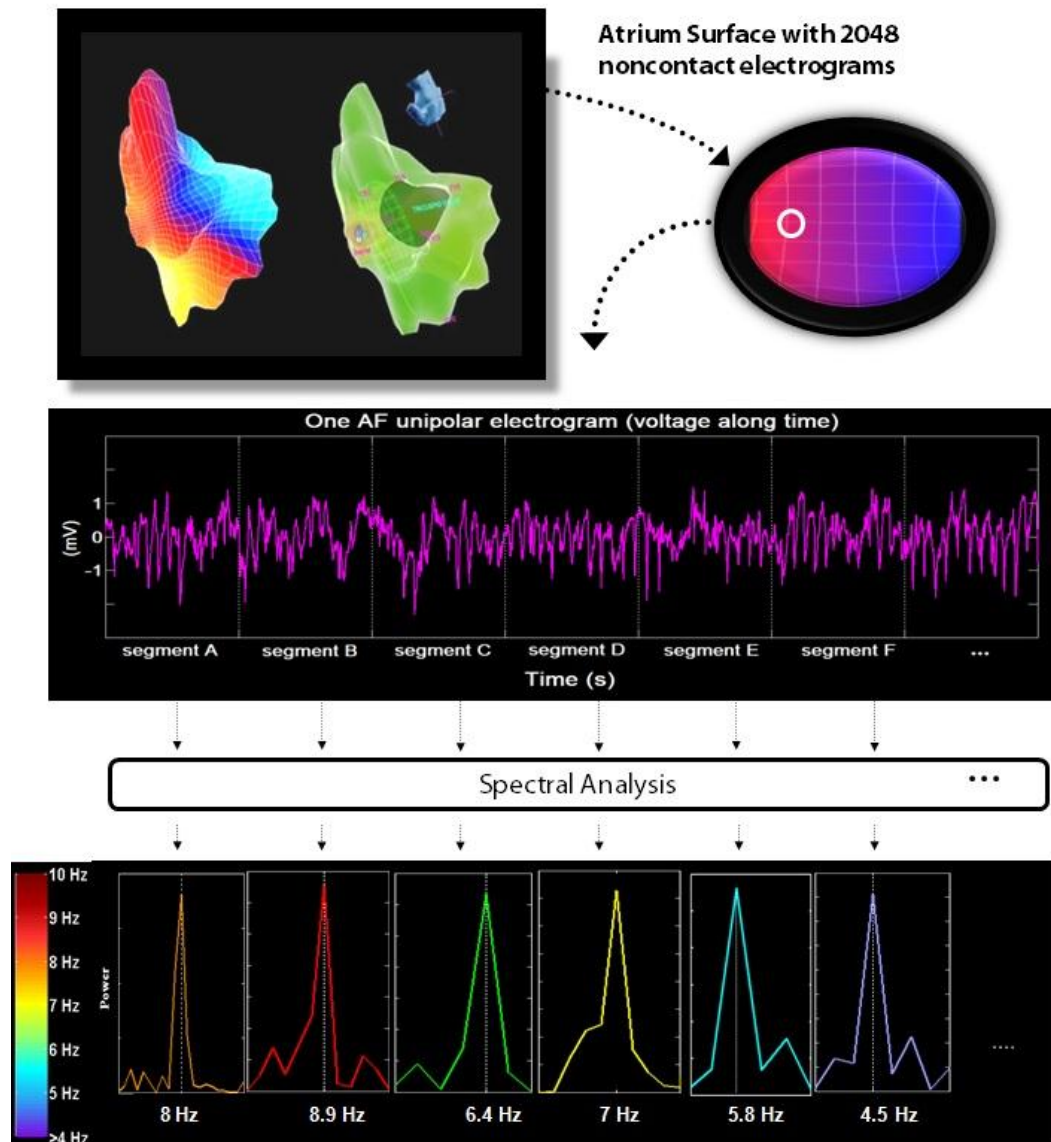


Figure 2.4 Spectral analysis methodology of the electrogram. The data collected by the Ensite 3000 system allow manipulation of the atrium on the screen (e.g. Rotating the 3D surface). We obtain the DF of the atrial electrograms for each segment along time and then colour code the surface according to the frequency of the each point (surface element).

Figure 2.5 shows an example of the 3D DF mapping of 2048 noncontact unipolar electrograms of the LA with two different views where the highest DF (10 Hz) is coded as dark red and the lowest value (4 Hz) in purple.

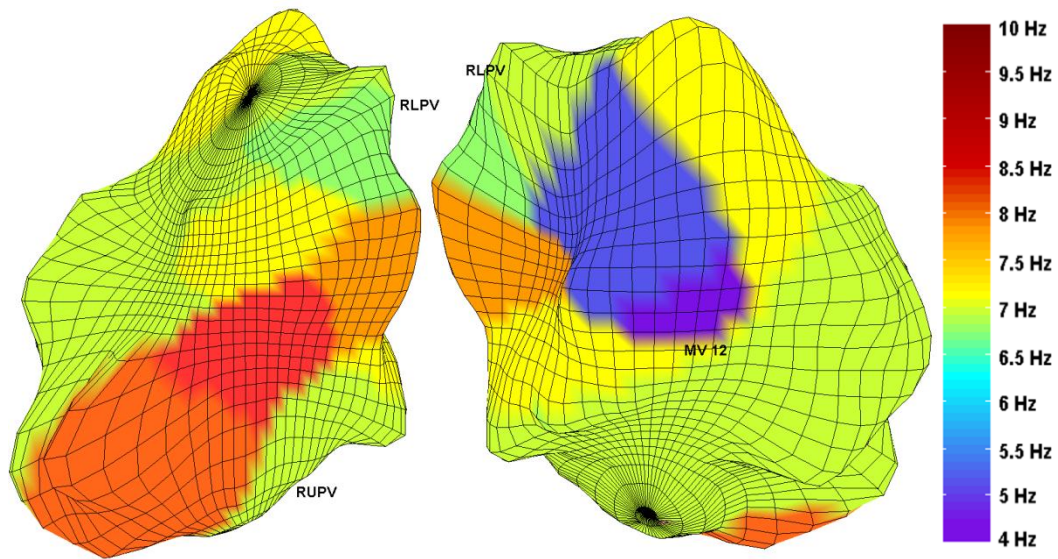


Figure 2.5 3D DF mapping of the LA with two different views of the 3D DF mapping. RLPV is 'right lower PV', RUPV is 'right upper PV' and MV 12 is 'MV' in the 12 o'clock position.

Investigation of the spatio-temporal DF activity of the simultaneous points can be accessed by looking at the time sequence of consecutive frames that are 2 seconds apart after cancellation of the ventricular far field on the AEGs (see chapters 3 and 4 for more details) (Salinet Jr *et al.*, 2013b). An illustrative example is shown in figure 2.6, where sixteen DF maps are presented sequentially. Two DF clouds were highlighted (DF clouds 'a' and 'b') showing that DF points were not spatially stable over consecutively frames, although reappearance of DF values were noted (for more details see Chapter 4).

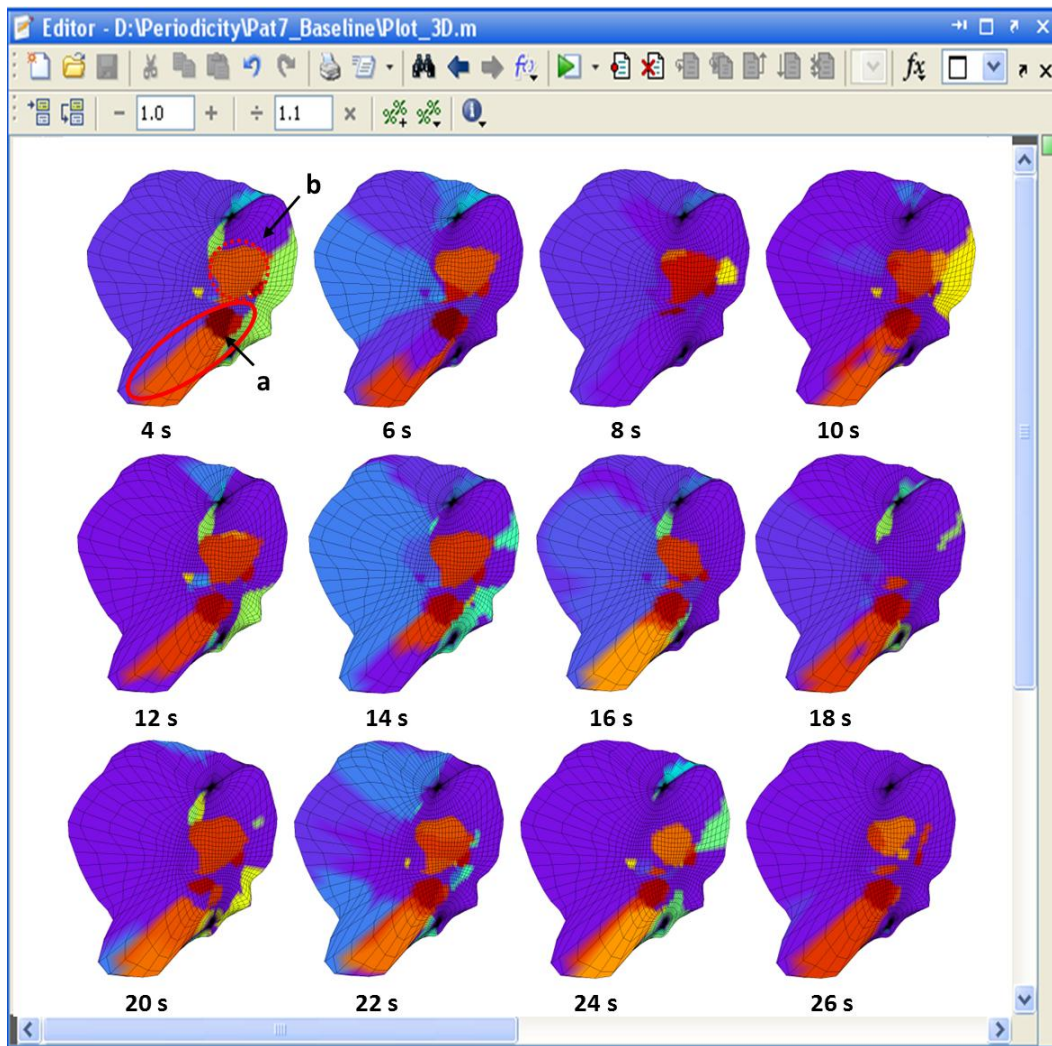


Figure 2.6 Sequence of 16 consecutive 3D DF mapping frames that are 2 seconds apart for each representation.

To produce a smoother animation of the DF maps to help in tracking the movement of several frequency zones in the atrium, the percentage of overlap can be modified (Salinet Jr *et al.*, 2011a). Increasing the percentage of window overlap, more DF maps are created, thus reducing the time difference between consecutive frames. That also allows measuring the velocity of propagation of DF activity. An example is

shown in Figure 2.7 where the FFT window length is 4 s but an overlap of 97.5% (62.5 ms step between consecutive frames) was used.

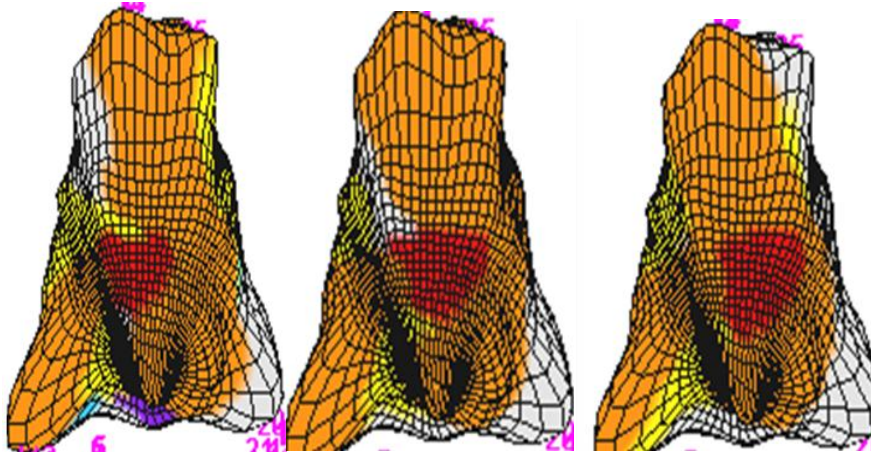


Figure 2.7 A sequence of three consecutive DF maps with an overlap of 97.5% (62.5 ms step between consecutive frames) showing a relative stable frequency distribution over the period displayed.

Associated with the tools from the 3D maps previously described and for further investigation, isolation of any particular area is also automatically permitted, such as areas of highest dominant frequency (HDFA) (Salinet Jr *et al.*, 2012c, Salinet Jr *et al.*, 2012d, Salinet Jr *et al.*, 2013d). These areas are believed to be a key point on the maintenance of AF and tracking their trajectory will facilitate the understanding of the electrical activity and its spatio-temporal pattern behaviour (see chapter 4).

Figure 2.8 illustrates on the left hand-side a 3D DF frame with a HDFA at 7.8 Hz and lower frequencies surrounding it. On the right hand-side the same 3D DF frame is presented but displaying only the HDFA delimited with a threshold of 0.25 Hz. Visualization of only the DF region can help doctors identify the potential locations where ablation might take place. For this purpose, our tool needs to both identify the

areas of highest DF, as well as use specific colour scales in the visualization to clearly identify these areas.

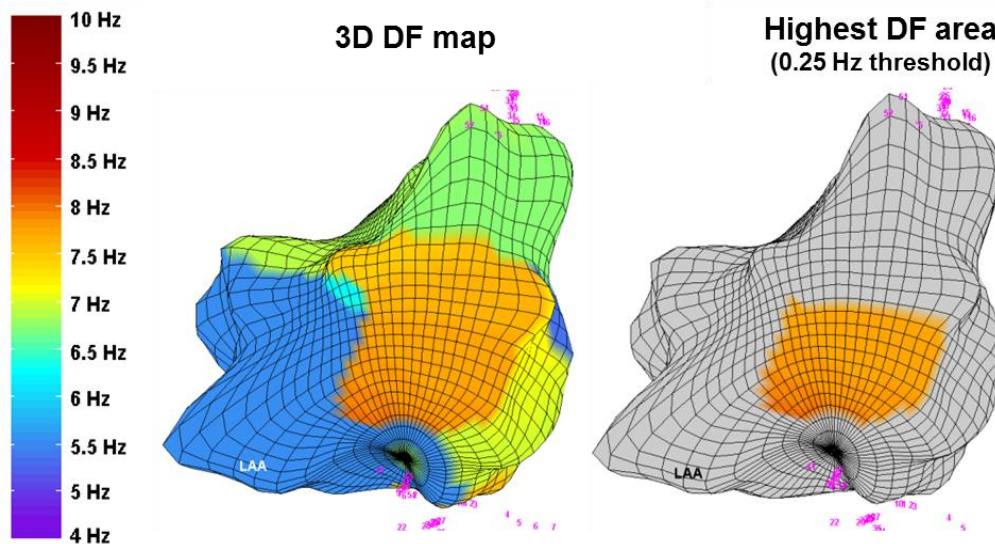


Figure 2.8 3D DF mapping and highest DF identification. (left-hand side) 3D representation including the mapping of the DFs. The DF mapping which will allow doctors to visualize the behaviour of the atrium’s electrical activation in the frequency domain. (right-hand side) the system can also automatically identify the region corresponding to the HDFA.

2.2.2.2. OTHER EXAMPLES OF ANALYSES AND COLOURING THE ATRIUM: 3D OI MAPPING

The 3D representation of the atrium endocardium can also be colour coded according to the results from different analyses on the AEGs. Figure 2.9 shows a 3D DF frame from the LA during AF (left-hand side) where the HDFA was isolated and its respective centre of gravity (CG) point calculated (middle). For the same window segment, the OI was calculated for each point as described in chapter 2 and Appendix. Briefly, for each point OI is the DF area and its harmonics divided by the

total area from the physiological relevant AF range. The higher is the OI is the more 'organised' the electrogram is.

In this example, the area of highest DF (dark orange) also has the highest OI (dark red). An electrogram from around the CG showed to have higher OI when compared with a site localised on the periphery with the same DF (Salinet Jr *et al.*, 2013d).

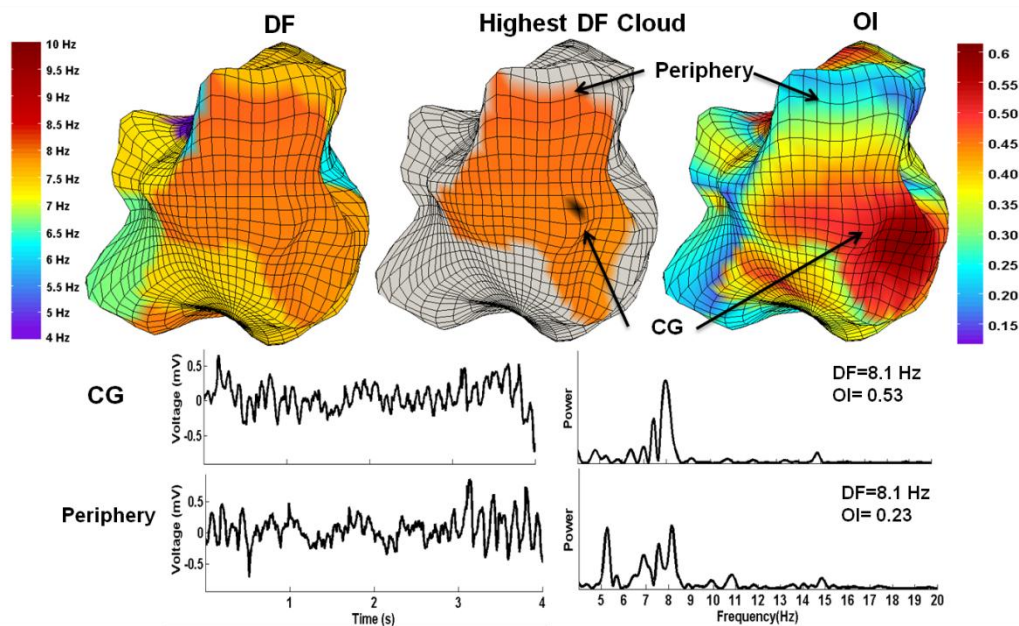


Figure 2.9 DF organisation from the HDFAs in two different positions: at the core and periphery.

2.3. DEVELOPMENT OF VIDEOS AS AN AUXILIARY TOOL FOR AF INVESTIGATIONS

Videos of 3D maps were produced to allow visualisation of simultaneous and sequential high resolution 3D maps and they are extremely useful in clinical meetings and conferences. There are different settings to create videos, such as number of frames per second, quality of the movies and compression. We have tested different settings including various quality levels and compression rates. The

advantage of using compression is that the size of the videos is smaller and they can be sent even via email as attachments. In terms of visual quality, the videos generated with compression do not suffer significant degradation and are suitable for our purposes.

Figure 2.10 illustrates a few snapshots of a film presented during the Heart Rhythm 2012 (Salinet Jr *et al.*, 2012c).

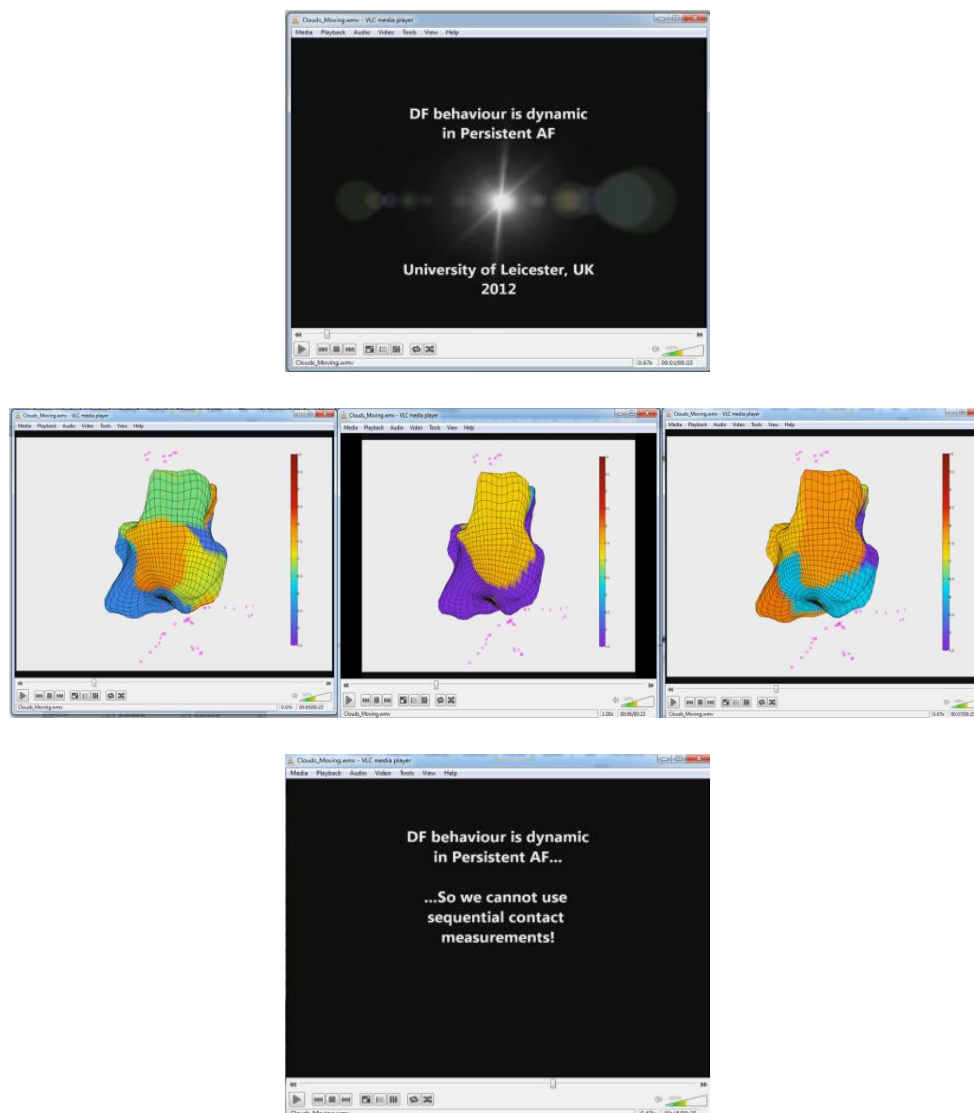


Figure 2.10 Snapshots of a video presented at the Heart Rhythm 2012 (Salinet Jr *et al.*, 2012c).

2.4. CONCLUSIONS

This current chapter presented how the 3D representation of the inner surface of the atrium with high resolution was generated and associated with the development of 3D colour-coded mapping from analyses performed on the AEGs, in special DF. In the next chapters the implementation of the maps described in this chapter will be presented as a tool for further investigation on characterisation of the AEGs recorded from persAF patients.

3. ANALYSIS OF QRS-T SUBTRACTION IN ATRIAL FIBRILLATION ELECTROGRAMS

3.1. INTRODUCTION

As presented in section 1.4.3, the presence of ventricular activity (VA) on the AEGs has hampered the analysis of AF behaviour with possibility of distorted results. It is important to study atrial activity (AA) without the influence of the VA to improve understanding of AF genesis and maintenance. As AA and VA overlap in time and frequency domains within the relevant AF frequency range (3 Hz to 15 Hz) (Sanders *et al.*, 2005), the use of standard linear filtering solutions is ineffective to separate them and isolation of the AA is difficult.

Averaging consecutive QRS-T segments to generate a template that is then subtracted from the raw signals has been the method of choice for ventricular cancellation (Shkurovich *et al.*, 1998). One classical implementation of this approach is the average beat subtraction (ABS) method, which relies on the fact that AF is uncoupled to VA (Slocum *et al.*, 1985, Shkurovich *et al.*, 1998). This method is characterised by a single-lead analysis of the ECG and by subtraction of a mean beat template. The template has the length of the shortest RR interval (Slocum *et al.*, 1985). The alignment is done either with the QRS fiducial point at the centre of the template or at the sample located after 30% of the beginning of the template, with the length of the template equal to the shortest RR interval and with the T-wave end defined as the last sample of that segment (Shkurovich *et al.*, 1998). A limitation of

this approach is that the QRS onset and T-wave end are fixed and the 30%-70% ratio used in their study frequently produces truncation of the T wave, but other choices for the truncation might give better results.

An alternative technique developed previously by our research group defines the QRS onset at 41.67 ms prior the QRS fiducial point and the QRS offset at 50 ms after the QRS fiducial point. These values were based on the length of typical QRS complex and the ratio 50/60 was selected because the fiducial point is the first point above the adaptive threshold (Ahmad *et al.*, 2011). In addition, the method avoids the problem of identifying a QRS template by replacing the signal over the QRS period with an interpolation, with the authors favouring a flat line interpolator (for more details see section 1.6.7). The three limitations of this approach are: (i) the length of the QRS to be removed is arbitrary and might not correspond to the actual onset or offset of some QRS complexes, resulting QRS residuals on the 'clean' signal; (ii) it does not attempt to preserve the AA during the QRS, as that part of the signal is simply replaced with a flat line, for instance, and (iii) it does not remove the ventricular repolarisation component.

This chapter presents a VA cancellation technique for AEGs, while it has recently been published as an original article in a peer review journal (Salinet Jr *et al.*, 2013a). The method does not suffer from some of the limitations of the classical ABS approach or of the 'QRS cancellation' method, as it is based on a segmentation of each individual QRS complex (Madeiro *et al.*, 2012) and T-wave end on the ECG (Qinghua *et al.*, 2006). The QRS-T templates are matched both in shape and in length to the individual signals (both onset and offset of the QRS-T complex). It also preserves the AA of the interval corresponding to the QRS-T interval.

3.2.METHODS

3.2.1. PROPOSED QRS-T CANCELLATION METHOD

The general block diagram from the proposed QRS-T subtraction method is presented in Figure 3.1. Firstly, the R peak, QRS onset and T-wave end are detected on the ECG (lead I for 6 patients and V5 for 2 patients) using the methods described by Madeiro *et al.* (2012) (for QRS segmentation) and Qinghua *et al.* (2006) (for detection of T-wave end).

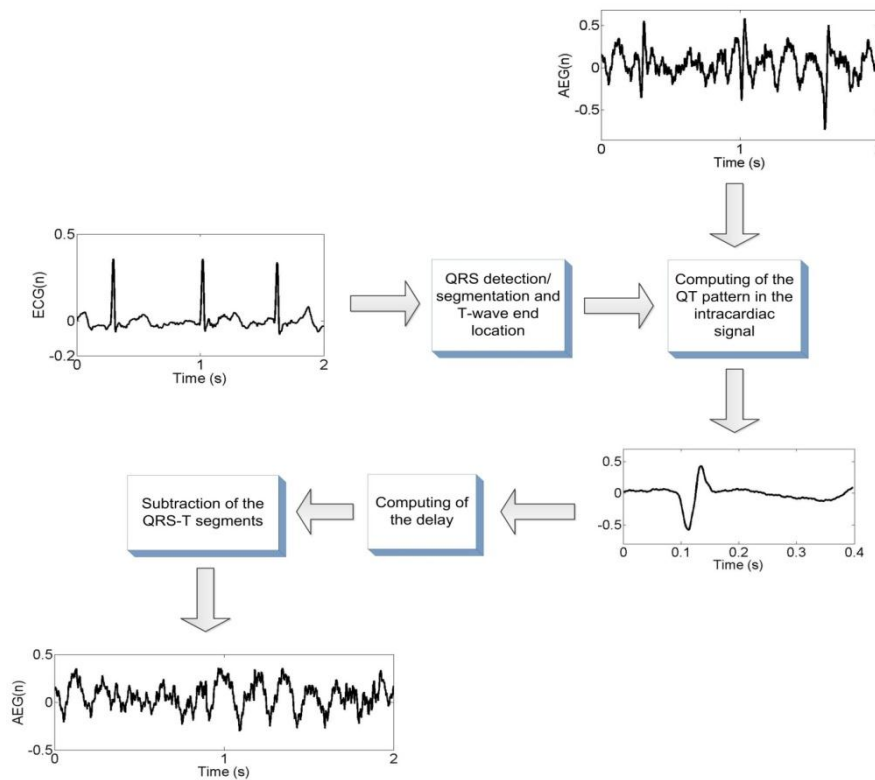


Figure 3.1 General block diagram for the proposed QRS-T subtraction method.

After segmentation of all QRS-T complexes in the ECG (see Figure 3.2 for QRS onset segmentation), the corresponding time locations of the fiducial points were used for the AEG signals. A pattern was obtained using median operator after their QRS-T fiducial points had been aligned. The instant of time with the maximum cross-

correlation between the pattern and the local VA in each intracardiac segment was used for time alignment. Then, subtraction was performed between the local VA and the pattern (see Figures 3.3 and 3.4). The steps are detailed further on.

In order to detect the QRS onset and T-wave end, first of all a 50 Hz notch filter was applied on the ECG to remove mains hum. Then, the timing position of the R-wave peaks and their respective QRS onset-offset were identified. The R-wave detection is divided in two stages: training and analysis. In the training stage, an initial 10 s long interval of the ECG is used. A detector that includes Wavelet transform, first-derivative filter, Hilbert transform and squaring function is applied over this training interval (see details in (Madeiro *et al.*, 2012)). After the training stage, an adaptive threshold technique was used to detect each QRS complex over the remaining of the ECG signal. This threshold is defined as (Madeiro *et al.*, 2012)

$$th[m] = \frac{\beta_1 * \hat{R}[m] + \beta_2 * R[m-1]}{\beta_1 + \beta_2} * \alpha, \quad (3.1)$$

where $th[m]$ is the threshold value for detecting the m -th QRS fiducial point, β_1 and β_2 are weight factors, $\hat{R}[m]$ is an estimation of the amplitude of the m -th beat based on the previous value of $th[m]$, $R[m-1]$ is the amplitude of the $[m-1]$ -th beat and α is a percentage factor.

If eventual occurrences of false-positive or false-negative are identified, based on the stored average and standard deviation of the intervals between beats, then the above referred pre-processing techniques are re-applied over the corresponding signal excerpts to emphasize QRS complexes and attenuate artefacts, noise and P/T waves (see details in (Madeiro *et al.*, 2012)).

After detection of QRS fiducial points, the QRS envelope was calculated. This envelope is defined as the absolute value of the analytical (complex) signal whose real and imaginary parts are the filtered ECG (real part) and the Hilbert transform of the filtered ECG (imaginary part) (Nygards and Sörnmo, 1983). Considering the QRS complex as a modulated waveform, the beginning and end of the QRS complex envelope calculated using the Hilbert transform coincide with the QRS onset and offset (Sörnmo and Laguna, 2005, Madeiro *et al.*, 2012). For QRS delineation the search for onset and end point within a time window is defined by $[R_P-300(\text{ms}), R_P+190(\text{ms})]$, where R_P is the location of the detected R peak and, for each window, the filtering process previously described for QRS detection is used. Calling the QRS envelope signal $E[n]$, an area indicator $A[n]$ is computed for a given QRS envelope (Illanes-Manriquez and Zhang, 2008, Madeiro *et al.*, 2012)

$$A[n] = \sum_{\tau=n-WL}^n (E[\tau] - E[n]) * \frac{1}{F_S} \quad (3.2)$$

where WL is the moving window's length, F_S is the sampling frequency and $A[n]$ is the area under the signal $E[\tau]$ above the horizontal line crossing the point n , $E[n]$ in the interval $[n-WL, n]$. It has been shown that $A[n]$ reaches its maximum value at the end of each QRS envelope, which corresponds to the offset of each QRS complex (Illanes-Manriquez and Zhang, 2008). For QRS onset detection the surface indicator $A[n]$ is defined as

$$A[n] = \sum_{\tau=n}^{n+WL} (E[\tau] - E[n]) * \frac{1}{F_S}, \quad (3.3)$$

reaching its maximum value at the beginning of each QRS envelope (see Figure 3.2).

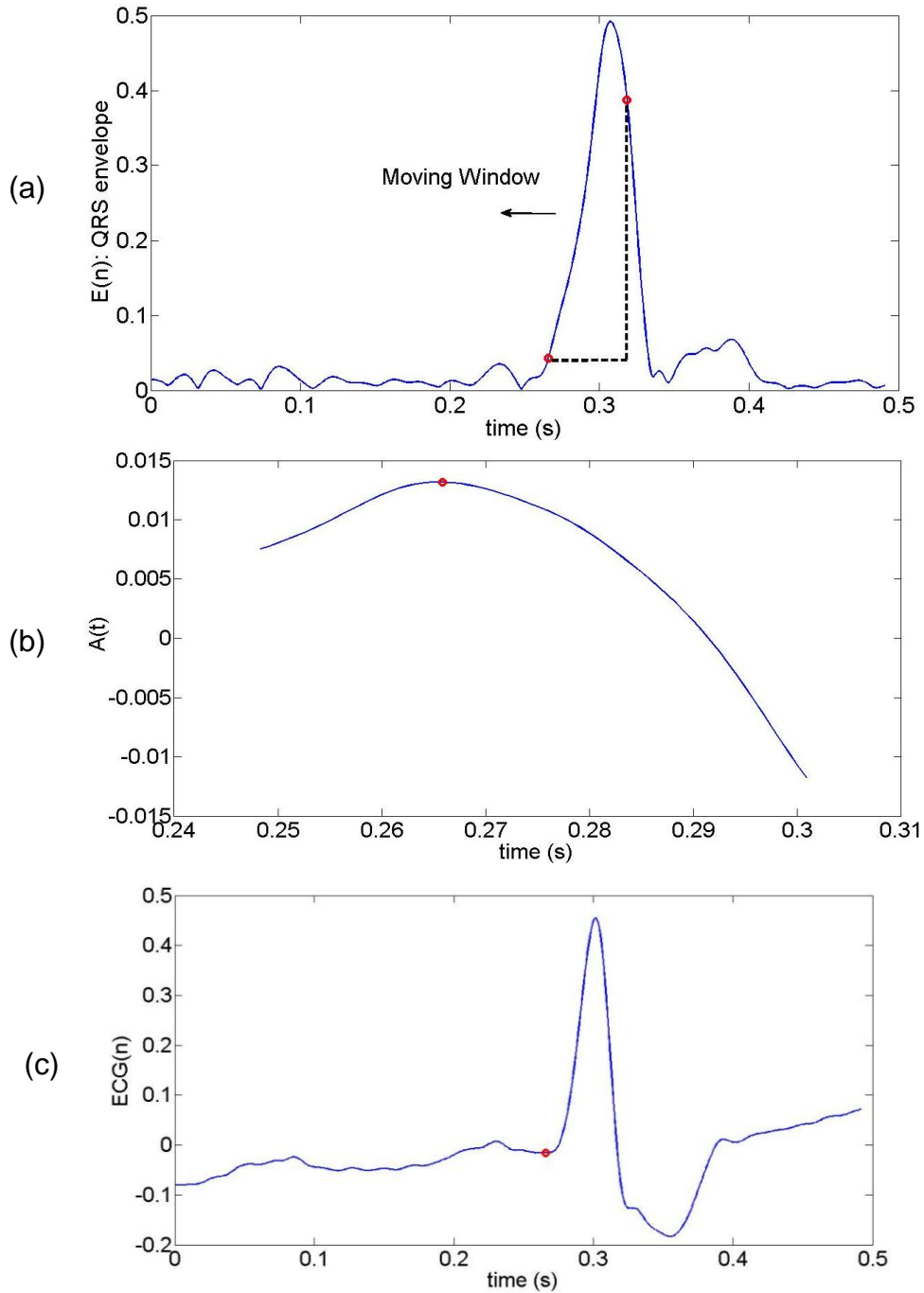


Figure 3.2 Detection of the QRS onset: (a) sliding moving window (WL) used to calculate the maximum area of the surface indicator $A[n]$ on the QRS envelope $E[n]$, (b) time position of the maximum value of the $A[n]$, and (c) respective time position identification of the QRS onset based at the beginning of the QRS envelope.

After the QRS segmentation, a baseline correction was applied by means of a cubic spline interpolation anchored on the QRS onset points (Lemay *et al.*, 2005).

The detection of T-wave end was also based on an indicator of the area of the T-wave (Qinghua *et al.*, 2006) and no additional pre-processing was necessary. Letting Q_f and Q_i be the samples (indices) related respectively to each QRS offset and the subsequent QRS onset, we define a moving sample k , $Q_f + w \leq k \leq Q_i - p - 1$, where p is the number of samples corresponding to 16 ms and w is the number of samples corresponding to 128 ms (Qinghua *et al.*, 2006). Then, for each k value, the following metrics were calculated

$$\bar{s}[k] = \frac{1}{2p+1} \sum_{j=k-p}^{k+p} s[j], \quad (3.4)$$

$$A[k] = \sum_{j=k-w+1}^k s[j] - \bar{s}[k], \quad (3.5)$$

where $s[j]$ refers to samples of the ECG inside the window and $A[k]$ will be used for the detection of the T-wave end as follows. The samples related to the maximum k' and the minimum k'' values of $A[k]$ are identified and for their corresponding values $A[k']$ and $A[k'']$, the inequality expression is tested

$$\frac{1}{6} < \frac{|A[k']|}{|A[k'']|} < 6. \quad (3.6)$$

If the inequality is satisfied, then the T-wave end in the current QRS offset-onset interval is located at the sample k' , if $k' > k''$, or k'' , if $k'' > k'$ (biphasic T-waves).

Otherwise, the T-wave end is located at the sample with the maximum amplitude of $|A(k)|$ (monophasic T-waves) (Qinghua *et al.*, 2006).

After the QRS-T segmentation, a pattern using median values was computed. In order to select the sliding window segment to compute a QRS-T pattern, firstly the first segment as the interval between 0 s to 7 s is defined. Then, for the next segment window, the end is the location of the next T-wave end and its beginning as 7 s earlier. It continues with an analogous approach till the last QRS-T complex.

The general block diagram to calculate a QRS-T pattern in a given segment window is presented in Figure 3.3. Initially the mean QT interval length is calculated, called *Lpat*.

QRS-T pattern

$Lpat$ (length) = mean length of QRS-T intervals
 $QRS-T_i$ = length of the local QRS-T segment
 $QRS-T_{on}$ = QRS-T onset
 $QRS-T_{off}$ = QRS-T offset

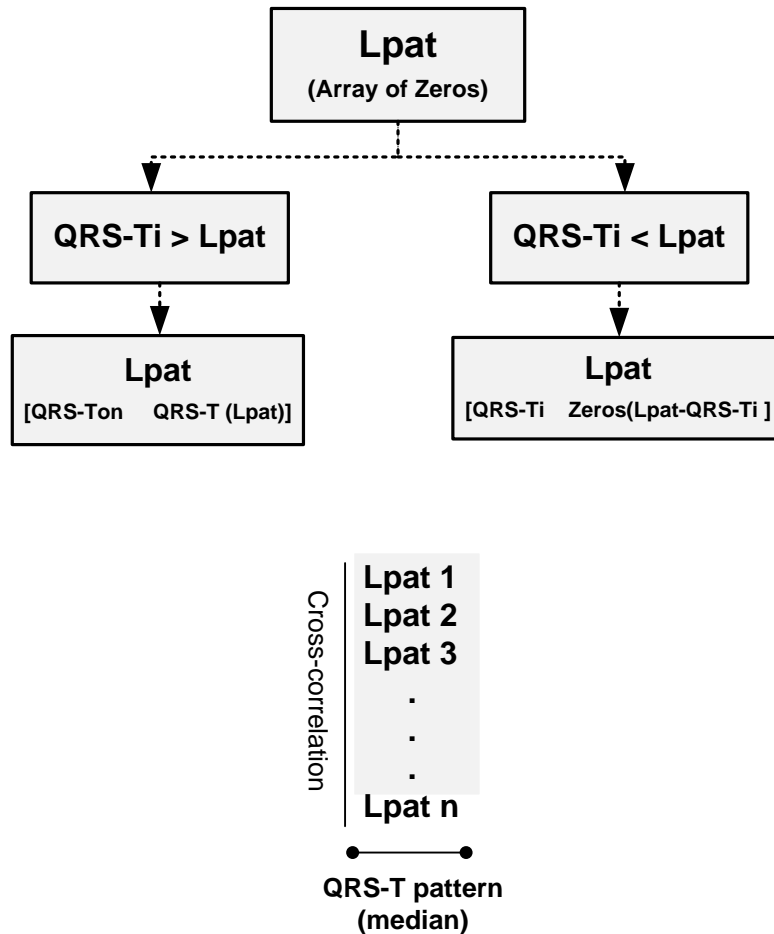


Figure 3.3 General schematic diagram to calculate the QRS-T pattern.

The complimentary descriptions from the steps presented in Figure 3.3 are described below:

- 1) An array of zeros with the same length of $Lpat$ is defined;
- 2) Then, it is selected the AEG segment which begins at the time instant related to the first QRS onset and ends at the time instant related to the first T-wave end point;

- 3) If that segment is larger than L_{pat} , then the array is filled out with the segment from the QRS onset until the sample related to the duration given by L_{pat} ;
- 4) Otherwise, if the segment referred in the step (2) is shorter than L_{pat} , then the array referred in the step (1) is filled out with the corresponding segment and the last array is left with samples with zeros;
- 5) For each other window in the AEG segment beginning at the next QRS onsets and finishing at the corresponding T-wave ends, we align it with the window referred in the step (2) using cross-correlation;
- 6) After aligning each QRS-T window with the window referred in the step (2), each one fills out an array of zeros similar to that one referred in the step (1), observing the same rule explained in steps (3) and (4);
- 7) A matrix ($N_s \times L_{pat}$) is built with the window defined in the step (2) and the set of aligned windows, where N_s is the number of QRS-T complexes in the corresponding AEG segment;
- 8) The median of each column of the matrix is obtained and a resultant array is built with the set of median results, which corresponds to the QRS-T pattern associated to that AEG segment.

The VA subtraction in the AEG signals is performed as follows:

- 1) For each QRS-T complex in the AEG segment, the delay between the corresponding fiducial points from the AEG raw signal and the QRS-T pattern was obtained using cross-correlation.

- 2) Then, for each QRS-T complex in the AEG segment, a window that begins at the sample related to QRS onset corrected by the delay and ends after L_{pat} is selected.
- 3) Finally, the local VA influence identified in the AEG is subtracted by the QRS-T pattern.

3.2.2. TIME AND FREQUENCY ANALYSIS APPROACHES USED TO COMPARE THE CANCELLATION METHODS

The segmentation of each QRS complex and T-wave in the ECG is the first step for QRS-T subtraction in AEGs. Examples of QRS and QRS-T segmentation using the three different methods are presented in Figure 3.4. The first approach (Figure 3.4a) was implemented by Ahmad *et al.* (Ahmad *et al.*, 2011) and the QRS onset (marked with squares) and offset (circles) are marked, respectively, as 41.67 ms (50 samples) prior the QRS fiducial point, and 50 ms (60 samples) after the QRS fiducial point. Figure 3.4b presents the classical ABS approach: The QRS-T pattern length has the same length as the shortest RR interval (Shkurovich *et al.*, 1998). In addition, the onset (marked with squares) and offset (circles) from the QRS-T complex were defined such that 30% of the corresponding window precedes the QRS fiducial point and 70% follows it. The proposed method is presented in Figure 3.4c. The delineation of each QRS-T complex is done by individual detections of QRS onset (marked with squares) and T-wave end (circles) (Qinghua *et al.*, 2006, Madeiro *et al.*, 2012). The corresponding time location of each fiducial point detected in the ECG is marked in the AEG signal (Figure 3.4d).

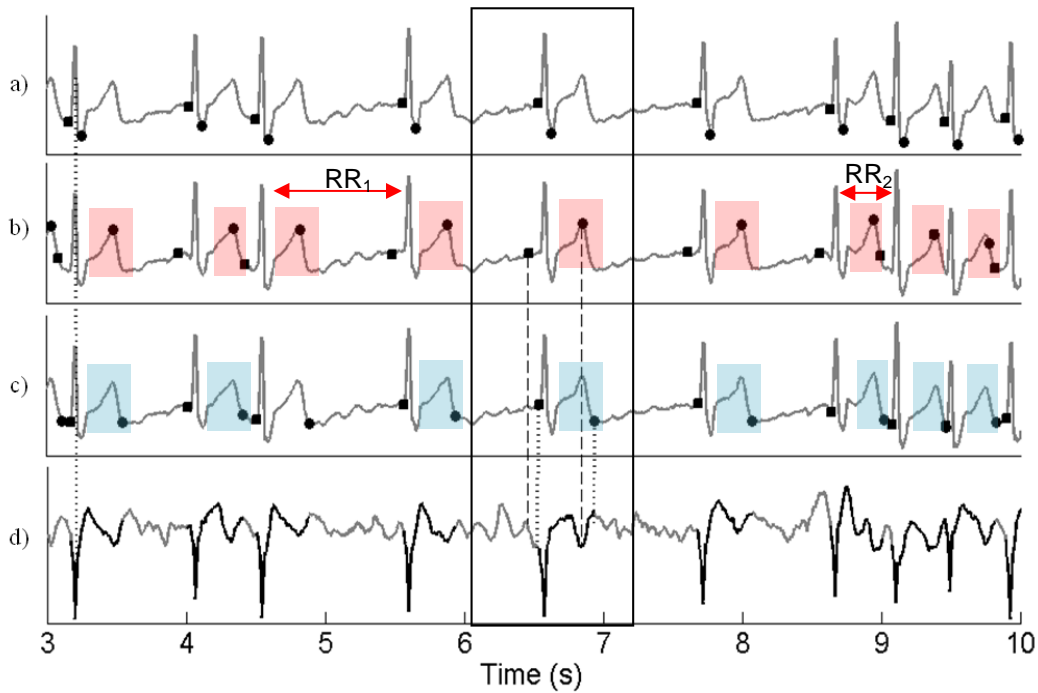


Figure 3.4 VA detection: (a) QRS segmentation, (b) QRS-T segmentation using ABS, (c) QRS-T segmentation using the proposed method and (d) AEG simultaneously recorded with the ECG showing both QRS-T segmentation intervals (from b and c).

The ECG segmented by the ABS method (Figure 3.4b) had the T-wave ends systematically wrong segmented (examples highlighted by the red boxes). In this figure it is also possible to observe the variability of the RR intervals and how it affects the segmentation (difference in length between RR_1 and RR_2). In contrast, on the ABS method, the length of the QRS-T does not depend of the shortest RR interval and both the QRS onset and T-wave end are individually and customized segmented. Figure 3.4c presents the same ECG now segmented by the proposed approach. The circles presented on the figure systematically match with the T-wave end segmentation and are highlighted by the blue boxes. In addition, the dotted vertical trace on the left corner of Figure 3.4 shows that the QRS fiducial points of

the ECG (Figure 3.4a-c) are aligned with the VA disturbances on the AEG (Figure 3.4d). The rectangular solid trace box between around 6.0 s and 7.5 s highlights the ventricular segmentation in a single VA on the ECGs proposed by the three methods (Figure 3.4a-c) and the corresponding AEG (Figure 3.4d). The bold black solid traces in the AEG (Figure 3.4d) are the projections of the QRS-T segments as identified by the proposed method. The first two vertical traces localised before the VA fiducial point in the AEG are the QRS onset segmentation respectively identified by the ABS approach (dashed trace) and the proposed method (dotted trace). In addition, the T-wave end segmentation identified by the ABS (dashed trace) and the proposed method (dotted trace) are highlighted on the trace of Figure 3.4d.

After ECG segmentation for each previously described technique (QRS only, QRS-T using ABS and QRS-T using the proposed method) Figure 3.5 presents a comparison between three cancellation methods on an AEG signal. In Figure 3.5a, QRS-T segments are highlighted in the original electrogram. Figure 3.5b presents an AEG signal after QRS cancellation (Ahmad *et al.*, 2011). Figures 3.5c and 3.5d show the AEG signal after QRS-T subtraction respectively using the ABS and the proposed approach. The patterns used by both QRS-T methods to cancel the VA are presented in Figures 3.5e and 3.5f, respectively.

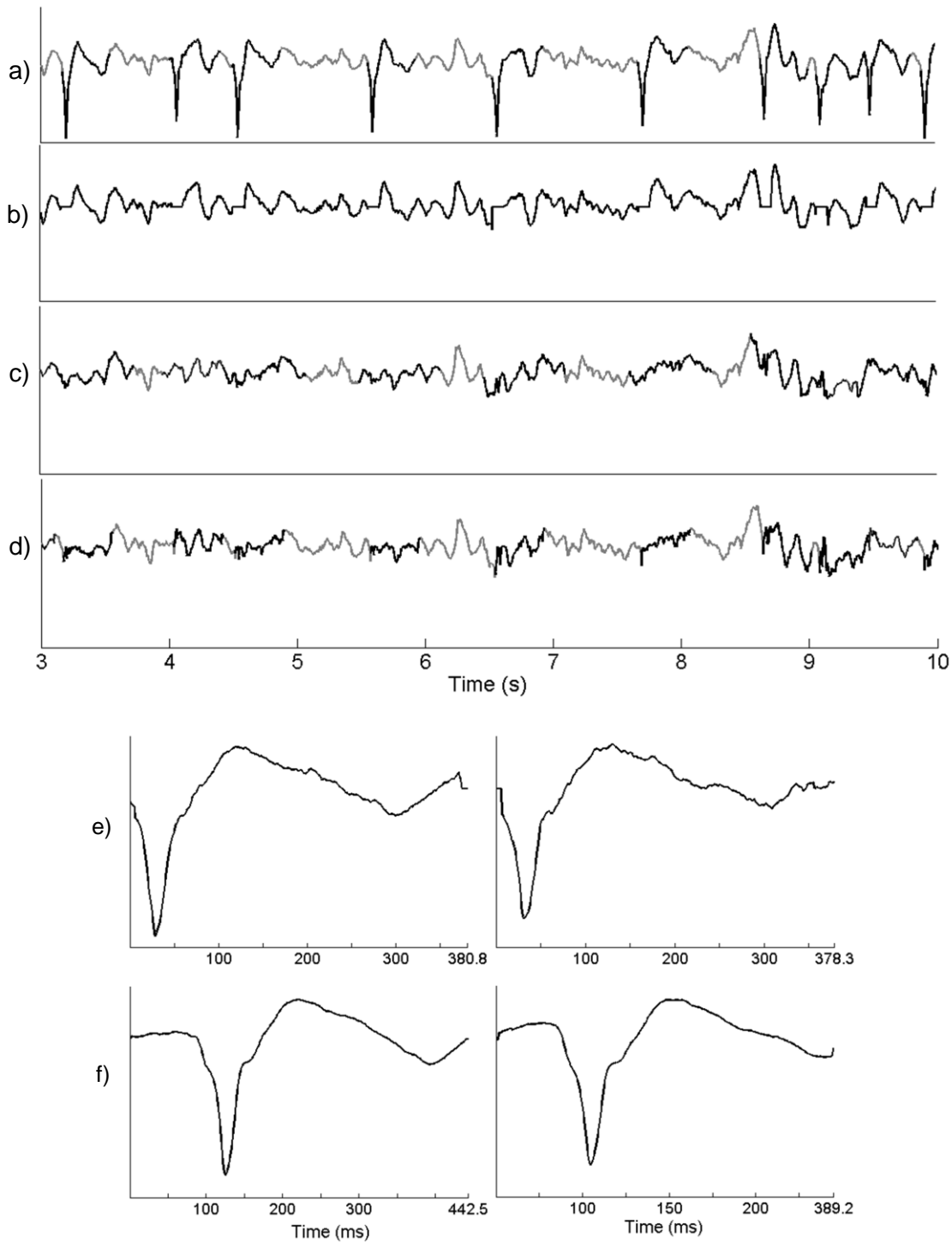


Figure 3.5 Ventricular subtraction in AEG signals: (a) AEG raw signal, (b) after QRS cancellation, (c) after QRS-T subtraction using ABS, (d) After QRS-T subtraction using the proposed method, (e) QRS-T patterns for the proposed approach considering the intervals between 0-7s and 3s-10s respectively and (f) computed patterns calculated by the abs approach for the same intervals.

Spectrum analysis was used to help compare the techniques in the frequency domain and was performed using the FFT with a hamming window to reduce spectral leakage. Zero padding was introduced to improve spectral peaks identification (to frequency steps of 0.05 Hz).

The frequency spectrum impact of each ventricular cancellation technique in different areas of the LA was also investigated (Figure 3.6). This allows one to observe the ventricular influence on the AEGs in areas of relevance to the arrhythmia (PVs, roof and septum) and to observe the VA impact in areas even far from the MV.

Figure 3.6 presents the average spectrum of four pre-classified areas of the LA: close to the PVs, roof, septum and close to the MV. For each area, 12 points were selected following their identification. For the PV region, three points were selected close to each of the four PVs. Spectrum analysis allowed identifying the spectrum for each individual AEG over 20 s. The AF 'physiological range' was selected between 3 to 12 Hz and we used a window 4 s, and an overlap of 50% (moving 2 s at a time). The spectral resolution was 0.25 Hz and zero padding was applied to produce frequency steps of 0.05 Hz. The average spectrum from the 12 points for each 4 s of 20 s was calculated (total of 9 windows). The average of all windows represents the average spectrum of each particular LA area, making it possible to compare spectra for each ventricular far-field cancellation.

The average spectrum of the entire LA was also investigated. In this analysis, we performed the average of the spectra of the 2048 simultaneous AEGs for the different protocols: raw signals, after QRS cancellation and after each of the QRS-T subtraction methods using the spectral analysis strategy previously described. The whole LA spectrum allows one to observe the global effect of the cancellation

techniques on the AEGs. Figure 3.6 also hints that a wrong identification of the DF is possible if VA is not properly removed: On the spectra corresponding to the areas close to the MV, if one looks at the raw signal, a DF of about 4.8 Hz would be identified. For 'QRS only' removal, a DF of 2.8 Hz would be identified and for QRST-ABS or our QRST segmentation approaches the correct DF, at 6.5 Hz, is identified.

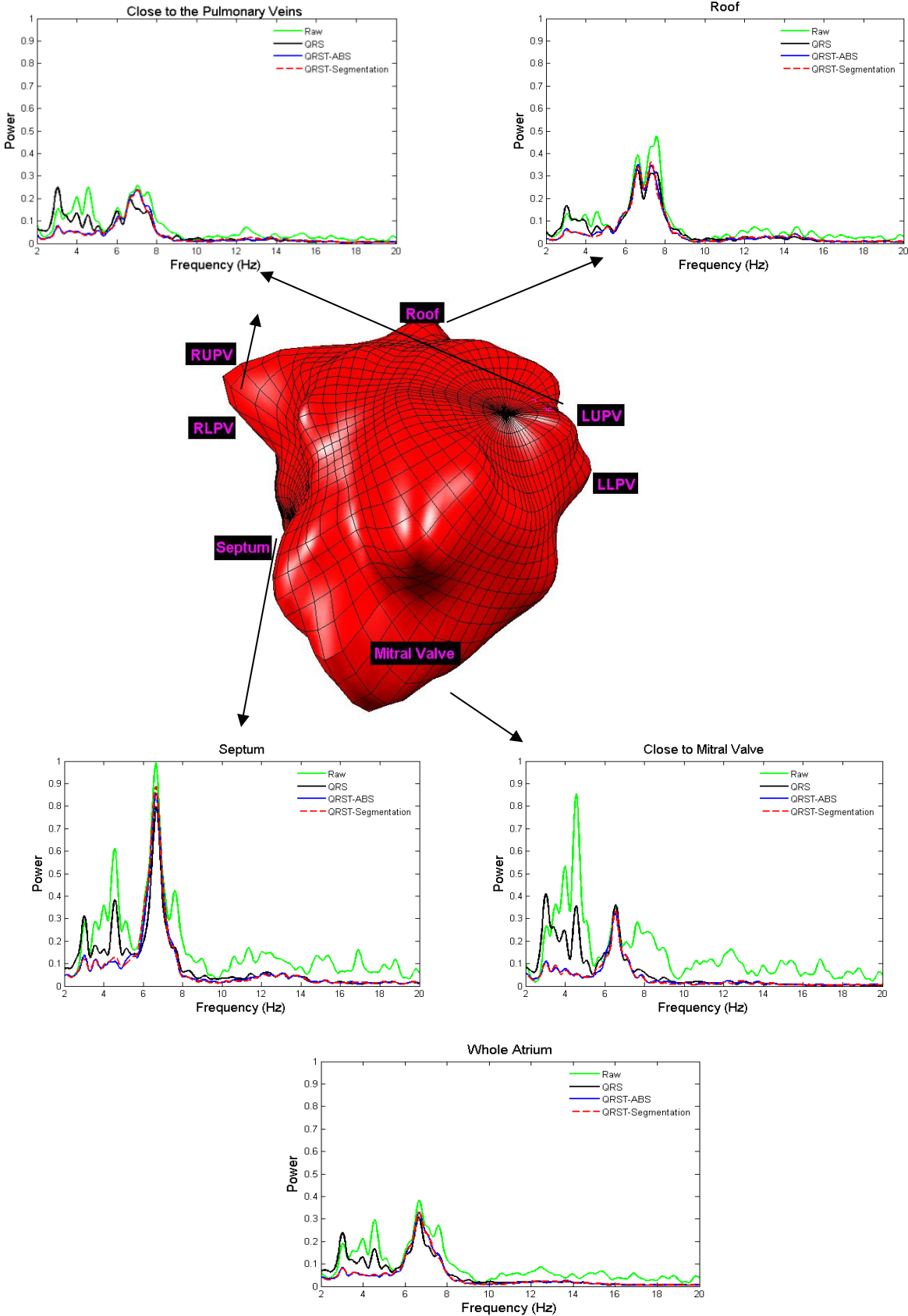


Figure 3.6 Average spectrum of the Raw AEG and for each of the three subtraction methods in the following areas: close to PVs, roof, septum, close to the MV, and for the whole LA.

The ratio between the frequency components' energy in the range [5.5-12 Hz] and [3-5.5 Hz], defined here as P_{ratio} , is shown in Tables 3.1 and 3.2 for each subtraction method. The results, synthesised on Table 3.1, are classified by specific regions of the LA. In Table 3.2, this ratio is calculated for all of the 2048 AEGs (the whole of the LA) for each patient. This metric, P_{ratio} , allows identifying the impact of the T wave subtraction over the AEG's spectrum, where higher values mean better repolarisation subtraction (small residual levels of the T-wave influence on the AEG signals). The equation for the Power ratio index is

$$P_{ratio} = \frac{P_{5.5-12}}{P_{3-5.5}} = \frac{\int_{5.5}^{12} P(f)df}{\int_3^{5.5} P(f)df} \quad (3.7)$$

where P_{ratio} is the metric (similar to a SNR) we use to measure the quality of VA removal and P_{a-b} is the area under the curve for the power spectrum between the frequencies a and b , in Hz.

3.3.RESULTS

3.3.1. TIME DOMAIN ANALYSIS

Figure 3.4 highlights the main differences between the proposed method and the ABS method for segmentation of the QRS-T: As the ABS method is based on a fixed time length around the QRS fiducial point, as we mentioned before the 30%-70% ratio used in their study frequently produces truncation of the T wave (as in the case shown on Figure 3.4b), with other choices possibly resulting better results. One justification for using such approach is that the QRS fiducial point is easier to identify reliably than the end of the T wave. Provided that the delimitation of the T wave is

done correctly we argue that the proposed method should be preferred. Figure 3.4d highlights this difference: Following the proposed approach the segment highlighted in the AEG (segment between the dotted lines) would be processed, while following the ABS approach the segment between the dashed lines would be processed (clearly not cancelling the whole of the T wave, see Figure 3.4c).

3.3.2. FREQUENCY DOMAIN ANALYSIS

The frequency spectra of the AEGs illustrated in Figures 3.5(a-d) are shown in Figures 3.7(a-c). The frequency spectrum of the AEG signal after the proposed QRS-T subtraction method (black trace in Figures 3.7a-c) is compared with the spectra of: Its respective raw signal (Figure 3.7a, grey trace), the electrogram after QRS cancellation (grey trace in Figure 3.7b) and the electrogram after the QRS-T subtraction by the ABS method (Figure 3.7c, grey trace).

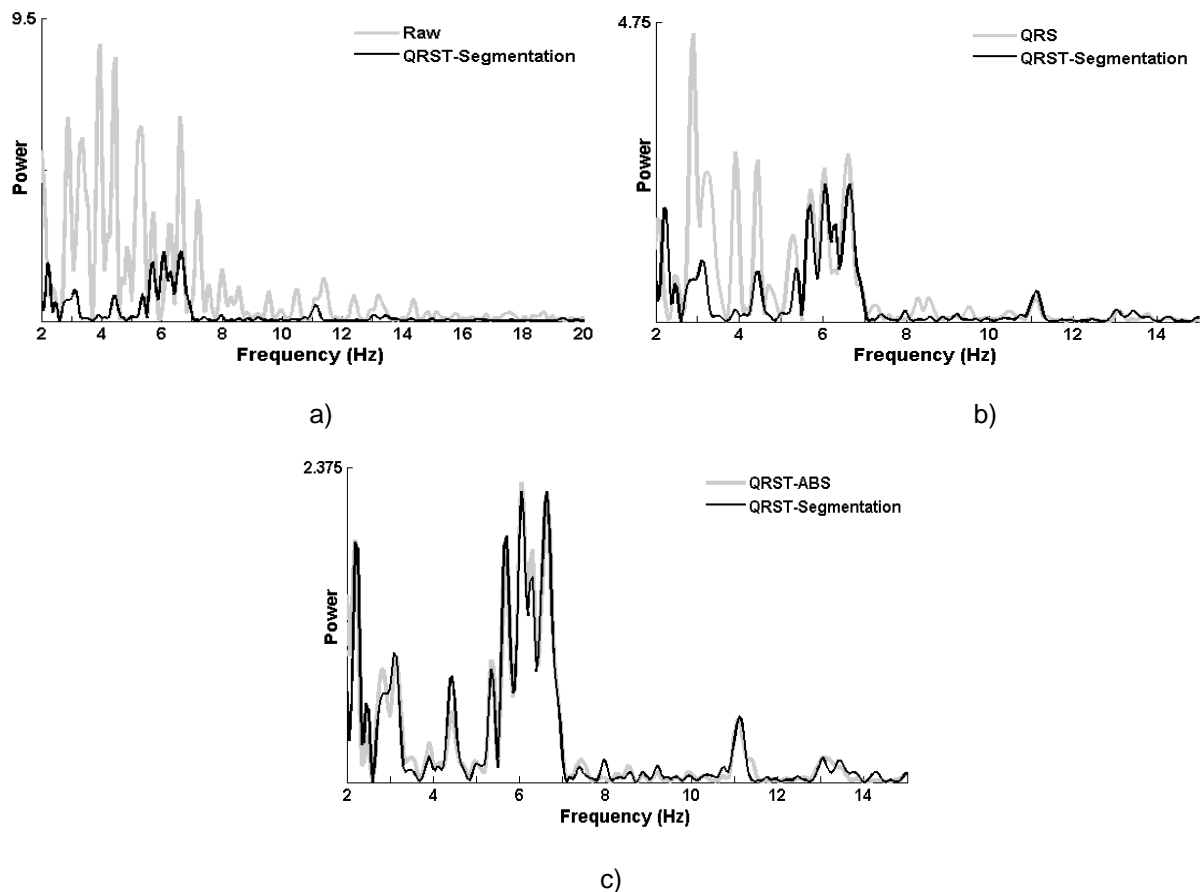


Figure 3.7 Frequency spectrum of the AEG of figure 3.4a compared between the different subtraction techniques: (a) proposed QRS-T subtraction (black trace) compared to raw signal (grey trace), (b) proposed QRS-T subtraction (black trace) compared to QRS subtraction only (grey trace), and (c) proposed QRS-T subtraction (black trace) compared to QRS-T/ABS technique (grey trace).

The results of using P_{ratio} for the comparison of the techniques are summarised on Tables 3.1 and 3.2 and show that either the ABS method or the technique proposed here do better than QRS-only removal technique and, as expected, the ‘raw’ signal (with no QRS or QRS-T removal). Based on the spectral analysis on AEGs, both the ABS method and the proposed method do well.

Table 3.1 Population averaged ratio between the frequency components in the range [5.5-12 Hz] and [3-5.5 Hz] for each QRS-T subtraction approach and each atrial region.

	MV	PVs	Roof	Septum
Raw	1.04	1.60	3.39	1.96
QRS	0.85	1.46	3.05	1.86
QRS-T-ABS	2.45	3.38	5.07	3.71
QRS-T-Seg	2.41	3.26	5.33	3.76

Table 3.2 Ratio between the frequency components in the range [5.5 – 12Hz] and [3-5.5Hz] for each QRS-T subtraction method for the average of the entire LA.

	Pat1	Pat2	Pat3	Pat4	Pat5	Pat6	Pat7	Pat8
Raw	0.88	1.82	4.05	1.96	2.99	0.96	0.93	2.79
QRS	0.78	1.63	3.37	1.23	3.01	0.84	1.00	3.79
QRS-T-ABS	2.90	3.58	3.28	2.12	2.31	1.10	1.84	4.60
QRS-T-Seg	2.31	3.51	3.58	2.25	2.66	1.07	1.94	4.54

3.4. DISCUSSION

In the ABS-based approach for QRS-T subtraction, several QRS-T segments showed an inaccurate delimitation of the QRS onset and T-wave end (see Figure 3.4b). In addition, the ABS-based template is often longer when compared with that of the proposed approach (Figures 3.5 e-f). We observed that the main reasons for this are (Figure 3.4): (i) for the presented case, the 30%-segment that precedes each QRS fiducial point covers a time longer than the 'true' interval between a QRS onset and its fiducial point; (ii) the 70%-segment *after* QRS fiducial point often falls before the T-wave end. If instead of using 30/70 other choices for the ratio such as 20/80, 15/85 are used, that might give better results, but we have not tested that. The proposed approach aims to match the *actual* length and timings of onset and offset for all individual QRS-T segments and does so adaptively, using a sliding 7 s window.

For Ahmad's QRS cancellation approach (Ahmad *et al.*, 2011), it can be observed that: (i) QRS onset and offset are based on a fixed time window, which certainly does not reflect the dynamic changes in the ventricular depolarization; (ii) there is no cancellation of the ventricular repolarisation component (the T-wave); (iii) there is no alignment between the QRS fiducial point in the ECG and the local VA detected in each AEG signal; (iv) during the subtraction, an interpolation method is applied (spline, flat or linear) to connect the onset and offset points, so any AA that overlaps with the QRS segment is also removed.

Regarding the frequency domain analysis, the AEG spectrum shown in Figure 3.5 illustrates that the proposed method attains a considerable attenuation for frequencies above 7 Hz (see also Figure 3.7a). Comparing the results of the QRS

cancellation method with the proposed approach (see Figure 3.7b), we observed that the frequencies between 3 Hz and 5 Hz were reduced suggesting that this range is mostly associated with the T-wave frequency content. For frequencies above 7 Hz, both methods produced similar attenuation which, we argue, is mostly related to the subtraction of the QRS activity. In addition, for frequencies between 5 Hz to 7 Hz, only a slight reduction in power was observed, basically preserving the signals within that frequency range. The spectra for both QRS-T subtraction approaches showed a similar overall behaviour for this illustrative example.

The average spectral behaviour for the four distinct areas of the atrium is shown in Figure 3.6. We observed different degrees of VA contribution over the raw signal across the spectrum. Areas close to the MV showed stronger frequency components (higher amplitudes) related to VA when compared with areas such as the roof and around the PVs. Regarding the proposed approach, it was noticed that components of frequencies above 10 Hz, and also the components of frequency range around 3 Hz to 6 Hz (3-5.5 Hz PVs, 3-5.2 Hz roof; 3-6 Hz septum; and 3-5.7 Hz MV) were attenuated due to, respectively, ventricular depolarisation and repolarisation subtraction. An agreement on these ranges was also observed when the overall average spectrum of the atrium was calculated. When both QRS-T subtraction methods were compared, similar results were identified in the frequency domain.

As an additional analysis, we also investigated the effectiveness of the ventricular repolarisation subtraction. The ratio between the frequency components related to physiological AF range excluding the VA repolarisation (5.5 Hz – 12 Hz) and the reported frequency components related to VA repolarisation (3 Hz – 5.5 Hz), P_{ratio} , was computed (eqn. 3.7, Tables 3.1 and 3.2). Previous studies have presented a slightly different approach (Xi *et al.*, 2002, Xi *et al.*, 2003), using a ratio between 4 to

9 Hz over the total spectrum power with focus on the QRS template cancellation on the ECG. Comparing P_{ratio} of signals which had ‘QRS cancellation’ with P_{ratio} of the raw signal, in Table 3.1, we observed that it has decreased for all atrium areas. This suggests that (i) the approach of QRS segment cancellation using flat interpolation results in a reduction for all frequency components; (ii) in particular the power above 10 Hz (corresponding mostly to the QRS complex) had a great reduction when compared with the raw signal; (iii) for the T wave frequency range, we observed a minor reduction, although reduction of T-wave activity is not a target for this cancellation method and there is an overlap in the frequency component of the QRS complex and the T-wave.

When the signals after both QRS-T subtraction methods were compared with the previous results, an improvement of P_{ratio} for all atrium areas could be observed. This suggests that: (i) frequency components corresponding to both QRS and T wave were dramatically reduced; and/or (ii) the remaining frequency content, which is mostly related to the main AA within the physiological AF range (above 5.5 Hz), clearly stands out from the frequency content related to the range [3–5.5 Hz], as consequence of an effective repolarisation subtraction.

When the ratios between both QRS-T subtractions methods were compared, the ABS approach produced a slightly higher P_{ratio} around the MV and in areas close to the PVs (2.45 and 3.38) when compared with the proposed method (2.41 and 3.26). In contrast, for the roof and septum, the proposed method presented slightly higher ratios (5.33 and 3.76) when compared with the ABS (5.07 and 3.71). We extended the analysis considering the average spectrum for the 2048 AEG signals of the whole atrium for individual patients (Table 3.2). Student’s T-test was applied on the results obtained by the QRST-ABS and the QRST-Seg across the study’s population

presented in Table 3.2 and it was found that both methods were not statistically significantly different ($p=0.439$). The population's mean from the QRST-ABS and QRST-Seg methods were respectively 2.71 ± 1.10 and 2.73 ± 1.09 .

As we can see from both tables, our method produces similar P_{ratio} index results to those of the ABS approach, but our templates are matched to the *actual* length and timings of onset and offset for individual QRS-T segments rather than using an arbitrary length based on the shortest R-R interval (Figure 3.4) and positioning the QRS onset fiducial point at either 30% or 50% of the total time. Considering the capabilities of the proposed method for adapting itself to the existing inter- and intra-patient variability in QRS durations and QT intervals, which define the length for each QRS-T complex, we argue that it should be preferred to the ABS approach.

Finally, concerning the limitations of the proposed technique, it is well known that T-wave end location is a difficult problem, especially when the signal to noise ratio is low (Qinghua *et al.*, 2006). Also the presence of the f-waves related to AF over the ECG adds an extra challenge, *e.g.* an extra physiological 'noise', to time location of T-wave end. These limitations may directly affect the QRS-T pattern and the accuracy of the QRS-T subtraction in the AEG signals. However the identification of the average of all QT intervals as the length of QRS-T pattern does reduce the effect of eventual misdetections.

3.5. CONCLUSIONS

The main clinical objective of identifying DF in AEGs is the location of key candidates for ablation to minimise the amount of burning and maximise the outcome of ablation procedures in persAF. Cancellation of ventricular influence on high density AEGs is a prerequisite to avoid 'contamination' of the AEGs that might alias as possible AF

triggers. As well as the QRS complex, VA repolarisation (the T-wave) also needs to be subtracted and using standard filters is not feasible as the frequency range of VA overlaps with the physiological AF spectrum. It can be performed using individual 'customized' and adaptive QRS-T segmentation and a coherent subtraction strategy. We have presented a novel approach that performs such cancellation and we have compared its performance to 2 previously published alternative techniques. Evidence has been presented that shows that the new approach is capable of reducing the influence of the VA on the AEGs and that it does not suffer from some of the disadvantages of the alternative techniques it was compared to.

4. DISTINCTIVE PATTERNS OF DOMINANT FREQUENCY TRAJECTORY BEHAVIOUR EXIST IN PERSISTENT ATRIAL FIBRILLATION: CHARACTERISATION OF SPATIO-TEMPORAL INSTABILITY

4.1. INTRODUCTION

It has been suggested that ablation at areas of high DF could be an effective way to terminate AF (Sanders *et al.*, 2005). In addition, ablation strategies which include PVI and additional linear lesions have also been shown to reduce local and/or global DF with an associated beneficial post-ablation outcome, highlighting DF as an important parameter (Sanders *et al.*, 2005, Atienza *et al.*, 2009, Tuan *et al.*, 2011). However, DF mapping during AF has been performed largely using point-by-point sequential mapping. Recent reports using NCM in the LA have suggested that DF may not be spatiotemporally stable (Jarman *et al.*, 2012). In addition, simultaneous bi-atrial CM (Narayan *et al.*, 2012a, Narayan *et al.*, 2012b) has also revealed certain characteristic rotor-like behaviours apparently important for ablation. The aim of this study was to characterise the spatiotemporal behaviour of DF during AF using NCM in patients with persAF to help further understanding the significance and utility of DF mapping. This chapter has been partially published in previous conferences (Salinet Jr *et al.*, 2010b, Salinet Jr *et al.*, 2011b, Salinet Jr *et al.*, 2012a, Salinet Jr *et al.*,

2012d, Salinet Jr *et al.*, 2013d) and its content also been accepted as an original article in a peer review journal (Salinet Jr *et al.*, 2013d).

4.2. METHODS

4.2.1. SIGNAL PROCESSING

After carrying out ventricular cancellation of the AEGs, spectral analysis was performed at each of the 2048 points using FFT with a Hamming window to produce high density 3D DF maps (Salinet Jr *et al.*, 2013b). As previously described in section 1.6.8, segments of 4 s were used with sequential windows producing a 50% overlap in a range between 4 Hz to 12 Hz.

4.2.2. TEMPORAL DF ANALYSIS

4.2.2.1. TEMPORAL DF STABILITY ANALYSIS

For the purpose of assessing temporal stability of DF, we compared the DF of all AEGs between consecutive time windows (at 2 s intervals), to assess if the DF remained within a defined threshold of ± 0.25 Hz or ± 0.50 Hz compared to the DF obtained from the first FFT window of the segment (Figure 4.1). Points whose DF values remained within these thresholds at each time segment were deemed temporally 'stable' (assessed over a period of up to 1 minute) and the resultant DFs were derived by averaging those DF values. If the DF wandered beyond the pre-defined threshold over time, the frequency value was deemed 'unstable' after that particular instant and no longer considered. The total proportion of 'stable' points, as defined by the above criteria, was plotted over time for assessment of temporal stability (Figure 4.2).

4.2.2.2. DF REAPPEARANCE ANALYSIS

After identifying that DF was not consistently stable over time (Figure 4.1b), further analysis on DF behaviour was performed to investigate if DF values show any temporal repetition or spatial 'reappearance', so as to quantify the presence of any potential DF partial 'periodicity'. This was done by using the first DF value from each point of interest as a reference, which was then compared with the DF values from the same location while moving forward in time at 2 s intervals (see Figure 4.3a for illustration). The proportion of DF points falling within the thresholds of ± 0.25 or ± 0.50 Hz compared to their corresponding reference DF value were plotted over time and defined as DF reappearance points. The time (in seconds) corresponding to any partial 'periodicity' or 'reappearance' of the overall DF behaviour was assessed by spectral estimation of the signal created by counting the number of points that fall within the specified thresholds (± 0.25 or ± 0.50 Hz of reference DF value) at the same position along time. This is termed the DF reappearance interval.

4.2.3. SPATIOTEMPORAL ANALYSIS

4.2.3.1. HIGHEST DF AREAS TRAJECTORY

To track the behaviour of HDFAs, the region in the 3D NCM with the highest DF value was identified for each time segment, together with its neighbouring sites, which contained DF values within 0.25 Hz of the highest DF (Figure 4.4a). This would produce an area consisting of a collection of points that reflect average regional activity, to minimise the effect of isolated high DF sites. The boundary of this area was highlighted to produce an area representative of a maximum DF 'cloud' at that particular instant. The centre of gravity (CG) for the cloud was then identified by

averaging the coordinate positions of each point in the cloud, weighted by their respective DF values (Assis, 2010). These CG points were obtained for each 4 s FFT window and tracked at 2 s intervals over a period of 1 minute to produce a total of 29 sequential CGs, so as to produce a HDFFA trajectory map (see Figure 4.4).

4.3. STATISTICAL ANALYSIS

All continuous variables are expressed as mean \pm standard deviation. Normally distributed data (assessed by Shapiro-Wilk test) were analysed using paired and unpaired Student's t-test. Categorical data were analysed using Chi squared or Fisher's exact test.

4.4. RESULTS

A total of 16384 AEGs and 232 sequential DF maps were analysed (see Patients' characteristics on Table 1.1, section 1.6.4).

4.4.1. TEMPORAL STABILITY ANALYSIS

Sequential analysis of individual AEGs and global DF maps revealed a general lack of temporal DF stability throughout, although periods of apparent stability were also observed (illustrative examples of sequential DF over time from single AEGs are shown in Figure 4.1a-b). Approximately 60% of the AEGs of all patients lost stability in the first 2 s when analysed using the 0.25 Hz threshold and 40% lost stability in the first 2 s using the 0.5 Hz threshold. Analysis of longer segments of continuous recording (Figures 4.1c-d) demonstrated DF values fluctuating beyond defined thresholds of stability, even when they may have appeared stable initially.

For each patient the overall percentage of stable DF points measured against both thresholds relative to initial DF at those points showed an exponential pattern of loss of stability within the first few seconds (Figures 4.2). The time constants of the best-fit exponential curves for both thresholds are presented in Table 4.1, and provide an assessment of how rapidly the DF loses temporal stability. The means of the time constants for the exponential decay when applying the ± 0.25 Hz and ± 0.5 Hz thresholds were 3.1 ± 1.4 s and 7.7 ± 3.1 s respectively.

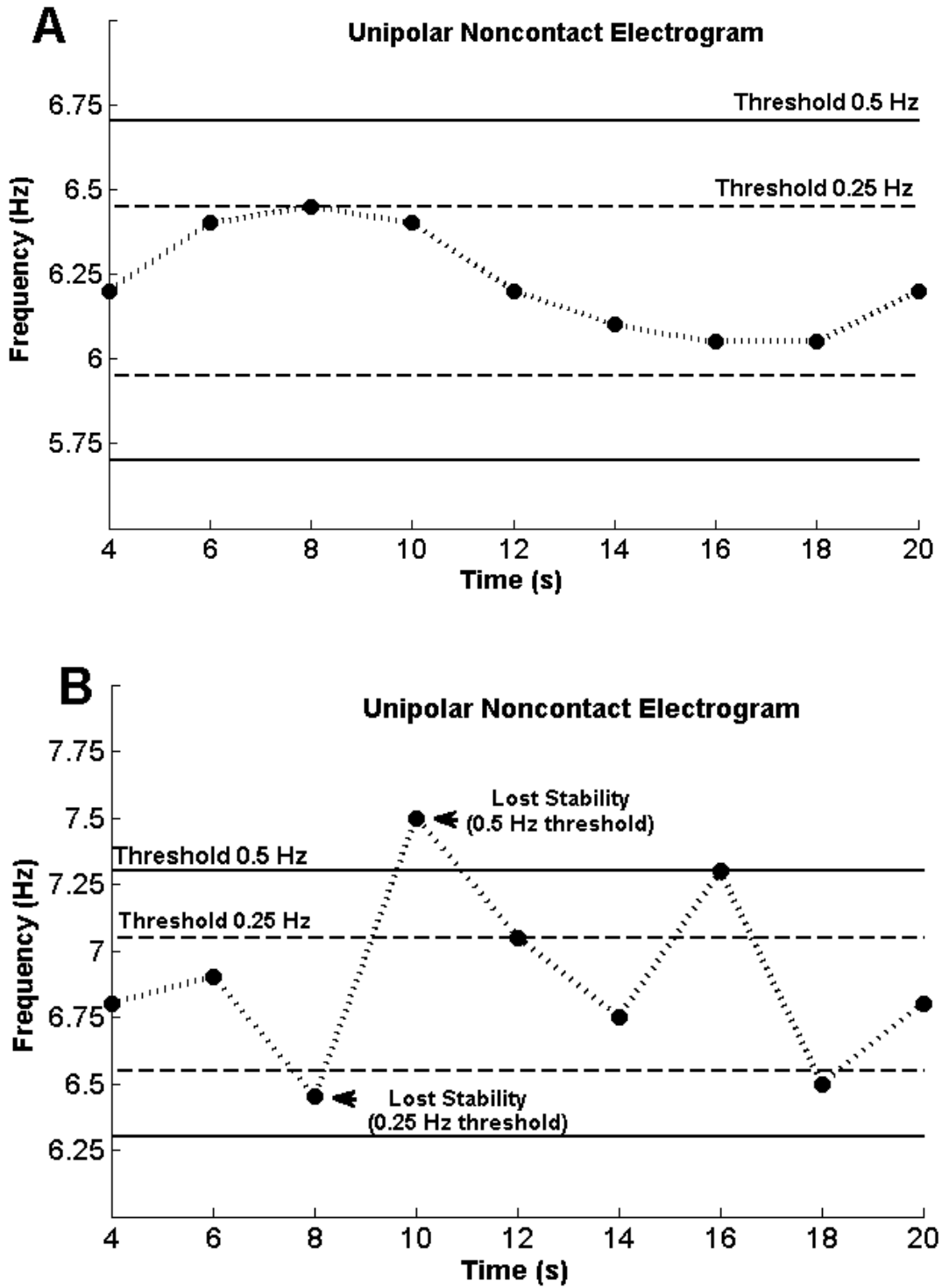


Figure 4.1 Plots of DF over time from single site AEGs. Examples of apparently stable (A) and unstable (B) DF behaviour in a patient are exhibited. Two longer recording examples showing transient stability of DF with subsequent fluctuations over time (C) and (D).

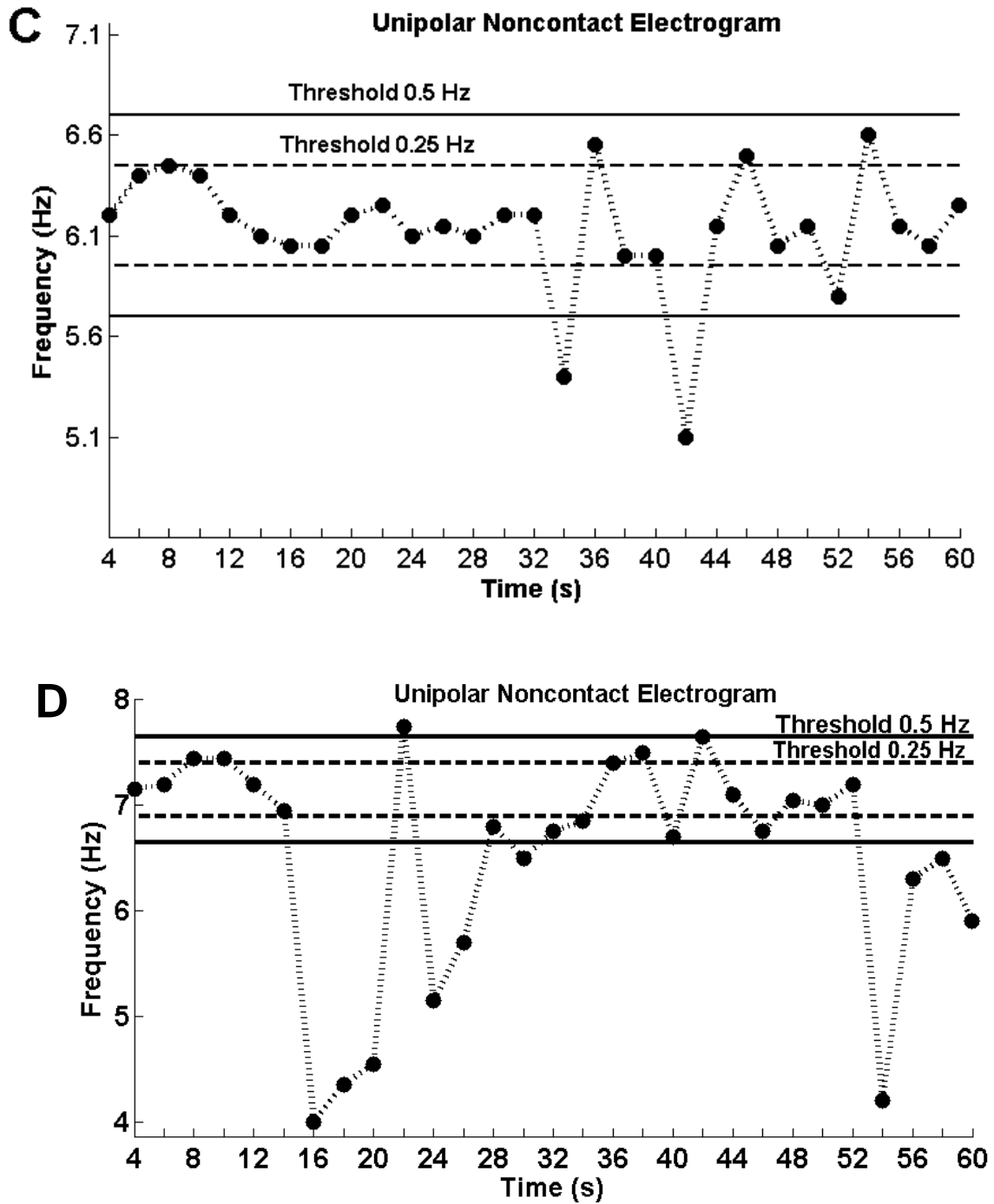


FIGURE 4.1 (continuation) Two longer recording examples showing transient stability of DF with subsequent fluctuations over time (c) and (d).

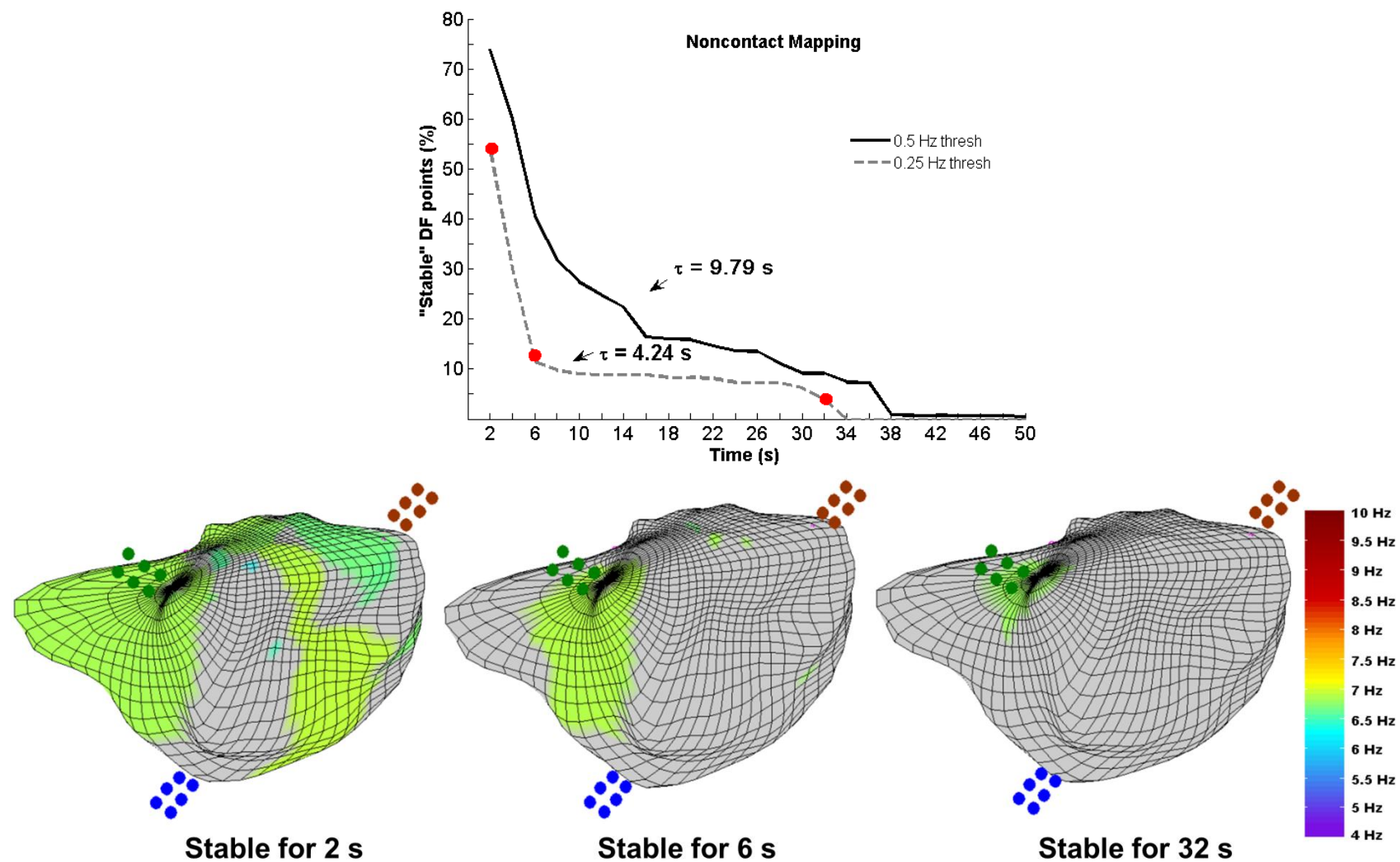
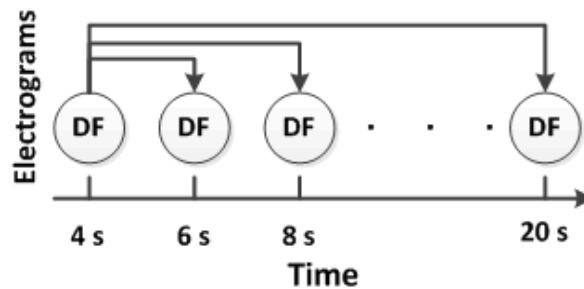


Figure 4.2 Sequence of 3D DF maps during AF for one patient and accompanying plot of percentage of stable DF points over time. It can be observed that the number of stable DF points out of 2048 AEGs decreases with time in an exponential pattern with time constants of 4.24 s and 9.79 s respectively for 0.25 Hz and 0.5 Hz thresholds. The 3D DF maps highlight the sites that remained temporally stable for 2 s, 6 s and 32 s within a threshold 0.25 Hz, with the sites that lost stability greyed out. (tags for RSPV, right superior PV): green, RLPV: blue, LSPV (left superior PV): brown and LLPV (left lower PV): cyan, not visible from this angle).

4.4.2. REAPPEARANCE OF THE DF

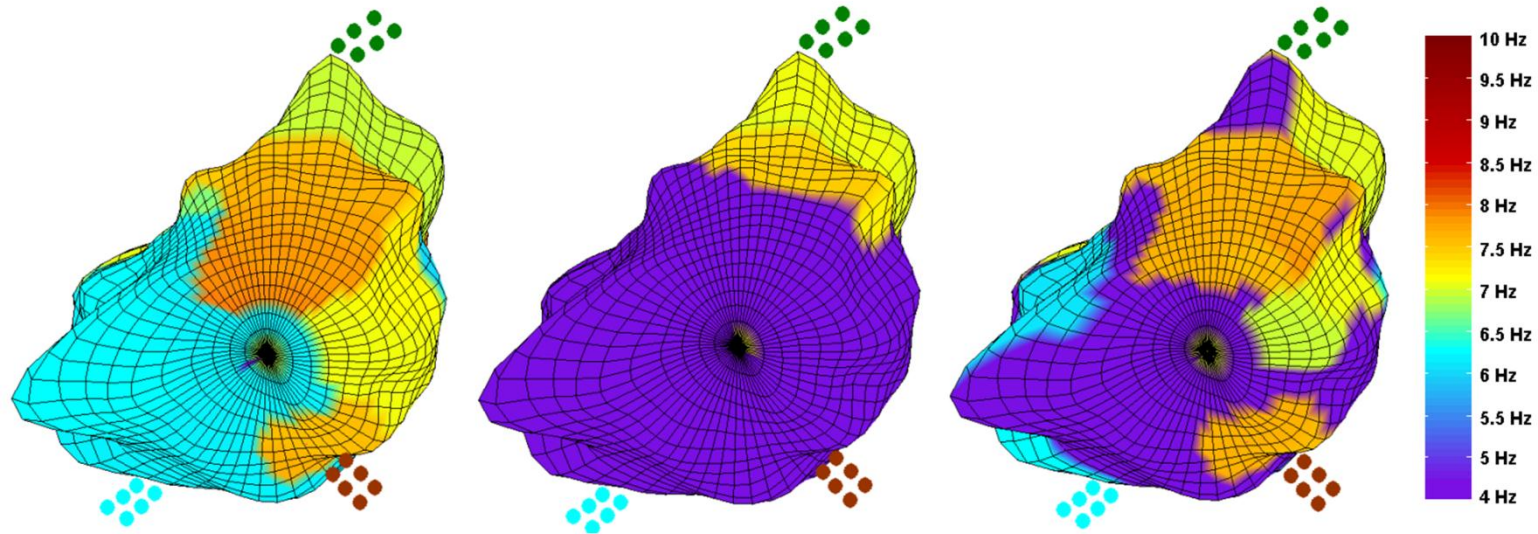
Individual analysis of AEGs also revealed episodes suggestive of repetition or reappearance of DF over time, where DF loses temporal stability, only to return to a value very close to that of the initial DF (Figure 4.1b-d). This can be readily appreciated by observing sequential noncontact DF maps (Figure 4.3b-c). DF reappearance analysis as described earlier was performed to quantify the observed behaviour by obtaining the DF reappearance interval (see Figure 4.3d and Table 4.1). The DF reappearance interval was similar when comparing short (20s) and longer (5 minutes) recordings in one patient; 6.9 vs. 6.5 s (0.25 Hz threshold) and 9.4 vs. 10.7 s (0.5 Hz threshold) respectively (Table 4.1 Patient 5).



(a)

Figure 4.3 Illustration of the method used for DF reappearance analysis; every DF map within the duration of the recording is compared with a reference DF map within the thresholds of ± 0.25 and ± 0.5 Hz for each of the 2048 points. This is carried out for every single point and repeated across the LA (a). An example of a DF map showing DF reappearance projected onto its 3D LA geometry is presented in (b) and also displayed as a 2D map (c) for better overall visualisation (at 4 s, 10 s and 18 s). Sites containing the higher DF values (in yellow and orange) at 4 s, no longer do so at 10 s, but reappear partially at 18 s (orange areas, for instance). The respective main lobe degree of DF reappearance for both thresholds is presented in (d).

(b)



(c)

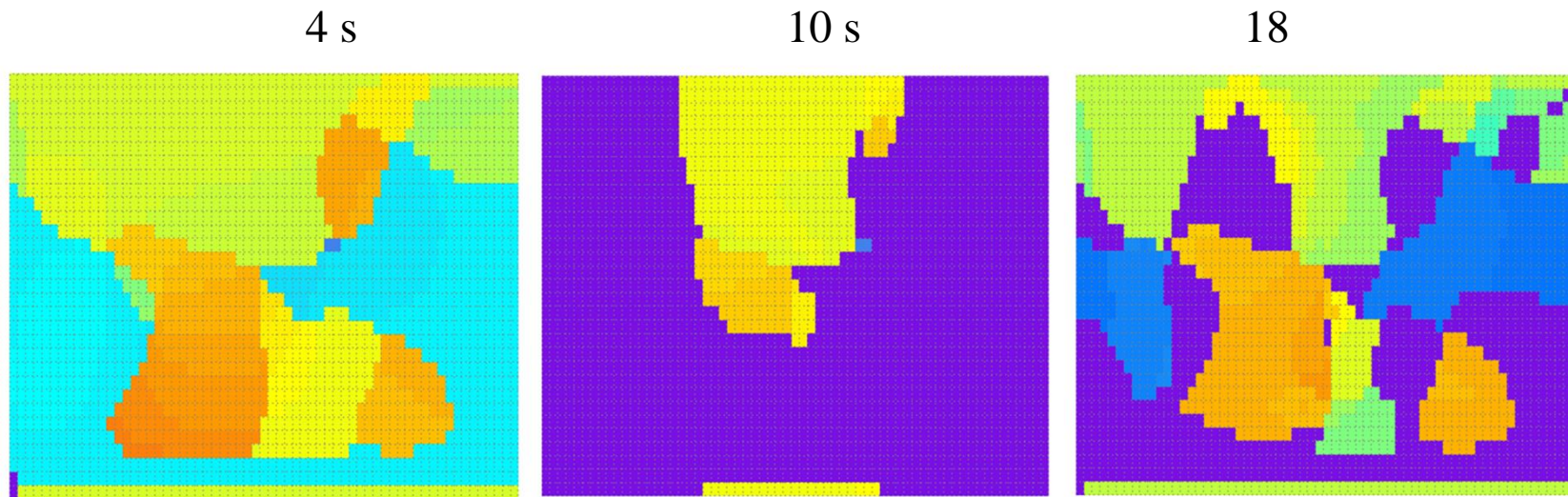


Figure 4.3 (continuation) An example of a DF map showing reappearance of DF projected onto its 3D LA geometry is presented in (b) and also displayed as a 2D map (c) for better overall visualisation (at 4 s, 10 s and 18 s). Sites containing the highest DF values (in yellow and orange) at 4 s, no longer do so at 10 s, but reappear partially at 18 s (orange areas, for instance).

(d)

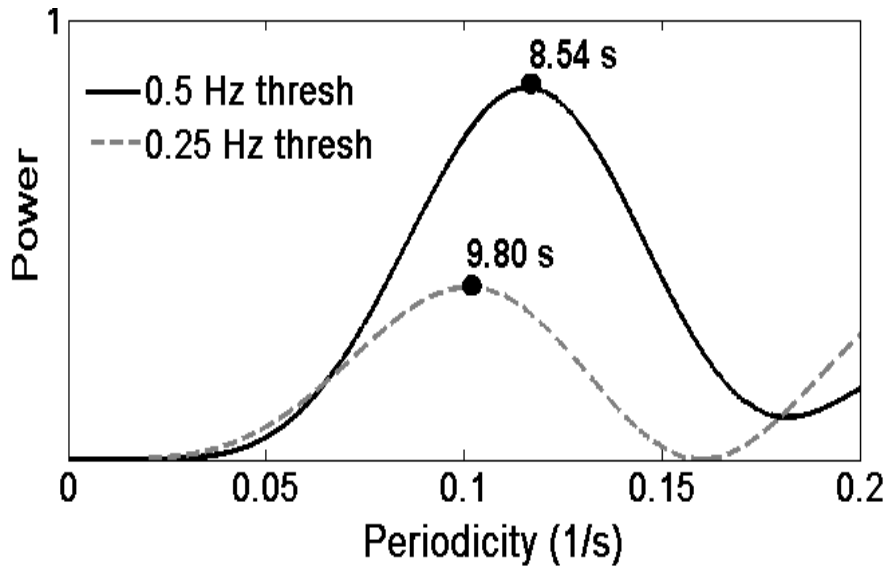


Figure 4.3 (continuation) The respective main lobe of DF reappearance for both thresholds is presented in (d)

Table 4.1 Overall DF temporal stability (time constant) and DF reappearance analyses of the 2048 simultaneous AEGs calculated for both DF thresholds (0.25 Hz and 0.5Hz).

	Time Constant (s)		DF Reappearance Interval (s)	
	0.25 Hz	0.5 Hz	0.25 Hz	0.5 Hz
Patient 1	1.2	2.5	9.8	8.5
Patient 2	2.3	4.2	5.8	5.0
Patient 3	2.6	8.7	7.8	7.7
Patient 4	1.6	11.1	11.7	7.8
Patient 5	4.2	9.8	6.9	9.4
Patient 6	4.3	10.1	10.8	7.4
Patient 7	4.4	6.2	5.5	6.9
Patient 8	3.8	9.4	5.8	8.5
Mean (SD)	3.1 (1.4)	7.7 (3.1)	8.0 (2.4)	9.8 (6.5)

SD indicates standard deviation

4.4.3. HIGHEST DF AREA AND ITS TRAJECTORY

Having seen the dynamic behaviour of DF and its lack of temporal stability, we proceeded with the tracking of HDFAs at each time point by plotting the trajectory of its CG, so as to determine its spatial-temporal characteristics. This revealed 3 patterns of behaviour (Figure 4.4):

- Type I (Local activity) – CG propagation trajectory area (total area encompassed by the trajectory) $< 5\%$ of the LA area over consecutive time frames;
- Type II (Cyclical) – CG propagation trajectory area $> 5\%$ of LA area but showing a trajectory that returns to the vicinity of at least one of its earlier CG sites over time;
- Type III (Irregular) – CG propagation trajectory area $> 5\%$ of LA area with a random pattern of movement and no overlap of CGs over consecutive time frames.

(a)

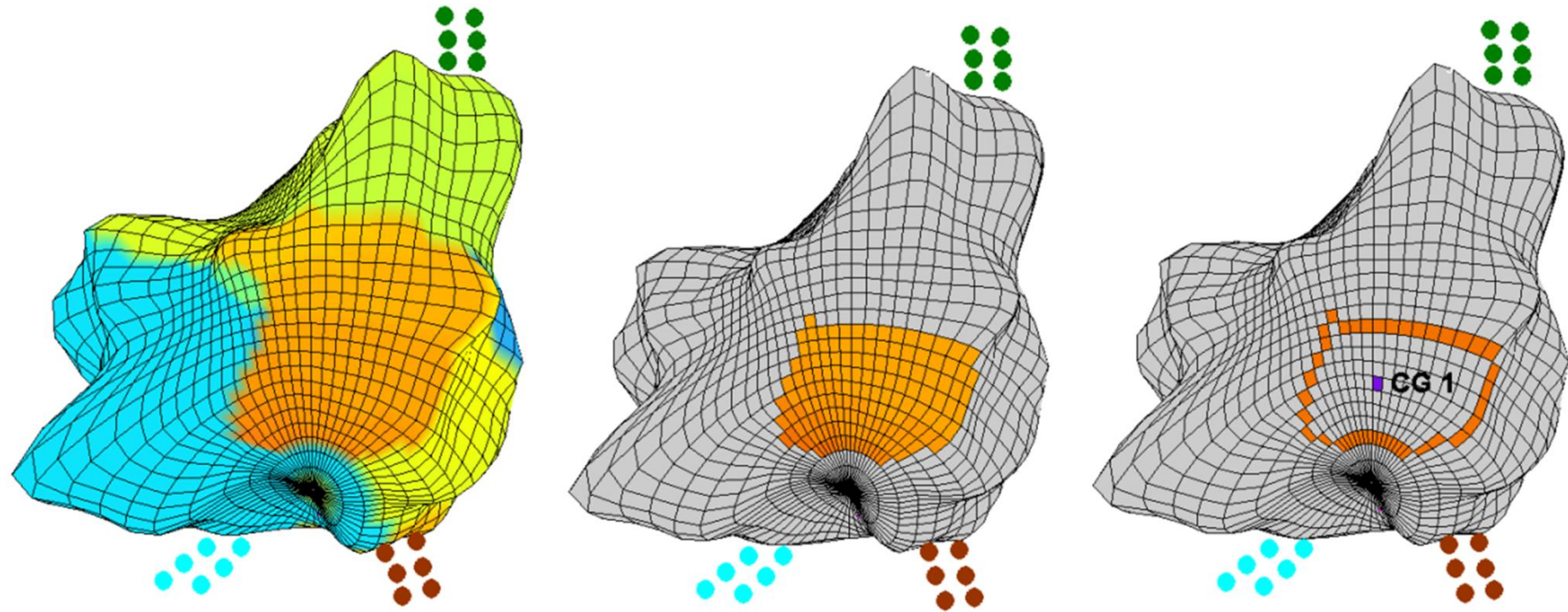


Figure 4.4 Identification and tracking of the CG of the HDFA for a specific time segment (a). 3 types of behaviour were seen: type 1 - Localised (b), type 2 - Cyclical (c) and type 3 - Irregular (d).

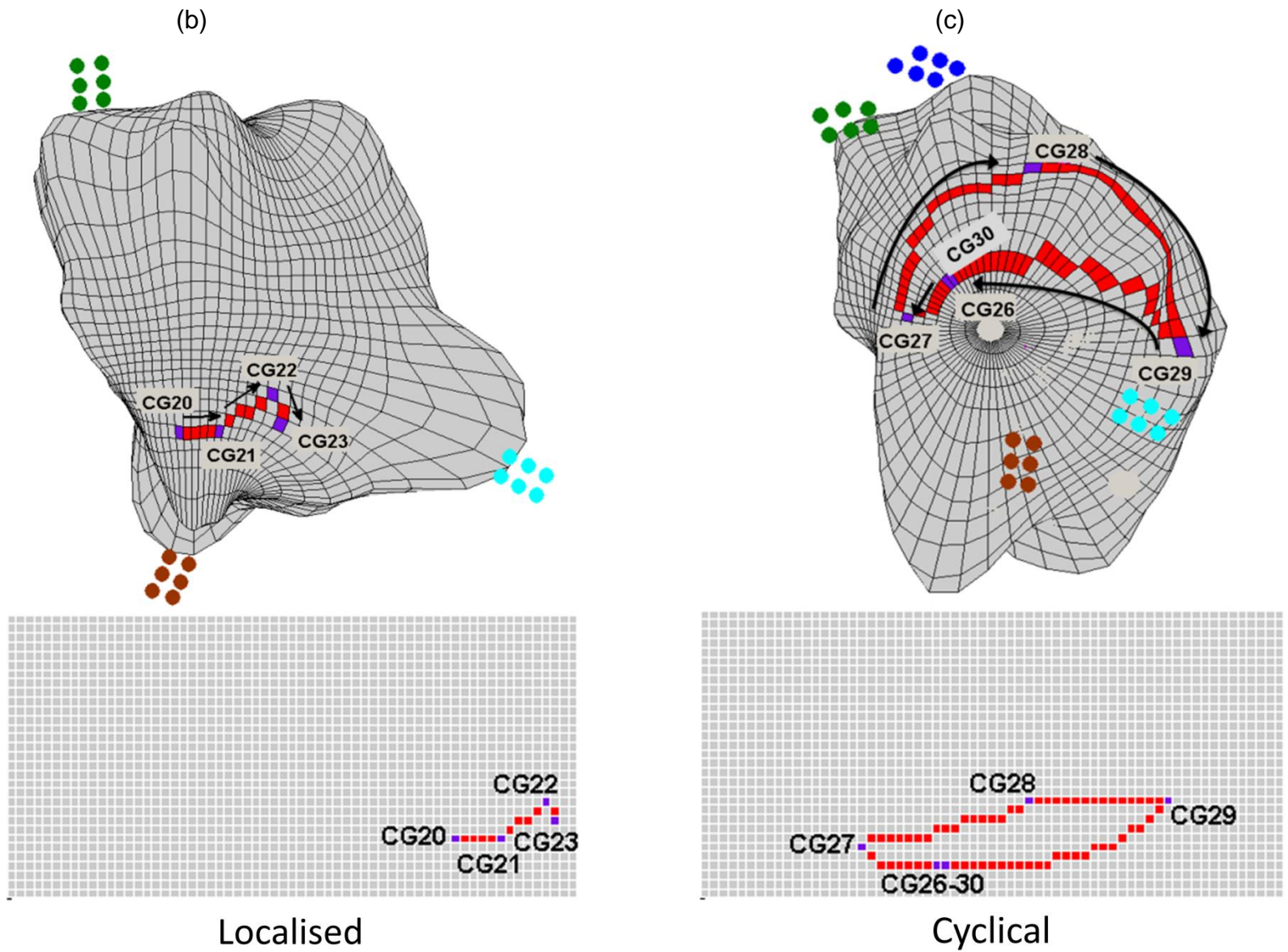


Figure 4.4 (continuation) 3 types of behaviour were seen: Type 1 - localised (b), Type 2 - cyclical (c) and

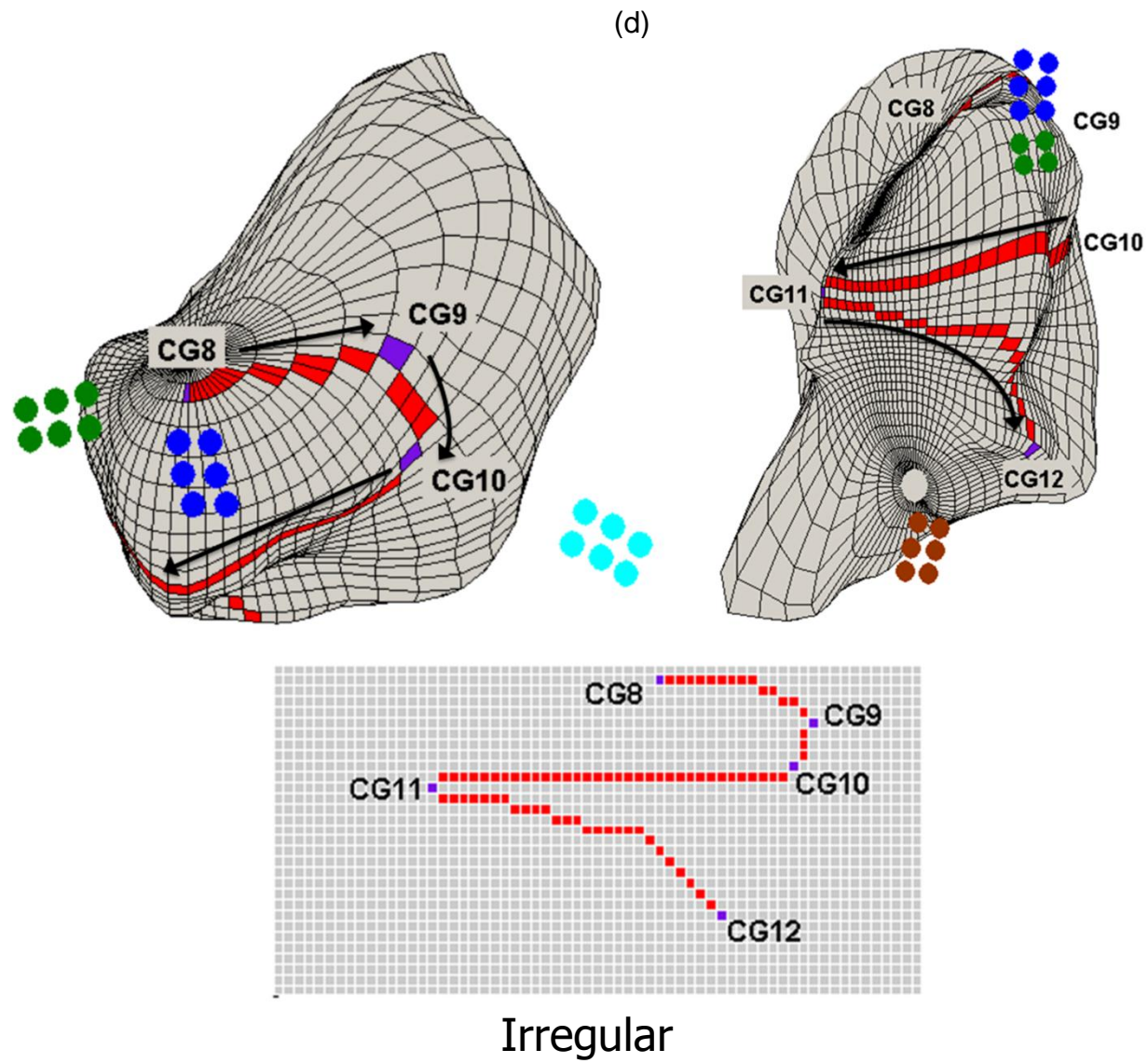


Figure 4.4 (continuation) Type 3 - irregular (d).

A total of 7 local activity events (mean time per event: 2.86 ± 1.07 s), 15 cyclical events (5.07 ± 1.49 s), and 2 irregular events (4.50 ± 1.91 s) were identified over a 20 s segment analysis in all patients. When we extended the analysis to 1 minute, the number of events increased respectively to 24, 54 and 6. The mean times spent in each separate event were similar between 20 s and 1 minute analyses (2.86 ± 1.07 s vs. 2.83 ± 1.55 s, $p = 0.9701$ for local activity; 5.07 ± 1.49 s vs. 5.14 ± 2.16 s, $p = 0.2620$ for cyclic activity; and 4.5 ± 1.91 s vs. 4.60 ± 0.97 s, $p = 0.29$ for irregular activity). The proportion of time spent in each pattern of behaviour is presented in Table 4.2. Cyclical activity was the most prevalent behaviour observed, followed by local and then irregular activity. All except one patient (patient 8) had cyclical activity as the predominant behaviour over 20 s and 1 minute. The DF trajectory showed a concentration of HDFAs in the roof and around the PVs. The mean HDFFA value was 7.29 ± 0.71 Hz.

The electrograms' DF organisation of the HDFAs at the CG core (OI_{CG}) was compared with its periphery (OI_{Per}) and sites with highest DF showing a greater degree of organisation at their core (CG) compared to their periphery: 0.43 ± 0.17 and 0.36 ± 0.10 respectively ($p = 0.0061$), CI [0.0186 0.1095], 95% confidence level (the details of this study is presented in the Appendix). In addition, as DF, the relevant OI areas are not spatio-temporally stable.

Table 4.2 Percentage of the time spent on each trajectory pattern for both short term (20 s) and long term (1 min) analysis during HDFAs trajectory propagation.

	Analysis during 20 s				Analysis during 1 min			
	Localised (% of time)	Cyclical (% of time)	Irregular (% of time)	Total (% of time)	Localised (% of time)	Cyclical (% of time)	Irregular (% of time)	Total (% of time)
Patient 1	0.0	100.0	0.0	100.0	16.6	83.4	0.0	100.0
Patient 2	33.0	67.0	0.0	100.0	30.0	70.0	0.0	100.0
Patient 3	33.0	67.0	0.0	100.0	30.8	61.2	8.0	100.0
Patient 4	0.0	50.0	50.0	100.0	12.5	62.5	25.0	100.0
Patient 5	33.0	67.0	0.0	100.0	27.3	54.7	18.0	100.0
Patient 6	33.0	67.0	0.0	100.0	30.0	60.0	10.0	100.0
Patient 7	33.0	67.0	0.0	100.0	28.5	57.5	14.0	100.0
Patient 8	50.0	25.0	25.0	100.0	40.0	40.0	20.0	100.0
Mean (SD)	26.9 (17.6)	63.8 (20.9)	9.4 (18.6)		27.0 (8.6)	61.2 (12.4)	11.9 (9.1)	

SD indicates standard deviation.

4.5. DISCUSSION

Using NCM analysis of AEGs, we have demonstrated that DF is not temporally stable during persAF, although reappearance of DF values can occur at times. By using a novel method of tracking the movement of HDFAs, we have also shown the presence of distinct localised, cyclical and irregular behaviour spatially.

4.5.1. SIGNIFICANCE OF DF MAPPING

Previous research has suggested that targeting sites of highest DF may be important for catheter ablation (Atienza *et al.*, 2009, Yoshida *et al.*, 2010). It has also been demonstrated that ablation reduces the DF of AF electrograms (Lemola *et al.*, 2006, Takahashi *et al.*, 2006, Tuan *et al.*, 2011) and that a decrease in DF may be associated with a more favourable outcome (Yoshida *et al.*, 2010). However, DF-guided ablation has not been widely adopted and published data using this approach is limited, partly because its clinical significance is not fully understood.

4.5.2. SPATIOTEMPORAL STABILITY

Spatiotemporal stability of DF sites has previously been studied by other authors. Schuessler *et al.* (Schuessler *et al.*, 2006) carried out epicardial CM of the atria of patients undergoing open heart surgery while in AF and found that the location of the HDFAs were variable and did not remain fixed in a significant proportion of the patients. Sanders *et al.* (Sanders *et al.*, 2005) reported that DF values from contact electrograms were stable over time, although this observation was limited by the sequential, point-by-point mapping technique used. A study comparing simultaneous multipolar CM with sequential mapping (Krummen *et al.*, 2009), found that potential AF driver sites were more readily identified via FFT analysis in the former technique.

Two recent studies (one using NCM (Jarman *et al.*, 2012) and another using multipolar catheter for CM (Habel *et al.*, 2010) also concluded that DF lacked temporal stability. There is therefore emerging evidence, including results from our study, that strongly support the notion that DF behaviour is dynamic and should be analysed ideally with simultaneous multipolar CM or NCM techniques.

As observed in our study, DF of AEGs was largely temporally unstable, although there appeared to be transient episodes of stable DF, as well as a degree of reappearance of DF activity over time, mostly within 10 s (see Table 4.1). It is therefore possible that apparent DF stability could be explained by: 1) the use of a single segment for the DF analysis (producing a “snapshot” and not the full sequence of DF behaviour); 2) choice of the length for the segments for DF analysis that is too short and using too few segments, resulting in the opportunistic capture of transiently stable DF signals; 3) reappearance behaviour causing the illusion of stability when DF values are averaged or collected sequentially; 4) choice of long FFT window segments, which would improve spectral resolution at the cost of reducing temporal resolution, effectively ‘blurring the video’ (see Figure 4.5 for comparison of different FFT window sizes in one of the study patients).

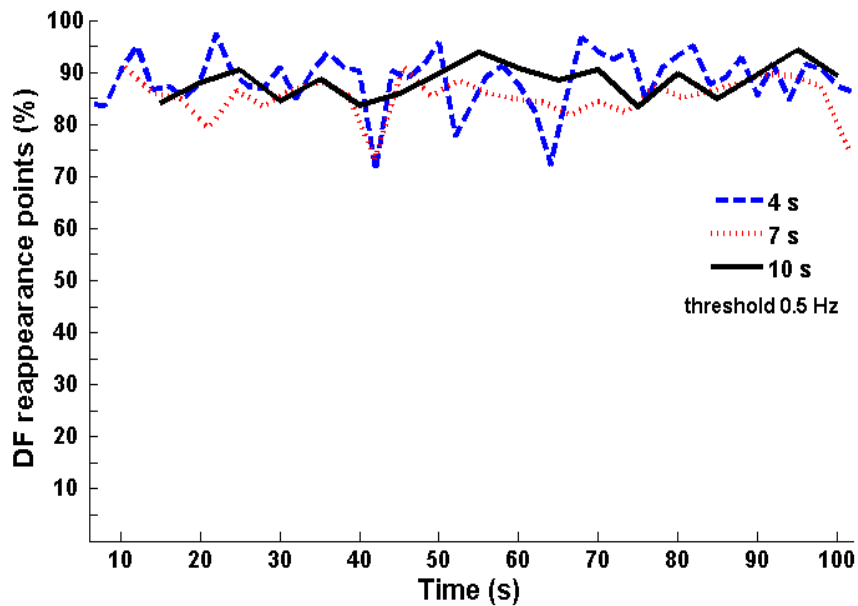


Figure 4.5 DF reappearance analysis using different FFT window sizes. This shows a reduction in variability of DF with increasing windows size, giving rise to an impression of increased temporal DF stability.

The evidences on the phenomenon of DF reappearance demonstrated that certain areas in the atrium change in time but then seem to return to the initial conditions (Figure 4.3). This is important to analyse possible target DF areas where their reappearance phenomenon would possible elucidate spatio-temporal behaviours of significance for maintaining the arrhythmia and with a 'predominant' relationship with the remaining areas of the atrium.

The periodicity of the DF reappearance was calculated comparing the DF values for consecutive time frames (Figure 4.3a) and it was found to be around 8 s and 10 s for the 2 frequency thresholds (see Table 4.1). Additionally, this time also gives an important idea to the clinicians on the theatre during treatment of persAF patients for letting them know the average time required to investigate a particular area in an attempt to observe a relevant AF activation. Lastly, the periodicity range of the DF

reappearance between short and long recordings seems to be similar (6.9 vs. 6.5 s for 0.25 Hz threshold and 9.4 vs. 10.7 s for 0.5 Hz threshold), but it needs to be reproduced for the entire population.

4.5.3. 3D TRAJECTORY MAPPING

Localised and cyclical DF cloud activity accounted for most of the observed behaviour in the patients we studied. While localised activity seen in our study could theoretically be attributed to a stable rotor or micro-reentrant behaviour, the finding of cyclical DF activity is not as intuitive. Using optical mapping of AF in sheep hearts, Skanes *et al.* (Skanes *et al.*, 1998) demonstrated the presence of periodic activity in the atrium, with local DF showing good correlation with DF of the atrium globally. The periodic activation was noted to be transient in most cases, although the patterns of periodicity tended to reappear over time. This was an interesting observation which is similar to what was seen in our study, where there was a predominance of a cyclical behaviour identified when the HDFAs were tracked. The reasons for this are not immediately clear. Potential explanations include interference by other competing activation sources, failure of local atrial tissue to sustain the same frequency of activation for long periods, or even potential migratory behaviour of rotors, if indeed present. A subsequent study using the same sheep AF model (Mandapati *et al.*, 2000) however, showed the presence of spatiotemporally stable rotor behaviour persisting for up to 30 minutes. This would appear to support an earlier animal study by Schuessler *et al.* (Schuessler *et al.*, 1992), where multiple re-entrant circuits were found to stabilise to a single, stable re-entrant circuit when AF became sustained over time. It has to be noted, however, that episodes of AF in this and the earlier

study were experimentally induced and may not necessarily reflect the clinical reality of persAF in human hearts.

Characterising dynamic electrical activation in the search for ‘rotors’ in human AF has continued to be an area of keen research interest. Using epicardial mapping of patients undergoing open heart surgery, Sahadevan *et al.* (Sahadevan *et al.*, 2004) found evidence for potential driver sites, producing fibrillatory conduction in the atria for most of the subjects studied. Three recent studies into the mapping of human AF however, have not been able to demonstrate convincing rotor activity (Cuculich *et al.*, 2010, de Groot *et al.*, 2010, Jarman *et al.*, 2012). Using a novel computational mapping technique, Narayan *et al.* (Narayan *et al.*, 2012a) found evidence for focal impulses and rotor activation patterns during AF in human subjects. An initial series of patients undergoing AF ablation guided by these maps, in addition to conventional ablation, have shown favourable outcomes compared to conventional ablation alone (Narayan *et al.*, 2012b).

4.5.4. SIGNIFICANCE OF FINDINGS AND CLINICAL IMPLICATIONS

Our results provide further insight into the potential mechanisms of persAF. Current mechanistic concepts include single re-entry with fibrillatory conduction (i.e. rotor driven) and the multiple wavelet hypotheses. Our findings show agreement with both proposed mechanisms. We observed a predominance of local and cyclical maximal DF activity, which may imply a higher proportion of rotor driven episodes, although the lack of spatiotemporal DF stability makes it unlikely that AF is being primarily sustained by anatomically stable high DF sites. The presence of a cyclical pattern does suggest a certain extent of spatial consistency and it may be important to characterise this in each individual patient to help guide ablation strategy. Irregular

maximal DF propagation seen in our study would be analogous to multiple wavelet activity. It is interesting to note that in our study, all 3 patterns of behaviour can be observed in the same individual patient over time.

Sites with highest DF showed a greater degree of organisation at their core (CG) compared to their periphery. It provides further insight into the potential mechanisms of persAF areas where regular, fast and organized activity were found at the core of the HDFAs and when moving to the HDFAs' periphery the DF organisation reduced significantly (multiple peaks at the electrograms' spectrum) probably due to collision of uncoordinated fibrillatory waves (see Chapter 1 for more details) . This is consistent with the presence of dynamic HDFAs activity triggering AF with fibrillatory conduction at its boundary (the details of this study are presented in the Appendix).

In addition, it is likely that more than one mechanism may be involved in AF perpetuation at different stages of the arrhythmia history in any given individual. Depending on the extent of electromechanical remodelling and autonomic influence, a particular mechanism may predominate, resulting in different subtypes of persAF. This could explain why an anatomical-based ablation strategy tends to produce only modest results for persAF. A tailored ablation approach should therefore be considered for each individual case, provided that effective real-time, high resolution DF mapping can be performed.

4.5.5. LIMITATIONS

This was a study involving a small number of patients, as our main objective was to describe the DF behaviour using high-density NCM of persAF. Electrogram analysis was restricted only to the LA, hence any potential contributions from the right atrium

were not studied. We acknowledge that some of the patients in the study were taking amiodarone which could potentially affect the DF of VEGMs. Nevertheless, our observations from the study would still be applicable to real-world practice, where patients are not infrequently put on this drug leading up to ablation. In addition, we have focused the current study on understanding the spatio-temporal behaviour of DF during persAF.

For DF reappearance analysis the DF values for consecutive time frames at 2s intervals were compared to their corresponding reference DF value (Figure 4.3a). Although this method was effective in showing evidence that certain relevant areas in the atrium changes in time but then seem to return to the initial conditions within a short time (Table 4.1), the choice of the reference map is important for the analysis. In this research we have focussed on the first 3D DF frame of the segment as the reference map and for real-time application at the theatre, during continuous recordings, it would be better whether clinicians identify a 3D DF frame of preference, such as with a 'relevant' spatio-temporal pattern behaviour which might be contributing to persistent AF. The investigation of reappearance at these areas might help the understanding of AF and contribute to decisions of where to ablate.

Previously, as in the current study, analysis of DF behaviour required a rather laborious process of exporting the continuous 2048 AEGs from the geometry which could only be done offline. With the purchase of more powerful computers, including the employment of parallel processing (Salinet Jr *et al.*, 2013b) (please see also Chapter 6 for details), we are now in a position to perform the analysis in real-time, which makes it possible to provide clinically useable data to guide strategy during the ablation procedure.

4.6. CONCLUSIONS

Using high density NCM of the LA, we have demonstrated that DF of AEGs lack spatiotemporal stability, hence targeting sites of peak DF from a single time frame is unlikely to be a reliable ablation strategy. Tracking of the CGs of the HDFAs revealed the presence of localised, cyclical and irregular patterns of propagation, providing further insight into potential mechanisms behind persAF where the cores of the HDFAs showed to be significantly more organised than their periphery. Studies should be performed to assess the efficacy of using dynamic 3D DF maps to aid ablation strategy for patients with persAF.

5. AUTOREGRESSIVE SPECTRAL ESTIMATION AND MODEL ORDER SELECTION FOR FREQUENCY MAPPING OF UNIPOLAR ATRIAL FIBRILLATION SIGNALS

5.1. INTRODUCTION

The large majority of the AF studies that applied spectral analysis aimed to identify the DF within a relevant physiological range of intracardiac electrograms (Biktashev, 1997) and were implemented using the classical spectral analysis techniques based on the FFT to estimate the Power Spectral Density (PSD) of the signals. Intrinsic assumptions adopted for this technique could limit its application (Kay, 1987, Ng *et al.*, 2006, Ng *et al.*, 2007). In an attempt to explore the use of alternative spectral estimation techniques in AF studies, we investigated the feasibility of using AR methods, with emphasis on selection of appropriate sampling rate and AR model order to estimate the DF for each of the 2048 simultaneous AEGs recorded in the LA of persAF patients. After the DFs were identified they were ranked and colour coded according to the frequencies and high density 3D DF maps were generated and compared with the 3D DF maps recently validated using FFT-based approach (Salinet Jr *et al.*, 2013b). Part of this chapter has been submitted as an original article in a peer review journal for publication.

5.2.METHODS

5.2.1. DATA COLLECTION

Patients were in AF and 2048 AEGs for 20.478 second-long segments (3 consecutive windows of 6.826 s) were exported for analysis, together with their anatomical location with Fs of 1200 Hz. The AEGs were high-pass filtered at 1 Hz and no further filtering was applied to the signals to preserve signal integrity and low frequency components (see section 1.6.5) (Gojraty *et al.*, 2009).

5.2.2. SPECTRUM ANALYSIS

Spectrum analysis was performed on data from each of those AEGs using different AR spectrum analysis techniques (section 5.2.3.) with emphasis on selection of appropriate sampling rate and AR model order selection (section 5.2.4.). The signals were re-sampled in the time domain with 9 different Fs values, from 600 Hz down to 37.5 Hz prior to spectral analysis (see Figure 5.1 for illustration). Three sequential 3D DF maps with 2048 points (3x6.826 s) were obtained to assess the behaviour and propagation of DF sites for each of the AR spectral analysis techniques and compared with the 3D DF maps recently validated using FFT-based approach (Salinet Jr *et al.*, 2013b).

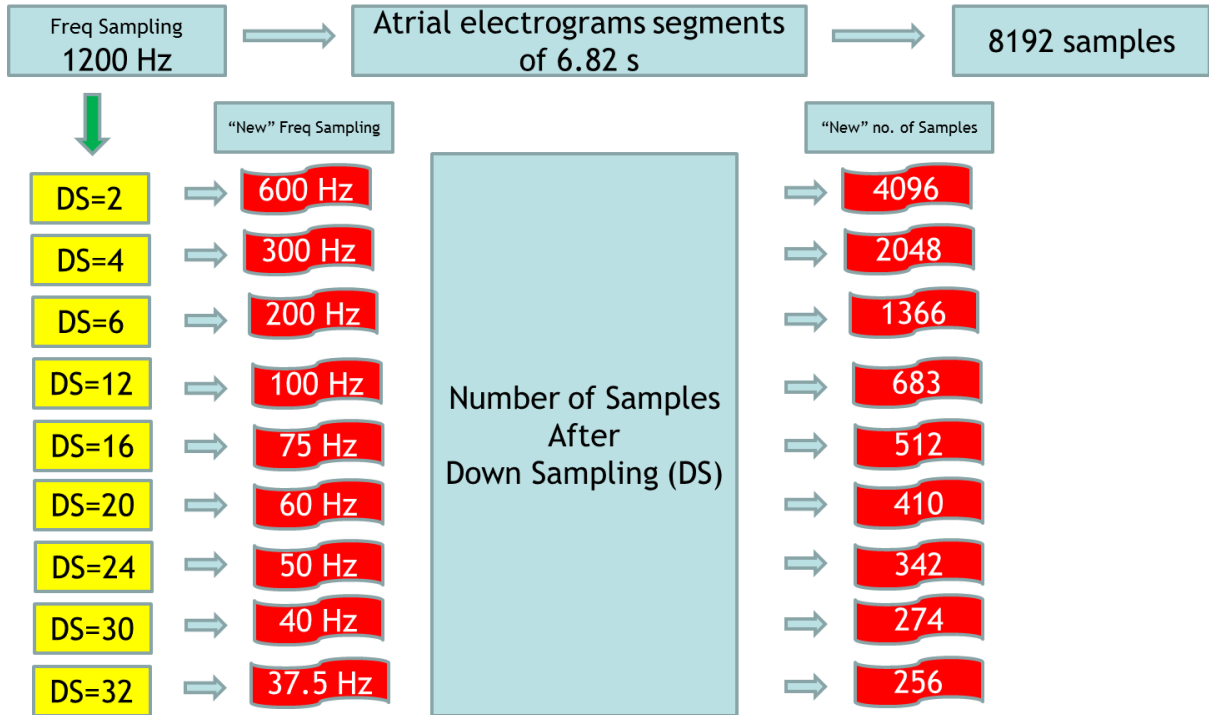


Figure 5.1 Illustration of the AEGs downsampling (DS) in the time domain with 9 different F_s values (from 600 Hz down to 37.5 Hz prior to spectral analysis).

5.2.3. AUTOREGRESSIVE MODEL ANALYSIS

In the AR model approach (Kay and Marple, 1981, Marple, 1987, Diniz *et al.*, 2010), the signal $x[n]$ is modelled as the result of filtering a white noise $n[n]$ by an all-pole filter of order p with coefficients a_k . These coefficients a_k are estimated using an optimisation criterion to minimise the residual error $e[n]$. This error is the difference between the signal $x[n]$ and the output of the filter $\tilde{x}[n]$. The AR coefficients a_k and variance σ^2 can be estimated by solving a set of linear equations (sections 5.2.3.1 to 5.2.3.4).

$$x[n] = \tilde{x}[n] + e[n] \quad (5.1)$$

$$\tilde{x}[n] = n[n] - \sum_{k=1}^p a_k x[n-k] \quad (5.2)$$

The verification of the AR model to assess if it can suitably describe the AEG signals was performed. It consisted in fitting AR model structure and order selection to data. The AR modelling effectively described the AEGs and the difference between the predicted and the true signal sequence values resulted in residuals which were random (uncorrelated in time) and normally distributed. The autocorrelation function of residuals fell inside the confidence interval of 95 % (red lines) and close to zero at all lags except for lag zero (Figure 5.2).

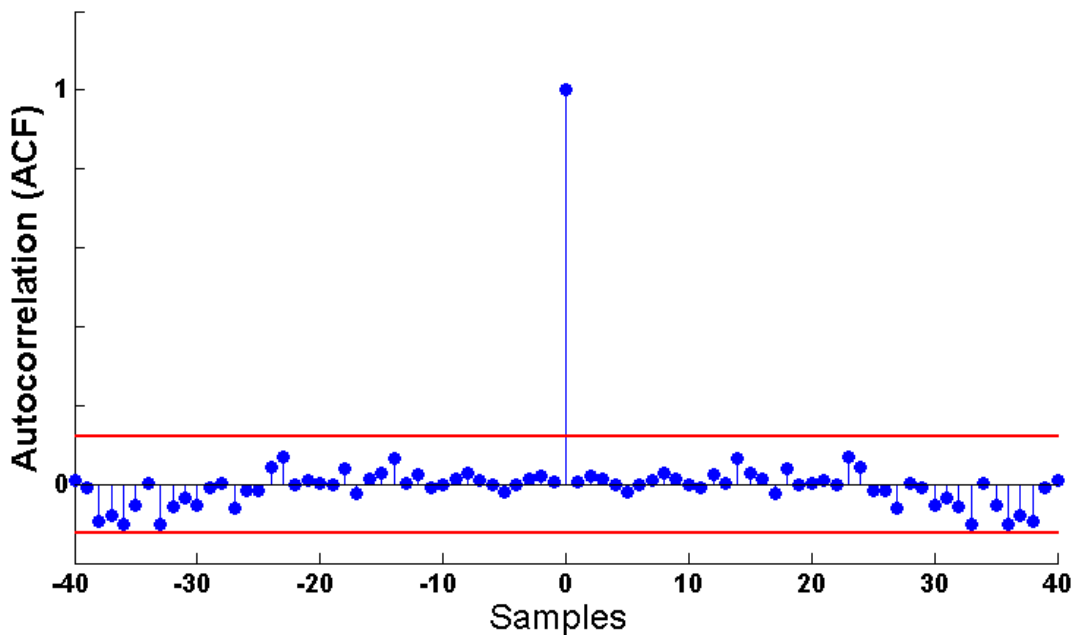


Figure 5.2 Autocorrelation function of the residuals, calculated by the difference between the predicted sequence values by the AR modelling and the true signal sequence, showing that the residuals are random (or uncorrelated in time) falling inside of the 95% confidence interval (red lines) and close to zero at all lags except for lag zero.

The AR-based PSD of an AR process is given by Eq. (5.3), where T is the sampling period.

$$P_{AR}[f] = \frac{\sigma^2 T}{\left| 1 + \sum_{k=1}^p a_k^{-j2\pi kT} \right|^2} \quad (5.3)$$

A variety of AR spectral estimation methods represent a trade-off between spectral estimation and computational efficiency (Kay and Marple, 1981, Kay, 1987, Diniz *et al.*, 2010). In this study we estimated the AR PSD using four different techniques (Yule-Walker, Covariance, Modified Covariance and Burg methods) applied to AEGs and the results were compared with those obtained using the FFT-based approach.

5.2.3.1. AUTOCORRELATION OR YULE-WALKER (YW) METHOD

The parameters of an AR process with zero mean and order p using the YW method with the Levinson-Durbin recursive algorithm are the solution of a set of linear equations which are obtained by the minimization of the estimate of the prediction error (Eq. 5.4) and with the extrapolation of the values of the autocorrelation function (ACF) $R_{xx}[k]$ estimated according to (Eq. 5.5). The Levinson-Durbin algorithm has the advantage of being computationally efficient, requiring an order of p^2 mathematical operations and it guarantees that the estimated poles lie within the unit circle.

$$\sigma^2 = \frac{1}{N} \sum_{n=-\infty}^{\infty} \left| x[n] + \sum_{k=1}^p a[k]x[n-k] \right|^2 \quad (5.4)$$

$$R_{xx}[k] = \frac{1}{N} \sum_{n=0}^{N-k-1} x[n+k]x[n] \quad (5.5)$$

Equation 5.5 is defined as the biased estimator of the ACF and is usually preferred since it tends to have smaller mean square error (variance) and decays faster in finite datasets when compared with the unbiased estimate (which uses the scaling term $1/(N-k)$ rather than $1/N$), where N is the number of samples (Kay and Marple, 1981, Kay, 1987, Diniz *et al.*, 2010). To estimate the coefficients and variance, the method first requires the estimation of the first order AR process parameters (Eq. 5.6). This is then followed by a recursive implementation for obtaining successively higher orders from $k = 2$ to the desired model order p (equations 5.7, 5.8 and 5.9) until the desired model order is reached. Two subscript indices are used to easily identify the coefficients $a_{Order, Coef. Number}$ (Kay and Marple, 1981).

$$a_{11} = -\frac{R_{xx}[1]}{R_{xx}[0]}, \quad \sigma_1^2 = (1 - |a_{11}|^2) R_{xx}[0] \quad (5.6)$$

$$a_{kk} = \frac{\left[R_{xx}[k] + \sum_{l=1}^{k-1} a_{k-1,l} R_{xx}[k-l] \right]}{\sigma_{k-1}^2} \quad (5.7)$$

$$a_{kr} = a_{k-r,r} + a_{kk} a_{k-1,k-r}^* \quad (5.8)$$

$$\sigma_k^2 = (1 - |a_{kk}|^2) \sigma_{k-1}^2 \quad (5.9)$$

The YW approach is computationally efficient when the Levinson-Durbin algorithm is employed (Kay, 1987), but it has been argued that this method produces poorer spectral resolution than alternative AR algorithms.

5.2.3.2. COVARIANCE METHOD

In the Covariance method the data set is windowed and the data points of the interval are used to compute the variance of the white noise. The estimated autocorrelation function $c_{xx}[j,k] = r_{xx}[j,k]$ (summation of $N-p$ lag products) for each window location k and the variance are calculated using the following equations (Kay and Marple, 1981, Marple, 1987, Diniz *et al.*, 2010):

$$c_{xx}[j,k] = \frac{1}{N-p} \sum_{n=p}^{N-1} x^*[n-j]x[n-k] \quad (5.10)$$

$$\hat{\sigma}^2 = \rho_{MIN} = c_{xx}[0,0] + \sum_{k=1}^p a_k x_{n-k} \quad (5.11)$$

5.2.3.3. MODIFIED COVARIANCE METHOD

In this method the AR parameters are estimated by minimising the average (Eq. 5.12) of the estimated forward (Eq. 5.13) and backward (Eq. 5.14) prediction errors.

$$\hat{\rho} = \frac{1}{2} (\hat{\rho}^f + \hat{\rho}^b) \quad (5.12)$$

$$\hat{\rho}^f = \frac{1}{N-p} \sum_{n=p}^{N-1} \left| x[n] + \sum_{k=1}^p a[k]x[n-k] \right|^2 \quad (5.13)$$

$$\hat{\rho}^b = \frac{1}{N-p} \sum_{n=0}^{N-1-p} \left| x[n] + \sum_{k=1}^p a^*[k]x[n+k] \right|^2 \quad (5.14)$$

This method diverges from the Covariance method by flipping the data around and identifying the forward and backward prediction errors in complex data (using

extra points). The overall prediction error is their average (Kay and Marple, 1981, Marple, 1987). The autocorrelation is estimated as

$$c_{xx}[j, k] = \frac{1}{2(n-p)} \left(\sum_{n=p}^{N-1} x^*[n-j]x[n-k] + \sum_{k=0}^{N-1-p} x[n+j]x^*[n+k] \right) \quad (5.15)$$

5.2.3.4. BURG METHOD

In contrast to the previous approaches, Burg's method computes the reflection coefficients directly (Eq. 5.16) and from these the remaining AR parameters are obtained using the Levinson-Durbin algorithm. The reflection coefficients are obtained by minimising the average of the backwards and forwards prediction errors in a constrained manner when compared with Modified Covariance Method. The method assumes that a_{kk} coefficient is estimated after the a_{kk-1} order prediction error filter coefficients had been estimated by minimizing the a_{kk-1} order prediction error power. First it is necessary to compute the estimate of the autocorrelation at lag zero with the forward and backward prediction errors (Eqs. 5.17 and 5.18). This is followed by the estimation of the reflection coefficients (Eq. 5.16), which are dependent of forward and backward prediction errors (Eq. 5.11 and 5.12) (Kay and Marple, 1981, Marple, 1987, Diniz *et al.*, 2010), $k=1, 2, \dots, p$.

$$a_{kk} = \frac{-2 \sum_{n=k}^{N-1} \hat{e}_{k-1}^f[n] \hat{e}_{k-1}^b[n-1]^*}{\sum_{n=k}^{N-1} \left(|\hat{e}_{k-1}^f[n]|^2 + |\hat{e}_{k-1}^b[n-1]|^2 \right)} \quad (5.16)$$

The recursive estimation of the variance and coefficients for the higher orders are calculated using equations 5.8 and 5.9 (Levinson-Durbin algorithm).

$$\hat{e}_k^f[n] = \hat{e}_{k-1}^f[n] + a_{kk} \hat{e}_{k-1}^b[n-1] \quad n = k+1, k+2, \dots, N-1 \quad (5.17)$$

$$\hat{e}_k^b[n] = \hat{e}_{k-1}^b[n-1] + a_{kk}^* \hat{e}_{k-1}^f[n] \quad n = k, k+2, \dots, N-1 \quad (5.18)$$

5.2.4. ORDER SELECTION CRITERIA

Since the AR order p is not usually known a priori, it is necessary to apply a model order estimation technique for finding the ‘optimum’ order for the AR model. This is critical because if a much larger than this ‘optimum’ model order is chosen the resulting spectrum might present spurious peaks and computational efficiency will also be compromised. Conversely, if too low a model order is selected a much smoothed spectral estimate will result.

In this study we considered 3 different techniques for identifying the order for AR spectral estimation of the AEGs during AF for each patient. All these methods work by increasing a tentative model order until the balance between the prediction error, which monotonically decreases with model order, and a weighting function, which monotonically increases with model order, reaches a minimum value. This is chosen as the ‘optimum’ order. In the description of the methods that follows p is the optimum order, σ_p^2 is the white noise variance and N is the number of samples of the data segment used.

The first method was suggested by Akaike (Akaike, 1974) and is usually referred to as *Akaike Information Criterion (AIC)*.

$$AIC_p = \ln(\sigma_p^2) + \frac{2(p+1)}{N} \quad (5.19)$$

The second method was proposed by Parzen (Parzen, 1975) and is denominated *Criterion AR Transfer Function (CAT)*.

$$CAT_p = \left(\frac{1}{N} \sum_{j=1}^p \frac{N-j}{N\sigma_j^2} \right) - \left(\frac{N-p}{N\sigma_p^2} \right) \quad (5.20)$$

A more recent method, the *Finite Information Criterion (FIC)* was proposed in 1993 and is defined by Eq. 5.21-5.23, where the description of the finite sample variance coefficient (v_i) is modified according to the AR method used (Broersen and Wensink, 1993).

$$FIC_p = \ln \sigma_p^2 + 2 \left[\sum_{j=1}^p v_i \right] \quad (5.21)$$

$$v_{i, YW} = \frac{N-j}{N(N+2)} \quad v_{i, Burg} = \frac{1}{(N+1-j)} \quad (5.22)$$

$$v_{i, Cov} = \frac{1}{(N+2-2j)} \quad v_{i, Mod Cov} = \frac{1}{(N+1.5-1.5j)} \quad (5.23)$$

The value of the ‘optimum’ order for each confidence level was chosen as the order which satisfied the 95%, 90%, 85% or 80% of the cumulative histogram sum computed in the 2048 AEGs in the whole segment (20.478 s) for at least three order selection methods: AIC, CAT and FIC (FIC_{YW} , FIC_{Burg} , FIC_{Cov} and $FIC_{Mod Cov}$).

5.2.5. STATISTICAL ANALYSIS

We fitted a linear mixed effects model to the data, which included as random effects: (1) patient, (2) patient*down sampling in the time domain of the AEGs with different sampling frequencies (down-sampled signal) and (3) patient*down-sampled

signal*DF estimation using each of the AR spectral techniques (YW, Covariance, Modified Covariance and Burg methods). As fixed effects we included: (1) DF estimation using each of the AR spectral techniques, (2) down sampling of the AEGs, and (3) AR spectral estimation techniques*down sampling of the AEGs. This tested whether any differences between the DF using the AR spectral estimation techniques varied by F_s , while properly allowing for the nested structure of the data (i.e. where the DF calculated by each AR spectral technique was measured at each F_s for each patient). The results were compared with those obtained using the FFT-based approach. This analysis was performed using the *nlme* (Pinheiro *et al.*, 2012) package in *R* (Team, 2012).

5.3.RESULTS

Figure 5.3 shows the time-domain of an AEG sampled at $F_s=1200$ Hz with a total of 8192 samples (upper trace). Down sampling 32 times (new sampling frequency of $F_s=37.5$ Hz) resulted in a ‘dramatic’ decrease of samples ($N=256$). The re-sampled signal is shown in the second trace. Spectral analysis performed using FFT (for the original signal) and AR YW (for the down-sampled signal) confirms that the DF of the signal can still be estimated after this level of down sampling using the AR approach. The FFT approach was applied to the original AEG sampled at 1200 Hz with 8192 points and zero padding of 4 times resulting in a total of 32768 samples produced a frequency step of 0.0366 Hz. The PSD using AR YW model was applied for two different AR model orders ($p=50$ and $p=18$) and as the AR spectrum is continuous, the number of spectral samples was chosen so that frequency steps were the same as applied by using the FFT approach.

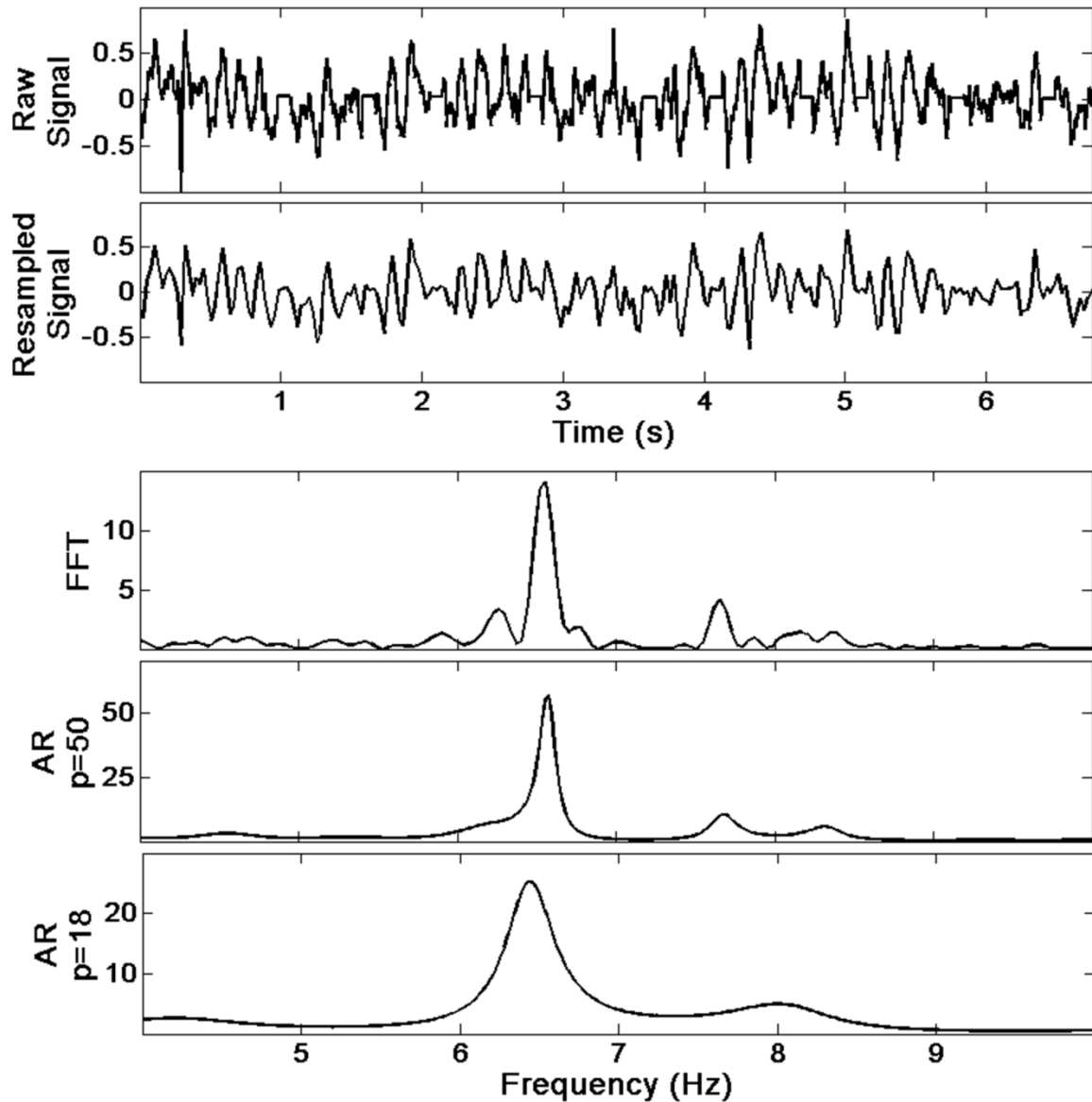


Figure 5.3 AEG (raw signal) sampled at 1200 Hz (upper trace) and corresponding signal after down sampling 32 times ($F_s = 37.5$ Hz). PSD estimation of the raw signal using FFT, followed by the PSD of the down-sampled signal using AR YW approach with model orders $p=50$ and $p=18$.

5.3.1. SELECTION OF MODEL ORDER FOR AF SIGNALS

The orders were estimated for different F_s considering each individual AR order estimation method AIC, CAT and FIC (FIC_{YW} , FIC_{Burg} , FIC_{Cov} and $FIC_{Mod\ Cov}$) previously described. For each individual patient, a 20.478 s long segment (3 consecutive 6.826 s long segments) for 2048 points was considered and results of the order estimation are illustrated in figure 5.4. Figure 5.4a shows the histogram of order selections produced by all methods for one patient whose original signal for an individual point was down-sampled to 75 Hz. The mode of the model order for that individual point was 11 and a similarity of the results of estimating the AR model order by the methods tested can also be seen.

Figure 5.4b shows the respective cumulative histogram of the points (in %) against order (for 2048 points). Four different ‘confidence levels’ (CL: 95%, 90%, 85% and 80%) were used to select the order for which at least three methods agreed. Odd orders were ignored as in this case one of the poles lie on the real axis not affecting much the DF; the order selected in this case is the next even value. The orders chosen were 24 for CL 95%, 22 for 90%, 22 for 85% and 20 for 80%. Figure 5.4c shows an example of the estimated order using CAT model applied for all patients with different F_s strategies considering a confidence level of 95%. The curve shows that the order decreases with the F_s and as the order value affects the processing time for AR spectral estimation, with lower orders corresponding to shorter times, as expected. The other order selection methods AIC, CAT and FIC (FIC_{YW} , FIC_{Burg} , FIC_{Cov} and $FIC_{Mod\ Cov}$) presented similar behaviour. Figure 5.4d shows the order selection for different F_s values and confidence levels. The ‘steps’ observed in the figure occur because the previous value in a specific F_s and

confidence level has lower order compared with the next point at a different confidence level.

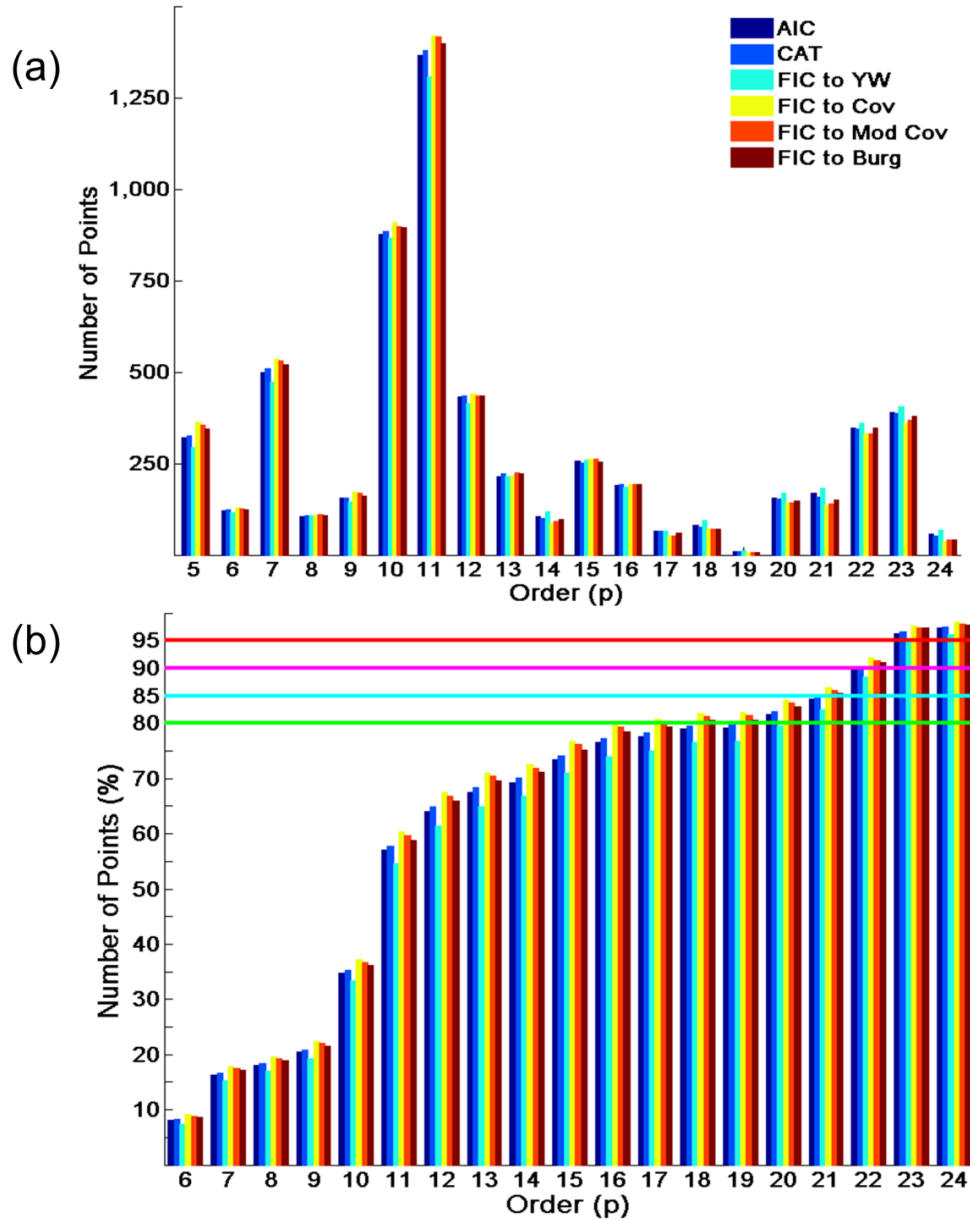


Figure 5.4 AR model order estimation. (a) Histogram of ‘optimum’ AR model orders estimated for patient 1 for $F_s=75$ Hz over 20.478 seconds. (b) cumulative histogram of the estimation order for patient 1 for $F_s=75$ Hz over 20.478 s. (c) ‘optimal’ model order calculated using the technique CAT for various F_s values and 95% of confidence level. (d) ‘optimal’ model order using the same technique as presented in (c) now with the different confidence levels (95%, 90%, 85% and 80%). See text for details.

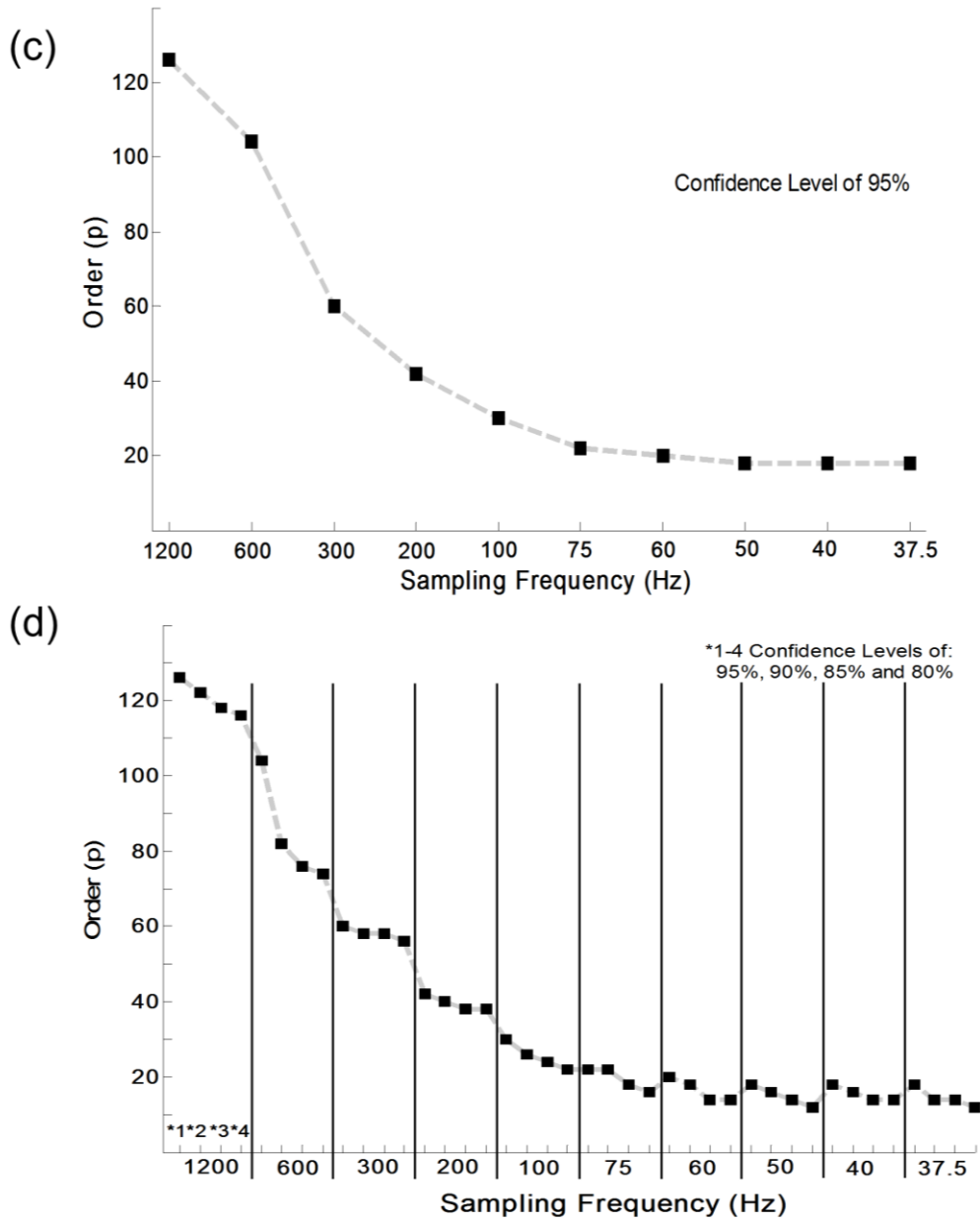


Figure 5.4 (continuation) (c) 'Optimal' model order calculated using the technique CAT for various Fs values and 95% of confidence level. (d) 'Optimal' model order using the same technique as presented in (c) now with the different confidence levels (95%, 90%, 85% and 80%). See text for details.

A summary of the order computed by all the methods for all patients and different F_s values is given in table 5.1.

Table 5.1 Summary of the results of the estimation of ‘optimum’ AR model order for the F_s values tested.

Order Estimation (p)				
F_s	Confidence Level			
	95%	90%	85%	80%
1200 Hz	134	122	118	116
600 Hz	104	82	76	74
300Hz	60	58	58	56
200 Hz	42	40	38	38
100 Hz	30	26	24	22
75 Hz	22	22	18	16
60 Hz	20	18	14	14
50 Hz	18	16	14	12
40 Hz	18	16	14	14
37.5 Hz	18	14	14	12

5.3.2. SPECTRAL ANALYSIS AND 3D DF MAPPING

Spectral Analysis of AEGs in persAF patients was obtained using FFT and four distinct AR spectral estimation methods (YW, Burg, Covariance and Modified Covariance). Three sequential 3D DF maps with simultaneous 2048 points were generated with different F_s values in 6.826 s long windows and the results were concentrated on the impact of high levels of down sampling on the AEGs (resulting F_s : 100 Hz, 75 Hz, 60 Hz, 50 Hz, 40 Hz and 37.5 Hz) to investigate the feasibility of the AR spectral analysis model as alternative tool to estimate DF. The 3D DF maps

are colour coded according to the frequency of the DF for all spectral estimation techniques, with purple-blue representing the lower frequencies and red-dark red corresponding to higher frequencies. The DF for FFT was defined as the frequency with the highest peak between 4 Hz and 12 Hz and for the AR methods as the frequency peak with the highest area (threshold 0.5 Hz either way) for the same frequency range. Zero padding was implemented for FFT and the number of spectral samples was chosen to produce frequency steps as described early in the results.

For the AR spectral analysis, the mixed model ANOVA of the entire AF segment (3x 6.826 s) showed that the down sampling factor on the AEG signal*DF estimation with AR spectral techniques (YW, Covariance, Modified Covariance and Burg methods) interaction had a non-significant effect ($F_{15, 126}=0.01$; p-value = 1). This showed that any differences between AR techniques did not depend on the re-sampling factor on the AEG. The main effect of the AR spectral estimation techniques (i.e. the effect of technique averaged over Fs) was also non-significant ($F_{3, 126}=0.59$; p-value = 0.62) as presented in Figure 5.5. This suggests no significant differences between AR techniques overall. Although there was no evidence of any significant differences between techniques, significant differences between Fs values were found ($F_{5, 35}=2.84$; p-value = 0.03) (Figure 5.6) (i.e. the effect of averaged techniques over Fs). As figure 5.6 shows, the Fs=37.5 Hz had the greatest level of agreement, while the Fs=100 Hz had the lowest level of agreement (albeit, at only around 2% lower than at 37.5 Hz).

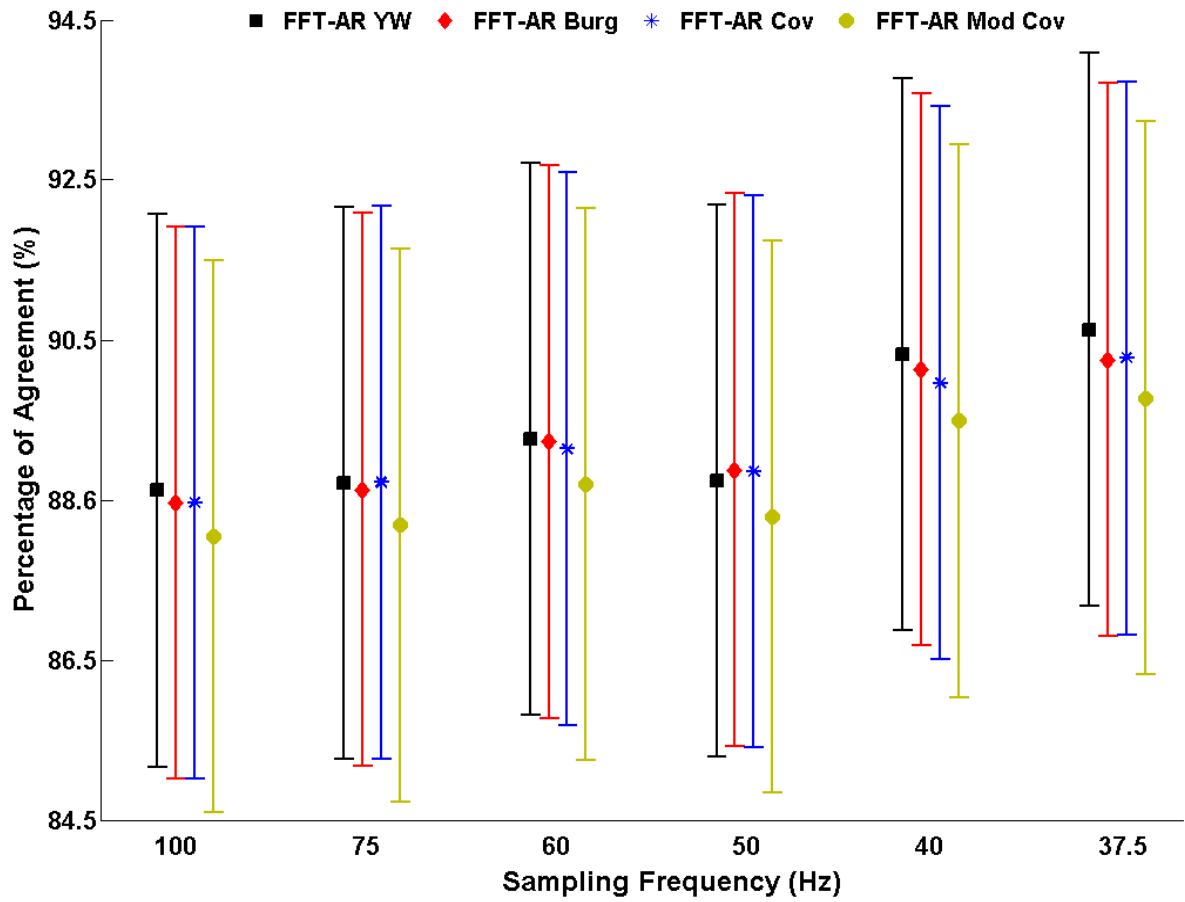


Figure 5.5 Percentage of agreement between the DF calculated using FFT and the DF calculated using the AR spectral analyses techniques with different re-sampling frequencies for the 2048 AEGs during 20.478 second-long segments (3 consecutive windows of 6.826 s). Error bars represent 95% confidence intervals.

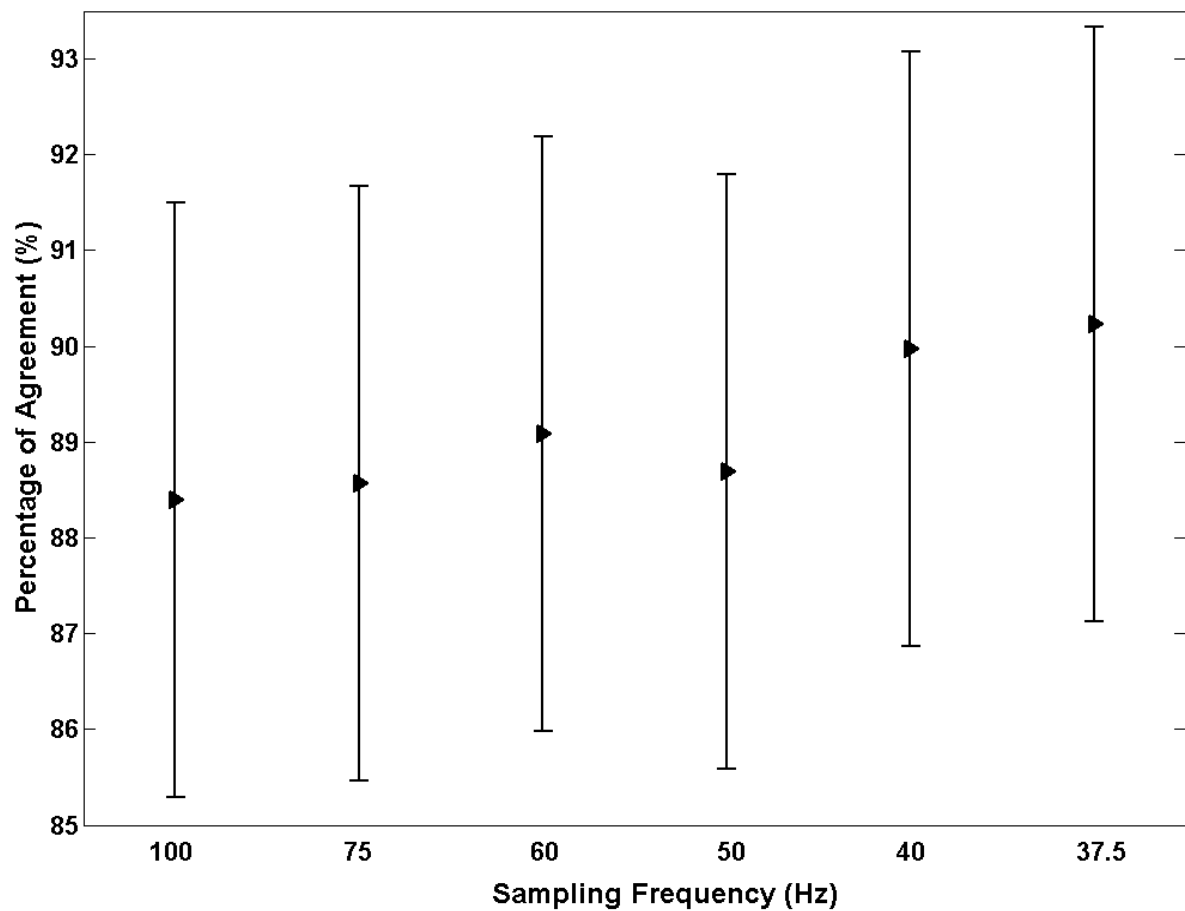


Figure 5.6 Percentage of agreement between the DF calculated using FFT and the DF calculated using the overall AR spectral analyses techniques with different re-sampling frequencies for the 2048 AEGs during AF for 20.478 second-long segments (3 consecutive windows of 6.826 s). Error bars represent 95% confidence intervals.

Figure 5.7 shows a typical case of a 3D representation of the DF maps of a 6.826 s segment window using the FFT-based approach and the four AR spectral estimation techniques. The 3D DF using FFT was applied to the original AEG sampled at 1200 Hz (8192 samples) and the PSD using AR methods were obtained after 32 times down sampling (resulting $F_s = 37.5$ Hz) of the AEG ($N = 256$ samples) with the selection of the model order p presented in the second column of table 5.1

(covering 95% of the intracardiac signals). Both methods showed similar 3D DF maps of AEG signals with a good agreement and the percentage of equal points between FFT vs. AR YW was 93.8%, FFT vs. AR Burg was 93.6%, FFT vs. AR Covariance was 93.8% and FFT vs. AR Modified Covariance was 93.2%.

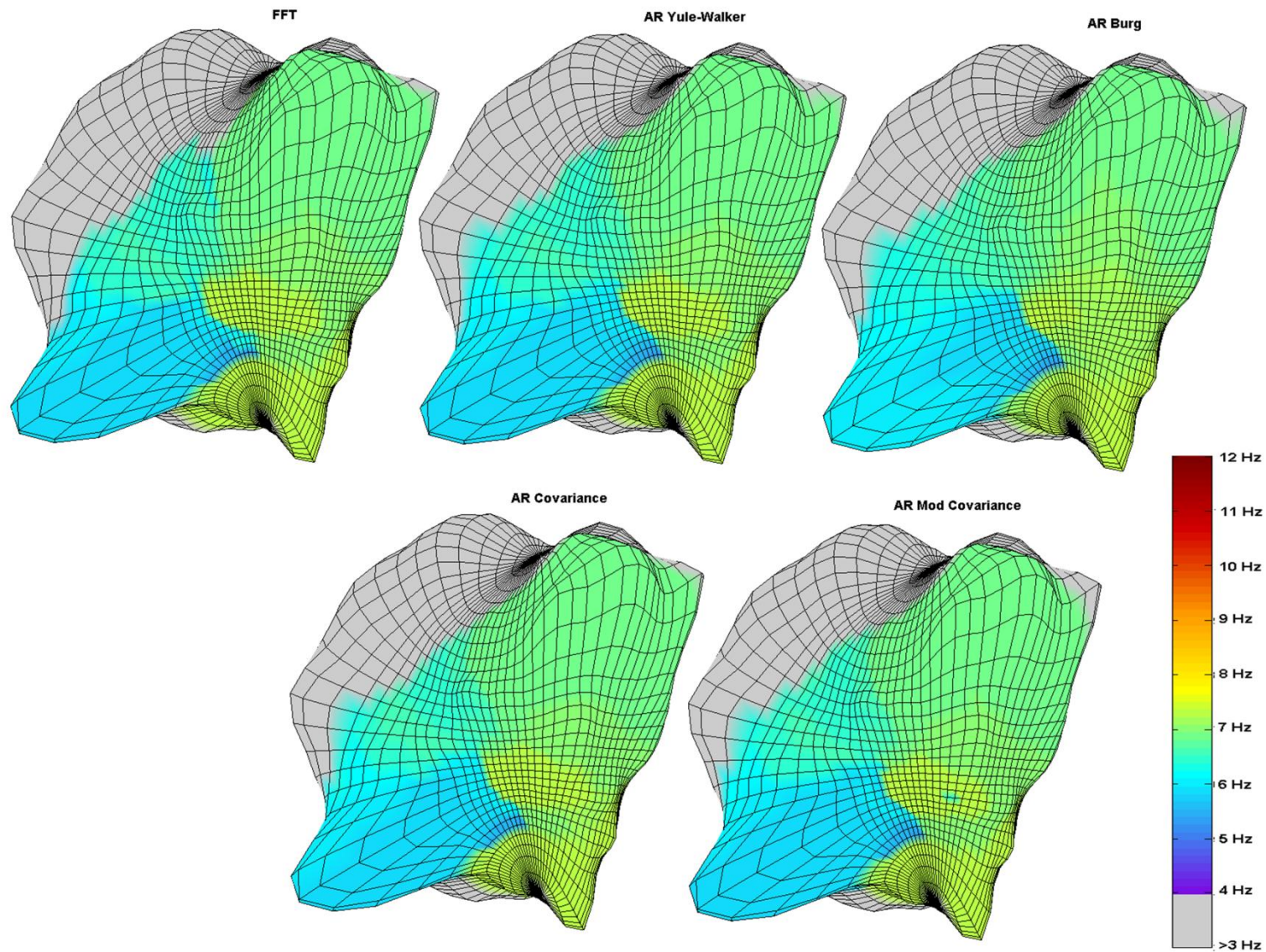


Figure 5.7 3D representation of the DF maps using different techniques for spectral estimation: (a) FFT technique with the original F_s (1200 Hz); (b) AR – YW; (c) AR – Burg; (d) AR – Covariance and (e) AR – Modified Covariance. All AR methods used a re-sampled frequency of 37.5 Hz.

DF estimation using AR YW method with the Levinson-Durbin recursive algorithm has the advantage of being computationally efficient over the three other AR methods (Burg, Covariance and Modified Covariance) by the fact that AR YW method applies the Levinson-Durbin algorithm to calculate the AR coefficients, the data points of the interval are not used to compute the variance of the white noise (AR Covariance) and the reflection coefficients do not need to be calculated by the minimization of the backwards and forwards prediction errors (AR Modified Covariance and AR Burg). Aiming to observe the impact of the sampling frequencies to generate the 3D DF maps, the processing times of FFT and AR YW were measured for estimation of DF of the 2048 points and the AR times are shown in Figure 5.8. The processing time for the FFT was 7.65 s and as expected, the processing time for the AR YW decreased with lower sampling frequencies (higher down samplings levels): 5.44 s ($F_s = 100$ Hz), 5.35 s ($F_s = 75$ Hz), 5.32 s ($F_s = 60$ Hz), 5.27 s ($F_s = 50$ Hz), 5.15 s ($F_s = 40$ Hz) and 5.05 s ($F_s = 37.5$ Hz).

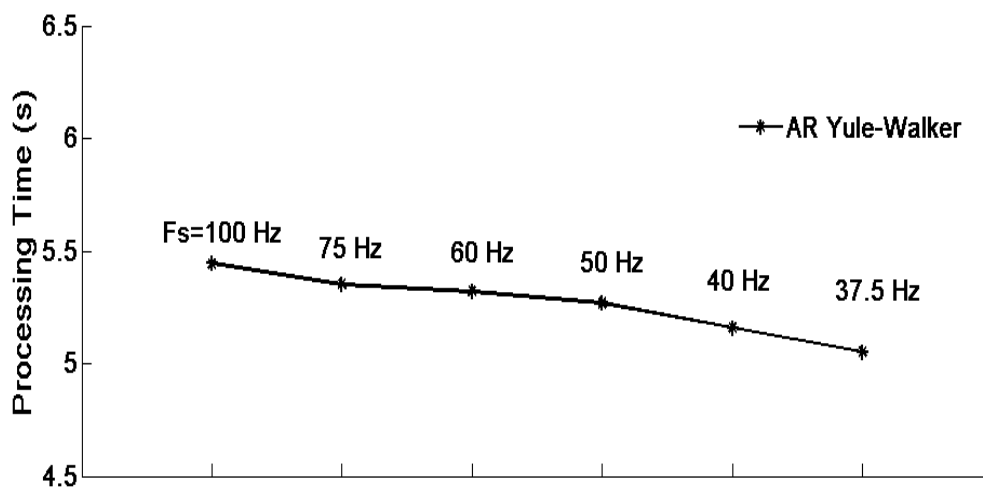


Figure 5.8 AR YW processing time.

5.4. DISCUSSION

Spectral analysis has been used for a while as a tool to provide information about the physiological behaviour of the electrical activity of the heart. In terms of AF the large majority of the studies that applied spectral analysis to identify DF of local endocardial electrograms during EP procedures used an FFT-based approach. This method identifies the most prominent frequencies and intensities of the periodicities of a signal modelled by sinusoids. Amplitude and frequency variability of a signal associated with increase of signal complexity may be unfavourable to the use of this technique (Kay, 1987, Ng *et al.*, 2006, Ng *et al.*, 2007). These limitations suggest the investigation of alternative spectral analysis methods (such as the AR-based approach) (Lovett and Ropella, 1992, Schlindwein and Evans, 1992) for analysis of the dynamic behaviour of AEGs. In addition, AR models can suitably describe AEGs from persAF patients resulting in white and uncorrelated residuals.

In this study, we have implemented a non-Fourier-based spectral estimation technique with emphasis on selection of appropriate sampling rate and AR model order as an alternative tool to generate high density 3D DF maps. These could be used as a complementary tool to currently used time-based analysis for ablation in persAF patients. We showed that 3D DF maps of AEGs using AR spectral estimation techniques produce good levels of agreement when compared with the frequency maps recently validated using FFT-based approach (Salinet Jr *et al.*, 2013b). The rates of DF agreement between AR techniques and FFT increased according to

higher levels of down sampling (lower sampling frequencies) on the AEGs (Figure 5.6). The $F_s=37.5$ Hz had the greatest level of agreement, while $F_s=100$ Hz had the lowest level of agreement (although the DF agreement difference is just around 2% lower). These results suggest that if a down sampling of 32 times is implemented in AEG of persAF patients, the 3D DF maps between FFT and AR model will have the highest level of DF similarity (an typical example of a 3D DF frame using a 6.826 s segment window is displayed on figure 5.7 with an average of the DF agreement between techniques at 93.6 ± 0.29 %).

Unfortunately, we could not assess which method estimated the 'true' DF that would represent the underlying AF behaviour for the recording points that the approaches disagreed. Simultaneous AF mechanism during persAF might cause uncoordinated waves collisions, which in turn can generate electrograms with short episodes of non-periodicity avoiding accurate predictions and therefore resulting in "false" interpretations by the FFT approach.

The authors also observed that there were no significant differences ($F_{3, 126}=0.59$; p-value = 0.62) between less usual AR spectral estimation techniques (Covariance, Modified Covariance and Burg) and the most studied AR technique (YW) although it has been argued that this method produces poorer spectral resolution than alternative AR algorithms (Kay, 1987). One important advantage of the YW approach is that it is much faster than the alternative AR spectral estimation techniques.

An important decision in AR-based spectral analysis is that of the model order. The optimal order of AR can be computed using methods

described in the literature as used here. These methods are widely applied but they do not consider the complexity of each field (Biomedical, Financial, Geography, Mechanical ...). So, the order suggested by the methods may need further adjustments. In our analysis, when using the orders selected (table 5.1), a good agreement of the DF maps produced using AR-based and FFT-based approaches was observed (Figures 5.5, 5.6 and 5.7). Slightly higher orders can be used to improve spectral resolution, but that will increase processing time.

Other studies on model order selection criteria for AR-based spectral estimation (Schlindwein and Evans, 1990) concluded that the use of higher orders (overestimation) is better than using lower orders (underestimation). In addition, they observed that for shorter segments the methods are more likely to produce an underestimation of the model order. Most studies from different fields have implemented AR modelling mainly using the YW technique; we have seldom observed the use of the less-traditional AR methods of Covariance, Modified Covariance and Burg. Although the literature showed differences of spectral estimation between the methods for test signals, with the YW method faring slightly worse than the other three approaches (Kay and Marple, 1981), our results showed no significant differences, with a slight advantage to YW in terms of DF similarity and processing time (figures 5.5, 5.6 and 5.7).

Our results suggest that AR YW approach can be used for spectral analysis of AEGs. We have studied the level of down sampling (DS); the model order (p); and the different AR parameter estimation methods which

can be used to produce the spectra and the DF maps in AEG signals from persAF patients (principle of parsimony).

We have shown that 3D DF maps of AEGs from persAF patients can be obtained using AR-based spectral estimation even after aggressive electrogram down sampling resulting in maps very similar to those obtained using FFT. No significant differences between AR techniques were found, but AR YW has greater computational efficiency compared to the three other AR methods. Similarly, the processing time for the AR-based approach is considerably shorter when lower orders and sampling frequencies are used, as higher levels of down sampling presented the highest rates of DF agreement in this study (F_s of 37.5 Hz). This is important when considering the possibility of implementing such technique in real-time with more advanced hardware and software environments (such as using parallel computational power available in current GPUs). This would represent an innovation that may have a high impact on clinical practice, allowing consideration of the 3D DF maps as part of the decision making process for targeting ablation in persAF.

6. REAL-TIME FREQUENCY MAPPING VISUALISATION USING GPUS

6.1. INTRODUCTION

DF mapping using high density of simultaneous AEGs has been shown throughout this thesis a powerful tool contributing to the currently knowledge on the understanding of the AF dynamic mechanism in persAF patients. The contents of this chapter has been partially published as an original article in a peer review journal (Salinet Jr *et al.*, 2013b).

The use of 3D DF mapping in real-time as an auxiliary clinical electrophysiological tool available in theatre, together with the currently used time domain voltage maps, to guide ablation would help cardiologists identify possible “driver” sites and propagation patterns that can be ablated with unprecedented accuracy.

For real time implementations, an affordable and recently popular approach is to take advantage of the computational power of GPUs to speed up scientific computational codes (Kirk and Hwu, 2010). The parallel processing of GPUs, with hundreds of cores, allows considerable performance speedups.

In this research, a multichannel signal analysis approach using GPUs was implemented including the identification and characterization of the DF in

each of the 2048 spectral estimations, followed by a 3D representation of the atrium chamber represented by the DF values. This achievement was possible due to the important collaborative contribution by Dr. João Comba and his PhD student Guilherme Oliveira both from the Federal University of Rio Grande do Sul who have worked in programming the GPU's in C++ and also in the some of the visual aspects of the 3D frequency maps. My contributions at this collaborative work were: 'off-line' data collection, Matlab codes created for signal processing and frequency analysis where the collaborative research group could reprogram in C++, QRS-T subtraction on the AEGs, Matlab code to calculate the FFTs using a single and multiples (4 cores) CPU cores through the Parallel Processing Toolbox, processing time calculation for the GPUs and CPUs to generate the 3D DF maps, data analysis, interpretation of results and statistics.

6.2. MATERIALS AND METHODS

6.2.1. HARDWARE

A 3.4-GHz Pentium i7 quadcore desktop with a video graphic card Nvidia GeForce GTX 570 containing 480 GPU processors and Matlab 64-bit R2012a software installed (with Parallel Processing Toolbox 6.0) was used to create the sequential DF maps.

6.2.2. SIGNAL PROCESSING

Each of the simultaneous 2048 AEGs underwent a pre-processing stage including high-pass filter with a cut-off frequency at 1 Hz and ventricular far-field subtraction prior spectral analysis calculation. Both methods have been described in detail previously (see chapters 1 to 4).

6.2.3. FREQUENCY MAPPING & PARALLEL PROCESSING

After carrying out ventricular cancellation of the AEGs using the method described in chapter 3, spectral analysis was performed on each of the 2048 points using FFT with a Hamming window to produce high density 3D DF maps (Salinet Jr *et al.*, 2013b). The zero-padding factor was set during the analysis between 1 and 5 for allowing the visualization of frequency powers at every 0.25 Hz and 0.05 Hz respectively.

The GPU was programmed in C++ and created each DF map by computing the 2048 FFTs in parallel in the GPUs with the Nvidia CUDA Fast Fourier Transform library (CUFFT). Each GPU calculates in average 4 FFTs. For comparison with the computer CPU performance, the program then identifies the frequency with highest amplitude for each FFT result, also in parallel, but now using CPU threads with OpenMP.

CUFFT library allows double precision computation, we calculated the FFTs with single precision to reduce time spent sending the input data to GPU memory and the output data back to RAM. Also, using double precision, depending on the window size, can require more memory than the graphics card has available, so the computation of the 2048 FFTs

would have to be divided into multiple, smaller batches. With single precision, we can compute 2048 FFTs in a single batch, which means a single pair of input-in and output-out data transfers and faster computation. Aware that this could possibly decrease precision and lead to errors, we evaluated the difference between the single-precision GPU-computed FFT results and the double-precision Matlab ones, and found the average mean squared-error values to be negligible.

6.2.4. 3D FREQUENCY MAPPING VISUALIZATION

3D visualization techniques were explored to improve the visual aspects and quality of the 3D frequency maps. Within the techniques, renderisation and camera light to the front face were used. The tools are based on the representation of the DF as colour maps onto a 3D anatomically accurate representation of the atrium.

6.2.5. PROCESSING TIME

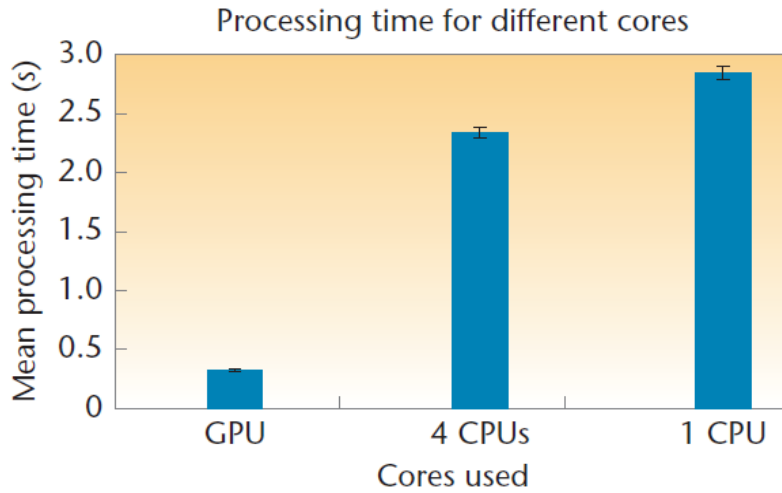
Real-time frequency mapping implementations were tested by calculating the processing time of sequential 3D DF frames using three different protocols: a single CPU core, multiple CPU cores (four cores) and the 480 GPU cores.

6.3.RESULTS

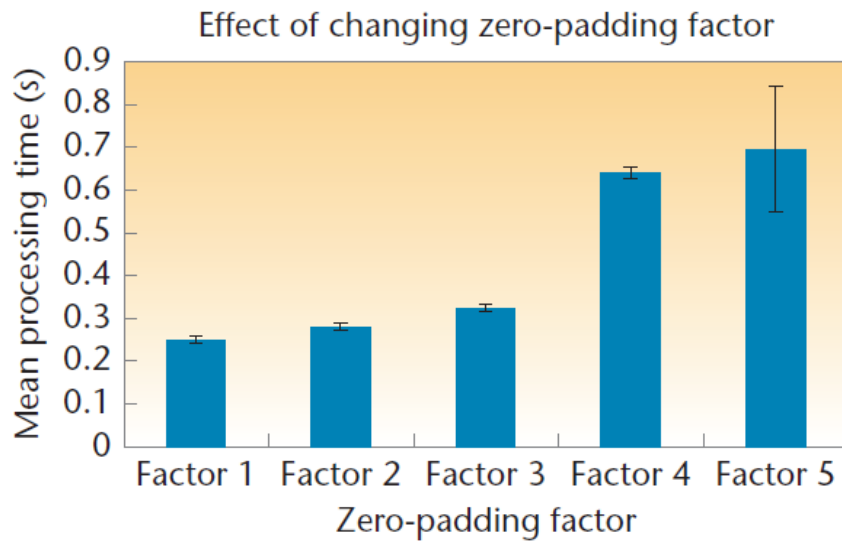
6.3.1. PROCESSING TIME

Using a single CPU core (under Matlab), DF maps could be generated within 2.46 ± 0.05 s. The processing time decreases to 2.03 ± 0.03 s when

four Pentium cores are used (under Matlab). This means that the loading is about 50%. A real-time DF mapping implementation would therefore be possible by using just the CPU (Pentium) cores. Using the GPUs for FFT calculation decreases processing time to 0.27 ± 0.01 s. This is 14.8 times faster than real time (a load of only 6.75%) (see Figure 6.1a). Even when the zero padding factor was increased to 5 (allowing visualization of frequency powers at every 0.05 Hz, which requires higher memory), the data processing using the GPUs was still 3.5 times faster than using 4 CPU cores under Matlab (see Figure 6.1b). These results therefore suggest that, where possible, using GPU cores for independent calculations on large amounts of data is preferable. This would allow the use of the CPU Pentium cores to run other tasks concurrently— for example, controlling data acquisition and storage. The timings consider different choices of zero-padding and Figure 6.1 shows the different approaches.



(a)



(b)

Figure 6.1 (a) Comparison of processing times between single and multiple CPU cores and the GPU cores for a factor-2 zero-padding (frequency step of 0.125 Hz). (b) estimated processing time for different factors of zero-padding.

6.3.2. FREQUENCY MAPPING VISUALIZATION

The C++ visualization displays the 3D DF frames where each vertex colour represents DF of its respective AEG position. The fast rendering lets us perform rotation on the atrium surface, and we can modify the use

of an interactive colour scale at any time to help visually isolate regions where the DFs are above a given threshold.

Two parameters can be set for consecutive sequential 3D DF frames: the zero-padding factor and the percentage of overlapping between input signal windows. Increasing the zero-padding factor will lead to a finer representation of the resulting frequencies of the FFTs and increasing the overlapping percentage creates more frames and a smoother animation that helps to understand how the different DF zones evolve over the surface along time.

Figure 6.2 presents a 3D DF frame of the LA with two different views. This figure is similar to the one shown in chapter 2 (Figure 2.5), but in this case the visual renderisation and camera light techniques highlighted even more the DF clouds and the 3D surface producing images more similar to the images as visualised by the clinicians on commercial systems.

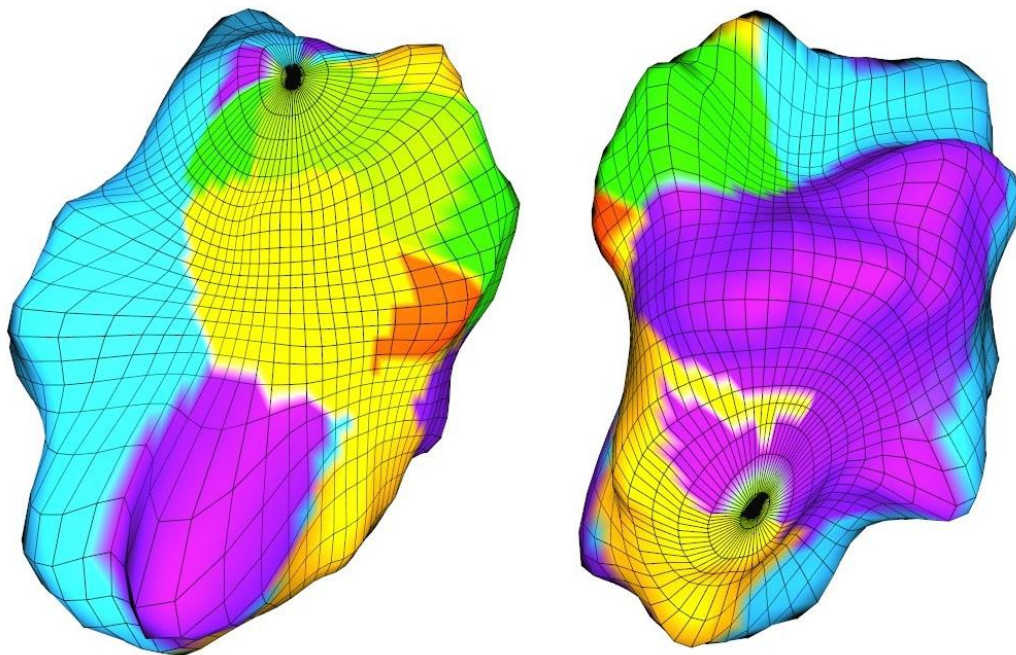


Figure 6.2 3D DF mapping of the LA with two different views of the 3D DF mapping.

When windows overlap, more DFs are created, thus reducing the time difference between consecutive ones. The result is a smoother animation of the DF maps, which helps to track the movement of several frequency zones in the atrium. Figure 6.3 shows an example of such smooth animation, where the window length was 4 seconds, (a) a sequence of four consecutive 3D DF frames generated 2 s sequentially apart (50 % overlap) and (b) with an overlap of 92 %. The same configuration as Figure 6.3b but with an overlap of half a window (50 %) would display only the first and sixth frames.

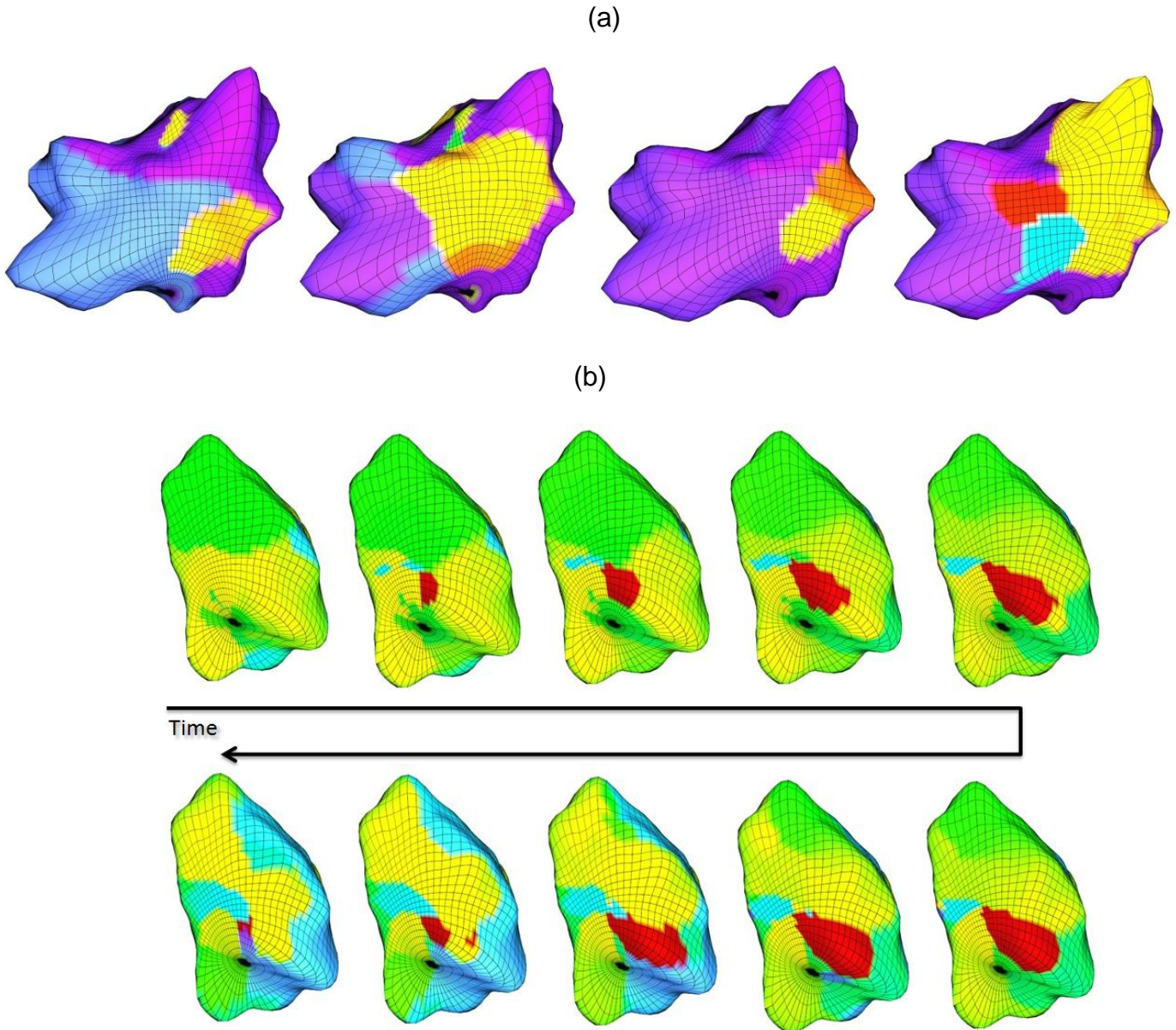


Figure 6.3 (a) Sequence of four consecutive 3D DF mapping frames that are 2 seconds apart for each representation (50% windows overlap). (b) consecutive DF maps using 92 % of overlapping between windows. Using more overlapping creates more frames and a smoother animation that helps to understand how the different DF zones evolve over the surface along time.

Associated with these maps and for further investigation, isolation of any particular area would also be automatically permitted, such the HDFAs believed to be a key point in the maintenance of this arrhythmia and track the trajectory of this area along time (for more details please refer to chapter 4). In Figure 6.4, we illustrate how the visualization of only the DF region can help doctors to identify the potential locations where ablation might take place. For this purpose, our tool needs to both identify the areas of highest DF, as well as use specific colour scales in the visualization to clearly identify these areas.

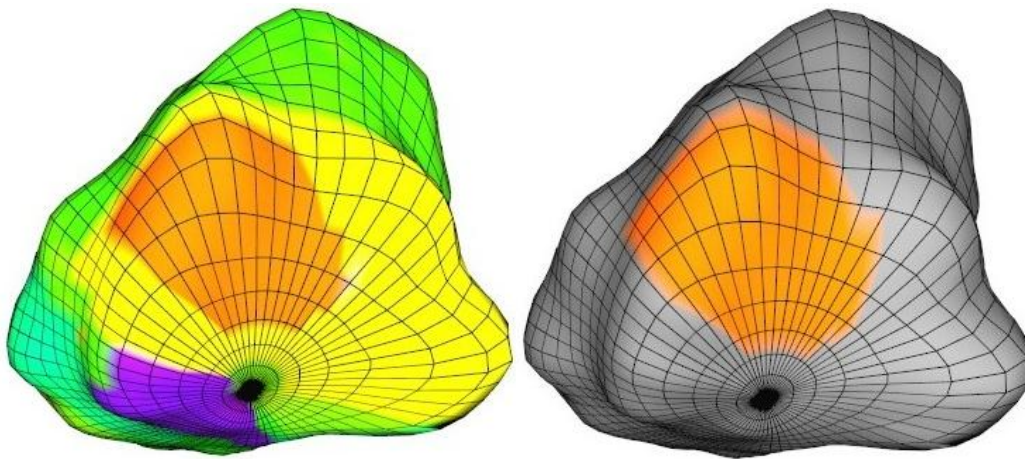


Figure 6.4 3D DF mapping and highest DF identification. (a) the LA's 3D representation, including the mapping of the DFs. The DFs (represented in a colour scale) help doctors visualize the behaviour of the atrium's electrical activation in the frequency domain in real time. (b) the system can also automatically identify the region corresponding to the HDFA.

This tool also allows monitoring the impact of the ablation procedure in the frequency domain by comparing the 3D DF maps before and after ablation. This helps verify the effectiveness of the procedure. Figure 6.5 shows that a substantial reduction of both the DF frequency and the areas

with high frequency occur after a successful ablation procedure. The lower part of Figure 6.5 shows the DF maps reproduced on the flat 32×64 matrix, while the top part shows them as a more useful 3D representation that takes the atrial geometry into consideration.

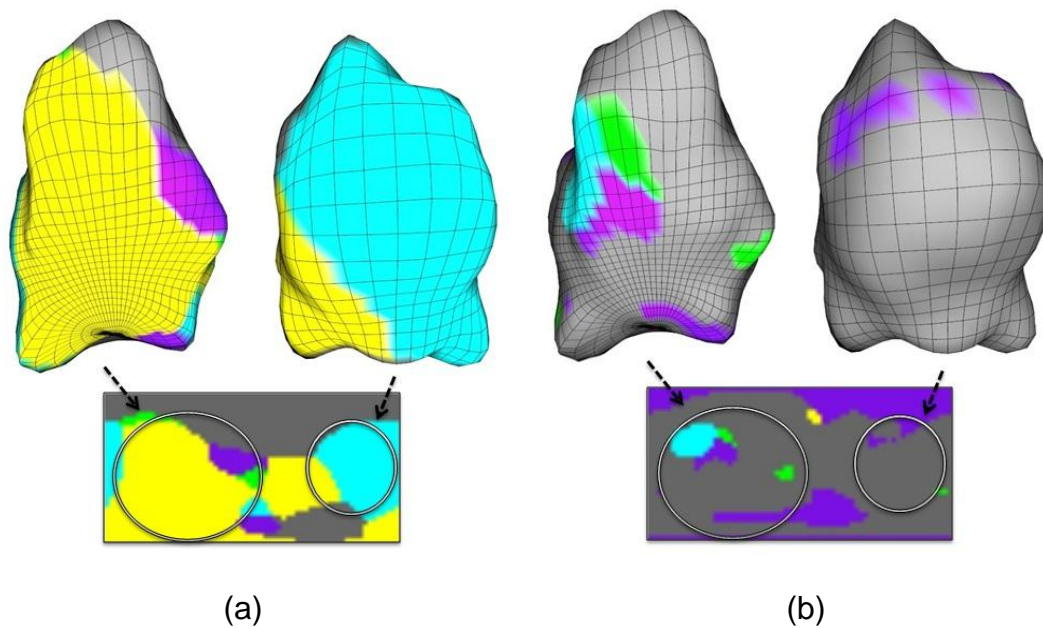


Figure 6.5 3D DF mapping of the LA of a patient with persAF. (a) the baseline DF map. (b) the DF immediately after the standard PVI procedure. This figure demonstrates a general reduction of the size of the DF areas, a reduction of the DF values, and a reduction in the complexity of the DF areas after the PVI procedure in this case.

6.4.DISCUSSION

Clearly, the processing time to calculate the 2048 FFTs using the GPU processors embedded in the video graphic card of the computer desktop showed the usefulness of this technique. In this case, the loading was under 7% (FFT's calculated in segments of 4 s) with the processing time 14.8 times faster than real-time. Moreover, in parallel to the FFTs

calculation by the GPUs, the multiple CPU cores from the desktop can still be used for other jobs, such as, controlling data acquisition and data transfer, or even displaying the results in more informative ways.

This great performance is also accompanied with the relative low cost where a good trade-off is observed mainly by comparing with the expensive EAM systems currently used by clinicians to treat AF patients.

The approaches described in this chapter allow the same current state-of-the-art bedside equipment used by clinicians nowadays to be easily modified to perform frequency domain analysis of the electrical activation of any chamber of the heart and generation of DF maps in real time. These 3D representations can be displayed with the same equipment and manipulated in exactly the same way as they are by cardiologists who perform the catheterization, and ablation procedures that are used for manipulating the time domain based images. With current technology and using a standard off-the-shelf PC with a modern graphics card, all of the approaches described here can be implemented and can help the cardiologist performing ablation in the theatre by displaying frequency domain-based information in real time.

6.5.CONCLUSION

With the advances in computing power and possibility of implementing more demanding mathematical manipulations of complex data, and the ability for producing and manipulating 3D imaging in real time as described here and recently validated (Salinet Jr *et al.*, 2013b), it is now possible to

implement a system that measures the DF over say 2048 points and produces a 3D representation of the DF map in real time just as easily as the time domain voltage maps currently used to guide ablation.

In this study the calculation of the FFTs by the GPUs was done after subtraction of ventricular far-field influence and its processing time was not considered here. The QRS-T removal method currently is the bottleneck of all processes to generate real-time 3D DF maps and its average processing time is in order of minutes when applied for short 2048 AEGs segments (up to 20 s).

7. MAIN FINDINGS, ORIGINAL CONTRIBUTIONS AND FUTURE RESEARCH ACTIVITIES

7.1. INTRODUCTION

Improving our understanding of the underlying AF behaviour is a key factor to contribute towards improving patient outcomes in special for persAF patients. Throughout this research different signal processing and visualisation techniques were developed and applied to simultaneous high density sets of AEGs obtained from persAF patients and displayed in the 3D representation of the patient's endocardium (Salinet Jr *et al.*, 2010a, Salinet Jr *et al.*, 2013b).

7.2. MAIN FINDINGS OF THE THESIS

- Development of the first real time high density 3D DF mapping to be potentially used as an auxiliary tool together with the current voltage mapping systems to help cardiologist performing ablation in the theatre (Chapters 2 and 6 and (Salinet Jr *et al.*, 2010a, Salinet Jr *et al.*, 2013b)).
- Development of a novel ventricular cancellation method for the AEGs where individual 'customised' and adaptive QRS-T segmentation is performed followed by a coherent subtraction strategy. Evidence has been shown that the novel approach is capable of reducing the ventricular influence on the

simultaneous high density AEGs which are affected even for areas far from the MV (Chapter 3 and (Salinet Jr *et al.*, 2012b, Salinet Jr *et al.*, 2013a)).

- The atrial electrogram's DF is not spatiotemporally stable invalidating the point-by-point sequential CM approach most commonly used to treat AF patients. In this method (see section 1.4.1 for more details), no measurements are made for significant duration between recordings and later the signals are assumed to be temporally stable and are merged together giving a false idea of being simultaneous. A lot of assumptions were made using this technology across basic science and clinical groups regarding the actual behaviour of the arrhythmia. The results of this thesis strongly support the notion that DF behaviour is dynamic and should be analysed ideally with simultaneous multipolar CM or NCM techniques and targeting sites of 'peak DF' from a single time frame is unlikely to be a reliable ablation strategy (Chapter 4 and (Salinet Jr *et al.*, 2010b, Salinet Jr *et al.*, 2012d, Salinet Jr *et al.*, 2013d)).
- Although there was lack of DF stability present in the AEGs, a certain degree of reappearance of DF activity over time was observed. The spatiotemporal analysis of the HDFA, represented by its CG, revealed the presence of localised, cyclical and irregular patterns of propagation (with predominance of local and cyclical activity) concentrated mostly in the LA roof followed by the PVs. The sites with highest DF showed a greater degree of organisation at their core (CG) compared to their periphery. In these areas (core) there were fast and organized activity and when moving to the HDFAs' periphery the DF organisation reduced significantly (multiple peaks at the electrograms'

spectrum) probably due to the collision of uncoordinated fibrillatory waves. The outcomes of this research provide further insight into potential mechanisms behind persAF (Chapter 4, Appendix and (Salinet Jr *et al.*, 2011b, Salinet Jr *et al.*, 2012a, Salinet Jr *et al.*, 2012d, Salinet Jr *et al.*, 2013d).

7.3. FUTURE RESEARCH OPPORTUNITIES

The outcomes obtained throughout this Thesis open the opportunity for developing new, exciting research. Some of the suggestions below are already being started by the current researchers from the group (including myself) and other opportunities might be considered for a newly awarded PhD student position.

7.3.1. PHASE ANALYSIS

The progression state of the depolarisation/repolarisation cycle from the myocardium cells are directly related with the phases of the APs (Umapathy *et al.*, 2010). Mapping the phase over time has been shown as an effective method for analysing the spatio-temporal behaviour during fibrillation (Gray *et al.*, 1998, Samie *et al.*, 2001, Bray and Wikswo, 2002, Rogers, 2004, Umapathy *et al.*, 2010, Pandit and Jalife, 2013). According to the investigators, the phase distribution changes over time depending on activation patterns and observation of the different phase patterns will contribute to the understanding of the fibrillatory dynamics and possibly clarify some of the AF mechanisms.

Also, identifying locations in the atria where the phase progresses through a complete cycle from $-\pi$ to π is of great interest in fibrillation. At these points, the phase becomes indeterminate and the activation wave fronts hinge on these points and rotate around them in an organized fashion forming re-entrant circuits (Samie *et al.*, 2001, Umapathy *et al.*, 2010, Pandit and Jalife, 2013). These points are called phase singularity (PS) points in the phase map.

Phase analysis with automatic identification of PS points on high density of simultaneous electrograms recorded during AF in persAF patients will allow better

understanding of the role of PS points and their organisation during AF, such as, correlation of wave breaks with PS points and their spatio-temporal propagation behaviour. Using this tool we will be able to identify AF triggers and propagation paths which could be compared with the current outcomes obtained with the DF spatio-temporal analysis.

The 3D endocardium surface can be colour-coded according to its phase. An example is shown in Figure 7.1 where the 3D surface is presented with two distinct orientations. The positions on the 3D with phase $-\pi$ receive black and $+\pi$ is white. Its respective 2D map (on the flat 32×64 matrix) is also presented giving the possibility to observe the entire surface area. The two marks on the 2D plot are PS points. The phase analysis was carried out by firstly performing zero-mean normalization. It was followed by identifying the imaginary part of the AEG signals after applying the Hilbert transform. Finally, the inverse tangent between surrogate signal and its AEG electrogram after zero-mean normalization allow generating the AF phase mapping.

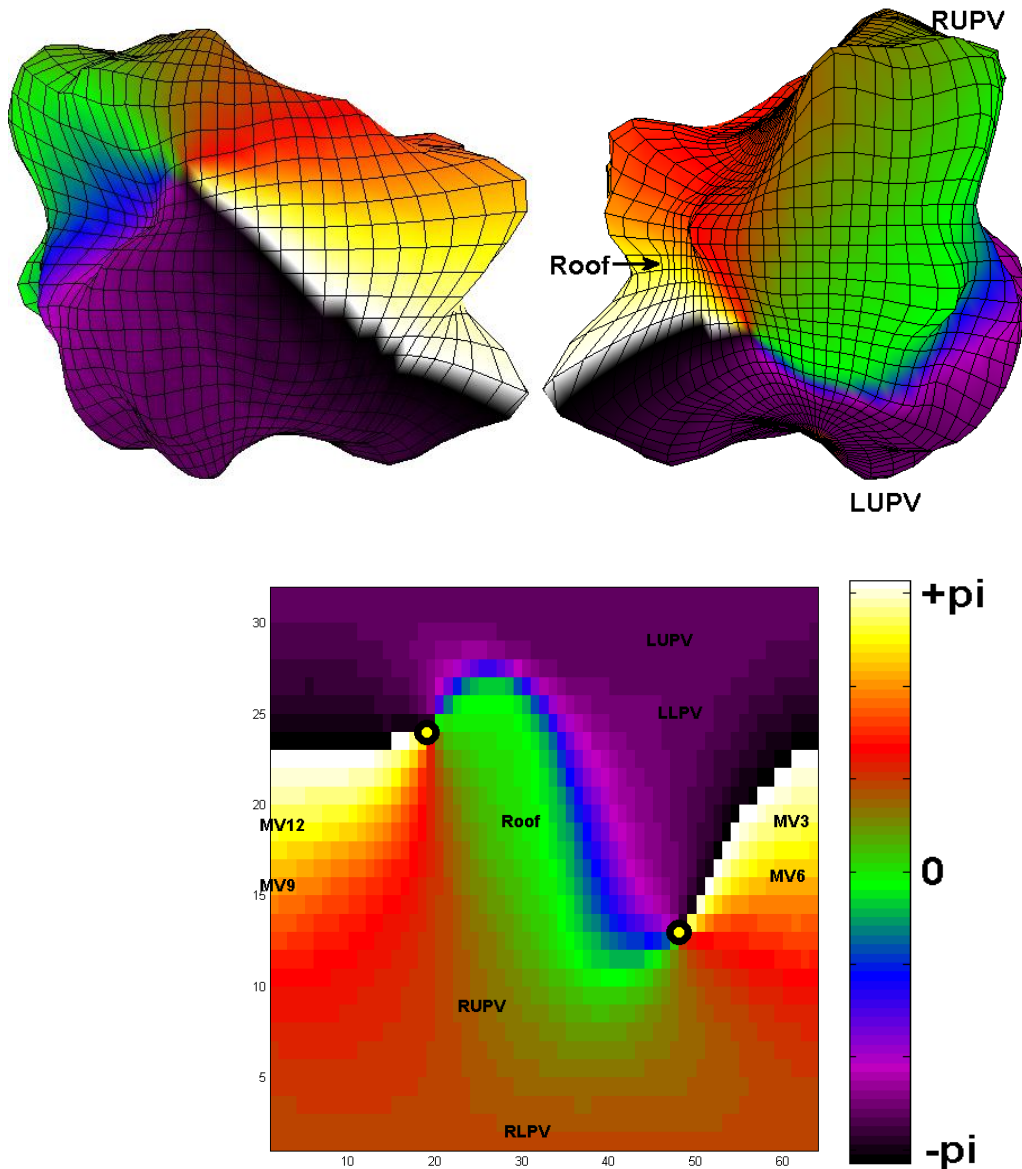


FIGURE 7.1 Colour code representation of the LA according to the phase analysis on the AEGs calculated using Hilbert Transform.

7.3.2. REAL TIME DF ABLATION IN PERSISTENT AF PATIENTS

A research investigation using NCM has been approved by the Ethical Committee of the University of Leicester where a Medical Doctor Research fellow will be performing catheter ablation in persAF. This new project will provide data from both atria mapped using the EnSite array. Additionally, Body Surface Potential Maps

(BSPM) will be recorded with a 128-electrode ActiveTwo system (BioSemi, Amsterdam, Netherlands). Invasive and non-invasive analysis will be performed simultaneously before, during and after the ablation procedure. Prior to the procedure, 3D DF maps of the atria will be generated and the areas of highest DF will be analysed. The ablation strategy in each patient will consider the 3D frequency maps and also time domain voltage maps currently used to guide ablation.

This new project provides many opportunities for further studying the clinical impact of DF mapping. The analysis of DF maps throughout the procedure will increase knowledge about the relation between DF and the mechanisms behind AF indicating possible areas for treatment which would be best for a specific AF patient. Alternatively, if a direct relation between ablating high DF regions and the reduction of AF sources is found, that will provide further evidence that DF mapping is an important tool for persAF patients' treatment and should be considered to improve success rates.

Besides this, by mapping both atria, knowledge can be gained regarding the effects of AF in one atrium on the other atrium. Since current research has focussed mainly on the LA, dual atrial mapping might give indications of high-DF sources in the RA, or interconnectivity between DF regions in both atria.

Lastly, by combining invasive and non-invasive data, the correlation of DF maps on the body surface and heart cavity can be investigated. Recent research has shown that there is a good correlation between both maps when directly compared (Guillem *et al.*, 2013). This project can further enhance this aspect. Additionally, after performing an inverse solution from BSPMs to epicardial data, this inverse solution and the endocardial map provided by the EnSite data can be compared to show the

correlation between endocardial and epicardial DF maps. This can again improve knowledge about the transmural propagation of AF signals.

7.3.3. THREE-DIMENSIONAL COMPLEX FRACTIONATED ATRIAL ELECTROGRAMS (3D CFAE MAPS)

A study proposed by Nademanee and colleagues (Nademanee *et al.*, 2004) showed that ablation of areas identified with complex fractionated electrical activity (CFAE) suppressed the arrhythmia, being effective in both acute termination of AF and maintenance of sinus rhythm (Nademanee, 2011). It is that still not a clear whether this ultra-rapid activity results from areas of abnormal conduction, rotors, neural activity or micro rotors (Crandall *et al.*, 2009).

Since CFAEs are defined as very low-amplitude electrograms with high-frequency (Nademanee *et al.*, 2004), current definitions of CFAEs rely on contact bipolar mapping techniques where several different 'subjective' CFAEs definitions have been proposed in the attempt of optimizing CFAEs mapping (Nademanee *et al.*, 2004, Monir and Pollak, 2008, Nademanee *et al.*, 2008, Porter *et al.*, 2008, Roux *et al.*, 2008, Verma *et al.*, 2008, Solheim *et al.*, 2010). However, our research group recently observed that applying distinct definitions results in different CFAE detections and consequently different results affecting both ablation strategies and outcome (Almeida *et al.*, 2013a).

This ongoing research has been investigating the current different definitions of CFAEs generated through 3D CFAE mapping tool and comparing these with successful ablated CFAE sites relating both with the CFAE definition and atrium subtract.

7.3.4. WAVELET TRANSFORM: ANALYSIS OF NONSTATIONARY SIGNALS

A study involving more advanced methods such as Wavelet analysis allows us to perform time and frequency domain analysis and has become a powerful tool for analysis of non-stationary AF signals recorded in patients with AF (Houben *et al.*, 2010, Zhao *et al.*, 2013). Briefly, wavelet technique is an approach able to decompose and describe other functions in frequency domain, so that we can analyse these signals in different frequency ranges and time providing a more sophisticated manner than the Fourier methods based on sine waves.

In wavelet transform, the base function used for the decomposition is called mother wavelet. The analysis of the different windows is performed by varying the scale of the mother wavelet function and translating it in time. The wavelet transform provides a significant advantage on analysis of discontinuities when compared to the Fourier transform and the STFT (Short Time Fourier Transform). This approach allows decomposing the signal into spectral components on the scales of the mother wavelet function, and also identifying the temporal location of high frequency components, even with low amplitude. In other words, wavelet transform allows determining not only "what are" the frequency components, but also "when" these frequencies occur.

The use of Wavelets on the high density simultaneous AEGs will allow investigating the time-frequency characteristics during persAF. We believe that this technique will help us to understand the fibrillatory dynamics and possibly clarify some of the AF mechanisms, even when fractionated electrograms are considered (Houben *et al.*, 2010).

7.3.5. NONLINEAR ANALYSIS IN ATRIAL FIBRILLATION

The use of linear modelling techniques employed in the majority of AF studies neglects the possible presence of nonlinear components which may have a clinical impact (Alcaraz and Rieta, 2008, Diaz et al., 2008). Nonlinear analysis on epicardial AF signals evidenced an underlying non-linear mechanism for each different AF type (Hoekstra et al., 1995). In addition, nonlinear spatiotemporal interactions and changing characteristics of nonlinear parameters were observed by Mainardi et al. (Mainardi LT et al., 2001) and Censi et al. (Censi et al., 2000).

Objective measures of disorganisation ('fractionation') of AF signals, in special CFAE, throughout non-linear techniques can potentially allow investigators to study the irregular dynamics present in AF electrograms and identify organisation of electrograms during AF and identify possible CFAE sites. We have recently initiated non-linearity studies on AEGs recorded in persAF patients (Salinet Jr *et al.*, 2012c, Almeida *et al.*, 2013b). In these studies two distinct Entropy measurements (Approximate entropy and Negative entropy) were applied to explore signal complexity and gaussianity. Further investigation using the above methods and possibly other non-linear techniques might allow quantification of CFAEs by objectively measuring the organisation of electrograms during AF.

APPENDIX

Spatiotemporal Characteristics of DF Organisation during Sequential Mapping

This study aimed to investigate the spectral property of electrical signals assessing spatio-temporal characteristics of the organisation index (OI) of DF areas during persAF. Part of this study was published at (Salinet Jr *et al.*, 2013c).

Methods:

3D DF and OI maps

DF and OI were calculated for the 2048 simultaneous AEGs over 20 s (windows of 4s with 50% overlap) after QRST subtraction (see section 1.5.7 for OI definition, Chapter 2 for the 3D DF and 3D OI maps and Chapter 3 for ventricular cancellation on the AEG signals). Briefly, OI is calculated by dividing the area under the DF and its harmonics by the total area of the AF spectrum range (see Figure 1 for illustration). The higher the OI the more organized the AF signal is. This index allows investigators to identify how 'dominant' the DF is across the whole AF spectrum.

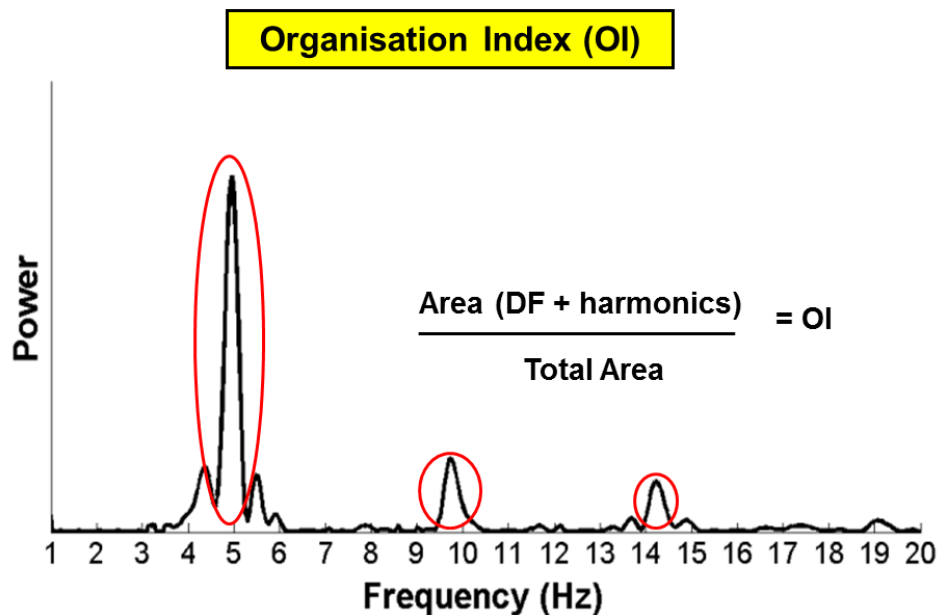


Figure 1 Spectrum of an AF electrogram showing the DF and its harmonics. The OI is calculated by dividing the area of the DF and its harmonics by the total area of the AF spectrum range (see section 1.5.7 Dominant Frequency ‘Organisation’ Indices for more details).

Once calculated the DF and its respective OI for each simultaneous point, sequential 3D DF and OI maps were obtained. The atrial electrogram’s DF for each segment along time is colour coded on the atrium 3D surface according to the frequency value. The OI maps were generated by the similar principle with the same colours range (purple for lower DF/OI values and dark-red for higher) (see Figure 2).

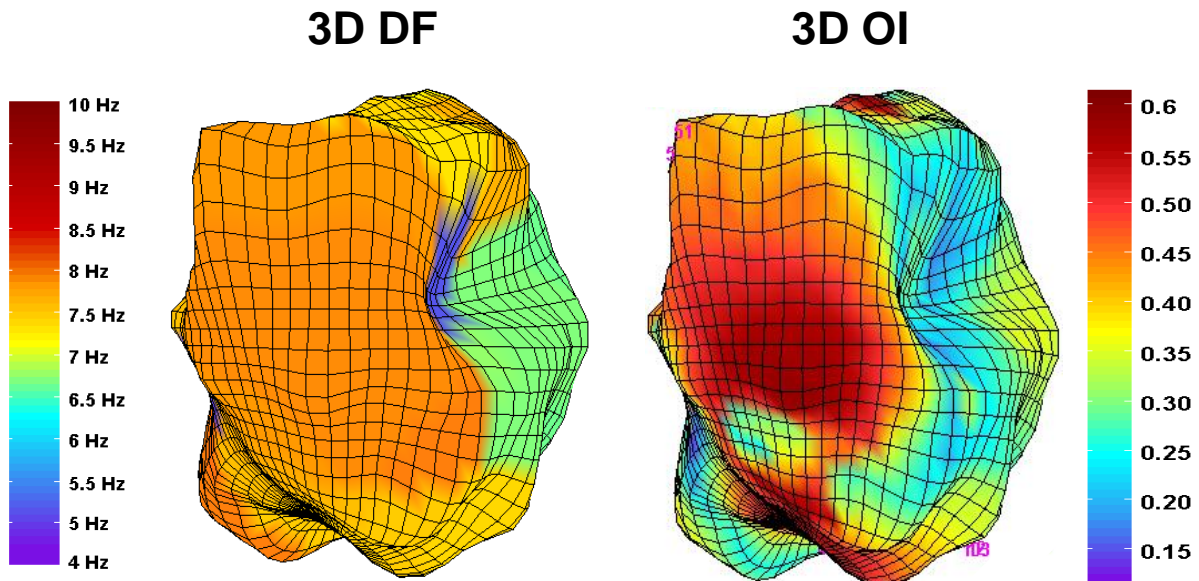


Figure 2 Example of a 3D DF map with its respective 3D OI map. The OI values were obtained according to Equation 1.5 and illustrated in Figure 1. Both maps were generated simultaneously using the same colours range.

Spatiotemporal Analysis

Once the 3D DF maps and their correspondent 3D OI maps were generated, the DF and OI spatio-temporal characteristics were investigated further. The spatio-temporal analysis focused in testing if HDFAs consistently present higher organisation (HOIAs). That was followed by investigating the temporal stability of the OI points to see if the behaviour is similar as evidenced by the DF lack of temporal stability (Chapter 4, section Temporal Stability Analysis).

Organisation Analysis

For each sequential DF map, the HDFAs were identified with its boundary defined as where DF drops 0.25 Hz from maximum (see Chapter 4 for more details). Its CG was

then found. The mean OI at the CG of the HDFA (OI_{CG}) was compared with the mean OI at periphery (OI_{Per}) (see Figure 3). To calculate the OI_{CG} , 25 points were considered (CG point in black plus its 24 neighbours in light green) and for the OI_{Per} all points at the entire boundary were chosen.

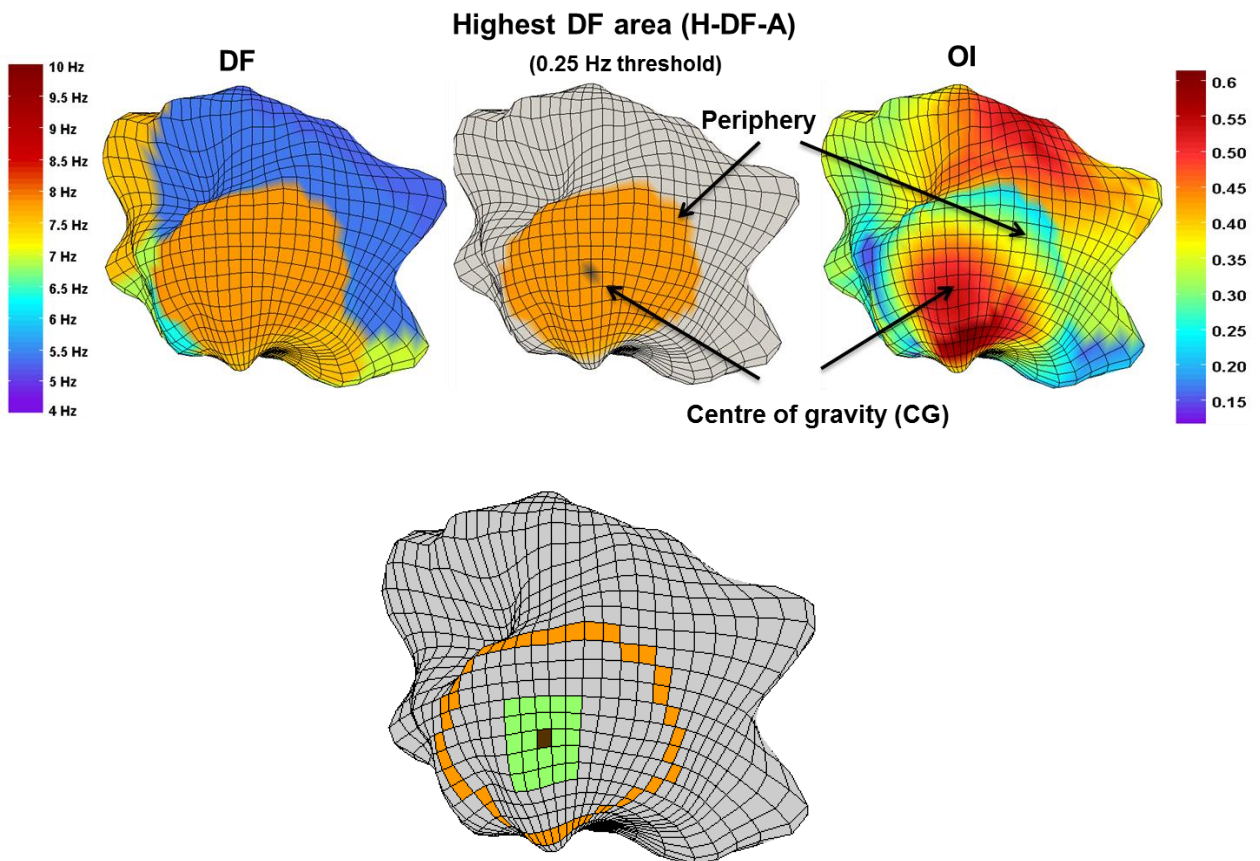


Figure 3 3D DF and OI maps focusing on the HDFAs identification. (left-hand side) 3D representation including the mapping of the DFs. (middle) The region with the HDFA is identified. (right-hand side) DF organisation from the HDFA showing that the OI at the core has a higher organisation when compared with its periphery. To calculate the OI_{CG} 25 points were selected: CG point in black and its 24 neighbours in light green. For OI_{Per} all points at boundary of the highest DF area were selected.

Statistics

All continuous variables are expressed as mean \pm standard deviation. Normally distributed data were analysed using paired and unpaired Student's t-test.

Results

Spatiotemporal Analysis

HDFAs did not bear consistent spatial relationship with highest OI. A typical example summarising the two different cases observed are presented in Figure 4. On the left-hand side, HDFA (dark orange) presents higher DF organisation when compared with the remaining DF areas of the 3D DF frame. Looking inside of the HDFA we could observe that part of this area presents even higher DF organisation. In contrast, case 2 shows that the HDFA presented much lower organisation when compared with the remaining areas. In Figure 4 (right-hand side) the HDFA (orange) presents lower OI followed by a slight intra DF gradient where the lower DF-value cloud (green) presented DF organisation.

The temporal stability analysis of the sequential 3D maps revealed that as DF (results from Chapter 4) the OI also lack temporal stability. Figure 5 presents data showing that the percentage of stable DF and OI decreased over time with a time constant of 3.04 s and 2.37 s respectively. Table 1 presents the population's time constant decay for both DF (τ_{DF}) and OI (τ_{OI}).

Table 1 Overall DF and OI temporal stability (time constant)

	τ_{DF}^*	τ_{OI}^{**}
Mean	3.04\pm1.29	2.37\pm0.50

*** 0.25 Hz threshold; ** 0.1 threshold**

Case 1: H-DF-A correspond to a H-OI-A

Case 2: H-DF-A does not correspond to a H-OI-A

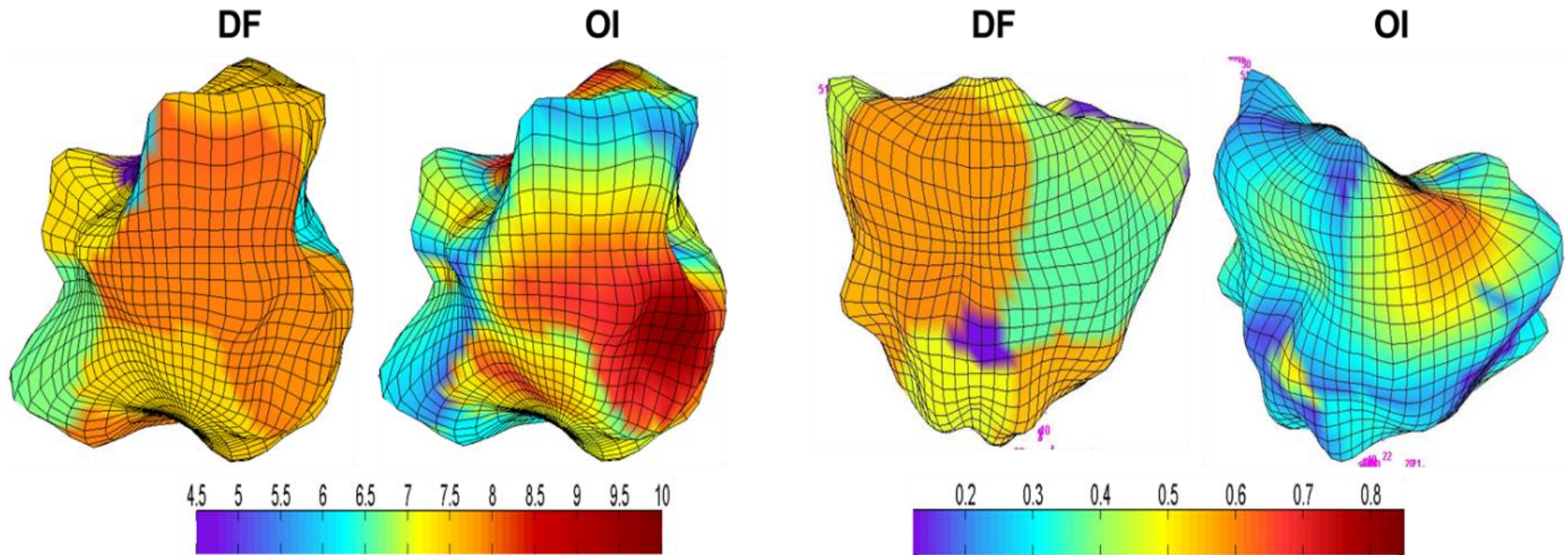


Figure 4 "H-DF-As correspond to Highest Dominant Frequency Areas". H-DF-As did not bear consistent spatial relationship with highest OI. (left-hand side) Case 1: HDFA (dark orange) presents higher DF organisation when compared with the remaining DF areas of the 3D DF frame. Looking inside of the HDFA there is a small area presenting even higher DF organisation. (right-hand side) HDFA (orange) presents lower OI but next to this area there is slight lower DF-value cloud (green) presenting much higher DF organisation.

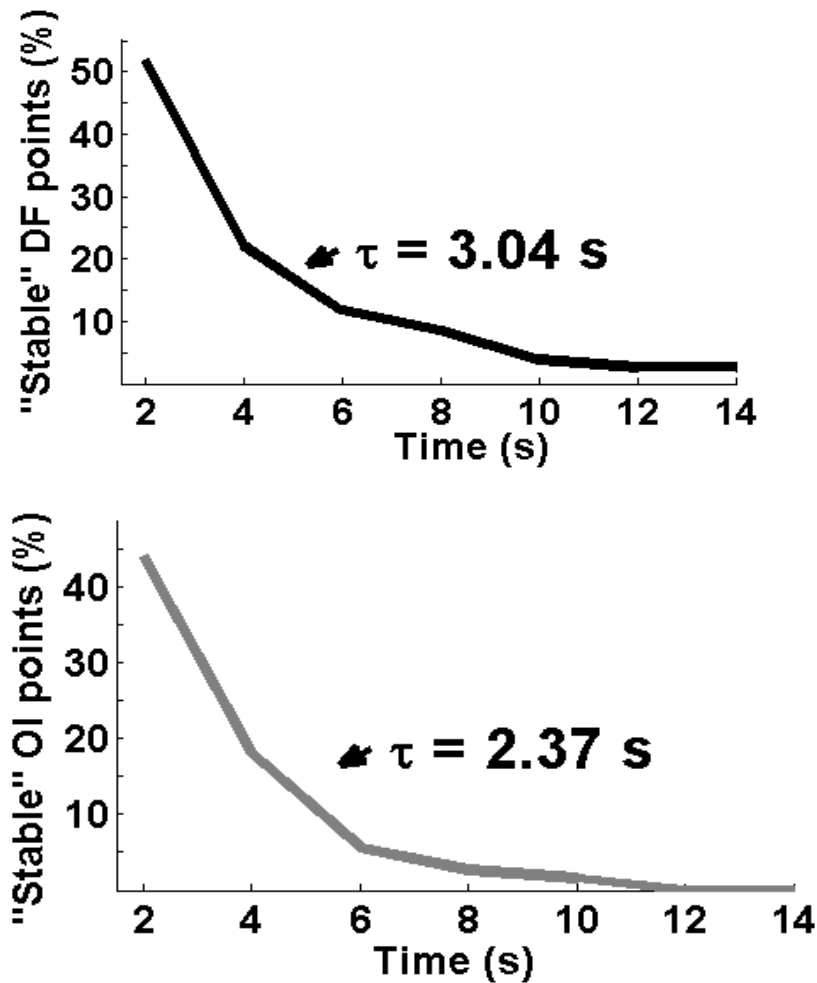


Figure 5 Percentage of stable DF and OI points over time. It can be observed that the number of stable DF and OI points out of 2048 AEGs decreases with time in an exponential pattern with time constants of 3.04 s and 2.37 s respectively for 0.25 Hz and 0.1 thresholds.

Organisation Analysis

Sites with highest DF showed a greater degree of organisation at their core (CG) compared to their periphery. Figures 6 and 7 illustrate two typical examples of 3D DF and OI frames highlighting this behaviour. In figure 6 two distinct points were selected (one at the core and other at the periphery) and the respective electrograms and spectrum presented. Although the DF at the core (CG) is similar when compared

with the periphery (8 Hz vs. 8.1 Hz), the DF organisation at the periphery is considerable lower (0.23 vs. 0.53). Similarly, Figure 7 shows that the DFs at the core and periphery are equal (7.8 Hz), but the DF organisation 0.58 and 0.31 respectively.

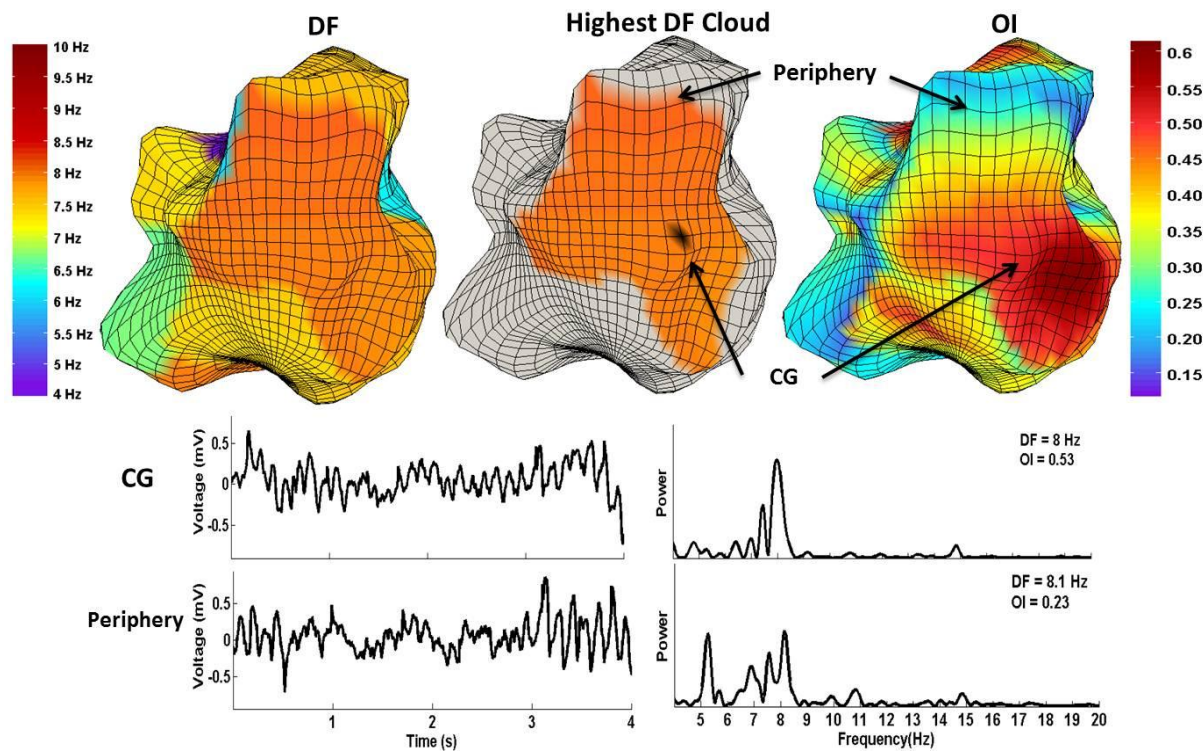


Figure 6 DF and OI mapping focusing on the HDFA identification. (left-hand side) 3D representation including the mapping of the DFs. (middle) The region with the HDFA is identified. (right-hand side) DF organisation from the HDFA shows that the OI at the core has a higher organisation when compared with its periphery. The electrogram of a point at the core and its spectrum are also presented and compared with a point at the periphery.

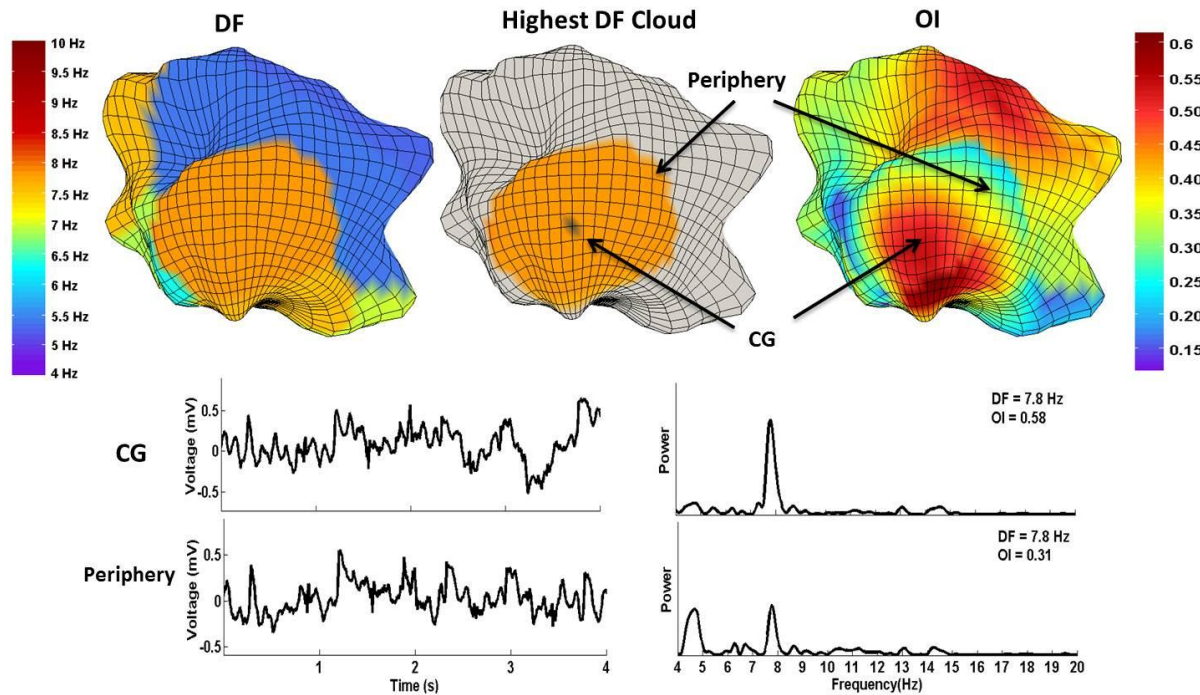


Figure 7 Another typical example showing the HDFA with a greater degree of organisation at the core (CG) compared to its periphery.

The analysis was expanded to the remaining persAF patients (total of 72 sequential 3D maps analysed). The OI_{CG} and OI_{Per} for each patient are presented in Table 2. The mean OI_{CG} and OI_{Per} of the population was 0.43 ± 0.17 and 0.36 ± 0.10 respectively ($p=0.0061$), CI [0.0186 0.1095], 95% confidence level. The mean cloud size of the HDFAs around $12.2 \pm 5.2\%$ of the entire LA surface.

Table 2 Degree of DF organisation at their core (OI_{CG}) vs. at the periphery (OI_{PER})

	OI_{CG}	OI_{Per}
Patient 1	0.40	0.35
Patient 2	0.38	0.31
Patient 3	0.37	0.35
Patient 4	0.52	0.41
Patient 5	0.36	0.30
Patient 6	0.56	0.53
Patient 7	0.48	0.36
Patient 8	0.35	0.27
Mean	0.43 ± 0.17	0.36 ± 0.10

Conclusions

Our results showed that areas of high DF and OI are not spatially consistent. Two typical cases were identified showing that in some cases HDFAs matched with HOIAs and in others they did not (HOIAs matched with areas of lower frequencies). As noticed for DF, the relevant OI areas are not spatio-temporally stable. More importantly, sites with highest DF showed a greater degree of organisation at their core (CG) compared to their periphery. This provides further insight into the potential mechanisms of persAF areas where regular, fast and organized activity was found at the core of the HDFAs and when moving to the HDFAs' periphery the DF organisation reduced significantly (multiple peaks at the electrograms' spectrum) probably due to collision of uncoordinated fibrillatory waves. This is consistent with the presence of dynamic HDFAs activity triggering AF with fibrillatory conduction at its boundary.

REFERENCES

- ABED, H. S., SAMUEL, C. S., LAU, D. H., KELLY, D. J., ROYCE, S. G., ALASADY, M., MAHAJAN, R., KUKLIK, P., ZHANG, Y., BROOKS, A. G., NELSON, A. J., WORTHLEY, S. G., ABHAYARATNA, W. P., KALMAN, J. M., WITTERT, G. A. & SANDERS, P. (2013) Obesity results in progressive atrial structural and electrical remodeling: Implications for atrial fibrillation. *Heart rhythm : the official journal of the Heart Rhythm Society*, 10, 90-100.
- AFA, A. F. A. (2010) Patient Information: What is Atrial Fibrillation? (<http://www.atrialfibrillation.org.uk/patient-information/atrial-fibrillation.html>). Chew Magna, Bristol, UK Atrial Fibrillation Association
- AHMAD, A. (2011) Dominant Frequency Estimation for Atrial Fibrillation Studies (PhD Thesis). *Department of Engineering*. Leicester, University of Leicester.
- AHMAD, A., SALINET JR, J. L., BROWN, P., TUAN, J. H., STAFFORD, P., NG, G. A. & SCHLINDWEIN, F. S. (2011) QRS subtraction for atrial electrograms: flat, linear and spline interpolations. *Medical and Biological Engineering and Computing*, 49, 1321-1328.
- AHMED, H. & REDDY, V. Y. (2009) Technical advances in the ablation of atrial fibrillation. *Heart Rhythm*, 6, S39-S44.
- AKAIKE, H. (1974) A new look at the statistical model identification. *IEEE Transactions on Automatic Control*, 19, 713-723.
- ALCARAZ, R. & RIETA, J. J. (2008) Wavelet bidomain sample entropy analysis to predict spontaneous termination of atrial fibrillation *Physiological Measurement*, 29, 65-80.
- ALLOT, E., HAISSAGUERRE, M. & JACKMAN, W. M. (2008) Catheter ablation of atrial fibrillation. Oxford, UK, Blackwell Publishing Ltd.
- ALLOT, E. & RUSKIN, J. N. (2008) Controversies in ablation of atrial fibrillation. *European Heart Journal* 10 (Supplement H):H32-H54.
- ALLESSIE, M. A., BONKE, F. I. & SCHOPMAN, F. J. (1977) Circus movement in rabbit atrial muscle as a mechanism of tachycardia. The "leading circle" concept: a new model of circus movement in cardiac tissue without the involvement of an anatomical obstacle. *Circulation Research* 41:9-18.
- ALMEIDA, T. P., SALINET JR, J. L., CHU, G., NG, G. A. & SCHLINDWEIN, F. S. (2013a) Different definitions of complex fractionated atrial electrograms do not concur with clinical perspective. *Computing in Cardiology (Computers in Cardiology)*. Zaragoza, Spain. To be published in September.
- ALMEIDA, T. P., SALINET JR, J. L., CHU, G., TUAN, J. H., SCHLINDWEIN, F. S. & NG, G. A. (2013b) Atrial electrogram complexity as an objective measurement of fractionation during atrial fibrillation. *Heart Rhythm* 10:S2.
- ANDRIKOPOULOS, G., TZEIS, S., MANIADAKIS, N., MAVRAKIS, H. E. & VARDAS, P. E. (2009) Cost-effectiveness of atrial fibrillation catheter ablation. *Europace* 11:147-151.
- ANTZELEVITCH, C., BURASHNIKOV, A. & DIEGO, J. M. D. (2008) Mechanism of cardiac arrhythmia IN GUSSAK, I. & ANTZELEVITCH, C. (Eds.) *Electrical diseases of the heart*. London, Springer.
- ARORA, S., MOOKADAM, F. & SRIVATHSAN, K. (2010) Interventional management of atrial fibrillation. *Expert Review of Cardiovascular Therapy* 8:949-958.
- ASSIS, A. K. T. (2010) *Archimedes, the center of gravity, and the first law of mechanics*, Montreal, C. Roy Keys Inc.
- ATIENZA, F., ALMENDRAL, J., JALIFE, J., ZLOCHIVER, S., PLOUTZ-SNYDER, R., TORRECILLA, E. G., ARENAL, A., KALIFA, J., FERNANDEZ-AVILES, F. & BERENFELD, O. (2009) Real-time dominant frequency mapping and ablation of dominant frequency sites in atrial fibrillation with left-to-right frequency gradients predicts long-term maintenance of sinus rhythm. *Heart Rhythm* 6:33-40.
- BARO, I. & ESCANDE, D. (2008) Basic Physiology of Ion Channel Function. IN GUSSAK, I. & ANTZELEVITCH, C. (Eds.) *Electrical Diseases of the Heart*. London, Springer.

- BASSO, C., HO, S. Y. & THIENE, G. (2008) Anatomic and histopathological characteristics of the conductive tissues of the heart. IN GUSSAK, I. & ANTZELEVITCH, C. (Eds.) *Electrical diseases of the heart*. London, Springer.
- BERENFELD, O., ENNIS, S., HWANG, E., HOOVEN, B., GRZEDA, K., MIRONOV, S., YAMAZAKI, M., KALIFA, J. & JALIFE, J. (2011) Time and frequency domains analyses of atrial fibrillation activation rate: the optical mapping reference. *Heart Rhythm* 8:1758-1765.
- BERENFELD, O., KALIFA, J. & JALIFE, J. (2008) Mechanisms of atrial fibrillation in animals and humans. IN ALIOT, E., HAISSAGUERRE, M. & JACKMAN, W. M. (Eds.) *Catheter ablation of atrial fibrillation*. Oxford, Blackwell Publishing.
- BIKTASHEV, V. N. (1997) Control of re-entrant vortices by electrical stimulation. IN ALEXANDER V. PANFILOV, A. V. H. (Ed.) *Computational biology of the heart*. Chichester, John Wiley & Sons Ltd.
- BOLLMANN, A. & LOMBARDI, F. (2006) Electrocardiology of atrial fibrillation: Current knowledge and future challenges. *IEEE Engineering in Medicine and Biology* 25:15-23.
- BOTTERON, G. & SMITH, J. (1996) Quantitative assessment of the spatial organization of atrial fibrillation in the intact Human heart. *Circulation* 93:513-518.
- BRAY, M. A. & WIKSWO, J. P. (2002) Considerations in phase plane analysis for nonstationary reentrant cardiac behavior. *Physical Review. E, Statistical, Nonlinear, and Soft Matter Physics* 65:1-8.
- BROERSEN, P. M. & WENSINK, H. E. (1993) On Finite Sample Theory for autoregressive model order selection. *IEEE Transactions on Signal Processing* 41:194-204.
- BROOKS, A. G., KUKLIK, P. & SANDERS, P. (2009) Frequency mapping: Hype or hope? *Heart Rhythm Society* 6:41-43.
- BROOKS, A. G., STILES, M. K., LABORDERIE, J., LAU, D. H., KUKLIK, P., SHIPP, N. J., HSU, L. F. & SANDERS, P. (2010) Outcomes of long-standing persistent atrial fibrillation ablation: a systematic review. *Heart Rhythm* 7:835- 846.
- BURKHARDT, J. D. & NATALE, A. (2009) New technologies in atrial fibrillation ablation. *Circulation* 120:1533-1541.
- CALKINS, H., BRUGADA, J., PACKER, D. L., CAPPATO, R., CHEN, S.-A., CRIJNS, H. J. G., DAMIANO, R. J., DAVIES, D. W., HAINES, D. E., HAISSAGUERRE, M., IESAKA, Y., JACKMAN, W., JAIS, P., KOTTKAMP, H., KUCK, K. H., LINDSAY, B. D., MARCHLINSKI, F. E., MCCARTHY, P. M., MONT, J. L., MORADY, F., NADEMANEE, K., NATALE, A., PAPPONE, C., PRYSTOWSKY, E., RAVIELE, A., RUSKIN, J. N., SHEMIN, R. J., HEART RHYTHM SOCIETY, EUROPEAN HEART RHYTHM ASSOCIATION, EUROPEAN CARDIAC ARRHYTHMIA SOCIETY, AMERICAN COLLEGE OF CARDIOLOGY, AMERICAN HEART ASSOCIATION, SOCIETY OF THORACIC SURGEONS(2007) HRS/EHRA/ECAS expert consensus statement on catheter and surgical ablation of atrial fibrillation: recommendations for personnel, policy, procedures and follow-up. *Europace* 9(6):335-379.
- CALKINS, H., REYNOLDS, M. R., SPECTOR, P., SONDHI, M., XU, Y., MARTIN, A., WILLIAMS, C. J. & SLEDGE, I. (2009) Treatment of atrial fibrillation with antiarrhythmic drugs or radiofrequency ablation: two systematic literature reviews and meta-analyses. *Circulation* 2:349-361.
- CENSI, F., BARBARO, V., BARTOLINI, P., CALCAGNINI, G., MICHELUCCI, A., GENSINI, G. F. & CERUTTI, S. (2000) Recurrent patterns of atrial depolarization during atrial fibrillation assessed by recurrence plot quantification. *Annals of Biomedical Engineering* 28:61-70.
- CHINITZ, L. A. & SETHI, J. S. (2006) How to perform noncontact mapping. *Heart Rhythm* 3:120-123.
- CHRISTOPHER PIORKOWSKI & HINDRICKS, G. (2009) Principles of NavX Mapping. In MOHAMMAD SHENASA, GERHARD HINDRICKS, MARTIN BORGGREFE & BREITHARDT, G. (Eds.) *Cardiac mapping*. Third Edition ed. , Blackwell Publishing.
- CHUGH, S. S., BLACKSHEAR, J. L., SHEN, W.-K., HAMMILL, S. C. & GERSH, B. J. (2001) Epidemiology and natural history of atrial fibrillation: clinical implications. *Journal of the American College of Cardiology* 37:371-378.
- CONDITIONS, N. C. C. F. C. (2006) Atrial fibrillation: national clinical guideline for management in primary and secondary care. London, Royal College of Physicians.
- CONNOLLY, S. J. (2011) Atrial fibrillation in 2010: advances in treatment and management. *Nature Reviews Cardiology* 8:67-68.
- COOLEY, J. W., LEWIS, P. A. W. & WELCH, P. D. (1969) The fast fourier transform and its applications. *IEEE Transactions on Education* 12:27-34.

- COX, J. L., BOINEAU, J. P., SCHUESSLER, R. B., FERGUSON, T. B. J., CAIN, M. E., LINDSAY, B. D., CORR, P. B., KATER, K. M. & LAPPAS, D. G. (1991) Successful surgical treatment of atrial fibrillation. Review and clinical update. *Journal of the American Medical Association* 266:1976-1980.
- COX, J. L., SCHUESSLER, R. B. & BOINEAU, J. P. (2000) The development of the Maze procedure for the treatment of atrial fibrillation. *Seminars in Thoracic and Cardiovascular Surgery* 12:2-14.
- CRANDALL, M. A., BRADLEY, D. J., PACKER, D. L. & ASIRVATHAM, S. J. (2009) Contemporary management of atrial fibrillation: update on anticoagulation and invasive management strategies. *Mayo Clinic Proceedings* 84:643-662.
- CRAWFORD, T. (2011) Left atrial diastolic dysfunction: a new complication after catheter ablation for atrial fibrillation? *Heart Rhythm* 8:1372-1373.
- CUCULICH, P. S., WANG, Y., LINDSAY, B. D., FADDIS, M. N., SCHUESSLER, R. B., DAMIANO, R. J., LI, L. & RUDY, Y. (2010) Noninvasive characterization of epicardial activation in humans with diverse atrial fibrillation patterns / clinical perspective. *Circulation* 122:1364-1372.
- DE GROOT, N. M. S., HOUBEN, R. P. M., SMEETS, J. L., BOERSMA, E., SCHOTTEN, U., SCHALIJ, M. J., CRIJNS, H. & ALLESSIE, M. A. (2010) Electropathological substrate of longstanding persistent atrial fibrillation in patients with structural heart disease / clinical perspective. *Circulation* 122:1674-1682.
- DIAZ, J., GONZALEZ, C., ESCALONA, O., GLOVER, B. M. & MANOHARAN, G. (2008) Nonlinear analysis of the ECG during atrial fibrillation in patients for low energy internal cardioversion. *Engineering in Medicine and Biology Society. 30th Annual International Conference of the IEEE (EMBS)*.
- DINIZ, P. S. R., DA SILVA, E. A. B. & NETTO, S. L. (2010) Spectral estimation. *Digital signal processing: system analysis and design*. 2nd ed. Cambridge, Cambridge University Press.
- EARLEY, M. J., ABRAMS, D. J. R., SPORTON, S. C. & SCHILLING, R. J. (2006) Validation of the noncontact mapping system in the left atrium during permanent atrial fibrillation and sinus rhythm. *Journal of the American College of Cardiology* 48:485-491.
- ELAYI, C. S., DI BIASE, L., BARRETT, C., CHING, C. K., AL ALY, M., LUCCIOLA, M., BAI, R., HORTON, R., FAHMY, T. S., VERMA, A., KHAYKIN, Y., SHAH, J., MORALES, G., HONGO, R., HAO, S., BEHEIRY, S., ARRUDA, M., SCHWEIKERT, R. A., CUMMINGS, J., BURKHARDT, J. D., WANG, P., AL-AHMAD, A., CAUCHEMEZ, B., GAITA, F. & NATALE, A. (2010) Atrial fibrillation termination as a procedural endpoint during ablation in long-standing persistent atrial fibrillation. *Heart Rhythm* 7:1216-1223.
- ENCYCLOPEDIA, T. C. (2012a) Etruscan civilization. *The Columbia Encyclopedia* 6th ed ed.
- ENCYCLOPEDIA, T. C. (2012b) Indo-European Language. *The Columbia Encyclopedia* 6th ed ed.
- ETYMONLINE (2013) <http://www.etymonline.com/index.php?search=Right+atrium+of+the+heart>.
- EVERETT, T. & OLGIN, J. E. (2008) Signal processing of fibrillatory electrograms. IN ALIOT, E., HAISSAGUERRE, M. & JACKMAN, W. M. (Eds.) *Catheter ablation of atrial fibrillation*. Oxford, Blackwell Publishing.
- EVERETT, T. H., KOK, L., VAUGHN, R. H., MOORMAN, J. R. & HAINES, D. E. (2001) Frequency domain algorithm for quantifying atrial fibrillation organization to increase defibrillation efficacy. *IEEE Transactions on Biomedical Engineering* 48:969-978.
- FISCHER, G., STÜHLINGER, M. C., NOWAK, C. N., WIESER, L., TILG, B. & HINTRINGER, F. (2007) On computing dominant frequency from bipolar intracardiac electrograms. *IEEE Transactions on Biomedical Engineering* 54:165-169.
- FUSTER, V., RYDEN, L. E., CANNOM, D. S., CRIJNS, H. J., CURTIS, A. B., ELLENBOGEN, K. A., HALPERIN, J. L., LE HEUZEY, J.-Y., KAY, G. N., LOWE, J. E., OLSSON, S. B., PRYSTOWSKY, E. N., TAMARGO, J. L., WANN, S., ACC/AHA TASK FORCE, M., SMITH, S. C., JR., JACOBS, A. K., ADAMS, C. D., ANDERSON, J. L., ANTMAN, E. M., HUNT, S. A., NISHIMURA, R., ORNATO, J. P., PAGE, R. L., RIEGEL, B., ESC COMMITTEE FOR PRACTICE, G., PRIORI, S. G., BLANC, J.-J., BUDAJ, A., CAMM, A. J., DEAN, V., DECKERS, J. W., DESPRES, C., DICKSTEIN, K., LEKAKIS, J., MCGREGOR, K., METRA, M., MORAIS, J., OSTERSEPEY, A. & ZAMORANO, J. L. (2006) ACC/AHA/ESC 2006 Guidelines for the management of patients with atrial fibrillation--executive summary: a report of the american college of cardiology/american heart association task force on practice guidelines and the european society of cardiology committee for practice guidelines (writing committee to revise the 2001 guidelines for the management of patients with atrial fibrillation):

- developed in collaboration with the European Heart Rhythm Association and the Heart Rhythm Society. *Circulation* 114:700-752.
- GARREY, W. E. (1914) The nature of fibrillary contraction of the heart. Its relation to tissue mass and form. *American Journal of Physiology* 33:397-414.
- GO, A. S., HYLEK, E. M., PHILLIPS, K. A., CHANG, Y., HENAULT, L. E., SELBY, J. V. & SINGER, D. E. (2001) Prevalence of diagnosed atrial fibrillation in adults: national implications for rhythm management and stroke prevention: the anticoagulation and risk factors in atrial fibrillation (ATRIA) study. *The Journal of the American Medical Association* 285:2370-2375.
- GOJRATY, S., LAVI, N., VALLES, E., KIM, S. J., MICHELE, J. & GERSTENFELD, E. P. (2009) Dominant frequency mapping of atrial fibrillation: comparison of contact and noncontact approaches. *The Journal of Cardiovascular Electrophysiology* 20:997-1004.
- GORNICK, C. C., ADLER, S. W., PEDERSON, B., HAUCK, J., BUDD, J. & SCHWEITZER, J. (1999) Validation of a new noncontact catheter system for electroanatomic mapping of left ventricular endocardium. *Circulation* 99:829-835.
- GRAY, R. A., JALIFE, J. & PANFILOV, A. V. (1995) Mechanisms of cardiac fibrillation. *Science* 270:1222-1223.
- GRAY, R. A., PERTSOV, A. M. & JALIFE, J. (1998) Spatial and temporal organization during cardiac fibrillation. *Nature* 392:75-78.
- GUILLEM, M. S., CLIMENT, A. M., MILLET, J., ARENAL, A., FERNANDEZ-AVILES, F., JALIFE, J., ATIENZA, F. & BERENFELD, O. (2013) Noninvasive localization of maximal frequency sites of atrial fibrillation by body surface potential mapping. *Circulation: Arrhythmia and Electrophysiology* 6:294-301.
- HABEL, N., ZNOJKIEWICZ, P., THOMPSON, N., MULLER, J. G., MASON, B., CALAME, J., CALAME, S., SHARMA, S., MIRCHANDANI, G., JANKS, D., BATES, J., NOORI, A., KARNBACH, A., LUSTGARTEN, D. L., SOBEL, B. E. & SPECTOR, P. (2010) The temporal variability of dominant frequency and complex fractionated atrial electrograms constrains the validity of sequential mapping in human atrial fibrillation. *Heart Rhythm* 7:586-593.
- HAISSAGUERRE, M., JAIS, P., SHAH, D. C., TAKAHASHI, A., HOCINI, M., QUINIOU, G., GARRIGUE, S., LE MOUROUX, A., LE METAYER, P. & CLÉMENTY, J. (1998) Spontaneous initiation of atrial fibrillation by ectopic beats originating in the pulmonary veins. *New England Journal of Medicine* 339:659-666.
- HAISSAGUERRE, M., MARCUS, F. I., FISCHER, B. & CLEMENTY, J. (1994) Radiofrequency catheter ablation in unusual mechanism of atrial fibrillation: report of three cases. *Journal of Cardiovascular Electrophysiology* 5:743-751.
- HARRIS, F. (1978) On the use of windows for harmonic analysis with the discrete fourier transform. *Proceedings of the IEEE* 66:51-83.
- HEERINGA, J., VAN DER KUIP, D. A. M., HOFMAN, A., KORS, J. A., VAN HERPEN, G., STRICKER, B. H. C., STIJNEN, T., LIP, G. Y. H. & WITTEMAN, J. C. M. (2006) Prevalence, incidence and lifetime risk of atrial fibrillation: the Rotterdam study. *European Heart Journal* 27:949-953.
- HINDRICKS, G. & KOTTKAMP, H. (2001) Simultaneous noncontact mapping of left atrium in patients with paroxysmal atrial fibrillation. *Circulation* 104:297-303.
- HOEKSTRA, B. P., DIKS, C. G., ALLESSIE, M. A. & DEGOEDE, J. (1995) Nonlinear analysis of epicardial atrial electrograms of electrically induced atrial fibrillation in man. *Journal of Cardiovascular Electrophysiology* 6:419-440.
- HOLMQVIST, F., OLESEN, M. S., TVEIT, A., ENGER, S., TAPANAINEN, J., JURKKO, R., HAVMÅLLER, R., HAUNSA, S., CARLSON, J., SVENDSEN, J. H. & PLATONOV, P. G. (2011) Abnormal atrial activation in young patients with lone atrial fibrillation. *Europace* 13:188-192.
- HOUBEN, R. P. M., DE GROOT, N. M. S. & ALLESSIE, M. A. (2010) Analysis of fractionated atrial fibrillation electrograms by wavelet decomposition. *IEEE Transactions on Biomedical Engineering* 57:1388-1398.
- ILLANES-MANRIQUEZ, A. & ZHANG, Q. (2008) An algorithm for robust detection of QRS onset and offset in ECG signals. *Computing in Cardiology (Computers in Cardiology)* 857-860. *Bologna, Italy*.
- JAIS, P., HISSAGUERRE, M., SHAH, D. C., CHOUAIRI, S., GENCEL, L., HOCINI, M. & CLEMENTY, J. (1997) A focal source of atrial fibrillation treated by discrete radiofrequency ablation. *Circulation* 95:572-576.

- JALIFE, J., BERENFELD, O. & MANSOUR, M. (2002) Mother rotors and fibrillatory conduction: a mechanism of atrial fibrillation. *Cardiovascular Research* 54:204-216.
- JALIFE, J., BERENFELD, O., SKANES, A. & MANDAPATI, R. (1998) Mechanisms of atrial fibrillation: mother rotors or multiple daughter wavelets, or both? *Journal of Cardiovascular Electrophysiology* 9(8 Suppl):S2-12.
- JARMAN, J. W. E., WONG, T., KOJODJOJO, P., SPOHR, H., DAVIES, J. E., ROUGHTON, M., FRANCIS, D. P., KANAGARATNAM, P., MARKIDES, V., DAVIES, D. W. & PETERS, N. S. (2012) Spatiotemporal behaviour of high dominant frequency during paroxysmal and persistent atrial fibrillation in the human left atrium. *Circulation: Arrhythmia and Electrophysiology* 5(4):650-658.
- JARMAN, J. W. E., WONG, T., SPOHR, H., KOJODJOJO, P., DAVIES, D. W., FRANCIS, D. P., DAVIES, J. E., MARKIDES, V. & PETERS, N. S. (2006) The use of spectral analysis and noncontact mapping to study the impact of circumferential ablation on atrial fibrillation. *Heart Rhythm* 3 (P3-82):S204-S205
- JASON, N. G. & GOLDBERGER, J. J. (2007) Understanding and interpreting dominant frequency analysis of AF electrograms. *Journal of Cardiovascular Electrophysiology* 18:680-85.
- HING, J., WANG, P. J., AL-AHMAD, A. (2008) Electroanatomical mapping: an atlas for clinicians IN AL-AHMAD, A., CALLANS, D., HSIA, H. AND NATALE, A. (Ed.) *Electroanatomical mapping: an atlas for clinicians*. Blackwell Publishing.
- KADISH, A., HAUCK, J., PEDERSON, B., BEATTY, G. & GORNICK, C. (1999) Mapping of atrial activation with a noncontact, multielectrode catheter in dogs. *Circulation* 99:1906-1913.
- KAY, S. M. (1987) Autoregressive spectral estimation: methods. *Modern spectral estimation* New Jersey, Prentice-Hall.
- KAY, S. M. & MARPLE, S. L., JR. (1981) Spectrum analysis- a modern perspective. *Proceedings of the IEEE* 69:1380-1419.
- RAJAPPAN, K. & SCHILLING, R. J. (2009) Principles of noncontact endocardial cardiac mapping. IN SHENASA, M., HINDRICKS, G., BORGGREFE, M. & BREITHARDT, G. (Eds.) *Cardiac Mapping*. Third Edition ed., Blackwell Publishing.
- KIRCHHOF, P. & ECKARDT, L. (2010) Ablation of atrial fibrillation: for whom and how? *Heart* 96: 1325-1330.
- KIRK, D. B. & HWU, W.-M. W. (2010) *Programming massively parallel processors: a hands-on approach*, San Francisco, Elsevier.
- KODAMA, I., HONJO, H., DOBRZYNSKI, H. & BOYETT, M. R. (2004) Cellular mechanism of sinoatrial activity. IN JALIFE, J. & ZIPES, D. P. (Eds.) *Cardiac electrophysiology: from cell to bedside*. China, SAUNDERS.
- KRUMMEN, D. E., PENG, K. A., BULLINGA, J. R. & NARAYAN, S. M. (2009) Centrifugal gradients of rate and organization in human atrial fibrillation. *Pace-Pacing and Clinical Electrophysiology* 32:1366-1378.
- KUIJPERS, N. H. L., POTSE, M., VAN DAM, P. M., TEN EIKELDER, H. M. M., VERHEULE, S., PRINZEN, F. W. & SCHOTTEN, U. (2011) Mechanoelectrical coupling enhances initiation and affects perpetuation of atrial fibrillation during acute atrial dilation. *Heart rhythm* 8:429-436.
- LANGLEY, P., BOURKE, J. P. & MURRAY, A. (2000) Frequency analysis of atrial fibrillation. *Computing in Cardiology (Computers in Cardiology)* 65:68. Piscataway, NJ, USA.
- LAPAGE, M. J. & SAUL, J. P. (2011) Update on rhythm mapping and catheter navigation. *Current Opinion in Cardiology* 26:79-85.
- LARS ECKARDT & BREITHARDT, G. (2009) Construction and interpretation of endocardial maps: from basic electrophysiology to 3D mapping. IN MOHAMMAD SHENASA, GERHARD HINDRICKS, MARTIN BORGGREFE & BREITHARDT, G. (Eds.) *Cardiac mapping*. Third Edition ed., Blackwell Publishing.
- LEMAY, M., JACQUEMET, V., FORCLAZ, A., VESIN, J. M. & KAPPENBERGER, L. (2005) Spatiotemporal QRST cancellation method using separate QRS and T-waves templates.
- LEMOLA, K., TING, M., GUPTA, P., ANKER, J. N., CHUGH, A., GOOD, E., REICH, S., TSCHOPP, D., IGIC, P., ELMOUCHI, D., JONGNARANGSIN, K., BOGUN, F., PELOSI, F., MORADY, F. & ORAL, H. (2006) Effects of two different catheter ablation techniques on spectral characteristics of atrial fibrillation. *Journal of the American College of Cardiology* 48:340-348.
- LEWIS, T. (1909) Auricular fibrillation: A common clinical condition *Br Med Journal* 2, 1528.
- LEWIS, T. (1910) Auricular fibrillation and it's relationship to clinical irregularity of the heart *Heart*, 1, 306-372.

- LEWIS, T. (1921) Observations upon flutter and fibrillation. Part IX. The nature of auricular fibrillation as it occurs in patients. *Heart*, 8, 193-227.
- LEWIS, T. (1925) The mechanism and graphic registration of the heart beat. 3rd ed. London, Shaw.
- LEWIS, T., DRURY, A. N. & BULGER, H. A. (1921) Observations upon flutter and fibrillation. Part VII. The effects of vagal stimulation *Heart*, 8, 141-170.
- LIN, Y., HIGA, S., KAO, T., TSO, H., TAI, C., CHANG, S., LO, L., WONGCHAROEN, W. & CHEN, S. (2007) Validation of the frequency spectra obtained from the noncontact unipolar electrograms during atrial fibrillation. *Journal of Cardiovascular Electrophysiology* 18:1147-1153.
- LIN, Y. J., TSAO, H. M., CHANG, S. L., LO, L. W., HU, Y. F., CHANG, C. J., TSAI, W. C., SUENARI, K., HUANG, S. Y., CHANG, H. Y., WU, T. J. & CHEN, S. A. (2010) Role of high dominant frequency sites in nonparoxysmal atrial fibrillation patients: insights from high-density frequency and fractionation mapping. *Heart Rhythm* 7:1255-1262.
- LOVETT, E. G. & ROPELLA, K. M. (1992) Autoregressive spread-spectral analysis of intracardiac electrograms: comparison to Fourier analysis. *Computers in Cardiology 1992. Proceedings*.
- LOVETT, E. G. & ROPELLA, K. M. (1992) Autoregressive spread-spectral analysis of intracardiac electrograms: comparison to Fourier analysis. *Computing in Cardiology (Computers in Cardiology) 503-506. Durham, NC, USA.*
- MACFARLANE, P. W. (2011) The coming of age of electrocardiology. IN MACFARLANE, P. W., OOSTEROM, A. V., PAHLM, O., KLIGFIELD, P., JANSE, M. & CAMM, A. J. (Eds.) *Comprehensive electrocardiology*. London, Springer.
- MADEIRO, J. P. V., CORTEZ, P. C., MARQUES, J. A. L., SEISDEDOS, C. R. V. & SOBRINHO, C. R. M. R. (2012) An innovative approach of QRS segmentation based on first-derivative, hilbert and wavelet transforms. *Medical Engineering and Physics* 34(9):1236-1246.
- MAINARDI LT, PORTA A, CALCAGNINI G, BARTOLINI P, MICHELUCCI A & S., C. (2001) Linear and non-linear analysis of atrial signals and local activation period series during atrial-fibrillation episodes. *Medical & Biological Engineering & Computing* 39:249-54.
- MANDAPATI, R., SKANES, A., CHEN, J., BERENFELD, O. & JALIFE, J. (2000) Stable microreentrant sources as a mechanism of atrial fibrillation in the isolated sheep heart. *Circulation* 101:194-199.
- MANSOUR, M., MANDAPATI, R., BERENFELD, O., CHEN, J., SAMIE, F. H. & JALIFE, J. (2001) Left-to-right gradient of atrial frequencies during acute atrial fibrillation in the isolated sheep heart. *Circulation* 103:2631-2636.
- MARPLE, S. L., JR. (1987) Digital spectral analysis. New Jersey, Prentice-Hall.
- MEDICAL, S. J. (2011) Instruction for use - international edition. EnSite v.8.0.
- MEDICAL, S. J. (2012) EnSite system non-contact mapping introduction course. Non-contact mapping University. St. Jude Medical.
- MINES, G. R. (1913) On dynamic equilibrium in the heart. *The Journal of Physiology* 46:349-383.
- MIRANDA, R. I., SIMPSON, C. S., MICHAEL, K. A., ABDOLLAH, H., BARANCHUK, A. M. & REDFEARN, D. P. (2010) Advances in the treatment of atrial fibrillation. *Minerva Cardioangiologica* 58:637-48.
- MOE, G. K. (1962) On the multiple wavelet hypothesis of atrial fibrillation. *Archives Internationales de Pharmacodynamie et de Therapie* 140:183-8.
- MOE, G. K. & ABILDSKOV, J. A. (1959) Atrial fibrillation as a self-sustaining arrhythmia independent of focal discharge. *American Heart Journal* 58:59-70.
- MOE, G. K., RHEINOLDT, W. C. & ABILDSKOV, J. A. (1964) A computer model of atrial fibrillation. *American Heart Journal* 67:200-220.
- MOMMERSTEEG, M. T. M., CHRISTOFFELS, V. M., ANDERSON, R. H. & MOORMAN, A. F. M. (2009) Atrial fibrillation: a developmental point of view. *Heart Rhythm* 6:1818-1824.
- MONIR, G. & POLLAK, S. J. (2008) Consistency of the CFAE phenomena using custom software for automated detection of complex fractionated atrial electrograms (CFAEs) in the left atrium during atrial fibrillation. *Journal of Cardiovascular Electrophysiology* 19:915-919.
- NADEMANEE, K. (2011) Mapping of complex fractionated atrial electrograms (CFAE) as target sites for AF ablation. *The Bangkok Medical Journal* 2:67-72.
- NADEMANEE, K., MCKENZIE, J., KOSAR, E., SCHWAB, M., SUNSANEWITAYAKUL, B., VASAVAKUL, T., KHUNNAWAT, C. & NGARMUKOS, T. (2004) A new approach for catheter ablation of atrial fibrillation: mapping of the electrophysiologic substrate. *Journal of the American College of Cardiology* 43:2044-2053

- NADEMANEE, K., SCHWAB, M. C., KOSAR, E. M., KARWECKI, M., MORAN, M. D., VISESSOOK, N., MICHAEL, A. D. & NGARMUKOS, T. (2008) Clinical outcomes of catheter substrate ablation for high-risk patients with atrial fibrillation. *Journal of the American College of Cardiology* 51:843-849.
- NARAYAN, S. M., KRUMMEN, D. E. & RAPPEL, W.-J. (2012a) Clinical mapping approach to diagnose electrical rotors and focal impulse sources for human atrial fibrillation. *Journal of Cardiovascular Electrophysiology* 23:447-454.
- NARAYAN, S. M., KRUMMEN, D. E., SHIVKUMAR, K., CLOPTON, P., RAPPEL, W.-J. & MILLER, J. M. (2012b) Treatment of atrial fibrillation by the ablation of localized sources: CONFIRM (conventional ablation for atrial fibrillation with or without focal impulse and rotor modulation) trial. *Journal of the American College of Cardiology* 60:628-636.
- NATTEL, S. (2002) New ideas about atrial fibrillation 50 years on. *Nature*, 415, 219-226.
- NATTEL, S. & EHRlich, J. R. (2004) Atrial fibrillation. IN JALIFE, J. & ZIPES, D. P. (Eds.) *Cardiac electrophysiology: from cell to bedside*. China, SAUNDERS.
- NERBONNE, J. M. (2004) Heterogeneous expression of potassium channels in the mammalian myocardium. IN JALIFE, J. & ZIPES, D. P. (Eds.) *Cardiac electrophysiology: from cell to bedside*. China, SAUNDERS.
- NERBONNE, J. M. & KASS, R. S. (2005) Molecular physiology of cardiac repolarization. *Physiological Reviews* 85:1205-1253.
- NG, J. & GOLDBERGER, J. J. (2007) Understanding and interpreting dominant frequency analysis of af electrograms. *Journal of Cardiovascular Electrophysiology* 18:680-685.
- NG, J. & GOLDBERGER, J. J. (2011) Time- and frequency-domain analysis of AF electrograms: simple approaches to a complex arrhythmia? *Heart Rhythm* 8:1766-1768.
- NG, J., KADISH, A. H. & GOLDBERGER, J. J. (2006) Effect of electrogram characteristics on the relationship of dominant frequency to atrial activation rate in atrial fibrillation. *Heart Rhythm* 3:1295-1305.
- NG, J., KADISH, A. H. & GOLDBERGER, J. J. (2007) Technical considerations for dominant frequency analysis. *Journal of Cardiovascular Electrophysiology* 18:757-764.
- NYGARDS, M. E. & SÖRNMO, L. (1983) Delineation of the QRS complex using the envelope of the e.c.g. *Medical and Biological Engineering and Computing* 21:538-547.
- OLMOS, R. D. (2008) Fibrilação atrial aguda na emergência. *Annals of Emergency Medicine* 52:322-328.
- PACHÓN, J. C. M., PACHÓN, E. I. M., LOBO, T. J., PACHÓN, M. Z. C., PACHÓN, J. C. M., PACHÓN, D. Q. V., VARGAS, R. N. A., PIEGAS, L. S. & JATENE, A. D. (2007) Ablação da fibrilação atrial por cateter com radiofrequência guiada por mapeamento espectral endocárdico dos “ninhos de fa” em ritmo sinusal. *Arquivo Brasileiro de Cardiologia* 89:140-150.
- PANDIT, S. V. & JALIFE, J. (2013) Rotors and the dynamics of cardiac fibrillation. *Circulation Research* 112:849-862.
- PARZEN, E. (1975) Multiple time series: determining the order of approximating autoregressive schemes. *Technical Report no. 23. Buffalo: Statistical Sciences Division, State University of New York, Buffalo, NY.*
- PINHEIRO, J., BATES, D., DEBROY, S., SARKAR, D. & AND THE R DEVELOPMENT CORE TEAM (2012) Nlme: linear and nonlinear mixed effects models. IN PACKAGE, R. (Ed.) version 3.1-103 ed.
- PORTER, M., SPEAR, W., AKAR, J. G., HELMS, R. A. Y., BRYSEWICZ, N., SANTUCCI, P. & WILBER, D. J. (2008) Prospective study of atrial fibrillation termination during ablation guided by automated detection of fractionated electrograms. *Journal of Cardiovascular Electrophysiology* 19:613-620.
- PRYSTOWSKY, E. N. (2008) The history of atrial fibrillation: the last 100 years. *Journal of Cardiovascular Electrophysiology* 19:575-582.
- QINGHUA, Z., MANRIQUEZ, A. I., MEDIGUE, C., PAPELIER, Y. & SORINE, M. (2006) An algorithm for robust and efficient location of T-wave ends in electrocardiograms. *IEEE Transactions on Biomedical Engineering* 53:2544-2552.
- RAÚL, A. & JOSÉ JOAQUÍN, R. (2009) Time and frequency recurrence analysis of persistent atrial fibrillation after electrical cardioversion. *Physiological Measurement* 30:479-489.
- RENSMA, P. L., ALLESSIE, M. A., LAMMERS, W. J., BONKE, F. I. & SCHALIJ, M. J. (1988) Length of excitation wave and susceptibility to reentrant atrial arrhythmias in normal conscious dogs. *Circulation Research* 62:395-410.

- ROGERS, J. M. (2004) Combined phase singularity and wavefront analysis for optical maps of ventricular fibrillation. *IEEE Transactions on Biomedical Engineering* 51:56-65.
- ROPELLA, K. M., SAHAKIAN, A. V., BAERMAN, J. M. & SWIRYN, S. (1988) Effects of procainamide on intra-atrial electrograms during atrial fibrillation: implications for detection algorithms [published erratum *Circulation* 1988 77(6):1344]. *Circulation* 77:1047-1054.
- ROSENBAUM, D. S. & COHEN, R. J. (1990) Frequency based measures of atrial fibrillation in man. *IEEE Engineering in Medicine and Biology* 12:582-583.
- ROSTOCK, T., SALUKHE, T. V., STEVEN, D., DREWITZ, I., HOFFMANN, B. A., BOCK, K., SERVATIUS, H., MULLERLEILE, K., SULTAN, A., GOSAU, N., MEINERTZ, T., WEGSCHEIDER, K. & WILLEMS, S. (2011) Long-term single- and multiple-procedure outcome and predictors of success after catheter ablation for persistent atrial fibrillation. *Heart rhythm* 8:1391-1397.
- ROUX, J. F., GOJRATY, S., BALA, R., LIU, C. F., HUTCHINSON, M. D., DIXIT, S., CALLANS, D. J., MARCHLINSKI, F. & GERSTENFELD, E. P. (2008) Complex fractionated electrogram distribution and temporal stability in patients undergoing atrial fibrillation ablation. *Journal of Cardiovascular Electrophysiology* 19:815-820.
- RYU, K., SAHADEVAN, J., KHRESTIAN, C. M., STAMBLER, B. S. & WALDO, A. L. (2009) Frequency analysis of atrial electrograms identifies conduction pathways from the left to the right atrium during atrial fibrillation—studies in two canine models. *Journal of Cardiovascular Electrophysiology* 20:667-674.
- SAFFITZ, J. E., LERNER, D. L. & YAMADA, K. A. (2004) Gap junction distribution and regulation in the heart. IN JALIFE, J. & ZIPES, D. P. (Eds.) *Cardiac electrophysiology: from cell to bedside*. China, SAUNDERS.
- SAHADEVAN, J., RYU, K., PELTZ, L., KHRESTIAN, C. M., STEWART, R. W., MARKOWITZ, A. H. & WALDO, A. L. (2004) Epicardial mapping of chronic atrial fibrillation in patients. *Circulation* 110:3293-3299.
- SALINET JR, J. L., AHMAD, A., STAFFORD, P., NG, G. A. & SCHLINDWEIN, F. S. (2010a) Three-dimensional frequency mapping from the noncontact unipolar electrograms in atrial fibrillation. *Computing in Cardiology (Computers in Cardiology)* 745-748. Belfast, Northern Ireland.
- SALINET JR, J. L., AHUJA, J., BROWN, P., STAFFORD, P., SCHLINDWEIN, F. S. & NG, G. A. (2012a) Trajectory propagation of dominant frequency areas using high density noncontact mapping reveals distinct behaviour in persistent atrial fibrillation. *Heart Rhythm* 9:S4-5.
- SALINET JR, J. L., BROWN, P. D., AHMAD, A., TUAN, J. H., STAFFORD, P. J., SCHLINDWEIN, F. S. & NG, G. A. (2011a) High density noncontact frequency mapping reveals distinct dominant frequency behaviour in persistent atrial fibrillation. *Heart Rhythm* 8:S146.
- SALINET JR, J. L., BROWN, P. D., LOHIYA, G. R., BIDDER, S., STAFFORD, P., SCHLINDWEIN, F. S. & NG, G. A. (2011c) Evidence for cyclic temporal variability from high frequency re-entrant circuits in persistent atrial fibrillation. *EP Europace* 13:iv20-24.
- SALINET JR, J. L., MADEIRO, J. P. V., CORTEZ, P. C., MARQUES, J. A. L., STAFFORD, P., NG, G. A. & SCHLINDWEIN, F. S. (2012b) Removing ventricular influence from intracardiac atrial fibrillation electrograms. *XXIII Congresso Brasileiro de Engenharia Biomédica (XXIII CBEB)*. Porto de Galinhas, Pernambuco, Brazil.
- SALINET JR, J. L., MADEIRO, J. P. V., CORTEZ, P. C., STAFFORD, P. J., NG, G. A. & SCHLINDWEIN, F. S. (2013a) Analysis of QRS-T subtraction in unipolar atrial fibrillation electrograms. *Medical & Biological Engineering & Computing*, 51, 1381-1391.
- SALINET JR, J. L., MARQUES, J. A. L., TUAN, J., STAFFORD, P., SCHLINDWEIN, F. S. & NG, G. A. (2012c) A new approach to identify and measure fractionated atrial electrograms. *Heart Rhythm* 9:S365-366.
- SALINET JR, J. L., OLIVEIRA, G. N., VANHEUSDEN, F. J., COMBA, J. L. D., NG, G. A. & SCHLINDWEIN, F. S. (2013b) Visualizing intracardiac atrial fibrillation electrograms using spectral analysis. *Computing in Science & Engineering* 15:79-87.
- SALINET JR, J. L., TUAN, J., SANDILANDS, A. J., MADEIRO, J. P. V., STAFFORD, P., SCHLINDWEIN, F. S. & NG, G. A. (2012d) Distinctive patterns of dominant frequency trajectory behaviour exist in persistent atrial fibrillation: characterisation of spatio-temporal instability. *EP Europace* 14:iv3.
- SALINET JR, J. L., TUAN, J., SANDILANDS, A. J., STAFFORD, P., SCHLINDWEIN, F. S. & NG, G. A. (2013d) Distinctive Patterns of Dominant Frequency Trajectory Behaviour in Drug-Refractory Persistent Atrial Fibrillation: Preliminary Characterisation of Spatio-temporal Instability. *Journal of Cardiovascular Electrophysiology*, (In Press) DOI: 10.1111/jce.12331.

- SALINET JR, J. L., TUAN, J., STAFFORD, P., SCHLINDWEIN, F. S. & NG, G. A. (2013c) High density noncontact mapping of persistent atrial fibrillation: spatiotemporal characteristics of dominant frequency and organization index during sequential mapping. *Heart Rhythm* 10:S1-2.
- SALINET JR, J. L., TUAN, J. H., BROWN, P. D., STAFFORD, P. J., NG, G. A. & SCHLINDWEIN, F. S. (2010b) The spatial and temporal variability of the 3D dominant frequency mapping from 2048 noncontact unipolar electrograms in human atrial fibrillation. *EP Europace* 12:ii22.
- SAMIE, F. H., BERENFELD, O., ANUMONWO, J., MIRONOV, S. F., UDASSI, S., BEAUMONT, J., TAFFET, S., PERTSOV, A. M. & JALIFE, J. (2001) Rectification of the background potassium current: a determinant of rotor dynamics in ventricular fibrillation. *Circulation Research* 89: 1216-1223.
- SANDERS, P., BERENFELD, O., HOCINI, M., JAIS, P., VAIDYANATHAN, R., HSU, L., GARRIGUE, S., TAKAHASHI, Y., ROTTER, M., SACHER, F., SCAVÉE, C., PLOUTZ-SNYDER, R., JALIFE, J. & HAISSAGUERRE, M. (2005) Spectral analysis identifies sites of high-frequency activity maintaining atrial fibrillation in humans. *Circulation* 112:789-97.
- SARMAST, F., KOLLI, A., ZAITSEV, A., PARISIAN, K., DHAMMOON, A. S., GUHA, P. K., WARREN, M., ANUMONWO, J. M. B., TAFFET, S. M., BERENFELD, O. & JALIFE, J. (2003) Cholinergic atrial fibrillation: IK,ACh gradients determine unequal left/right atrial frequencies and rotor dynamics. *Cardiovascular Research* 59:863-873.
- SCHERF, D. (1947) Studies on auricular tachycardia caused by aconitine administration. *Proceedings of the Society for Experimental Biology and Medicine* 64:233-239.
- SCHILLING, R. J., KADISH, A. H., PETERS, N. S., GOLDBERGER, J. & DAVIES, D. W. (2000) Endocardial mapping of atrial fibrillation in the human right atrium using a non-contact catheter. *European Heart Journal* 21:550-564.
- SCHILLING, R. J., PETERS, N. S. & DAVIES, D. W. (1999) Feasibility of a noncontact catheter for endocardial mapping of human ventricular tachycardia. *Circulation* 99:2543-2552.
- SCHILLING, R. J., PETERS, N. S. & DAVIES, W. (1998) Simultaneous endocardial mapping in the human left ventricle using a noncontact catheter - comparison of contact and reconstructed electrograms during sinus rhythm. *Circulation* 98:887-898.
- SCHILLING, R. J., PETERS, N. S., GOLDBERGER, J., KADISH, A. H. & DAVIES, D. W. (2001) Characterization of the anatomy and conduction velocities of the human right atrial flutter circuit determined by noncontact mapping. *Journal of the American College of Cardiology* 38:385-393.
- SCHLINDWEIN, F. S. & EVANS, D. H. (1990) Selection of the order of autoregressive models for spectral analysis of doppler ultrasound signals. *Ultrasound in Medicine & Biology* 16:81-91.
- SCHLINDWEIN, F. S. & EVANS, D. H. (1992) Autoregressive spectral analysis as an alternative to fast Fourier transform analysis of doppler ultrasound signals. *Diagnostic Vascular Ultrasound*. Hodder Arnold Publication
- SCHUESSLER, R. B., GRAYSON, T. M., BROMBERG, B. I., COX, J. L. & BOINEAU, J. P. (1992) Cholinergically mediated tachyarrhythmias induced by a single extrastimulus in the isolated canine right atrium. *Circulation Research* 71:1254-67.
- SCHUESSLER, R. B., KAY, M. W., MELBY, S. J., BRANHAM, B. H., BOINEAU, J. P. & DAMIANO, R. J. (2006) Spatial and temporal stability of the dominant frequency of activation in human atrial fibrillation. *Journal of Electrocardiology* 39:S7-S12.
- SEGAL, O. R., KOA-WING, M., JARMAN, J., PETERS, N., MARKIDES, V. & DAVIES, D. W. (2011) Intracardiac Mapping IN MACFARLANE, P. W., OOSTEROM, A. V., PAHLM, O., KLIGFIELD, P., JANSE, M. & CAMM, J. (Eds.) *Comprehensive electrocardiology*. Second ed. London, Springer.
- SHEN, M. J., CHOI, E.-K., TAN, A. Y., HAN, S., SHINOHARA, T., MARUYAMA, M., CHEN, L. S., SHEN, C., HWANG, C., LIN, S.-F. & CHEN, P.-S. (2011) Patterns of baseline autonomic nerve activity and the development of pacing-induced sustained atrial fibrillation. *Heart Rhythm* 8:583-589.
- SHKUROVICH, S., SAHAKIAN, A. V. & SWIRYN, S. (1998) Detection of atrial activity from high-voltage leads of implantable ventricular defibrillators using a cancellation technique. *IEEE Transactions on Biomedical Engineering* 45:229-234.
- SINGH, S. M., HEIST, E. K., KORUTH, J. S., BARRETT, C. D., RUSKIN, J. N. & MANSOUR, M. C. (2009) The relationship between electrogram cycle length and dominant frequency in patients with persistent atrial fibrillation. *Journal of Cardiovascular Electrophysiology* 20:1336-1342.

- SKANES, A., MANDAPATI, R., BERENFELD, O., DAVIDENKO, J. M. & JALIFE, J. (1998) Spatiotemporal periodicity during atrial fibrillation in the isolated sheep heart. *Circulation* 98:1236-1248.
- SLOCUM, J., BYROM, E. & MCCARTHY, L. (1985) Computer detection of atrioventricular dissociation from surface electrocardiograms during wide QRS complex tachycardias. *Circulation* 72:1028-1036.
- SOLHEIM, E., OFF, M., HOFF, P., SCHUSTER, P., OHM, O.-J. & CHEN, J. (2010) Characteristics and distribution of complex fractionated atrial electrograms in patients with paroxysmal and persistent atrial fibrillation. *Journal of Interventional Cardiac Electrophysiology* 28:87-93.
- SÖRNMO, L. & LAGUNA, P. (2005) *Bioelectrical Signal Processing in Cardiac and Neurological Applications*, Oxford, Elsevier.
- SRA, J. & AKHTAR, M. (2007) Mapping techniques for atrial fibrillation ablation. *Current Problems in Cardiology* 32:669-767.
- STEVENSON, W. G. & ALBERT, C. M. (2012) Catheter ablation for paroxysmal atrial fibrillation. *New England Journal of Medicine* 367:1648-1649.
- STEVENSON, W. G. & SOEJIMA, K. (2005) Recording techniques for clinical electrophysiology. *Journal of Cardiovascular Electrophysiology* 16:1017-1022.
- STILES, M. K., BROOKS, A. G., JOHN, B., SHASHIDHAR, WILSON, L., KUKLIK, P., DIMITRI, H., LAU, D. H., ROBERTS-THOMSON, R. L., MACKENZIE, L., WILLOUGHBY, S., YOUNG, G. D. & SANDERS, P. (2008a) The effect of electrogram duration on quantification of complex fractionated atrial electrograms and dominant frequency. *Journal of Cardiovascular Electrophysiology* 19:252-258.
- STILES, M. K., BROOKS, A. G., KUKLIK, P., JOHN, B., DIMITRI, H., LAU, D. H., WILSON, L., DHAR, S., ROBERTS-THOMSON, R. L., MACKENZIE, L., YOUNG, G. D. & SANDERS, P. (2008b) High-density mapping of atrial fibrillation in humans: relationship between high-frequency activation and electrogram fractionation. *Journal of Cardiovascular Electrophysiology* 19: 1245-1253.
- SY, R. W., THIAGALINGAM, A. & STILES, M. K. (2012) Modern electrophysiology mapping techniques. *Heart, Lung and Circulation* 21:364-375.
- TACCARDI, B., ARISI, G., MACCHI, E., BARUFFI, S. & SPAGGIARI, S. (1987) A new intracavitary probe for detecting the site of origin of ectopic ventricular beats during one cardiac cycle. *Circulation* 75:272-281.
- TAI, C.-T., HUANG, J.-L., LIN, Y.-K., HSIEH, M.-H., LEE, P.-C., DING, Y.-A., CHANG, M.-S. & CHEN, S.-A. (2002) Noncontact three-dimensional mapping and ablation of upper loop re-entry originating in the right atrium. *Journal of the American College of Cardiology* 40:746-753.
- TAI, C. & CHEN, S. (2009a) Noncontact mapping of the heart: how and when to use. *Journal of Cardiovascular Electrophysiology* 20:123-126.
- TAI, C. & CHEN, S. (2009b) Noncontact mapping of the heart: how and when to use. *Journal of Cardiovascular Electrophysiology* 20:123-126.
- TAKAHASHI, Y., SANDERS, P., JAIS, P., HOCINI, M., DUBOIS, R., ROTTER, M., ROSTOCK, T., NALLIAH, C. J., SACHER, F., CLÉMENTY, J. & HAISSAGUERRE, M. (2006) Organization of frequency spectra of atrial fibrillation: relevance to radiofrequency catheter ablation. *Journal of Cardiovascular Electrophysiology* 17:382-88.
- TEAM, R Development Core Team (2012) R: A language and environment for statistical computing. R Foundation for Statistical Computing. Vienna, Austria. ISBN 3-900051-07-0, url <http://www.R-project.org/>.
- TERASAWA, T., BALK, E. M., CHUNG, M., GARLITSKI, A. C., ALSHEIKH-ALI, A. A., LAU, J. & IP, S. (2009) Systematic review: comparative effectiveness of radiofrequency catheter ablation for atrial fibrillation. *Annals of Internal Medicine* 151:191-202.
- TORTORA, G. J. & DERRICKSON, B. (2006) The cardiovascular system: The heart. IN ROESCH, B. & STONE, C. (Eds.) *Principles of anatomy and physiology*. 11th ed., John Wiley & Sons, Inc.
- TSUCHIYA, T. (2012) Three-dimensional mapping of cardiac arrhythmias - String of Pearls. *Circulation* 76:572-581.
- TUAN, J., JEILAN, M., KUNDU, S., NICOLSON, W., CHUNG, I., STAFFORD, P. J. & NG, G. A. (2011) Regional fractionation and dominant frequency in persistent atrial fibrillation: effects of left atrial ablation and evidence of spatial relationship. *EP Europace* 13(11):1550-1556.
- UMAPATHY, K., NAIR, K., MASSE, S., KRISHNAN, S., ROGERS, J., NASH, M. P. & NANTHAKUMAR, K. (2010) Phase mapping of cardiac fibrillation. *Circulation: Arrhythmia and Electrophysiology* 3:105-114.

- VERMA, A., WULFFHART, Z., BEARDSALL, M., WHALEY, B., HILL, C. & KHAYKIN, Y. (2008) Spatial and temporal stability of complex fractionated electrograms in patients with persistent atrial fibrillation over longer time periods: relationship to local electrogram cycle length. *Heart Rhythm* 5:1127-1133.
- WAKTARE, J. & CAMM, A. J. (2000) *Atrial Fibrillation*, London, Martin Dunitz, Ltd.
- WAUGH, A. & GRANT, A. (2011) The cardiovascular system. *Ross and Wilson anatomy and physiology in health and illness*. China, CHURCHILL LIVINGSTONE ELSEVIER.
- WIJFFELS, M. C., KIRCHHOF, C. J., DORLAND, R. & ALLESSIE, M. A. (1995) Atrial fibrillation begets atrial fibrillation. A study in awake chronically instrumented goats. *Circulation*, 92, 1954-1968.
- WINFREE, A. T. (1997) Rotors, fibrillation and dimensionality. IN ALEXANDER V. PANFILOV, A. V. H. (Ed.) *Computational biology of the heart*. Chichester, John Wiley & Sons Ltd.
- WINTERBERG, H. (1907) Studien u"ber herzflimmern. I. U ber die wirkung des N. vagus und accelerans auf das Flimmern des Herzens. *Pflugers Arch Physiol* 117, 223-256.
- WOLF, P. A., BENJAMIN, E. J., BELANGER, A. J., KANNEL, W. B., LEVY, D. & D'AGOSTINO, R. B. (1996) Secular trends in the prevalence of atrial fibrillation: the Framingham Study. *American Heart Journal* 131(4):790-795.
- WRIGHT, M., HAISSAGUERRE, M., KNECHT, S., MATSUO, S., O'NEILL, M. D., PHIL, D., NAULT, I., LELLOUCHE, N., HOCINI, M., SACHER, F. & JAIS, P. (2008) State of the art: catheter ablation of atrial fibrillation. *Journal of Cardiovascular Electrophysiology* 20:583-592.
- WYNSBERGHE, D. V., NOBACK, R. C. & CAROLA, R. (1995) The cardiovascular system: The heart. IN PRANCAN, K. M., CLOUD, D. & GORDON, H. (Eds.) *Human anatomy and physiology*. New York, McGraw-Hill, Inc.
- XI, Q., SAHAKIAN, A. V. & SWIRYN, S. (2002) The influence of QRS cancellation on signal characteristics of atrial fibrillation in the surface electrocardiogram. *Computing in Cardiology (Computers in Cardiology)* 13-16. Memphis, Tennessee, USA.
- XI, Q., SAHAKIAN, A. V. & SWIRYN, S. (2003) The effect of QRS cancellation on atrial fibrillatory wave signal characteristics in the surface electrocardiogram. *Journal of Electrocardiology* 36: 243-249.
- YITZHACK SCHWARTZ & BEN-HAIM, S. A. (2009) Principles of nonfluoroscopic electroanatomical and electromechanical cardiac mapping. IN MOHAMMAD SHENASA, GERHARD HINDRICKS, MARTIN BORGGREFE & BREITHARDT, G. (Eds.) *Cardiac mapping*. Third Edition ed., Blackwell Publishing.
- YOSHIDA, K., CHUGH, A., GOOD, E., CRAWFORD, T., MYLES, J., VEERAREDDY, S., BILLAKANTY, S., WONG, W. S., EBINGER, M., PELOSI, F., JONGNARANGSIN, K., BOGUN, F., MORADY, F. & ORAL, H. (2010) A critical decrease in dominant frequency and clinical outcome after catheter ablation of persistent atrial fibrillation. *Heart Rhythm* 7:295-302.
- ZHAO, J., YAO, Y., HUANG, W., SHI, R., ZHANG, S., LEGRICE, I. J., LEVER, N. A. & SMAILL, B. H. (2013) Novel methods for characterization of paroxysmal atrial fibrillation in human left atria. *The Open Biomedical Engineering Journal* 7:29-40.
- ZIPES, D. P. & JALIFE, J. (2004) *Cardiac electrophysiology from cell to bedside*. 4th ed. Philadelphia, SAUNDERS.